

# **Isomerization dynamics of photochromic compounds in solution and single crystals**

**Dissertation**  
**zur Erlangung des Doktorgrades**  
**an der Fakultät für Mathematik, Informatik und**  
**Naturwissenschaften**  
**Fachbereich Physik der Universität Hamburg**

vorgelegt von

**Simon Felix Bittmann**

**Hamburg**

**2022**

Gutachter/innen der Dissertation:	Prof. Dr. Nils Huse Prof. Dr. R. J. Dwayne Miller
Zusammensetzung der Prüfungskommission:	Prof. Dr. Michael Potthoff Prof. Dr. R. J. Dwayne Miller Prof. Dr. Nils Huse Prof. Dr. Robert Blick Prof. Dr. Arwen Pearson
Vorsitzende/r der Prüfungskommission:	Prof. Dr. Michael Potthoff
Datum der Disputation:	08.12.2022
Vorsitzender des Fach-Promotionsausschusses PHYSIK:	Prof. Dr. Wolfgang J. Parak
Leiter des Fachbereichs PHYSIK:	Prof. Dr. Günter H. W. Sigl
Dekan der Fakultät MIN:	Prof. Dr.-Ing. Norbert Ritter

# Eidesstattliche Versicherung / Declaration on oath

Hiermit versichere ich an Eides statt, die vorliegende Dissertationsschrift selbst verfasst und keine anderen als die angegebenen Hilfsmittel und Quellen benutzt zu haben.

Hamburg, den 20.02.2023



Unterschrift des Doktoranden

---

# Abstract

Photochromic compounds are excellent model systems for the study of photoisomerization dynamics with atomic resolution using ultrafast electron diffraction (UED), which promises to deepen the fundamental understanding and optimization of chemical processes. These molecules have multiple stable isomers with distinct absorption properties, which can be selectively converted via light irradiation. Many photochromics undergo isomerization even in the crystalline phase, which is beneficial for the use of time-resolved diffraction techniques. However, before the realization of UED experiments, the suitability of a specific photochromic molecule needs to be assessed and the dynamics characterized, which can be done by means of transient absorption spectroscopy (TAS).

Within the scope of this thesis, representatives from two different classes of photochromics, spiropyrans and diarylethenes, have been investigated by means of TAS and preliminary UED experiments, in both the crystalline phase and solution, including the construction of dedicated optical setups.

Spiropyrans when excited in the ultraviolet undergo a ring-opening and planarization reaction associated with a bathochromic shift of the absorption spectrum into the visible range. The derivative spironaphthopyran (SNP) was studied via TAS in solution and the ring opening found to occur in the  $S_1$  electronic state under formation of an open-ring intermediate with a time constant of 300 fs, followed by relaxation to the planar isomer with a lifetime of 1.2 ps. Based on a newly developed spectral analysis, subsequent vibrational cooling was characterized and associated with lifetimes between 10 and 13 ps.

The TAS results for SNP in the crystalline phase exhibit nearly identical isomerization dynamics, with time constants of 0.3 and 1.3 ps for the formation of the intermediate and product species, respectively. However, population of the open-ring isomer was found to decay with a lifetime of 650 ps. Supported by complementary UED experiments, this process was assigned to restoring forces from the crystal lattice.

In the presence of a strong acid, spiropyrans become protonated having two stable open-ring isomers (Z and E), switchable by light. This motivated TAS investigations into the dynamics of the switching process for two different derivatives (spirobenzopyran and nitro-spirobenzopyran). The forward reaction was found to entail multiple species in the ground state, formed from a rapidly decaying excited state with a lifetime of  $\approx 200$  fs. Subsequent reaction to the planar E-isomer follows a biexponential behavior in the ps-time domain, indicating the involvement of two distinct intermediates. The reverse reaction was determined to occur via an excited-state intermediate with a lifetime of 3.5 ps as well as a ground-state intermediate with a 40 ps lifetime.

The third project in this thesis deals with the photo-induced ring-closing dynamics of three different diarylethene derivatives, ethyl-dithienylethene, butyl-dithienylethene and propyl-difurylethene, which were investigated in a comparative TAS study in solution and single crystals. Varying in the length of the alkyl chains at the reactive carbon atoms

---

between which the bond is formed, as well as exchange of the heteroatom in the aryl-substituents was found to significantly affect the cyclization. The determined reaction time in propyl-difurylene of 300-400 fs was faster than in the dithienylene derivatives, for which two distinct ring-closing pathways were found. Thus, the dominant factor was the nature of the heteroatoms rather than the alkyl length, which points towards the reaction being governed by the electronic structure rather than steric hindrance. Overall, the results from the crystalline samples were less complex than in solution due to the absence of other conformers and cyclization rates generally increased. Furthermore, static electron diffraction tests strongly suggest the suitability of all three compounds for systematic UED studies, since a distinct difference in the diffraction between open- and closed-ring isomer was observed.

---

# Zusammenfassung

Photochrome Verbindungen eignen sich hervorragend als Modellsysteme für die Untersuchung von Photoisomerisationsprozessen mit atomarer Auflösung mithilfe von ultraschneller Elektronenbeugung (UED). Diese Moleküle besitzen mehrere stabile Isomere mit charakteristischen Absorptionseigenschaften und können selektiv durch Einstrahlung von Licht ineinander umgewandelt werden. Darüber hinaus gibt es viele dieser Verbindungen, die auch im Kristall isomerisiert werden können, was der Verwendung von Beugungsmethoden zuträglich ist. Bevor Experimente mit einem bestimmten photochromen Molekül realisiert werden können, muss jedoch deren Eignung überprüft und die Reaktionsdynamik so gut wie möglich charakterisiert werden. Hierzu eignet sich die etablierte Methode der transienten Absorptionsspektroskopie (TAS).

Im Rahmen dieser Dissertation wurden Vertreter zweier unterschiedlicher Klassen photochromer Moleküle mithilfe von TAS und UED-Experimenten untersucht: Spiropyran und Diarylethen. Für beide wurden Versuche im Kristall und in Lösung durchgeführt und die benötigten optischen Aufbauten konstruiert.

In Spiropyranen verursacht die optische Anregung im ultravioletten Bereich einen Bindungsbruch sowie die anschließende Planarisierung des Moleküls, welche mit einer Rotverschiebung des Absorptionsspektrums einhergeht. Dieser Prozess wurde untersucht für Spironaphthopyran (SNP) und die Ergebnisse der TAS in Lösung deuten darauf hin, dass der Bindungsbruch die Bildung eines Intermediats im angeregten Zustand zufolge hat, welches innerhalb von 300 fs nach Anregung entsteht und mit einer Lebensdauer von 1.2 ps zum planaren Produkt reagiert. Eine eigens entwickelte Spektralanalyse erlaubte die Charakterisierung der anschließenden Energiedissipation mit Lebensdauern zwischen 10 und 13 ps.

Die Ergebnisse der TAS an kristallinem SNP zeigen, dass die Isomerisation auch im Kristall stattfindet, und dies auf nahezu identische Weise, mit Zeitkonstanten von 0.3 und 1.3 ps für die jeweiligen Reaktionsschritte. Allerdings wurde beobachtet, dass die Absorption der planaren Spezies, anders als in Lösung, mit einer Lebensdauer von 650 ps abfiel. Dieser Prozess wurde erklärt durch Rückstellkräfte des durch die Isomerisation verzerrten Kristallgitters, wofür Indizien in komplementären UED-Experimenten gefunden wurden.

Spiropyrane agieren in Gegenwart von starken Säuren als Protonakzeptoren, was ebenfalls einen Bindungsbruch zur Folge hat. Die so gebildete Spezies besitzt zwei stabile Konformere (Z und E), welche wiederum durch Lichteinstrahlung ineinander konvertiert werden können. Dieser Prozess wurde untersucht mittels TAS in Lösung für zwei verschiedene Spiropyranderivate, Spirobenzopyran und Nitro-spirobenzopyran. Für die Vorwärtsreaktion wurde eine kurze Lebensdauer des angeregten Zustands von 200 fs festgestellt. Diese Relaxation führt allerdings nicht direkt zur Bildung des E-Isomers, sondern indirekt über mehrere Intermediate im Grundzustand. Die Rückreaktion zum Z-Isomer involviert ein

---

Intermediat im angeregten Zustand und einen metastabilen Grundzustand mit Lebensdauern von 3.5 ps beziehungsweise 40 ps.

Das dritte Projekt dieser Doktorarbeit umfasst die Untersuchung des lichtinduzierten Ringschlusses in drei verschiedenen Diarylethenen (Ethyl-Dithienylethen, Butyl-Dithienylethen und Propyl-Difurylethen) in einer Vergleichsstudie mittels TAS in Lösung und einkristallinen Filmen. Es wurde festgestellt, dass Unterschiede in der Länge der Alkylsubstituenten und in der Art der Heteroatome sowohl Geschwindigkeit als auch Mechanismus der Reaktion beeinflussen. Während für den Ringschluss in Propyl-Difurylethen eine direkte Relaxation mit einer Zeitkonstante von 300-400 fs ermittelt wurde, wurden für die beiden Dithienylethene zwei verschiedene Reaktionswege gefunden. Von diesen waren selbst die schnelleren Reaktionspfade jeweils langsamer als im untersuchten Difurylethen. Es wurde somit geschlossen, dass die Art der Heteroatome und damit einhergehende Veränderungen in der elektronischen Struktur des Moleküls maßgeblicher sind als die Länge der Alkylsubstituenten und mögliche damit assoziierte sterische Effekte. Verglichen mit den Lösungen waren die TAS-Ergebnisse im Kristall weniger komplex und der Ringschluss generell beschleunigt. Zusätzlich zu den TAS-Experimenten wurden statische Elektronenbeugungsversuche durchgeführt, bei denen charakteristische Intensitätsänderungen beobachtet wurden, was alle drei Verbindungen als exzellente Kandidaten für Experimente mit zeitaufgelöster Beugung ausweist.

---

# Acknowledgements

I would like to thank the many people who have supported me throughout the years in my scientific undertakings at the Max-Planck Institute for the Structure and Dynamics of Matter. I sincerely thank my supervisor Prof. Dr. R. J. Dwayne Miller for sharing his vision and enthusiasm for science with me, as well as ideas on how to realize my envisioned experiments. His genuine concern for my progress and his willingness to provide advice whenever things did not go as planned, despite all his various obligations, were highly appreciated. I also thank my co-supervisor Dr. Heinrich Schwoerer, with whom I could always discuss the state of my projects and who supported me in various ways, for instance in planning the optical setups for my experiments. I thank Prof. Dr. Nils Huse for taking over formally as thesis supervisor after Dwayne's transition back to Toronto and for regular discussions of my scientific progress.

Most of the skills I learned in the course of my work, I owe to the thorough introduction into the experimental methods by Dr. Khalid Siddiqui and Dr. Stuart Hayes. They equipped me with the tools I needed to start tackling my research projects autonomously and which even allowed me to start supporting others in their scientific works. Besides that and maybe even more importantly, they have been great colleagues to work alongside with in the laboratory.

Furthermore, I would like to thank Dr. Raison Dsouza not only for his contributions to our shared projects, but also for being a great friend. Further thanks are expressed to Soumyajit Mitra, who shared the lab with me in the second half of my PhD and with whom I worked together on a few projects, for stimulating scientific and non-scientific conversations. Dr. Valentyn Prokhorenko's guidance on various aspects of time-resolved spectroscopy and its analysis was highly appreciated and he kindly provided me with a few analysis scripts, based on which I wrote my own. I thank Dr. Ayman Mostafa for collaboration on the protonated spiropyrans and Dr. Ajay Jha, Dr. Hong-Guang Duan and Dr. Vandana Tiwari for many small, but helpful exchanges.

I cordially thank Dr. Kamil Krawczyk and Dr. Antoine Sarracini not only for allowing me to work with their UED setup at the University of Toronto, but also for actively helping me in the lab and of course for a very warm welcome. I will always gratefully remember the brief, but intense period of time I spent there. I would like to extend these thanks to the other members of the group in Toronto, who made my stay more than pleasant, especially Dr. Olivier Paré-Labrosse, Dr. Ryan Field, Dr. Pascal Hogan-Lamarre, Nariman Khazai and Dr. Lai Chung Liu. I also thank Dr. Yifeng Jiang for involving me in a research project of his and the accompanying scientific discussions.

On the Hamburg side, I would like to thank all members of the former atomically resolved dynamics department and the SSU machine physics for a pleasant working environment and all sorts of enjoyable activities outside of work. In particular I thank my colleagues and friends Dr. Lindsey Bultema, Hyein Hwang, Meghanad Kayanattil, Dr. Andriy Kru-

---

tilin, Djordje Gitaric, Nita Ghosh, Dr. Rajib Ghosh, Dr. Andreas Rossos, Dr. Maria Katsiaflaka, Dr. Sascha Epp, Dr. Gabriele Tauscher, Dr. Friedjof Tellkamp, Hendrik Schikora, Jan-Philipp Leimkohl, Dr. Pedram Mehrabi, Dr. Robert Bücken and Dr. Günther Kassier for their companionship and help in various ways. Furthermore, I want to thank all of my friends outside of work, who have provided an important balance for the sake of my own well-being, especially Hans Werners, Sebastian Graf-Schreiber, Merle Schreiber, Sönke Wengler-Rust, and all members of skalinka.

Lastly, I would like to thank my family who has thoroughly supported me and given me joy throughout the years: My parents Magdalena and Felix, my brother Jonas and his family, and of course my own family: my wife Anke and my son Linus.

---

# Contents

<b>1</b>	<b>Introduction</b>	<b>1</b>
1.1	Towards Direct Observation of Chemical Dynamics . . . . .	1
1.2	Photochromic Molecules as Model Systems . . . . .	4
1.3	Scope of the Thesis . . . . .	5
1.4	Contributions . . . . .	6
<b>2</b>	<b>Experimental Methods and Setups</b>	<b>8</b>
2.1	Ultrafast Optics . . . . .	8
2.1.1	Ultrashort optical pulses and their generation . . . . .	8
2.1.2	Light propagation through a medium . . . . .	10
2.1.3	Pulse compression . . . . .	11
2.1.4	Non-linear optics . . . . .	11
2.2	Laser Systems . . . . .	14
2.3	Non-collinear Optical Parametric Amplifiers . . . . .	15
2.3.1	Broadband phase matching . . . . .	16
2.3.2	NOPA setups . . . . .	17
2.4	Transient Absorption Spectroscopy . . . . .	21
2.4.1	Probing electronic states and their populations . . . . .	21
2.4.2	Optical setup . . . . .	25
2.4.3	Data acquisition . . . . .	29
2.4.4	Setup characterization . . . . .	31
2.4.5	Measurement and processing routines . . . . .	32
2.4.6	Data analysis methods . . . . .	35
2.4.7	Interactive data analysis software . . . . .	41
2.5	Ultrafast Electron Diffraction . . . . .	42
2.5.1	Electron diffraction fundamentals . . . . .	43
2.5.2	Electron pulse generation and propagation . . . . .	46
2.5.3	Experimental approaches and setups . . . . .	47
2.6	Sample Preparation . . . . .	51
2.6.1	Crystallization . . . . .	51
2.6.2	Ultramicrotomy . . . . .	52

---

<b>3</b>	<b>Ring-Opening Dynamics of Spiroanthopyran</b>	<b>55</b>
3.1	Spiroanthopyran Photochemistry . . . . .	55
3.2	Transient Absorption of Spiroanthopyran in Solution . . . . .	58
3.2.1	Solution preparation and steady-state absorption . . . . .	59
3.2.2	Transient absorption experiments . . . . .	62
3.2.3	Theoretical studies . . . . .	75
3.2.4	Concluding discussion . . . . .	78
3.3	Transient Absorption Spectroscopy of Spiroanthopyran in Crystal . . . . .	79
3.3.1	Sample preparation . . . . .	79
3.3.2	Experimental details . . . . .	80
3.3.3	Observations . . . . .	81
3.3.4	Analysis and discussion . . . . .	82
3.3.5	Summary . . . . .	89
3.4	Ultrafast Electron Diffraction . . . . .	89
3.4.1	Experimental details . . . . .	90
3.4.2	Results . . . . .	90
3.4.3	Discussion . . . . .	93
3.5	Summary and Outlook . . . . .	95
<b>4</b>	<b>Isomerization Dynamics of pH-gated Spiroanthopyrans</b>	<b>97</b>
4.1	Acidochromism in Spiroanthopyrans . . . . .	97
4.2	Solution Preparation and Steady-State Absorption . . . . .	100
4.3	Z-to-E-Isomerization Dynamics . . . . .	102
4.3.1	Experimental details . . . . .	103
4.3.2	Results and analysis . . . . .	104
4.3.3	Concluding discussion . . . . .	119
4.4	E-to-Z-Isomerization Dynamics . . . . .	121
4.4.1	Experimental details . . . . .	121
4.4.2	E-Nitro-MCH <sup>+</sup> TA . . . . .	122
4.4.3	E-MCH <sup>+</sup> TA . . . . .	131
4.4.4	Concluding discussion . . . . .	134
4.5	Light-Induced Protonation of Spirobenzopyran in H <sub>3</sub> PO <sub>4</sub> Solution . . . . .	135
4.5.1	Experimental details . . . . .	135
4.5.2	Results and discussion . . . . .	136
4.5.3	Conclusion . . . . .	140
4.6	Summary and Outlook . . . . .	141
<b>5</b>	<b>Ring-Closing Dynamics of Diarylethenes</b>	<b>143</b>
5.1	Ring-Closing Reaction in Diarylethene Derivatives . . . . .	144
5.1.1	Diarylethene photochromism . . . . .	144

---

5.1.2	Relevant reported studies . . . . .	146
5.2	Experimental Details . . . . .	153
5.2.1	Sample preparation . . . . .	153
5.2.2	Transient absorption . . . . .	154
5.2.3	Electron diffraction . . . . .	154
5.3	Difurylene Cyclization Dynamics . . . . .	155
5.3.1	Solution TA . . . . .	155
5.3.2	Crystal TA . . . . .	160
5.3.3	Summary . . . . .	164
5.4	Dithienylene Cyclization Dynamics . . . . .	164
5.4.1	Solution TA . . . . .	164
5.4.2	Crystal TA . . . . .	174
5.4.3	Summary . . . . .	180
5.5	Electron Diffraction Experiments . . . . .	181
5.5.1	Photostationary state signal . . . . .	181
5.5.2	Time-resolved tests and future work . . . . .	185
5.6	Concluding discussion . . . . .	186
<b>6</b>	<b>Conclusion</b>	<b>189</b>
	<b>Bibliography</b>	<b>190</b>
<b>A</b>	<b>Appendix</b>	<b>216</b>
A.1	Analysis Software . . . . .	216
A.1.1	Global and target analysis . . . . .	216
A.1.2	Trace fits and DLSA . . . . .	219
A.2	Steady-State Absorption Spectroscopy . . . . .	219
A.2.1	Excitation fraction calculation . . . . .	220
A.2.2	Protonated spiropyrans excitation fractions . . . . .	222
A.2.3	Diarylene absorption spectra . . . . .	222
A.3	Fluence Dependences . . . . .	223
A.4	Transient Absorption Addendum . . . . .	228
A.4.1	SNP solution . . . . .	228
A.4.2	SNP crystal . . . . .	230
A.4.3	Protonated spiropyrans . . . . .	234
A.4.4	Diarylene . . . . .	239
A.5	Electron diffraction . . . . .	239
A.5.1	Orientation finding and indexing . . . . .	239
A.5.2	SNP ED addendum . . . . .	239
A.5.3	DTE UED frame analysis . . . . .	240
A.6	Optical Setups Addendum . . . . .	245

---

A.7	Miscellaneous . . . . .	246
A.7.1	Kinetic model derivation . . . . .	246
A.7.2	Beam size calculation . . . . .	248
A.7.3	Peak fluence calculation . . . . .	248
A.7.4	NOPA phase matching angle calculation . . . . .	249
A.7.5	Electron pulse generation . . . . .	250

---

# List of Figures

2.1	Example for an ultrashort optical pulse. . . . .	9
2.2	Working principle of a prism compressor. . . . .	12
2.3	Beam geometry in non-collinear optical parametric amplification. . . . .	16
2.4	Vis-NOPA phase matching angle for various internal angles. . . . .	17
2.5	Schematic of the NOPA setup for UV pulse generation. . . . .	18
2.6	Schematic of the SFG setup for UV pulse generation. . . . .	19
2.7	NOPA spectra (vis and UV). . . . .	20
2.8	Signals in transient absorption spectroscopy and their interpretation. . . . .	23
2.9	Transient absorption spectroscopy setup. . . . .	27
2.10	Dual spectrometer for parallel probe referencing. . . . .	30
2.11	Measurements and fit of the CPM in the TAS setup. . . . .	33
2.12	Time-zero scans in the TAS setup. . . . .	34
2.13	Exemplary TA fluence dependence measurement. . . . .	36
2.14	Main page of the TA analysis GUI. . . . .	42
2.15	Example for an electron diffraction pattern. . . . .	43
2.16	DC electron gun schematic. . . . .	49
2.17	RF electron gun pulse compression scheme. . . . .	50
2.18	Crystallization via vapor diffusion. . . . .	51
2.19	Ultramicrotomy working principle. . . . .	53
2.20	Ultrathin samples for TAS and UED. . . . .	53
3.1	Reaction scheme of the spiropyran photoisomerization. . . . .	56
3.2	Summary of the dynamics of SNP in solution. . . . .	58
3.3	Steady-state absorption spectra of SNP in solution. . . . .	60
3.4	Steady-state absorption of SNP in solution: Interpretation. . . . .	61
3.5	Visible transient absorption of SNP in solution. . . . .	64
3.6	UV transient absorption of SNP in solution. . . . .	65
3.7	Global analysis of SNP solution TA data (vis). . . . .	67
3.8	Kinetic model of SNP solution TA (vis). . . . .	68
3.9	Global analysis of SNP solution TA data (UV). . . . .	70
3.10	Dynamic line-shape analysis of SNP in solution. . . . .	73

---

3.11	Bond-breaking time according to MD simulations. . . . .	77
3.12	Schematic of the SNP reaction dynamics in solution. . . . .	78
3.13	Single crystals of spironaphthopyran, grown via vapor diffusion. . . . .	80
3.14	Steady-state absorption of crystalline spironaphthopyran. . . . .	80
3.15	Transient absorption data of crystalline spironaphthopyran. . . . .	82
3.16	SVD of SNP crystal TA data. . . . .	84
3.17	Global fit results for crystalline SNP. . . . .	85
3.18	Global and target analysis of crystalline SNP (sub-ns range). . . . .	86
3.19	SNP crystal TA: Integrated absorption bands. . . . .	88
3.20	Static diffraction pattern from single-crystalline SNP. . . . .	91
3.21	UED signal from photoexcited SNP in crystal. . . . .	92
3.22	UED signal of SNP in polar coordinates. . . . .	92
3.23	Coarse fit of the observed peak broadening in UED of SNP. . . . .	93
3.24	Summary of the SNP dynamics in crystal. . . . .	95
4.1	Z-E-Photoisomerization of protonated spiropyran. . . . .	97
4.2	Photo-acidochromic switching cycle of spiropyran. . . . .	98
4.3	Light-induced protonation cycle of BIPS in H <sub>3</sub> PO <sub>4</sub> . . . . .	100
4.4	Steady-state absorption spectra of protonated spiropyrans. . . . .	101
4.5	Schematic energy diagram of the Z-to-E-isomerization of MCH <sup>+</sup> . . . . .	103
4.6	TA data of MCH <sup>+</sup> Z-to-E-Isomerization . . . . .	105
4.7	TA data of Nitro-MCH <sup>+</sup> Z-to-E-Isomerization . . . . .	106
4.8	Dynamic line shape fit of Z-MCH <sup>+</sup> : Spectral traces . . . . .	107
4.9	Dynamic line shape fit of Z-MCH <sup>+</sup> : Position and width . . . . .	108
4.10	DLSA of Z-MCH <sup>+</sup> : Voigt profile integral fits. . . . .	109
4.11	DLSA results from photoexcited Z-Nitro-MCH <sup>+</sup> TA. . . . .	113
4.12	Z-to-E-isomerization of protonated Spiropyrans: Global analysis . . . . .	116
4.13	Z-Nitro-MCH <sup>+</sup> TA: Single-point kinetic fits. . . . .	118
4.14	Schematic energy diagram of the Z-to-E-isomerization of MCH <sup>+</sup> . . . . .	120
4.15	Summary of the E-to-Z-isomerization of protonated spiropyran. . . . .	121
4.16	Vis TA data of E-Nitro-MCH <sup>+</sup> . . . . .	123
4.17	UV TA data of E-Nitro-MCH <sup>+</sup> . . . . .	124
4.18	Single-point kinetic fits of photoexcited E-Nitro-MCH <sup>+</sup> in the visible . . . . .	125
4.19	SVD of E-Nitro-MCH <sup>+</sup> TA . . . . .	127
4.20	Global and target analysis of E-Nitro-MCH <sup>+</sup> TA in the visible. . . . .	128
4.21	Global fit of the UV-TA data from E-Nitro-MCH <sup>+</sup> . . . . .	130
4.22	Vis TA data of E-MCH <sup>+</sup> . . . . .	132
4.23	Single-point exponential fits of photoexcited E-MCH <sup>+</sup> . . . . .	133
4.24	Summary of the E-to-Z-isomerization of protonated spirobenzopyran. . . . .	134
4.25	TA of BIPS in AcN/H <sub>3</sub> PO <sub>4</sub> . . . . .	137

---

4.26	Target analysis results of BIPS in AcN/H <sub>3</sub> PO <sub>4</sub> . . . . .	138
4.27	BIPS TA in H <sub>3</sub> PO <sub>4</sub> /AcN: Target analysis and integral fit. . . . .	139
4.28	TA of BIPS in H <sub>3</sub> PO <sub>4</sub> /AcN without solution exchange. . . . .	140
5.1	Results summary for the investigated diarylethene derivatives. . . . .	143
5.2	Diarylethene reaction scheme and investigated derivatives. . . . .	145
5.3	Steady-state absorption spectra of the investigated derivatives. . . . .	147
5.4	TA spectra of Me-DTE in <i>n</i> -hexane. . . . .	151
5.5	Summary of the Pr-DFE cyclization dynamics. . . . .	156
5.6	Pr-DFE solution TA data. . . . .	157
5.7	Pr-DFE solution TA: Global and target analysis. . . . .	158
5.8	Semi-sequential global fit of photoexcited Pr-DFE in solution. . . . .	158
5.9	TA of single-crystalline Pr-DFE. . . . .	161
5.10	Global and target analysis of photoexcited Pr-DFE in crystal. . . . .	162
5.11	Schematic of the Pr-DFE reaction dynamics. . . . .	163
5.12	Summary of the DTE cyclization dynamics. . . . .	165
5.13	TA data from Et-DTE in AcN. . . . .	166
5.14	Global and target analysis of Et-DTE in solution. . . . .	167
5.15	Et-DTE solution TA: Exponential fits. . . . .	168
5.16	Bu-DTE solution TA data. . . . .	169
5.17	Bu-DTE solution TA: Global and target analysis. . . . .	170
5.18	Bu-DTE solution TA: Kinetic fits. . . . .	171
5.19	TA of single-crystalline Et-DTE. . . . .	175
5.20	Et-DTE crystal TA: Global and target analysis. . . . .	176
5.21	TA of single-crystalline Bu-DTE. . . . .	177
5.22	Bu-DTE crystal TA: Global and target analysis. . . . .	178
5.23	Crystalline DTE TA: Branched sequential models. . . . .	179
5.24	Summary of the dynamics of photoexcited DTE derivatives. . . . .	180
5.25	Diarylethene static electron diffraction patterns. . . . .	182
5.26	PSS difference diffraction patterns of the three derivatives. . . . .	183
A.1	TAS analysis software – global fit page. . . . .	217
A.2	TAS analysis software – global fit results . . . . .	218
A.3	TAS analysis software – line fit page. . . . .	220
A.4	TAS analysis software – DLSA window. . . . .	221
A.5	Diarylethene steady-state absorption spectra. . . . .	223
A.6	Excitation parameter dependence analysis software. . . . .	224
A.7	Fluence dependence analysis of SNP. . . . .	225
A.8	Fluence dependence analysis of HNBIPS <sup>+</sup> . . . . .	226
A.9	Fluence dependence analysis of BIPS and HBIPS <sup>+</sup> . . . . .	226
A.10	Fluence dependence analysis for the diarylethenes. . . . .	227

---

---

A.11 Global fits of SNP in the visible (1 ns range) . . . . .	228
A.12 Centers of gravity of SNP TA spectra . . . . .	229
A.13 Dynamic line shape analysis of SNP in <i>n</i> -hexane . . . . .	230
A.14 Dynamic line shape analysis of SNP in acetonitrile . . . . .	231
A.15 Dynamic line shape analysis of SNP in ethanol . . . . .	232
A.16 Populations from MD simulations of SNP. . . . .	232
A.17 SNP crystal TA: Additional spectral traces. . . . .	233
A.18 Dynamic line shape analysis of photoexcited Z-MCH <sup>+</sup> . . . . .	234
A.19 Dynamic line shape analysis of photoexcited Z-Nitro-MCH <sup>+</sup> . . . . .	235
A.20 Dynamic line shape analysis of Z-MCH <sup>+</sup> : Gamma and Sigma . . . . .	236
A.21 E-Nitro-MCH <sup>+</sup> TA: SVD addendum. . . . .	236
A.22 Target analysis of photoexcited E-MCH <sup>+</sup> , probed in the UV. . . . .	237
A.23 Global analysis of BIPS in H <sub>3</sub> PO <sub>4</sub> and non-acidic solutions. . . . .	238
A.24 Pr-DFE TA in crystal: additional kinetic traces. . . . .	239
A.25 Coarse indexing of SNP electron diffraction patterns. . . . .	240
A.26 Coarse indexing of diarylethene electron diffraction patterns. . . . .	241
A.27 Static diffraction pattern of SNP crystals grown by solvent evaporation. . . . .	242
A.28 SNP UED: Exemplary difference signal (time-resolved). . . . .	243
A.29 Total diffraction intensity per image of SNP during a UED scan. . . . .	243
A.30 Frame analysis of DTE differential diffraction. . . . .	244
A.31 CPM of 330 nm pump and visible probe. . . . .	245
A.32 Vis-NOPA example spectra. . . . .	245
A.33 Previous version of the TA setup. . . . .	246

---

# Introduction

## 1.1 Towards Direct Observation of Chemical Dynamics

Chemical phenomena, which constitute the basis for all life, are not static, they are dynamic. A statement seemingly trivial, but often overlooked in a society focused on results. However, and that should be similarly obvious: The process determines the outcome.

The primary step in the tremendously complex process of vision is a simple, photo-induced bond rotation within a small organic molecule, called retinal,<sup>[1,2]</sup> which triggers a cascade of chemical and physical events, all culminating into the formation of an image in the brain.<sup>[3]</sup> Not only is this event remarkably simple, but also highly efficient and fast.<sup>[4]</sup> The reason why that is so significant becomes evident considering what happens to a molecule when it is pushed out of equilibrium upon interaction with light. If a ball is lifted onto the top of a slope, it will roll down due to gravity, but for a molecule consisting of  $N$  atoms, there are  $3N-6$  possible intramolecular motions, or in this analogy  $3N-6$  directions in which the ball could roll, some of them leading upwards, some downwards. How does the "ball" know where to go? How does the retinal molecule know which of its  $N = 49$  atoms to move, and in what directions, in order to reach the product state, which – according to the observed high efficiencies – it appears determined to do? Random fluctuations of the atomic nuclei clearly fail to explain this; there needs to be a reduction in dimensionality from  $3N-6$  to only a few key vibrational modes that couple strongly to the excited state that the molecule is "lifted" into, and which drive a certain chemical reaction.

It is not just to satisfy curiosity why identifying these modes is important. Many photochemical processes in fact suffer from low efficiencies or selectivities and these essential modes may serve as a target for manipulating the reaction towards the desired outcome. This is possible in principle using complex light pulses in dedicated optical setups (*vide infra*), but a more straightforward way is that of chemical modification. Pursuing this based on static, equilibrium structures is what many chemists have done through the years and still do, using educated, trial-and-error synthesis and comparing the different outcomes. The more holistic approach on the other hand is trying to directly observe

the structural dynamics of chemical reactions, which essential molecular motions are involved and how they can be tuned via chemical modification. However, this is also the much less trivial approach, as will be laid out in the following.

The requirements for the direct observation of chemical reactions are sub-Å spatial and sub-100 fs temporal resolution.<sup>12</sup> These inconceivably fast time scales have been accessible experimentally for several decades now, via the use of ultrashort laser pulses, taking advantage of the fact that the rapid speed of light ( $3 \cdot 10^8$  m/s) translates an ultrashort difference in arrival time into more tangible spatial displacements on the order of micrometers ( $10 \text{ fs} \hat{=} 3 \mu\text{m}$ ). Hence, utilizing two optical pulses, one to trigger a certain process and the other to probe it, and varying the time delay between them allows to temporally resolve photo-induced dynamics.

One of the most ubiquitous examples of these so-called pump-probe techniques is the methodology of transient spectroscopy. In transient absorption spectroscopy (TA or TAS) in particular,<sup>3</sup> chemical reaction dynamics can be observed indirectly through associated changes in the absorption properties of the molecules, or more simply put the molecules changing their color, on the femtosecond time scale.<sup>[9–11]</sup> As will be discussed in more detail later,<sup>4</sup> these absorption dynamics provide valuable information about the quantum mechanical states playing a role in the reaction, but the method is not directly sensitive to the structural dynamics. Nevertheless, in specific cases, signatures of molecular vibrations can be found in the TA data, which give information about the eigenfrequencies of particular modes that are essential for the reaction.<sup>[12,13]</sup> In fact, strategies have been developed to specifically drive these modes and thereby steer the chemistry in a particular direction.<sup>5</sup> However, such fortunate cases are not always given. Especially if multiple key modes drive a reaction, a specific vibrational mode to be targeted can become like the proverbial needle in a haystack.

In search for a more immediate way to observe and control chemical reaction dynamics, the advent of ultrafast diffraction techniques and ceaseless efforts of extending their capabilities into the femtosecond domain have recently led to numerous breakthroughs.<sup>[5,16–19]</sup> Based on the interference of a wave scattered off an object, diffraction contains direct structural information<sup>6</sup> if the size of the object and the wavelength are comparable. In

---

<sup>1</sup>One angstrom (Å) is one tenth of a nanometer or a billionth of 10 cm ( $10^{-10}$  m). A femtosecond (fs) is the millionth of a billionth of a second ( $10^{-15}$  s).

<sup>2</sup>This rule of thumb is based on typical atomic displacements whilst moving at the speed of sound [5, 6].

<sup>3</sup>Also known as flash photolysis, the fundamental principle was developed in the middle of the 20<sup>th</sup> century [7], which was awarded with the Nobel Prize in Chemistry in 1967 [8].

<sup>4</sup>Section 2.4, in particular subsection 2.4.1.

<sup>5</sup>Driving photochemical reactions via specific modes through interference between them and a tailored optical pulse is known as coherent control [14, 15].

<sup>6</sup>N.B.: This is a deliberate simplification. Diffraction is directly sensitive to the structure, but part of the information is lost as only the intensity of the diffracted wave is measurable. This can however be overcome either exploiting potential symmetries of the investigated system or through reconstruction using *a priori* knowledge about the investigated species in equilibrium [20].

order to achieve atomic resolution, the most suitable probes are either X-ray or electron pulses,<sup>7</sup> both of which have their own advantages and drawbacks.<sup>[5]</sup> Since no ultrafast X-ray diffraction was carried out for this work, the following overview of what is possible and what has been achieved with ultrafast diffraction will be limited to the case of electrons.

Pioneering time-resolved electron diffraction experiments were already conducted in the 1980's,<sup>[21]</sup> thanks to the relatively straightforward generation of short electron pulses with an ultrafast laser (see section 2.5.2). In the following years, important achievements were made towards atomically resolved chemical dynamics on the picosecond ( $10^{-12}$  s) time scale.<sup>[22–24]</sup> However, it took 20 more years before the crucial regime of a few 100 fs time resolution was reached in 2003,<sup>[25,26]</sup> due to fundamental limitations that needed to be overcome and will be discussed in more detail in a later section. Since then even more improvements have been made,<sup>[27–30]</sup> pushing the time resolution of ultrafast electron diffraction (UED) routinely below the 100 fs barrier,<sup>[31–35]</sup> and even into the attosecond<sup>8</sup> regime.<sup>[36]</sup> These records were set however in the limit of only a small number of electrons per pulse in order to avoid space-charge broadening (*vide infra*), but the source brightness needs to be considered when approaching atomic resolution. It has been demonstrated that time resolutions on the order of 100–200 fs are sufficient to resolve coupled motions in excited molecules, if in exchange the increased source brightness enables resolutions in the 0.01 to 0.001 Å range.<sup>[20]</sup> Since this resolution is lower than the thermal motions of the molecule, it represents the fundamental spatio-temporal limit to imaging chemical reactions.<sup>[19,37]</sup>

Most of the past advancements were made either studying high-symmetry, strongly scattering compounds on the one hand, namely atomic solids<sup>[25,35,38–42]</sup> or so-called 2D materials,<sup>[43,44]</sup> both of which are experimentally more feasible than chemical systems, or small molecules in the gas phase on the other hand.<sup>9</sup> Nevertheless, a variety of crystalline metal-organic compounds have been studied using UED.<sup>[20,52–55]</sup> Rather than "classic" chemical processes such as bond breaking, formation or rotation the investigated structural dynamics were associated with light-induced phase transitions, which have the advantage of being fully reversible allowing for a large number of pump-probe cycles on a sample. Besides the general interest in the investigated phenomena itself, these studies helped pave the way towards the investigation of chemical reaction dynamics, since both experimental and analytical tools and procedures were established and improved to facilitate the work with (metal-)organic materials.

---

<sup>7</sup>Electrons as quantum mechanical objects possess wave properties and thus exhibit diffraction.

<sup>8</sup>1 as =  $10^{-18}$  s.

<sup>9</sup>The requirements of gas-phase UED fundamentally limit the number of available samples for such investigations. Furthermore, the signal-to-noise ratio for crystalline samples is usually better due to the constructive interference from multiple unit cells (see section 2.5.1). Nonetheless, the majority of reported UED studies on chemical systems to date have been carried out in the gas phase, see e.g. refs. [24, 45–51].

## 1.2 Photochromic Molecules as Model Systems

There was however one UED study on the ring closing of a purely organic compound reported by Jean-Ruel et al. in 2013,<sup>[56–58]</sup> the merit of which is difficult to overstate. In addition to the general challenges when dealing with organic molecular crystals in UED, such as thin-film sample preparation on the nanometer scale,<sup>10</sup> vacuum stability and the inherent weak scattering signal from molecules consisting of mostly light atoms,<sup>[59]</sup> the investigated diarylethene molecules were also thermally irreversible. This however is a common feature of the vast majority of chemical reactions where one (or multiple) reactant(s) react to one (or multiple) product(s). There are two general ways to overcome this issue. The first is sample exchange between pump-probe cycles, as it is done in other techniques such as serial synchrotron crystallography.<sup>[60,61]</sup> Besides consuming a high amount of the chemical compound, the necessary vacuum conditions and spatial constraints (see section 2.5.2) would require a highly complex, specialized experimental setup in order to implement this strategy for UED. An analogous way with only one excitation cycle per sample consists in the use of a streak-camera, in which entire scans are mapped onto the detector screen.<sup>[29,62]</sup>

The second general strategy relies on actively reverting the sample into its initial state with another light source.<sup>[56,63]</sup> This evidently requires the product to be photo-reversible, at a wavelength at which the reactant does not absorb, i.e. the product and reactant having distinct colors. A class of molecules undergoing common photochemical reactions, and fulfilling these additional requirements are photochromic molecules.<sup>11</sup> The diarylethenes are such photochromics having two different configurations (isomers), one colorless and only absorbing in the ultraviolet, the other one colored with a prominent absorption band in the visible.<sup>[64]</sup> These isomers are photochemically convertible via ring opening and closing of a central cyclohexadiene core.

Thus, photochromics are an excellent target as model systems for the study of fundamental chemical processes using UED. There is a large variety of not only different diarylethene derivatives, but also other photochromic families such as azobenzenes, fulgides and spiropyranes. Hence, there seems to be a surplus of systems, sitting on the shelf and waiting to be studied by scientists who have the appropriate experimental equipment. In reality of course, it is not as simple as that. The first restriction, which already rules out a lot of compounds, is that current experimental capabilities are mostly limited to crystalline (or gaseous) samples,<sup>12</sup> and therefore the photochromic reaction, typically entailing a significant structural change, needs to be possible in the condensed phase. The next factor to be taken into account is how well-reversible the photochromic molecules are. An inef-

---

<sup>10</sup>See section 2.6.

<sup>11</sup>More information and references on photochromic compounds as well as the specific molecules studied within this work will be given in the respective chapters.

<sup>12</sup>There are ongoing efforts towards UED in solution, the discussion of which would go beyond the scope of this introductory section. Instead, the reader is referred to [65, 66].

efficient photoreversion process or the formation of byproducts may seriously impede the achievable reversibility. Furthermore, excitation of a large number of molecules (either way of the reaction) may permanently damage the sample, or crystal strain itself lead to measurement artifacts, prohibiting reconstruction of the atomically resolved dynamics. Lastly, the general requirements to any UED experiment stated above need still be met. All of these restrictions make careful evaluation of potential candidates crucial prior to the actual UED experiments. One of the most valuable tools for this purpose is the aforementioned transient absorption spectroscopy. Although non-trivial itself, it allows to test a large amount of the demands to a UED sample in a faster and more straightforward way, whilst in itself providing important insight into the chemical reaction dynamics, predominantly in terms of time scales and involved quantum mechanical states.

### 1.3 Scope of the Thesis

It is this duality between elucidating the chemical reaction dynamics of photochromic reactions by means of TAS and testing their suitability for UED investigations of the associated structural changes, that lies at the core of this thesis' work. Several photochromic compounds were investigated, each with their own scientific questions to be answered already on the level of transient absorption, either owing to a lack of published reports or contradictions in the literature.

The first study deals with spironaphthopyran, a representative of the spiropyran family, in both crystal and solution (chapter 3). It was inspired by reports that the photochromic reaction, despite encompassing drastic structural changes, was observed in the crystalline phase.<sup>[67]</sup> Indeed, this was possible to confirm in TAS experiments by comparison to analogous measurements in solution.<sup>13</sup> It turned out however, that standing disagreements regarding interpretation of the solution data were present in the literature, warranting further investigation and culminating in a stand-alone work published in [68]. Furthermore, UED experiments were conducted, the results of which can still be considered preliminary and will be discussed in the final section of the chapter.

One of the challenges for reconstruction of the spiropyran reaction dynamics lies in their complexity, involving bond-breaking and multiple bond rotations, as well as an open-ring reaction intermediate. The addition of a proton to the molecule by aid of a strong acid can thermally stabilize said intermediate structure in the ground state and isolate the bond-breaking step from the subsequent isomerization. This motivated a separate investigation of protonated spiropyrans (chapter 4). The outcome however was not the desired simplification, but yielded a complicated mechanism involving multiple intermediates, for which no indication was found in the non-protonated case. In addition to the forward reaction, it

---

<sup>13</sup>A manuscript based on the TAS experiments on crystalline spiropyran is currently in preparation.

was possible to study the reverse reaction, both of which was carried out for two different spiropyran derivatives (spirobenzopyran and nitrospiropyran).<sup>14</sup>

Lastly, inspired by the previous success in using a diarylethene derivative for UED, a comparative study between three other representatives of this family was conducted pursuing the question how different chemical modification influences the structural dynamics of the ring-closing reaction (chapter 5). Extensive analysis of the TAS results from all three samples in both solution and crystal showed significant differences despite seemingly minor modifications, potential reasons of which will be discussed in more detail. Although due to time constraints, it was not possible to carry out more than test measurements regarding UED, the general suitability of these samples for such experiments was demonstrated and specific requirements determined, which will be laid out in addition.<sup>15</sup>

Preceding these chapters dealing with particular scientific problems, a general chapter introduces the basic concepts necessary to understand the experimental procedures, data analysis methods, as well as the physical interpretation of the obtained results. Several optical setups were constructed or improved for the experiments and will be described in detail. Thus, this chapter covers experimental and analytical methods and concepts ubiquitous throughout this thesis, allowing to be referred back to in the later chapters to avoid redundancy.

## 1.4 Contributions

Scientific work in the modern world is a collaborative effort and this thesis is no exception. In principle, all people acknowledged in the preface have in some manner contributed to this thesis. Nonetheless, the more significant scientific contributions by people other than myself shall be noted in the following. The research was carried out in the group of and the projects supervised by Prof. Dr. R. J. Dwayne Miller and co-supervised by Dr. Heinrich Schworer. The latter was involved specifically in planning, conduction and interpretation of the experiments on protonated spiropyrans (chapter 4). Responsible for the laboratory and involved in all experiments was Dr. Stuart Hayes, who was also in charge of the DC electron gun utilized for the diffraction experiments in chapter 5. The transient absorption setup in its original form was constructed by Dr. Gastón Corthey and Dr. Khalid Siddiqui, The latter initially led the experimental efforts on spironaphthopyran (chapter 3) and contributed to construction of the optical setups as well as the development of the dynamic line shape analysis (see section 2.4.6). Dr. Raison Dsouza carried out TD-DFT molecular dynamics simulations for spiropyran in solution, the results of which are part of his thesis (ref. [69]), but will also be discussed briefly here due to their crucial role in the respective project. The UED experiments on SNP at the University of

---

<sup>14</sup>A manuscript based on the findings in this chapter is currently in preparation, pending complementary theoretical calculations.

<sup>15</sup>The transient absorption results are the basis of another manuscript currently in preparation.

Toronto were carried out together with Dr. Kamil Krawczyk and Dr. Antoine Sarracini. Soumyajit Mitra contributed to the TAS experiments on the diarylethenes (chapter 5), aiding in setup maintenance and optimization as well as building of the prism compressor. Nita Ghosh assisted in the UED tests on diarylethenes and construction of the NOPA for experiments with the Pharos laser system (section 5.5).

# Experimental Methods and Setups

In this chapter, the experimental techniques applied in this work are introduced and explained. In addition to a general overview of each approach, the fundamental physics necessary to understand both the respective working principles and the investigated photochemical processes are summarized briefly. Furthermore, specific designs of the constructed or modified setups as well as the applied data analysis methods are detailed.

## 2.1 Ultrafast Optics

This section provides a brief overview of the most relevant optical processes, in order to facilitate their subsequent description.<sup>1</sup>

### 2.1.1 Ultrashort optical pulses and their generation

An optical pulse is an electromagnetic wave whose amplitude is only finite within a limited time window. It can thus be described in terms of the electric field component  $\vec{E}(t)$  as a plane wave with carrier frequency  $\omega_0$  and temporal phase  $\phi(t)$ , multiplied by a time-dependent envelope function  $\vec{E}_0(t)$ :

$$\vec{E}(t) = \vec{E}_0(t) \exp(i(\omega_0 t - \phi(t))) + c.c. \quad (2.1)$$

As shown in Fig. 2.1, it is common to approximate  $\vec{E}_0(t)$  with a Gaussian function whose full width at half maximum (FWHM) is used as a measure for the pulse duration. Pulses on the order of a picosecond ( $10^{-12}$  s) or shorter fall into the ultrashort regime. Alternatively to the time domain, the pulses can be described in the frequency domain ( $\tilde{E}(\omega)$ ):

$$\tilde{E}(\omega) = E_0(\omega - \omega_0) \exp(-i\phi(\omega - \omega_0)) + E_0(-\omega - \omega_0) \exp(i\phi(-\omega - \omega_0)) \quad (2.2)$$

<sup>1</sup>For the fundamental parts in this section, no individual references will be given. Unless indicated otherwise the content is based on refs. [70–72].

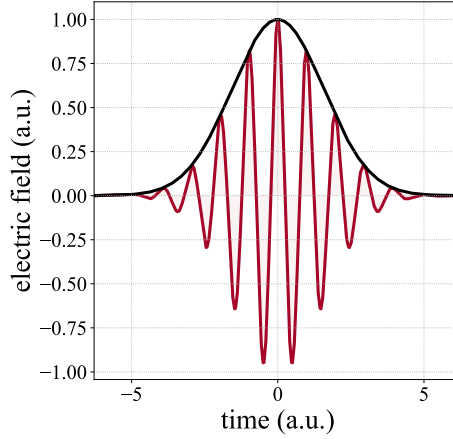


**Figure 2.1:** Simplified example for an ultrashort optical pulse, shown in terms of the electric field component in one dimension (red curve). The black line represents the Gaussian carrier envelope function.

$\varphi(\omega)$  is called the spectral phase and an important quantity for the characterization of ultrashort pulses. The two alternative descriptions are linked by the well-known Fourier transform:

$$E(t) = \frac{1}{2\pi} \int_{-\infty}^{\infty} \tilde{E}(\omega) \exp(i\omega t) d\omega \quad (2.3)$$

$$\tilde{E}(\omega) = \int_{-\infty}^{\infty} E(t) \exp(-i\omega t) dt \quad (2.4)$$

Derived from the Fourier transform, there are several important relationships between  $E(t)$  and  $\tilde{E}(\omega)$ , two of which are especially important for the following discussions. The first one is the time-shift theorem which links a temporal shift  $t_0$  to the multiplication with a phase factor in the frequency domain:<sup>2</sup>

$$\begin{aligned} E(t) &\rightarrow E(t - t_0) \\ \Leftrightarrow \tilde{E}(\omega) &\rightarrow \tilde{E}(\omega) \exp(i\omega t_0) \end{aligned} \quad (2.5)$$

The second important consequence from the Fourier relations is that a short pulse duration (narrow envelope function) corresponds to a broad spectral bandwidth and vice versa. Thus, it is possible to determine a lower limit for the product of duration and bandwidth, which is known as the time-bandwidth-product (TBP) and whose value depends on the shape of the envelope functions. For a Gaussian curve it is given by<sup>3</sup>

$$\Delta\nu\Delta t \geq \frac{2\ln 2}{\pi} \approx 0.441 \quad (2.6)$$

<sup>2</sup>An analogous relationship exists for spectral shifts, but is less relevant for the physics discussed here.

<sup>3</sup>N.B.: In equation 2.6,  $\Delta t$  refers to the temporal width of the pulse intensity rather than the amplitude.

The existence of such a lower limit can be rationalized by considering the generation principle of ultrashort laser pulses via constructive interference of multiple modes. The more modes involved, i.e. the larger the bandwidth, the shorter will be the time range during which there is constructive interference between all of them. Furthermore, for the pulses to be stable, the participating modes need to have a constant (or linear)<sup>4</sup> phase relation. In practice, these requirements are met by mode-locked laser oscillators. The working principle is based on a periodic intensity modulation inside the laser cavity, with a frequency inverse to its round-trip time, which maximizes the gain of modes that are in phase. While this intensity modulation can be achieved actively via acousto- or electro-optic modulators,<sup>[73]</sup> passive strategies such as Kerr-lens mode-locking exist as well.<sup>[74]</sup> In the latter, the non-linear optical effect of self-focusing (*vide infra*) is exploited by arranging the optical elements such that the higher intensity modes, which are focused more strongly, experience higher gain in the laser medium.

### 2.1.2 Light propagation through a medium

Propagation of light pulses through any medium leads to a modulation of the electric field described by the spectral phase transfer function  $\varphi_m(\omega)$  and the spectral amplitude response  $\tilde{R}(\omega)$ .

$$\tilde{E}_{out}(\omega) = \tilde{R}(\omega) \exp(-i\varphi_m(\omega)) \tilde{E}_{in}(\omega). \quad (2.7)$$

The modulation thus leads to an addition of  $\varphi_m(\omega)$  to the initial phase. Since the spectral phase transfer function is generally non-linear in frequency, the resulting spectral phase of the output pulse will be as well. This represents a deviation from the ideal case required for bandwidth-limited pulse durations and induces a broadening of the pulse in time. An approximate description of this effect in dependence of the propagation distance  $L$  can be made by a series expansion of  $\varphi_m(\omega)$  up to the second order, using the relationship between the spectral phase and the corresponding refractive index  $n(\omega)$ :

$$\varphi_m(\omega) = k(\omega)L = \frac{\omega}{c}n(\omega)L \quad (2.8)$$

The first and second derivatives for the expansion immediately follow:

$$\frac{d\varphi_m(\omega)}{d\omega} = \frac{L}{c} \left( n + \omega \frac{dn}{d\omega} \right) \quad (2.9)$$

$$\frac{d^2\varphi_m(\omega)}{d\omega^2} = \frac{L}{c} \left( 2 \frac{dn}{d\omega} + \omega \frac{d^2n}{d\omega^2} \right) \quad (2.10)$$

The first derivative encompasses a linear phase shift, which is equivalent to a delay of the light pulse according to the time-shift theorem (*vide supra*) and therefore called group delay (GD). The second derivative is called the group-delay dispersion (GDD) since the

<sup>4</sup>Linear and constant phase relations are equivalent due to the time-shift theorem.

introduction of a quadratic spectral phase is equivalent to a quadratic temporal phase, which leads to a linear time dependence of the instantaneous frequency, the latter being the first derivative of the former. Therefore, pulses with a finite bandwidth are broadened in time when propagating through a medium, which is commonly referred to as chirp. The GDD normalized to the propagation distance, thus becoming an inherent property of the material, is called group velocity dispersion (GVD).

### 2.1.3 Pulse compression

The group-delay dispersion induced by propagation through transparent media is usually positive leading to the temporal delay of higher frequency components with respect to lower ones (up-chirp), broadening the temporal pulse profile. Therefore, strategies for the compression of non-bandwidth-limited pulses involve the introduction of a negative GDD. The most common principles rely on (spatially) dispersive elements, such as prisms or gratings, in a geometry such that the pathlength for higher frequencies is longer than for lower ones. The simplest case of such a setup is a prism compressor, shown schematically in Fig. 2.2. It consists of two prisms and a mirror, causing the beam to pass through each prism twice.<sup>5</sup> The prisms are oriented such that the pathlength between the first prism and the mirror is longer for shorter wavelengths, which are refracted more strongly. Using angular dispersion thus introduces a negative GDD, which can be calculated to design the compression of a pulse with a known GDD. The depicted design was used within the scope of this thesis to improve the temporal resolution in the experiments as well as the efficiency of certain non-linear optical processes, which will be introduced in the next section.

### 2.1.4 Non-linear optics

As laid out in the previous sections, at moderate light intensities, the medium affects the light pulse, but not vice versa, and the polarization  $\vec{P}(t)$  of the medium responds linearly with the incident electric field depending on the linear susceptibility  $\chi^{(1)}$ . When higher light intensities are reached, the linear approximation for small amplitudes of the polarization breaks down and higher order terms of the response have to be taken into account:

$$\vec{P}(t) = \chi^{(1)} \otimes \vec{E}(t) + \chi^{(2)} \otimes \vec{E}^2(t) + \chi^{(3)} \otimes \vec{E}^3(t) + \dots \quad (2.11)$$

with the n-th order susceptibility tensors  $\chi^{(n)}$ . The involvement of higher-order terms, specifically the second and third orders, gives rise to various non-linear optical effects. Ultrashort pulses typically exhibit high peak powers with the energy condensed in a short

---

<sup>5</sup>Alternatively a symmetric, four-prism configuration can be used, which is easier to adjust but requires more space.

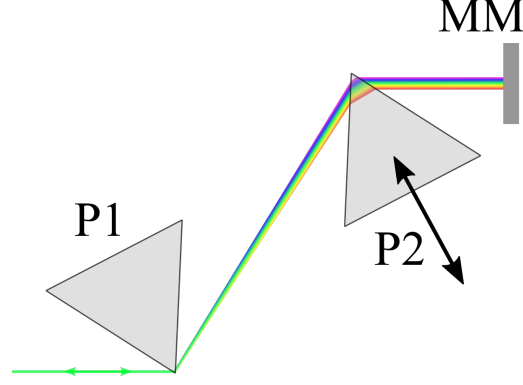


**Figure 2.2:** Working principle of a prism compressor. In this geometry, the optical path-length between the two prisms (P1, P2) is extended for shorter wavelengths, introducing a negative GDD. This is compensated partially by the propagation distance through P2, which can be used to fine-tune the pulse duration. A metallic mirror (MM) back-reflects the beam in order to remove the introduced spatial dispersion, but also reducing the required distance between P1 and P2.

amount of time making these effects accessible as well as their application in ultrafast experimental techniques. The most important non-linear optical phenomena applied within the scope of this thesis will be explained briefly in the following. Most of them are based on the second order term of the series expansion from equation 2.11, formulated in the frequency domain:

$$\vec{P}^{(2)}(\omega) = \chi^{(2)}(\omega; \omega_i, \omega_j) : \vec{E}(\omega_i) \vec{E}(\omega_j) \quad (2.12)$$

Deviating from the single-frequency case discussed before, this equation is generalized to the contribution of two frequencies.<sup>6</sup> A series expansion of the second-order polarization itself results in the following terms:

$$\begin{aligned} P^{(2)}(\omega) \propto & E_1^2 \exp(2i\omega_1 t) + (E_1^*)^2 \exp(-2i\omega_1 t) + E_2^2 \exp(2i\omega_2 t) + (E_2^*)^2 \exp(-2i\omega_2 t) \\ & + 2E_1 E_2 \exp(i(\omega_1 + \omega_2)t) + 2E_1^* E_2^* \exp(-i(\omega_1 + \omega_2)t) \\ & + 2E_1 E_2^* \exp(i(\omega_1 - \omega_2)t) + 2E_1^* E_2 \exp(-i(\omega_1 - \omega_2)t) \\ & + 2|E_1|^2 + 2|E_2|^2 \end{aligned} \quad (2.13)$$

These individual terms can be attributed to different non-linear optical effects. The first four terms represent the generation of oscillatory components at twice the incident frequencies, which is referred to as second harmonic generation (SHG). The second row shows components with the sum of the two fundamental frequencies (sum-frequency generation or mixing, SFG/SFM), while the third row accounts for the difference between them (difference-frequency generation, DFG).

In order to select one of these processes in practice and provide sufficient efficiency, the incident wave and the respective generated waves need to remain in phase, a requirement

<sup>6</sup>The two descriptions are equivalent and the single-frequency case is readily inferred from equation 2.12.

that is called phase matching. In conventional media, this condition is not satisfied since the speed of light in materials is frequency dependent and pulses with different wavelengths generally do not travel through the material at the same speed. In birefringent materials however, there are two different refractive indices for parallel and perpendicular light polarizations,<sup>7</sup> the ordinary and extraordinary refractive indices  $\eta_o$  and  $\eta_e$ . While the former is independent of the light propagation direction,  $\eta_e$  depends on the angle  $\theta$  between the propagation axis and the optical axis of the crystal. Thus, a certain angle exists, where  $\eta_o(\omega)$  is equal to  $\eta_e(\omega')$ , with  $\omega'$  being for instance the second harmonic frequency  $2\omega$  for the case of SHG. This angle is called the phase-matching angle  $\theta_{\text{pm}}$ . For many non-linear processes at common laser wavelengths, birefringent crystals are commercially available, being cut in such a way that a perpendicularly incident beam propagates along the respective phase-matching angle.

Instead of involving higher order non-linear terms of the polarization, the third and fourth harmonic can be generated by either the combination of SHG and SFG or two-stage SHG, respectively. For the third harmonic (THG), the output of the SHG is mixed with the fundamental beam in another crystal, cut to the appropriate phase matching angle. In practice, the inherent group delay between the two differently colored pulses needs to be compensated. Since the output wave in (Type I) SHG has a polarization perpendicular to the fundamental, this can be achieved with another birefringent crystal. Fourth-harmonic generation (FHG) uses the output directly for a second SHG process and therefore only requires sufficient peak intensities of the pulses.

The final non-linear optical effect to be discussed here and vital for the constructed setups is supercontinuum generation,<sup>[75,76]</sup> yielding broadband pulses with spectral widths on the order of 400 nm for center frequencies in the visible range. While this process is highly complex and itself still subject of ongoing research,<sup>[77]</sup> the general principle is based on the third-order non-linear effect of self-phase modulation. At very high fields the electric susceptibility and thereby the refractive index  $n$  are altered and become time-dependent, which far from resonances is linked to the third-order susceptibility tensor and proportional to the electric field intensity  $I(t)$ :

$$n(t) = n_0 + n_2 \cdot I(t) \quad (2.14)$$

with the non-linear refractive index  $n_2 = \frac{2\pi}{n_0} \chi^{(3)}$ . This change in refractive index is equivalent to a time-dependent phase shift:

$$\Delta\phi(z, t) = \Delta k(t)z = \frac{\omega}{c_0} n_2 I(t) z \quad (2.15)$$

---

<sup>7</sup>N.B.: Parallel and perpendicular here refer to the plane of incidence. In practice, the crystal is rotated perpendicularly to the optical axis to match the crystal axes with the respective light polarization(s).

with the vacuum speed of light  $c_0$ , the propagation distance  $z$  inside the medium and  $\Delta k$  being the change in wave vector associated with the non-linear refractive index. The additional phase factor in time corresponds to a spectral shift, in analogy to the time-shift theorem. Since the instantaneous frequency is the first derivative of the phase, the spectral shift is proportional to the intensity gradient and the propagation distance:

$$\Delta\omega(z, t) = \omega(z, t) - \omega_0 = -\frac{\omega_0}{c_0} n_2 z \frac{\partial I(t)}{\partial t} \quad (2.16)$$

Thus, for ultrashort pulses, where  $\partial I/\partial t$  is high, the significant spectral broadening described above can be achieved. However, self-phase modulation is only one of multiple effects contributing to the spectral broadening, such as self-focusing, cross-phase modulation or stimulated Raman scattering.<sup>[78]</sup> Nonetheless, equation 2.16 has important practical implications, considering the dependence on the material thickness and the intensity profile of the pulse.

This concludes the discussion of the underlying optical processes relevant to understand the design of the utilized ultrafast laser setups, described in the following sections.

## 2.2 Laser Systems

In total, three different ultrafast laser systems were used for the scientific projects presented in this thesis, all of which utilize the principle of chirped-pulse amplification,<sup>[79]</sup> in which broadband pulses are generated in an oscillator and subsequently broadened in time via a stretcher, before being amplified in a second laser crystal and re-compressed to the bandwidth limit. The vast majority of the results were obtained using a titanium sapphire (Ti:Sa) regenerative amplifier system, which will be described briefly in this section, before discussing differences to the other applied systems.

It was manufactured by Coherent, Inc.<sup>[80]</sup> with a Micra-5 oscillator and a Legend Elite regenerative amplifier and provided 800 nm pulses with a bandwidth-limited duration of  $\approx 35$  fs and energies of 4 mJ at a repetition rate of 1 kHz. The Micra-5 oscillator produces a femtosecond pulse train via Kerr-lens modelocking, at a repetition rate of 85 MHz, with bandwidths around 90 nm and durations of 30 fs, according to factory specifications. The pulse stretcher prior to amplification employs a diffraction grating to introduce spectral dispersion, in the opposite way to the working principle of a prism or grating compressor. This is done in order to avoid damaging of the gain medium in the regenerative amplifier due to high peak powers of the (amplified) pulses. The amplification process itself entails repeated passing of a single pulse through an optically excited gain medium until the pulse energy is saturated due to population depletion. This is controlled by two electro-optic modulators (Pockels cells), which are synchronized to the oscillator and, in combination with polarization optics, control the number of times a pulse passes through the laser cavity before exiting the amplifier unit. The gain medium is pumped by a Nd:YLF

nanosecond laser,<sup>8</sup> which is also synchronized with the Pockels cells so that the excitation can be optimized to the entrance timing of the pulse. After amplification, the pulses are recompressed close to the bandwidth limit with a grating compressor.

The regenerative amplifier system used for experiments with the RF compression UED setup at the University of Toronto (*vide infra*) was highly similar to the one described above, utilizing the same oscillator model and a similar regenerative amplifier, which produced 800 nm pulses with durations around 50 fs and energies of 0.5 mJ. It has been described in more detail elsewhere, for instance in refs. [57, 58, 81].

The third femtosecond laser system<sup>9</sup> on the other hand employs a different gain medium, neodymium-doped yttrium aluminum garnet (Nd:YAG), and provides pulses with central wavelengths of 1030 nm, durations of 170 fs and energies of  $\approx 800 \mu\text{J}$  at 1 kHz repetition rate.<sup>10</sup> It was used for the preliminary ultrafast electron diffraction experiments on diarylethene derivatives, presented in chapter 5.

## 2.3 Non-collinear Optical Parametric Amplifiers

The specific experimental requirements associated with the investigated samples demanded the availability of wavelengths beyond the second and third harmonic of the fundamental 800 nm beam from the Ti:Sa laser system at sufficient intensity.<sup>11</sup> Firstly, synchronized photoreversion<sup>12</sup> of the diarylethene compounds required a tunable, pulsed<sup>13</sup> laser source in the wavelength range between 500 and 650 nm. Secondly, it was shown that for these compounds, excitation at 266 nm was not feasible due to rapid sample fatigue, thus demanding excitation pulses within the wavelength range between 300 and 380 nm, above which the samples do not absorb. Therefore, for both purposes, tunable frequency converters were built based on non-collinear optical parametric amplification. The working principle of the latter will be laid out briefly, followed by a description of the specific designs.

---

<sup>8</sup>Neodymium-doped yttrium lithium fluoride nanosecond laser utilizing Q-switching, 532 nm central wavelength.

<sup>9</sup>Pharos by Light Conversion, see [82]

<sup>10</sup>These are the specifications used for operation in the laboratory.

<sup>11</sup>Unless explicitly specified, the Ti:Sa system refers to the 4 mJ system at the MPI for the Structure and Dynamics of Matter.

<sup>12</sup>Synchronized photoreversion was developed by Dr. Siddiqui (see ref. [63]) as an improvement of previous CW photoreversion of thermally irreversible photochromic molecules by Dr. Jean-Ruel (see refs. [56, 57, 83])

<sup>13</sup>While it can be argued that a pulsed source is beneficial due to the prevention of crystal strain associated with the isomerization reactions, the main motivation for this was the potential to study the reverse reactions of these compounds.

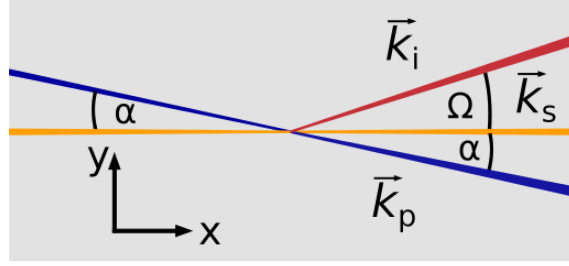


**Figure 2.3:** Beam geometry inside a BBO crystal for non-collinear optical parametric amplification.  $\vec{k}_p$ ,  $\vec{k}_s$  and  $\vec{k}_i$  are the respective wave vectors of the pump, signal and idler beams.  $\alpha$  and  $\Omega$  are the internal angles between pump and signal (or seed) as well as signal and idler, respectively.

### 2.3.1 Broadband phase matching

The process of optical parametric amplification (OPA) represents a seeded form of optical parametric generation (OPG), which is based on the same non-linear optical effect as difference-frequency generation. From a high intensity pump pulse, two pulses of lower frequency are generated, whose added frequencies are equal to the pump frequency. The addition of another, lower intensity beam as the seed induces its amplification. The amplified beam is called the signal while the other generated beam is called idler. Using a broadband, chirped seed allows for control of the signal wavelength via the delay between the pump and the seed pulses, since only those modes will be amplified which temporally overlap with the pump pulse.

Like in case of the non-linear processes discussed above, phase matching between the differently colored beams is a crucial condition, limiting the practically achievable bandwidth of the signal beam. This issue can be mitigated in part by moving from a collinear beam geometry to a non-collinear one (non-collinear OPA, NOPA), which induces an additional degree of freedom via the internal angles  $\alpha$  between the pump and the signal beams and  $\Omega$  between the signal and the idler beams (see Fig. 2.3). It can be shown that under these circumstances, the phase matching condition in terms of the difference in wavevectors<sup>14</sup> between the involved frequencies becomes:<sup>[84]</sup>

$$\begin{pmatrix} \Delta k_x \\ \Delta k_y \end{pmatrix} = \begin{pmatrix} k_p \cos \alpha - k_s - k_i \cos \Omega \\ k_p \sin \alpha - k_i \sin \Omega \end{pmatrix} = \begin{pmatrix} 0 \\ 0 \end{pmatrix} \quad (2.17)$$

For Type I mixing, an expression for the phase matching angle depending on the signal and pump wavelengths as well as the internal angle has been derived (see ref. [84]) and can be found in the appendix (equation A.20). This expression was used in order to determine the ideal internal angle  $\alpha$  for broadband phase matching in a  $\beta$ -barium borate

<sup>14</sup>N.B.: The phase matching condition in terms of the wavevector difference is of course equivalent to and can be converted into the one using the refractive indices used previously.

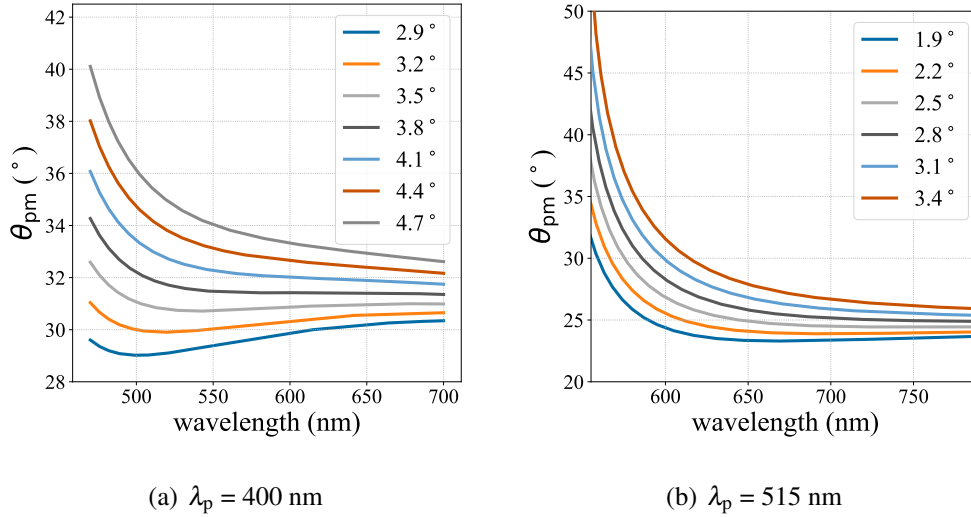


**Figure 2.4:** Vis-NOPA phase matching angle  $\theta_{\text{pm}}$  as a function of the signal wavelength for various internal beam angles ( $\alpha$ ) and for pump wavelengths  $\lambda_p$  of (a) 400 nm (Ti:Sa) and (b) 515 nm (Nd:YAG).

crystal (BBO) as well as the corresponding  $\theta_{\text{pm}}$  as a cut angle for the utilized non-linear crystals. This was carried out for pump wavelengths of 400 and 515 nm and the results are shown in Fig. 2.4. For broadband phase matching at a single angle, the phase matching curve needs to be as flat as possible in the respective wavelength range. By inspection, the optimal internal angles were determined to be  $3.8^\circ$  for 400 nm and  $2.5^\circ$  for 515 nm, corresponding to external angles of  $5.9^\circ$  and  $3.8^\circ$ . The associated crystal cut angles for the BBO crystals were  $31.5^\circ$  and  $24.4^\circ$ , respectively.

### 2.3.2 NOPA setups

Within the course of this PhD project, three individual NOPAs were constructed for different purposes. One of them was built for preliminary experiments with the Nd:YAG laser and will not be discussed in more detail, since its design was nearly identical to the design of the other two except for the difference in the angle between pump and seed ( $\alpha$ ), the phase matching angle ( $\theta_{\text{pm}}$ ) and wavelength-specific optics. The remaining two NOPAs were again similar in design, both using 400 nm as the pump and a visible supercontinuum as the seed, and can thus be described together. One of them was used for synchronized photoreversion experiments, predominantly for the diarylethene derivatives discussed in chapter 5. The other one was built for the purpose of sum-frequency mixing its output with the fundamental 800 nm beam to yield broadband pulses in the ultraviolet with wavelengths longer than 300 nm. These pulses were required in particular for excitation of the diarylethene derivatives (see chapter 5), but were also used for other samples, unless shorter excitation wavelengths were necessary.

Fig. 2.5 shows the design of the broadband UV pulse generation setup including the visi-

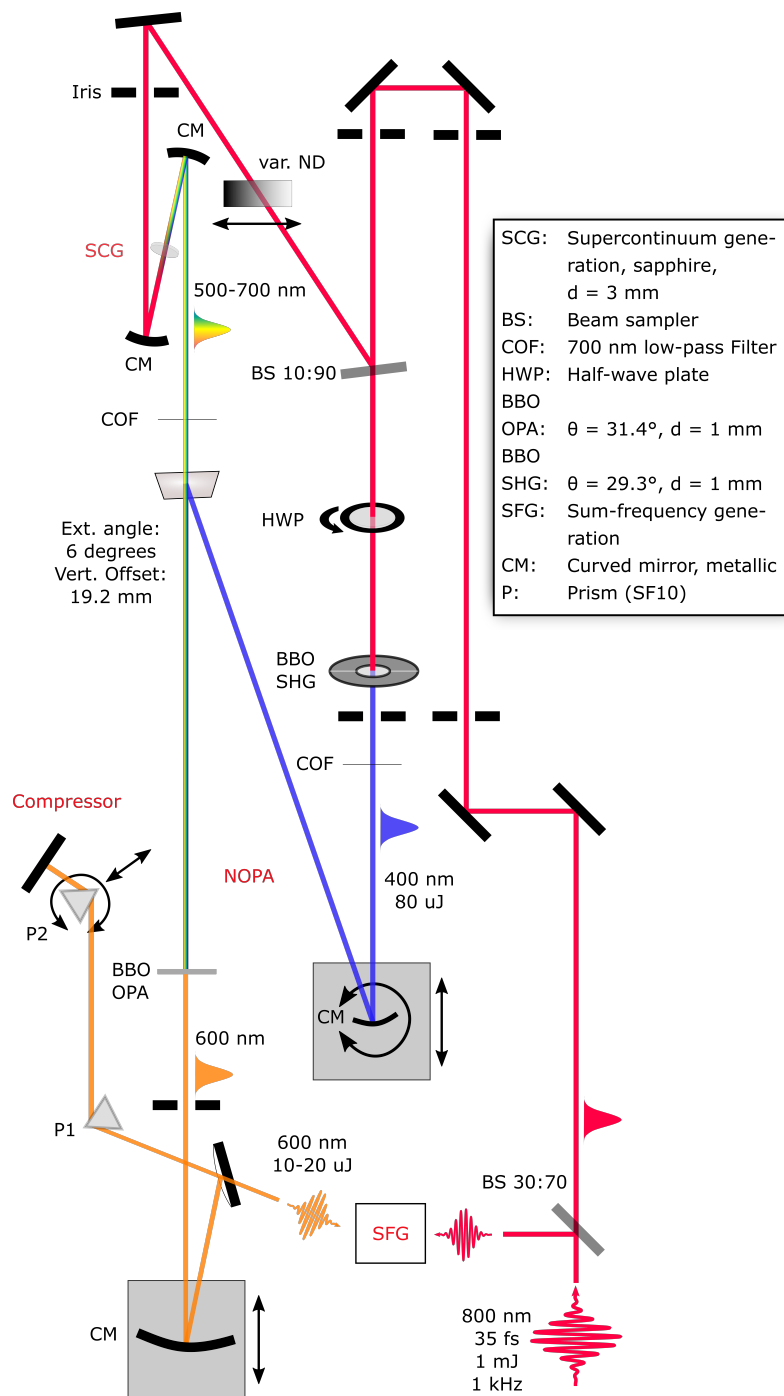


**Figure 2.5:** Design of the visible NOPA and prism compressor as part of the broadband UV pulse generator. The required angle between the pump and seed beams is introduced through a vertical offset prior to focusing into the BBO for the OPA process. Before the NOPA beam is directed into the SFG setup (see Fig. 2.6), the pulses are compressed with a two-prism compressor (SF10).

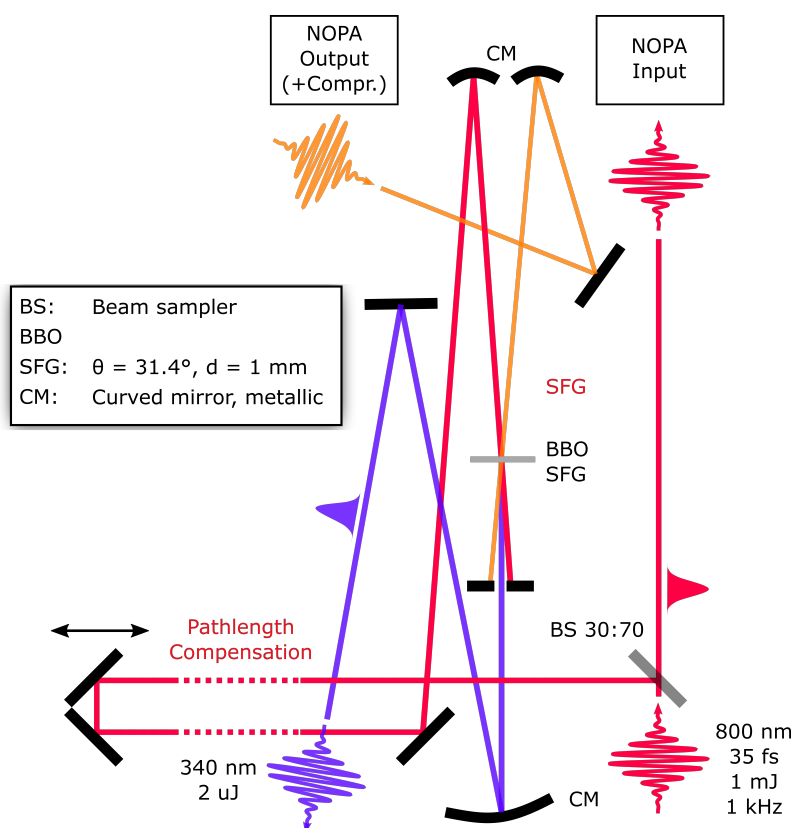


**Figure 2.6:** Layout of the sum-frequency mixing stage between the visible NOPA output at  $\approx 600$  nm (see Fig. 2.5) and the fundamental 800 nm, producing broadband pulses in the UV (see Fig. 2.7).

ble NOPA and a compressor prior to the sum-frequency generation stage. For a sufficient SFG efficiency, relatively high output pulse energies on the order of  $10 \mu\text{J}$  from the visible NOPA were required. Therefore, the entire setup was fed by a large portion of the laser system's pulse energy ( $\approx 1.1$  mJ), of which 30 % were separated for the SFG with a beam sampler. The remaining  $730 \mu\text{J}$  were again split, leaving 10 % for the seed supercontinuum generation and 90 % for the second-harmonic generation of the pump. The latter was generated in a BBO ( $\theta = 29.3^\circ$ ) and its intensity controlled by detuning the polarization with a half-wave plate (HWP). Generation of the seed beam was done by focusing the attenuated beam in a 3 mm thick sapphire disk. By varying the distance between the focusing and collimating mirror, the seed was re-focused at the position of the OPA crystal (BBO OPA,  $\theta = 31.4^\circ$ ). The angle between the beams was created by lowering down the pump beam using the focusing mirror (750 mm focal length), before redirecting it upwards to overlap it with the seed beam in the BBO, at an external angle of  $\approx 6^\circ$ . The maximum pump pulse energy at the OPA crystal was around  $90 \mu\text{J}$  with a beam diameter of  $205 \mu\text{m}$ .<sup>15</sup> Under these conditions, signal pulse energies of  $13 \mu\text{J}$  at 600 nm were routinely accessible, with some more extensive optimization even higher

<sup>15</sup>In part due to some losses from the optics, but mostly by sampling the beam with an aperture, the pulse energy of the 800 nm beam prior to the SHG was  $560 \mu\text{J}$  resulting in 400 nm pulse energies around  $110 \mu\text{J}$  behind the high-pass filter.

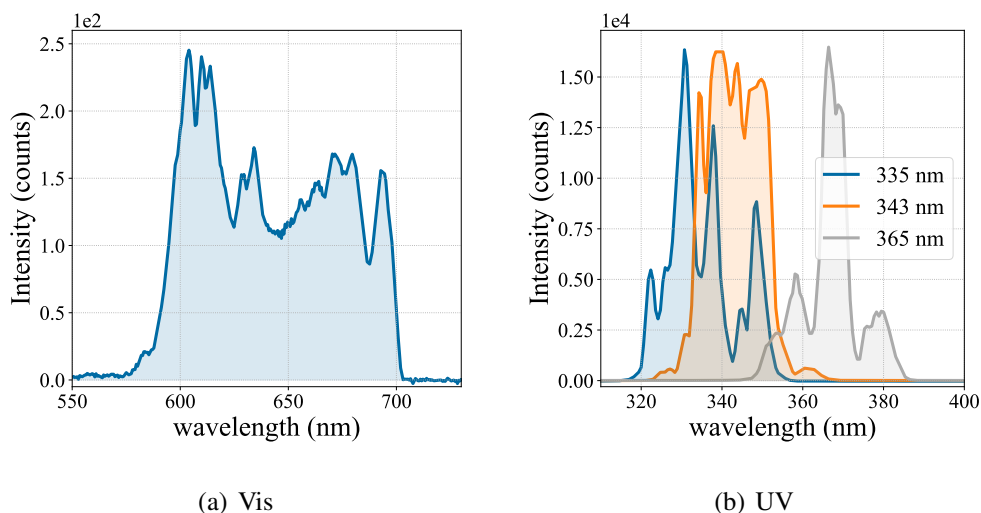


**Figure 2.7:** Example spectra from the broadband UV laser pulse generator. (a) spectrum from the visible NOPA at 650 nm central wavelength, (b) output spectra of the sum-frequency mixing stage for different central wavelengths between 300 and 400 nm.

(15–16  $\mu\text{J}$ ), and bandwidths around 50 nm. An example spectrum of the NOPA output is shown in Fig. 2.7 (a).

Behind the OPA crystal, the signal beam was collimated with another metallic mirror and sent into the prism compressor (SF10 prisms, cut at the Brewster angle for  $\approx 600$  nm). The parameters of the compressor were preliminarily set according to calculations<sup>[85]</sup> and estimates of the initial pulse durations but optimized empirically to increase the SFG efficiency. After compression, the NOPA beam was directed to the sum-frequency generation stage shown in Fig. 2.6 where it was focused into the SFG BBO crystal ( $\theta_{\text{pm}} = 31.5^\circ$ , 0.3 mm thickness), together with the 800 nm beam in a non-collinear geometry.<sup>16</sup> The delay between the two pulses was compensated by using an assembly of multiple mirrors in the path of the 800 nm beam as well as a manual delay stage for day-to-day optimization of the temporal overlap. Behind the crystal, the sum-frequency signal was again collimated and sent to the specific setup.<sup>17</sup> For transient absorption spectroscopy, the UV pulses were compressed once more with another prism compressor (UV fused silica prisms).

Under the given conditions, pulse energies of up to 2.3  $\mu\text{J}$  and a bandwidth of up to 30 nm at a central wavelength of 340 nm were achieved. However, since the sum-frequency generation process was highly dependent on multiple factors such as the incident pulse energies, bandwidths, durations, beam sizes, crystal orientation as well as the delay between the pulses, this was not feasible to achieve on a daily basis. Nonetheless, energies around 1  $\mu\text{J}$  and bandwidths of 15–20 nm were routinely obtained (see Fig. 2.7 (b)). The

<sup>16</sup>While somewhat detrimental for the efficiency, this geometry provided an inherent spatial separation of the generated sum-frequency beam from the others.

<sup>17</sup>Even though it is not shown in Fig. 2.5 for simplicity, the visible NOPA beam was also re-collimated and could be used for experiments.

second NOPA in comparison to the first one shown in Fig. 2.5 was operated at about half the pulse energy (40  $\mu\text{J}$  at 400 nm, 5-6  $\mu\text{J}$  visible output), which was sufficient since the pulses were used directly for experiments rather than for another non-linear optical process. Bandwidths around 25 nm at 500-600 nm central wavelengths were commonly used (see Fig. A.32 in the appendix). Although larger bandwidths were feasible (up to 100 nm), they were not desirable since this NOPA was used predominantly for photoreversion where scattering signals potentially affect the acquired transient absorption data. Furthermore, for the purpose of photoreversion it was not necessary to compress the NOPA pulses.

## 2.4 Transient Absorption Spectroscopy

The vast majority of experimental results analyzed and discussed in this thesis were acquired using the experimental technique of transient absorption spectroscopy (TAS). In this section, after a brief introduction into the underlying physics, the fundamental working principles and the utilized setup design in various configurations are presented. The general experimental procedure as well as data processing are described followed by an overview of the most important data analysis methods that were applied and will be discussed throughout this thesis.<sup>18</sup>

### 2.4.1 Probing electronic states and their populations

In transient absorption spectroscopy, the time-resolved difference in transmission of a multichromatic light pulse through an optically excited system is measured and compared to the system at equilibrium.<sup>19</sup> It thus enables capturing photoinduced dynamics by probing the associated changes in optical transitions between states of the system, providing information on both their populations and relative energies. In order to correctly interpret TAS experiments, an understanding of these optical transitions is required, for which the most important concepts will be introduced briefly in the following. Since the subjects of investigation throughout this thesis work are photochemical reaction dynamics, this overview is mostly limited to the particular properties of small molecules.

Molecules are fully quantum mechanical objects and their wave functions are eigenfunctions of the corresponding Hamiltonian accounting for all their nuclei and electrons. Within the Born-Oppenheimer approximation, nuclear and electronic wave functions can be separated due to the significant difference in mass, allowing the electronic configuration to adopt quasi-instantaneously to changes in the nuclear configuration.<sup>[89]</sup> This

---

<sup>18</sup>The fundamental parts in this section are based on refs. [86–88]. Further references will be given if going beyond the content of these textbooks or in order to highlight the original source.

<sup>19</sup>The transmission  $T = I/I_0$ , not the absorption, is indeed what is measured, from which the extinction immediately follows. Assuming changes in the latter to be exclusively due to changes in absorbance of the system allows to calculate the differential absorption (see eqn. 2.20).

allows to describe electronic states (eigenstates of the electronic Hamiltonian) as multidimensional, adiabatic potential energy surfaces (PES), which depend on the nuclear coordinates. The gradients of these potential energy surfaces along certain coordinates, including slopes, maxima and minima generally determine the nuclear motion and give rise to processes such as bond breaking or formation.<sup>20</sup> Since the energy differences between the electronic eigenstates for small molecules typically lie within the visible or ultraviolet wavelength range, they can be probed along with the associated populations by means of UV/Vis spectroscopy, where transitions between them are optically induced. In general, optical transitions between states are induced via perturbation of the system by an electromagnetic wave. For the transition from an initial state  $|i\rangle$  to a final state  $|f\rangle$  with energies  $E_i$  and  $E_f$ , the transition probability is given by Fermi's golden rule:

$$P_{i \rightarrow f} = \frac{2\pi}{\hbar} \langle f | \hat{H}_1 | i \rangle \delta(E_f - E_i - E_p) \quad (2.18)$$

where  $\hat{H}_1$  is the Hamiltonian of the perturbation and  $E_p$  the photon energy. Besides the fundamental requirement for a match between  $E_p$  and the energy difference of the two states due to energy conservation, the transition probability is dictated by the matrix element  $\langle f | \hat{H}_1 | i \rangle$  of the perturbation operator, i.e. the overlap between the wave functions of the final state with the perturbed initial state. In the electric dipole approximation, the perturbation can be treated as an oscillating dipole field which induces a resonantly oscillating dipole in the molecule.<sup>21</sup> The matrix element  $\langle f | \hat{\mu} | i \rangle$  of the dipole operator  $\hat{\mu}$  is called the transition dipole moment of  $i \rightarrow f$ . Its absolute square,  $|\hat{\mu}_{if}|^2$ , is a measure for the strength of the transition, analogously to the classical oscillator strength, and the coupling of  $\hat{\mu}$  to the external electric field essential for the optical transition probability. Despite the delta function in equation 2.18, optical spectra in the visible have a finite width. This caused by different mechanisms of line broadening, out of which two are most relevant for the samples discussed in this thesis. The first is due to the finite lifetime of excited states and therefore an intrinsic property of any optical excitation.<sup>22</sup> The second mechanism of broadening is due to fluctuations in the electronic potential caused by interactions between the molecule and its surroundings. Depending on whether the mechanism is homogeneous throughout the probed ensemble, it is classified as either homogeneous or inhomogeneous broadening, which affect the spectral width and shape in a different manner (*vide infra*).

According to the Born-Oppenheimer approximation, optical transitions between electronic states are vertical in the nuclear configuration space. As a consequence, the probabilities for transitions into the vibrational states within  $|f\rangle$  are influenced by the overlap

<sup>20</sup>However, the nuclear motion itself is restricted by the laws of quantum mechanics allowing only discrete vibrational energies within the electronic potentials.

<sup>21</sup>More precisely, the perturbation creates a coherent superposition state of the two eigenstates, which in non-isolated quantum systems eventually dephases into one of them (see for example [90–93]).

<sup>22</sup>Conf. the discussion above concerning temporal and spectral bandwidths.

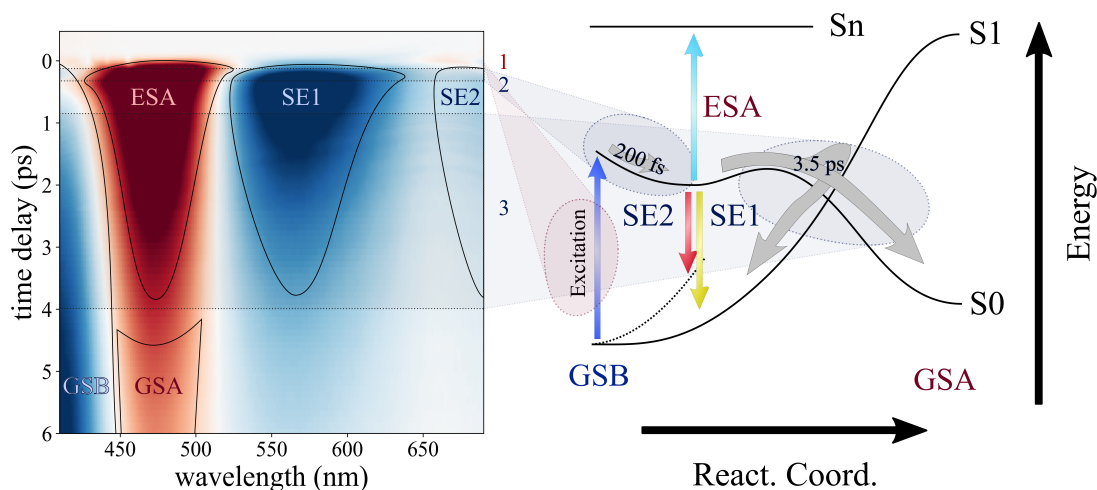


**Figure 2.8:** Common signals in transient absorption spectroscopy and their physical interpretation. Shown on the left is an example measurement of protonated Nitrobenzospiropyran from chapter 4 with the signal types indicated in the map. On the right, the deduced reaction mechanism is depicted in form of a schematic diagram of the potential energy surface along the reaction coordinate. ESA = excited-state absorption, GSB = ground state bleach, GSA = ground state absorption, SE = stimulated emission.

between the respective vibrational wave functions and the (populated) ground-state vibrational wave functions. This principle is called the Franck-Condon principle and the initially occupied vibronic state distribution after excitation the Franck-Condon (FC) state.

Having discussed these fundamental concepts behind probing chemical reaction dynamics via optical transitions now allows to pursue the question what happens when a molecule is optically excited and how this can be investigated by means of time-resolved optical spectroscopy. For this purpose, let us consider an exemplary transient absorption measurement ( $\Delta A(\lambda, \Delta t)$ ) from this thesis, shown in Fig. 2.8 along with a schematic energy diagram to relate the acquired data to the photochemical reaction.<sup>23</sup> The energy diagram represents a one-dimensional slice of the multidimensional potential energy surfaces in the configurational space of the nuclei. The slice is cut along one or multiple vibrational modes of the molecule, which are conjointly treated as the generalized reaction coordinate, since they link the initial and final molecular configurations.

Prior to excitation, the molecule is in the unperturbed, singlet ground state, denoted as  $S_0$ .<sup>24</sup> Excitation into the Franck-Condon state on the  $S_1$  (first singlet excited state) man-

<sup>23</sup>The energy diagram is based on the interpretation of an extensive analysis of the data presented in section 4.4 and partly open to discussion, as elaborated there. For simplicity it will be treated as factual here.

<sup>24</sup>Singlet corresponds to a (total) spin angular momentum of  $S = 0$ , i.e. multiplicity  $(2S + 1)$  of 1, in contrast to triplet states with  $S = 1$  and multiplicity 3. Optical excitations are only allowed between states of same  $S$ .

ifold creates a coherent superposition state which dephases faster than the temporal resolution of the experiment and thus the system which is accessible in the data can be understood semiclassically as a wave packet propagating on the  $S_1$  potential energy surface. As a consequence of the excitation, there is a depletion of the  $S_0$  population and thus a decrease compared to equilibrium in any associated absorption signals within the probed range. The resulting negative signal is commonly denoted as ground state bleach (GSB). In the current data, the  $S_0$  to  $S_1$  transition energy corresponds to a wavelength around 400 nm and thus a negative absorption signal is visible in the transient spectrum. If, like in the case shown here, a large fraction of molecules reacts to a distinct, thermally stable product, the GSB signal persists (after a slight initial recovery) until the end of the measurement window. The permanence of the GSB signal also indicates a finite quantum yield of the reaction, which is the fraction of excited molecules that eventually reach the product state.

The created FC state is a broad distribution of configurations on the  $S_1$  PES from which multiple transitions to higher-lying excited states  $S_n$  are allowed. An optical probe pulse can induce these transitions, which gives rise to an increased absorption probability at the respective wavelengths, resulting in a positive differential absorption signal (excited-state absorption, ESA), in this case with a maximum around 475 nm. On the other hand, photons of the optical probe can induce the radiative decay of the  $S_1$  population via stimulated emission (SE), leading to an increase in detected photons at the emission wavelength, which manifests in an apparent increase in transmission or equivalently a decrease in  $\Delta A$ . Two SE bands are visible in the present data, one centered around 570 nm and the other at  $\geq 700$  nm.

Since – if not by chance – the FC state is not at a local minimum in configuration space, the gradient on the PES causes relaxation of the molecule towards the nearest minimum. This involves the occupation of lower vibrational levels on the  $S_1$  PES by distributing energy into vibrational modes of the molecule, which is therefore termed intramolecular vibrational relaxation (IVR). If the molecule was also excited into a higher lying electronic state, rapid internal conversion (IC) into the lowest singlet excited state would occur at the same time.<sup>25</sup> In organic molecules, this usually takes place faster than any significant structural change due to the large density of vibronic states in this regime, which is why most photochemical reaction dynamics happen on the lowest excited state PES.<sup>26</sup> Transfer from a singlet excited state to a triplet state is another process that can occur in electronically excited molecules and called inter-system crossing (ISC). Coming

---

<sup>25</sup>IC is interlinked with IVR for two reasons: Internal conversion from one electronic state into the other necessitates IVR towards an intersection of (or a point of a sufficiently small gap between) the two PES. Furthermore, IC may result in the initial occupation of a higher vibrational level on the electronically lower state, from which it may subsequently relax via IVR. Often, the process of IVR is implied to occur when speaking of IC, without explicit mention.

<sup>26</sup>Due to its ubiquity, this phenomenon is known as Kasha's rule (see [94]), although it is not without exceptions.

back to the example data, the process of IVR from the FC state to a local minimum on the  $S_1$  PES is associated with a blue-shift in the excited-state absorption as lower vibrational levels are populated. These so-called hypsochromic shifts are commonly observed when dealing with vibrational relaxation unless other processes alter the PES significantly.

Subsequent relaxation to the ground state occurs either radiatively via fluorescence (or phosphorescence) or non-radiatively via coupling to vibrational modes. During the latter, certain points in configurational space are reached, where the  $S_0$  and  $S_1$  PES become degenerate in energy, called conical intersections.<sup>27</sup> Non-radiative decay through a conical intersection can lead to either formation of the chemical reaction product<sup>28</sup> or a return to the reactant. Regardless of the reaction channel, the population of the excited state decays in time and so do the associated ESA and SE signals. Populations  $N$  which decay stochastically with a time-independent rate constant  $k$  obey the following general differential equation:

$$\frac{dN}{dt} = -k \cdot N \quad (2.19)$$

the solution of which is an exponential function in time with  $-k$  as the exponential pre-factor. Consequently, the ESA and SE signals associated with population of the  $S_1$  state decay exponentially, in this case with a life time of 3.5 ps. If the absorption spectrum of the reaction product(s) is within the probing range and well-separated from the other signals, the simultaneous exponential rise of the former can be observed as well, which is not the case in the present data, but for instance in case of photoexcited spiropyran, dealt with in chapter 3. The formed product usually undergoes further vibrational relaxation, via IVR on the one hand, but also via dissipation of thermal energy to surrounding molecules, which is referred to as vibrational cooling. This can again entail a blue-shift of the spectrum, but also narrowing of the bandwidth due to a reduction in thermal motions.

## 2.4.2 Optical setup

All transient absorption experiments presented in this thesis were performed in a home-built setup. It had been constructed and operated prior to the start of the experimental projects discussed here and results from it have been published, for instance in refs. [63, 96]. Its original design is described in detail in ref. [97] and a schematic can be found in the appendix (Fig. A.33). However, while most of the data presented in chapter 3 was still acquired using the setup in the former configuration, it was re-designed and -built entirely within the scope of this thesis including additions to the optical setup, the data acquisition unit and the acquisition software, with the goal to improve both the data quality and the experimental workflow. The resulting setup design is shown schemati-

---

<sup>27</sup>See ref. [95]. As a consequence of this degeneracy, the Born-Oppenheimer approximation breaks down at the points of conical intersection, since non-adiabatic coupling between the electronic states is no longer negligible.

<sup>28</sup>The product of the chemical reaction here means anything other than the reactant and can thus be one (or more) of multiple possible (by-)products.

cally in Fig. 2.9. Its main purpose lies in the accommodation of two differently colored excitation beams, usually for the purpose of synchronized photoreversion, with as many different wavelength combinations as possible, while allowing for either solution or solid-state samples, with the option of cooling the latter to cryogenic temperatures. Another major aspect of the optical arrangement was its adaptability regarding pump, re-pump and probe wavelengths allowing for effortless switching between different samples with only few adjustments and without the need to re- or disassemble any parts of the setup.

The optical assembly will be described in the following. Both the second and the third harmonic of the fundamental 800 nm beam from the Ti:Sa laser system were available permanently and separated by a dichroic mirror behind the third-harmonic generation stage.<sup>29</sup> As is common, the THG stage consisted of a BBO crystal for generation of the second harmonic ( $\theta = 29.3^\circ$ , 1 mm thickness) and a second BBO for Type II mixing of the second harmonic and the fundamental ( $\theta = 55.5^\circ$ , 1 mm), with a calcite group delay compensator ( $\theta = 45^\circ$ , 1 mm) between the two. The THG stage was fed by the fundamental beam entering the setup ( $\approx 500 \mu\text{J}$ ) after splitting off  $\approx 20\%$  for generation of the probe beam, resulting in an input energy of  $\approx 400 \mu\text{J}$  for the THG. Prior to the BBO crystals, the beam was reduced in size using a Galilean telescope (-100 mm and 200 mm focal lengths) to improve the efficiency. After separation of the 266 and 400 nm beams, an arrangement of mirrors introduced a pathlength difference between the two and allowed for selective control of their repetition rates using optical choppers before recollimation via a second dichroic mirror. This allowed for a synchronized photoreversion scheme using these two wavelengths with collinear beams, which was applied to the sample dealt with in chapter 4, prior to implementation of a flow-cell based solution. In addition to these permanent, low-maintenance options for excitation wavelengths, broadband tunable pulses in the visible and the UV were accessible from the constructed NOPA systems described in the previous section. Thus, the available excitation wavelength options encompassed 266 nm, 310-370 nm, 400 nm, 490-650 nm and 800 nm, as well as possible combinations of these, depending on the experimental requirements. Therefore, it was possible with this setup to accommodate not only the research projects associated with the present thesis, but a multitude of other samples during the same time period.<sup>30</sup>

Selection of the pump beam(s) was done using beam blocks and flip mirrors, guiding the respective beams to the sample, onto which they were focused using metallic mirrors, a UV-enhanced aluminum mirror for 266 nm and the UV NOPA on the one hand and a silver mirror for the 400 nm, 800 nm and the visible NOPA beams on the other hand. For solid-state samples, the pump (and re-pump) polarizations were made circular by aid of quarter-waveplates (QWP), in order to eliminate any polarization dependence in the

---

<sup>29</sup>The 800 nm fundamental beam after the THG stage was also separated via another dichroic mirror and available for potential experiments, but this was not applied within the scope of this thesis.

<sup>30</sup>Examples for the photochemical processes investigated in addition to those in this work are intramolecular proton transfer, furylfulgide cyclization, spin-crossover in metal complexes, singlet fission and more.

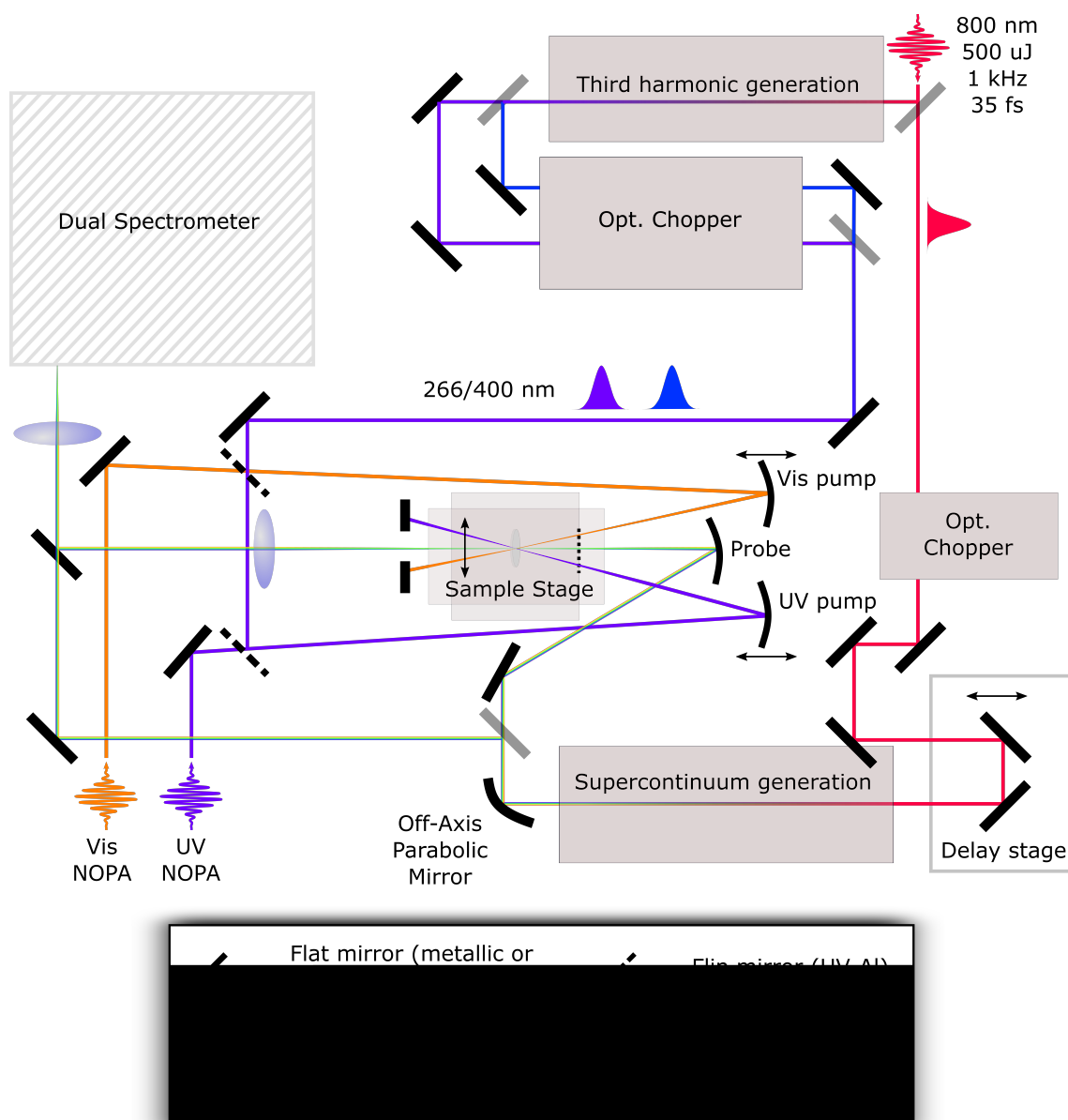


**Figure 2.9:** Schematic of the transient absorption spectroscopy setup. The three-beam arrangement has been designed to facilitate running synchronized photoreversion experiments using a wide range of excitation wavelengths from 266 nm to 800 nm whilst probing in either the visible or the UV. Selection of the required wavelengths is possible without having to change the setup significantly. The sample stage is exchangeable, to enable experiments with sample solutions as well as solid-state samples with or without cooling to cryogenic temperatures.

sample plane unless it was specifically intended to select a specific transition. In the latter case this was achieved by optimization of the signal using a half-waveplate (HWP) for the respective wavelengths.<sup>31</sup> For solution samples, a HWP was used to set the angle between the pump and probe polarizations to  $54.7^\circ$ , at which artifacts from molecular rotation are negligible (magic angle).<sup>[98]</sup> While the probe repetition rate was usually kept at 1 kHz,

<sup>31</sup>However, this was only necessary or useful for samples which are not part of this thesis.

the pump repetition rate needed to be reduced to 500 Hz or less in order to enable the serial acquisition scheme described below. This was achieved by one or multiple optical choppers,<sup>32</sup> placed inside the setup in case of the harmonic wavelengths (see Fig. 2.9) or outside in case of the NOPA beams.

A broadband supercontinuum (SC) either in the visible (380-750 nm) or in the UV (250-350 nm) was used as a probe in the TAS experiments. The visible probe was generated by focusing of the 800 nm beam into a cuvette containing deionized water and with an optical pathlength of 2 mm. While focusing was achieved using a convex lens with antireflective coating for 800 nm, collimation after the SC generation was done by aid of an off-axis parabolic mirror in order to reduce the spatial dispersion and better preserve the mode of the beam. Prior to focusing, the initial beam diameter was reduced to 1-2 mm with an aperture, which has beneficial effects on the stability of self-focusing,<sup>[77]</sup> and the pulse energy was optimized using a variable neutral density filter. In case of the UV supercontinuum, CaF<sub>2</sub> was used as a medium, which was rotated continuously in order to prevent damage of the material, and another SHG BBO was inserted to obtain the 400 nm seed. Furthermore, a QWP was utilized to mitigate the effects of rotating the crystal by circular polarization of the beam. Further components of the probe line prior to the SC generation comprised a motorized delay stage controlled by the acquisition software to create well-defined pump-probe delays and an optional optical chopper for the application of a dual-chopping acquisition scheme if necessary (*vide infra*). After collimation of the supercontinuum, a part of the probe beam was separated using a 10:90 beam sampler and used as the reference beam in the dual detection routine described below, while the remainder was guided to and focused onto the sample via a concave metallic mirror. After passing through the specimen, the probe beam was re-collimated with a convex lens before being focused into the spectrometer, together with the reference beam.

Three different sample stages were available and fully interchangeable to meet the specific experimental requirements. For solution experiments, a flow-cell system was utilized, in which the sample solution flowed through a UV quartz cuvette with an optical pathlength of 500  $\mu\text{m}$ . The solutions were contained in a flask and pumped through a tubing system<sup>33</sup> using a micropump from TCS, United Kingdom,<sup>[100]</sup> whose flow rate, and thereby the sample exchange in the irradiated volume, was sufficiently high to allow for experiments at 500 Hz (optical) pump repetition rate. Solid-state samples, predominantly ultramicrotomed single crystals (*vide infra*), were placed on circular UV fused silica disks (UVFS, 1 inch diameter, 1 mm thickness), for which a custom sample holder had been machined and placed on an xyz-translation stage. If cryogenic temperatures were required, the sample holder was replaced by a cryostat<sup>34</sup> with a liquid nitrogen bath ( $T \gtrsim 77$  K) and another

---

<sup>32</sup>Reduction of the repetition rate to less than 0.1 kHz required a second, synchronized chopper due to the finite beam size.

<sup>33</sup>Tygon tubing from Saint-Gobain Performance Plastics [99].

<sup>34</sup>Oxford Instruments, OptistatDN-X [101].

custom sample holder, made of copper for improved thermal conductivity.

The diameters of the pump, probe and – if applicable – re-pump beams at the sample were determined on a near-daily basis by measuring the transmission through one or multiple pinholes mounted on another UVFS disk which was placed inside the same sample holder.<sup>35</sup> By assuming a Gaussian intensity profile, the beam diameter at half maximum (FWHM) could be calculated from the ratio of transmitted intensities through the respective pinholes and through solely the substrate (see equation A.16). The beam size of the probe was minimized by translating the sample stage along the beam propagation axis, typically reaching beam sizes of 50-70  $\mu\text{m}$  FWHM diameter. The pump radius was adjusted to at least  $\sqrt{2}$  times the probe radius in order to provide approximately homogeneous irradiation of the probed volume. For synchronized photoreversion experiments, the re-pump beam diameter again was set to  $\sqrt{2}$  the pump diameter or more in order to avoid deviations in overlap upon translation of the sample stage.

### 2.4.3 Data acquisition

The probe spectra were recorded using a home-built grating spectrometer, incorporating a dispersive grating (300 lines/mm) and a linear CCD detector (2048 pixels, Hamamatsu Photonics)<sup>[102]</sup> whose read-out rate was fast enough to record probe spectra at the laser repetition rate of 1 kHz. As mentioned in the previous section, parallel acquisition using two separate beams, one passing through the excited and one through the unexcited sample, is not feasible for single crystalline samples. This is due to sample inhomogeneities in both thickness and crystallinity as well as potential polarization dependences. Instead, both spectra were acquired in succession, passing through the same sample region, which required the pump repetition rate to be equal to or less than half the probe repetition rate. The pump-on ( $I_{\text{ON}}$ ) and pump-off ( $I_{\text{OFF}}$ ) spectra were identified by measuring the intensity of a reflection of the pump beam with a photodiode, or in case the latter was not feasible, via an electronic trigger signal from the chopper and assignment by tests with a reference sample. The sorted spectra were then used to calculate the transient absorption signal in accordance with equation 2.20:

$$\Delta A(\lambda, \Delta t) = -\log \left( \frac{I_{\text{ON}}(\lambda, \Delta t)}{I_{\text{OFF}}(\lambda)} \right) \quad (2.20)$$

Nonetheless, within the scope of this thesis, a second detector of the same type was added in order to record a reference probe spectrum from a beam not passing through the sample (see Fig. 2.10). The purpose of this was to reduce the influence of shot-to-shot fluctua-

---

<sup>35</sup>For solution samples, the beam size was determined using the solid-state sample holder after establishing spatial pump-probe overlap. The latter was subsequently used as an indication for the sample position: The sample holder was replaced by the flow-cell and its position along the beam propagation direction adjusted such that the TA signal from a reference solution was maximized, thereby optimizing the pump-probe overlap, and attaining the position at which the beam sizes had been determined previously.

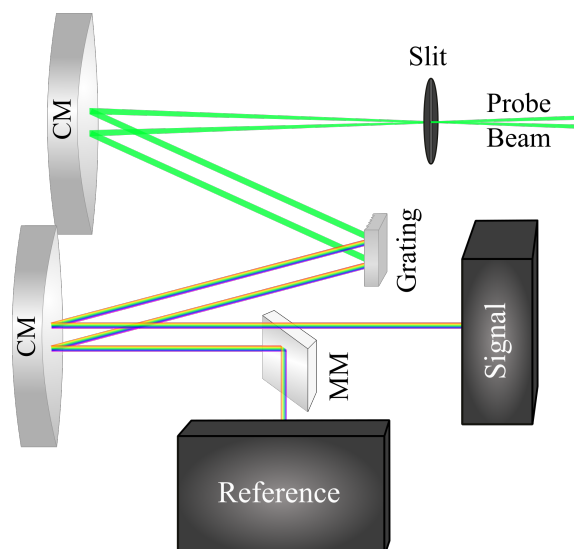


**Figure 2.10:** Layout of the dual spectrometer for parallel acquisition of the probe and reference beams. The signal and reference beams are vertically offset allowing for their separation via a rectangular mirror (MM) directing them onto the respective CCD detectors. The remaining parts are common components of a grating spectrometer including concave mirrors (CM), the (UV enhanced) aluminum grating (300 grooves/mm) and a slit at the beam entrance.

tions in the probe spectra, which can cause significant measurement artifacts, especially when dealing with a limited number of pump-probe cycles on the same sample due to its fatigue. For the reference beam, the same grating and focusing optics inside the spectrometer were used, but the beam was vertically offset. This allowed separation of the two beams with a rectangular metallic mirror directly before the CCD arrays. Both the pump-on and pump-off spectra from the sample were normalized to the respective spectra measured in the reference detector, before calculating the differential absorption.

In cases where the data was affected by a strong scattering signal from the excitation pulse, a dual-chopping strategy was applied, introducing a third category of spectra, in which only the strong scattering signal was present while the probe pulse was blocked (pump-on-probe-off).<sup>36</sup> The latter was identified by integration of the probe spectrum in a region where the scattering signal was absent, and subtracted from the pump-on(-probe-on) spectrum.

The data acquisition was synchronized using a digital delay generator (DDG), triggered by a transistor-transistor logic (TTL) signal from the regenerative amplifier. Acquisition cycles (via the DDG) as well as the motorized delay stage were controlled through a Visual C#-based, interactive user interface software, originally written by Dr. Gastón Corthey. Furthermore, while the pump-on and pump-off spectra were stored separately, the transient signal was calculated and displayed on the fly during the measurement, allowing for direct monitoring of the scan.

Within the scope of this thesis, several extensions to this software were made, due to

<sup>36</sup>For further details refer to the supporting information of ref. [68].

the additions to the experimental procedure on the one hand and in order to improve the general workflow on the other hand. The most important added feature encompasses integration of the probe reference detector into the data acquisition cycle, which required in-depth modification of the source code. Another important improvement of the software enabled a customized sequence of pump-probe delay steps, in which multiple time windows were assigned individual step sizes. This was predominantly done to adapt the time step size to the time scale of the measurement, which previously had only been achievable by recording separate scans for each time window, as in case of the data discussed in chapter 3. Furthermore, on-the-fly compilation of the signal obtained using dual-chopping via the described integration method was added to the software. A few minor additions allowed for the storage of the measured photodiode signal, enabling weighting of the signal intensity to the average pump fluence for each time delay, as well as assignment of the pump-on and pump-off spectra based on the chopper trigger (*vide supra*).

#### 2.4.4 Setup characterization

The sensitivity of the setup as a measure of the signal magnitude necessary for its detection was estimated based on the noise level of the averaged scans. Its value depended on the number of averaged spectra obtainable, which in turn depended on the sample robustness and feasible acquisition rate. For high cyclability as in case of solution samples or rapidly reversible solid-state samples, the sensitivity was  $10^{-4}$ . In case of the investigated photoisomerization reactions in crystal, requiring synchronized photoreversion at low pump repetition rates (20-30 Hz) and with a limited reversibility due to sample fatigue, a sensitivity of  $1 \cdot 10^{-3}$  was still achieved due to the improved signal-to-noise ratio through the implemented probe referencing.

The temporal resolution of the setup was fundamentally limited by the probe pulse, which was not compressed,<sup>37</sup> but also strongly dependent on the pump pulse duration as well as the investigated medium. It was estimated by two different methods, measurement of the CPM<sup>38</sup> signal in the neat solvent or the sample substrate, or the direct fit of an instantaneous absorption signal from the studied samples (or a reference sample). Depending on its shape, the CPM signal can be fit using different functions, such as the second derivative of a Gaussian curve,<sup>[97]</sup> a sine-modulated Gaussian<sup>[96]</sup> or the following sum of Hermite

---

<sup>37</sup>In the transient spectroscopy experiment, the time resolution is still significantly better than the mere convolution of the pulse durations and mostly limited by the pump pulse duration, since the chirp of the probe beam is spectrally resolved [103]. However, it is not equal to the temporal resolution when using a bandwidth-limited probe pulse. N.B.: Like the probe dispersion itself, the time resolution becomes wavelength dependent.

<sup>38</sup>Cross-phase modulation [103–106]. Non-linear optical process analogous to self-phase modulation, but for two different pulses overlapping in time, in this case the pump and probe pulse. Even though, as in case of supercontinuum generation, the actual cross-correlation signal contains contributions from other physical phenomena (most notably two-photon absorption and stimulated Raman amplification [105–107]), CPM as the most tangible effect is commonly used to refer to the observed transient signal.

polynomials:<sup>[58,81,108]</sup>

$$\Delta A_{\lambda}^{(\text{fit})}(t) = \sum_{n=0}^N b_{\lambda,n} \frac{(-1)^n}{\sqrt{2^n \cdot n!}} \cdot e^{x_{\lambda}(t)^2} \cdot \frac{d^n}{dx_{\lambda}^n} e^{-x_{\lambda}(t)^2} \quad (2.21)$$

with  $x_{\lambda}(t)$  being the argument of a Gaussian function centered at  $t = t_{0,\lambda}$  and with width parameter  $\sigma_{\lambda}$ :

$$x_{\lambda}(t) = \frac{t - t_{0,\lambda}}{\sigma_{\lambda}} \quad (2.22)$$

Examples for these fits are shown in Fig. 2.11. All of these methods come with the caveat that the CPM signal intensity depends on the derivative of the pulse intensities and is therefore inherently broader than the convoluted pulses themselves, which has to be taken into account when deducing the actual temporal resolution. The Hermite polynomials are all linked to the same Gaussian parameter, which in principle renders them the best approach. However, the resulting fit often suffers from high parameter correlation and fails when the signal becomes too complex for the sum of only the first few derivatives to be appropriate. Furthermore, for crystals the additional propagation distance in the substrate, which is orders of magnitudes thicker than the actual sample, will lead to a broader CPM signal. Thus, while the CPM can be used as an upper limit for the time resolution and therefore as a target for optimization, a more accurate description can be gained by fitting the transient absorption signal directly with a Gaussian-convoluted exponential function (see eqn. 2.23) while varying the Gaussian parameter  $\sigma$ .

Tab. 2.1 gives an overview of the estimated time resolutions under different circumstances regarding pump wavelength, compression<sup>39</sup> and sample phase. The values obtained from the CPM measurements lie within a range indicated in the table with the higher ones generally at longer wavelengths in the visible. This is because the temporal dispersion is higher at shorter wavelengths enhancing the advantageous effect of spectrally resolving the GDD of the pulse. In Fig. 2.11 (d), a turning point in this behavior can be distinguished around 430 nm, below which the Gaussian widths start to increase with decreasing wavelength. This marks the point beyond which the dispersion of the probe becomes too high to be compensated by the resolution of the spectrometer.

### 2.4.5 Measurement and processing routines

Since various different samples were studied in this setup and even more were tested within the course of this work, it was crucial to maintain a systematic routine for the conduction of the experiments as well as post-processing of the data. On each measurement day, before starting the measurements, the laser system was optimized including the fun-

<sup>39</sup>Out of the three displayed wavelengths, only the 330 nm pulses were compressed. However, this was only possible coarsely due to the lack of more sophisticated pulse characterization methods.

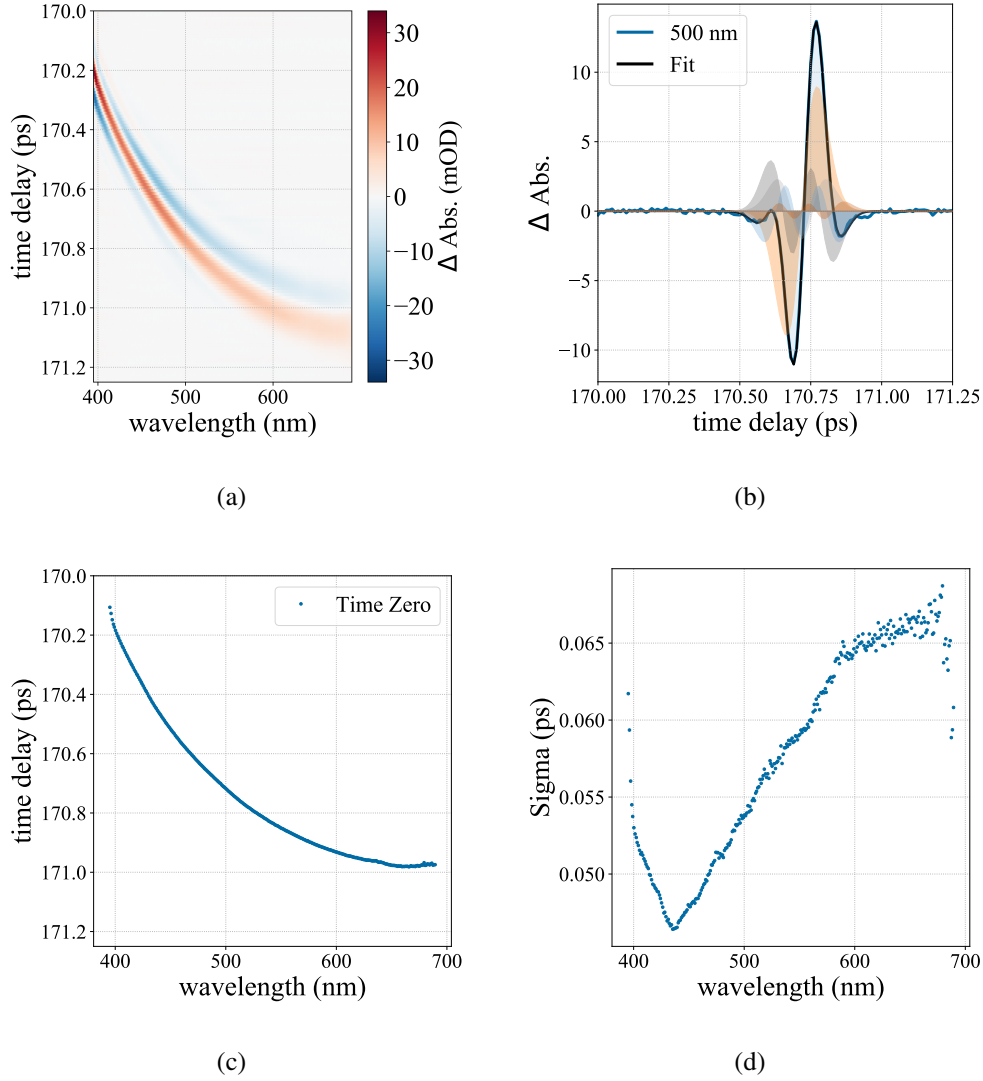


**Figure 2.11:** Measurements of the cross-phase modulation (CPM) in the TAS setup and fit using a weighted sum of the first five Hermite polynomials (see eqn. 2.21). (a) TA map of the fit, (b) example kinetic trace at 500 nm including the fit as well as the individual Hermite components, (c) resulting time zero curve for GDD correction, (d) Gaussian parameter  $\sigma$  of the polynomials for the respective wavelengths.

damental pulse duration via the built-in grating compressor of the regenerative amplifier, the efficiency of the NOPA(s) if they were used in the experiments (vide supra) as well as the supercontinuum stability by adjusting the pulse energy and the beam convergence via the iris. Both temporal and spatial overlap of pump and probe pulses were determined by running low-average test scans on a known sample (or solution).<sup>40</sup> For excitation wavelengths  $\lesssim 530$  nm, a Kapton tape was used, as it exhibited a strong and long-lived transient absorption signal and it was possible to place it directly onto the sample disk. For longer wavelengths, a thin gold film sputtered onto a sapphire substrate was utilized. If necessary, coarse spatial overlap of the beams was assured prior to this by aid of a pinhole

<sup>40</sup>As is common, the time delay where pump and probe pulses overlap will be referred to as time zero,  $t_0$  or point of excitation.

**Table 2.1:** Temporal resolutions (FWHM) of the TA setup in different configurations.

Pump wavelength (nm)	CPM Solution (fs)	CPM Crystal (fs)	IRF Crystal (fs)
266	110-150	110-160 <sup>a</sup>	125
400	120-170	≈110 <sup>b</sup>	78
330	70-120	≈200 <sup>b</sup>	75

<sup>a</sup>The pump pulse was broadened by the cryostat window in this case.

<sup>b</sup>These values are estimates, as the CPM shape was too complex (see Fig. A.31 in the appendix).

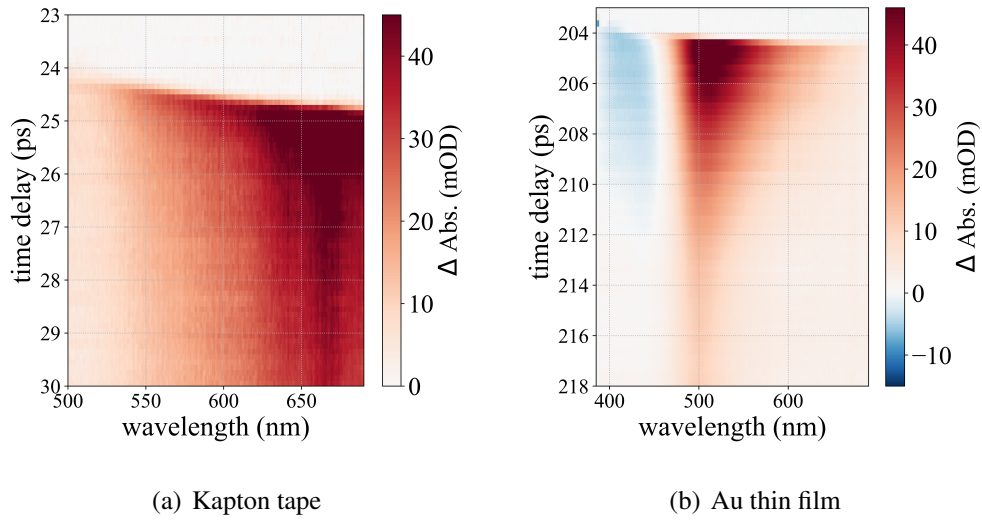


**Figure 2.12:** Non-GDD-corrected time-zero scans in the transient absorption setup. Exemplary scans from (a) Kapton tape, (b) thin gold film, both excited at 340 nm. N.B.: time delay in this context refers to the absolute position of the motorized delay stage, converted to ps.

placed onto the sample disk, before fine-tuning it based on the transient signal intensity. Examples for these time zero measurements are shown in Fig. 2.12.

When dealing with pulse durations below 100 fs and peak fluences on the few  $\text{mJcm}^{-2}$  scale or higher, peak powers up to  $100 \text{ GW}\cdot\text{cm}^{-2}$  are reached, which are known to cause multi-photon excitation in many systems, and which not only falsify the measured data but can also damage the sample.<sup>[109]</sup> In order to exclude these effects, fluence dependence measurements were routinely carried out, whenever a new sample or process was studied or significant changes to the laser setup had been made. If possible, entire scans were recorded at different fluences and the first singular values in the range after excitation were compared. Otherwise, a time domain in which the signal was constant was integrated in time and wavelength to yield a single value for each fluence. These values in either case were plotted and fit to determine the fluence range in which the signal was linear (see Fig. 2.13), which represents the range appropriate for the actual measurements,

prior to the onset of multi-photon absorption or other damaging effects.<sup>41</sup>

In a single transient absorption scan, multiple spectra per time step were recorded, usually between 24 and 1000, and averaged. For any data acquisition beyond mere testing and coarse determination of  $t_0$ , several scans with the same parameters and time steps were taken. This enabled monitoring and comparison of the scans to assure reproducibility and allowed for regular measurements of the excitation pulse energy. These scans were averaged in the post-processing routine and concatenated if individual scans with different time steps had been taken, i.e. before the improvements to the acquisition software. Finally, most of the data shown in this thesis was smoothed using a 2D Gaussian filter ( $\sigma = 0.8$  pixels) for clarity.

All transient absorption scans spectrally resolve the inherent group-delay dispersion of the probe pulse, leading to a wavelength dependence of the pump-probe delay, usually causing the TA signal at shorter wavelengths to appear earlier than at longer wavelengths (conf. Fig. 2.12). This artifact was corrected in post-processing using the following routine: First the wavelength-dependent  $t_0$  values were determined, either by analysis of the CPM signal, being inherently linked to the pump-probe overlap in time, or directly by the data obtained from the sample, if an instantaneous<sup>42</sup> signal at  $t_0$  was present.<sup>43</sup> Using these  $t_0$  values for the GDD, it was corrected by shifting the data matrix in time taking advantage of the time-shift theorem in Fourier space (conf. equation 2.5).

## 2.4.6 Data analysis methods

As will become evident in the following chapters, adequate selection and implementation of various data analysis strategies, based on the underlying photochemistry and the observed spectral dynamics, is crucial to appropriately describe, quantify and interpret transient spectroscopic data. This section gives a brief introduction into the applied methods as well as their advantages and disadvantages, and under which circumstances they are appropriate.

### Exponential models

A ubiquitous underlying principle in the analysis of transient processes is based on fitting the temporal progression of a certain parameter  $P(t)$ , in the simplest case the TA signal itself at a specific wavelength ( $\Delta A_\lambda(t)$ ), with the sum of  $N$  exponential decay functions:<sup>[110]</sup>

---

<sup>41</sup>The fluence dependence measurements for all experiments presented in this thesis can be found in section A.3 in the appendix.

<sup>42</sup>Instantaneous in this context means a rise time shorter than or equal to the instrument-response function of the setup.

<sup>43</sup>This often yielded a better outcome of the GDD correction, presumably because the CPM signal was too complex to yield reliable  $t_0$  values in these particular cases.

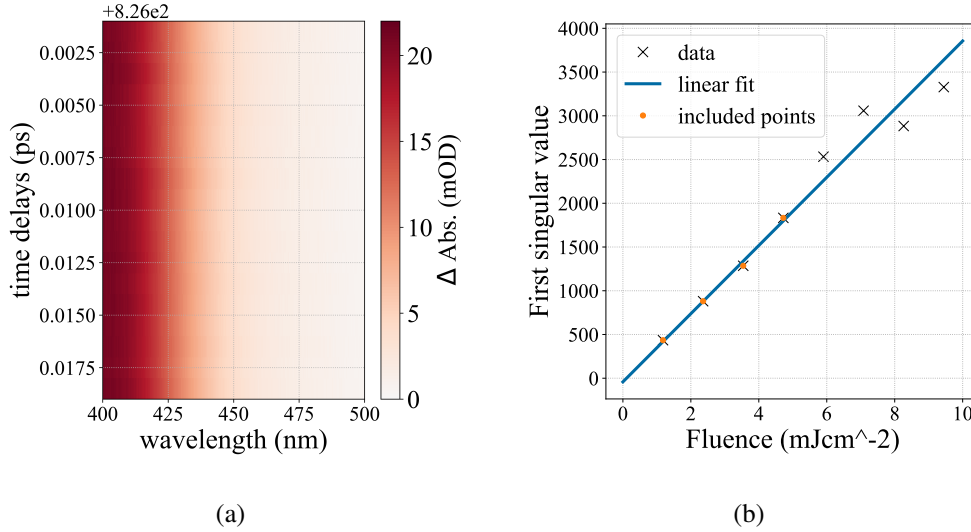


**Figure 2.13:** Exemplary fluence dependence measurement in transient absorption spectroscopy. (a) TA map of the data matrix for SVD, (b) singular values for the applied fluences and linear fit. While a linear fit above  $5 \text{ mJcm}^{-2}$  was still feasible, the evidently larger deviations motivated restricting the fit range and thereby the fluence range to be considered safe to  $<5 \text{ mJcm}^{-2}$ .

$$P(t) = \sum_{j=1}^N b_j \cdot \exp\left(-\frac{(t-t_0)}{\tau_j}\right) \otimes IRF(t-t_0) \quad (2.23)$$

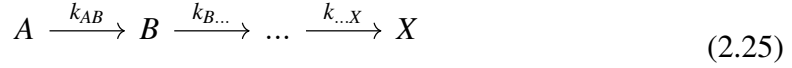
in which  $b_j$  is the amplitude (or weight) of the individual exponential decay component,  $\tau_j$  the associated exponential lifetime (also referred to as time constant),  $t_0$  the point of excitation and  $IRF$  the instrument-response function. The latter is usually a Gaussian function and required if time delays before and around time zero are included in the fit. Notably, in this sum of exponential functions, the amplitudes of the individual components are independent, which is appropriate for multiple, parallel decay (or rise) processes contributing to  $P(t)$ , each satisfying the following differential equation for the concentration  $c_A(t)$  of a corresponding, spectrally detectable species  $A$  (conf. eq. 2.19):

$$\frac{dc_A(t)}{dt} = -k_A c_A(t) \quad (2.24)$$

If interpreted appropriately, this parallel model is often sufficient, but more complex models require the solution of a set of interlinked differential equations. One of the most common approaches is the unidirectional sequential model (also referred to as kinetic chain), in which an initial species<sup>44</sup>  $A$  evolves towards an equilibrium state or (chemical) species

<sup>44</sup>Species in this case specifically means a spectrally visible species, which is associated with the population of one or multiple distinct (electronic or vibrational) states or one or multiple molecular configuration(s). It can be but is not necessarily equivalent to a chemical species, such as a distinct isomer or the product of a photochemical reaction. Thus, for the latter case the term chemical species will be used, while species refers to the more generalized case.

$X$ , possibly via one or multiple successive intermediates ( $B, C, \dots$ ):



wherein  $k_{AB}$  denotes the transfer rate constant from species  $A$  to  $B$  and so forth. The differential equations for concentrations (or populations)  $c$  of the species in equation 2.25 take the following form:

$$\begin{aligned} \frac{dc_A(t)}{dt} &= -k_{AB}c_A(t) \\ \frac{dc_B(t)}{dt} &= k_{AB}c_A(t) - k_{B\dots}c_B(t) \\ &\dots \\ \frac{dc_X(t)}{dt} &= k_{\dots X}c_{\dots}(t) \end{aligned} \quad (2.26)$$

While the solutions for the concentrations are of a similar form to the parallel decay model, the amplitudes  $b$  are no longer independent but depend on the rate constants of the preceding steps:

$$c_l(t) = \sum_{j=1}^l b_{jl} \exp(-k_j t) \otimes IRF(t) \quad (2.27)$$

for the concentration of species number  $l \in \mathbb{N}_{>0}$  in the unidirectional chain. In the unidirectional case, the amplitude factors  $b_{jl}$  can be calculated via the following equation:<sup>[111]</sup>

$$b_{jl} = \frac{\prod_{m=1}^{l-1} k_m}{\prod_{n=1}^l (k_n - k_j)} \quad (2.28)$$

Notably, equation 2.27 represents a general solution for sequential models, including branched ones, but in the latter case the amplitudes can no longer be generalized and some of them may be zero, depending on the model. For the particular branched models used in this thesis, the differential equations were solved by the common variation of the constant ansatz, for which an example can be found in the appendix (section A.1). Depending on the specific model to be tested, multiple concentrations  $c_l(t)$  were added together and their contributions to the investigated parameter  $P(t)$  weighted with individual amplitude factors.<sup>45</sup>

---

<sup>45</sup>For example, the transient absorbance at a given wavelength may be fit with a two-step (three-species) sequential model, from which only the first and last carry a significant contribution to the signal and the first has a higher transition dipole moment at this particular wavelength, e.g. by a factor of 2. This would result in the weighted sum of the three concentrations with amplitudes of  $a$  for the first ( $l = 1$ ), 0 for the second ( $l = 2$ ) and  $0.5 \cdot a$  for the last species ( $l = 3$ ).

### Spectral band analysis

As mentioned, the simplest case of spectral analysis is the application of one of the models above (parallel or sequential) to the temporal progression of the transient absorbance at a particular wavelength, also referred to as single-point kinetic fits. While the method is robust and straightforward, certain spectral dynamics invalidate the outcome of such fits, most prominently the influence of shifts in the spectral center position as well as dynamic changes in the spectral width. The former can be characterized by means of the spectral center of gravity  $SC$  (also referred to as centroid or spectral center of mass) for each discrete time delay  $t$  in the pixel range from pixel  $N$  to  $M$ :

$$SC_t = \frac{\sum_{i=N}^M \Delta A_{t,i} \cdot \tilde{\nu}_i}{\sum_{i=N}^M \Delta A_{t,i}} \quad (2.29)$$

The spectral centroid is calculated in the spatial frequency domain ( $\tilde{\nu}$ ), which is proportional to the (transition) energy and thus more appropriate. Being the inverse of the wavelength, it is readily converted back to the latter for easier comparison to the spectroscopic data. The temporal progression of the centroid can subsequently be fit using one of the exponential models discussed above.

The effects of spectral narrowing and shifts can also be mitigated by integration of the appropriate spectral region, if there is no influence from other spectral species in the same range. In this case, the spectral integral is directly proportional to the species' population assuming no significant changes in transition dipole moment(s). However, these ideal conditions are often not provided, especially for time delays shortly after the point of excitation, demanding for more complex and holistic analysis methods.

### Global and target analysis

Arguably the most popular strategy to disentangle contributions from multiple species to a transient absorption measurement is that of global and target analysis.<sup>[112–115]</sup> Rather than single wavelengths, the entire two-dimensional spectral map is approximated with a fit matrix  $F_{\lambda,t}$ , minimizing the least-square sum of the difference between it and the data matrix. The fits are composed of a temporal and a spectral part:

$$F_{\lambda,t} = \sum_i^N A_{\lambda,i} \cdot C_{i,t} \quad (2.30)$$

in which  $N$  is the number of components necessary to reconstruct the data,  $A_{\lambda,i}$  is the spectrum associated with component  $i$  and  $C_{i,t}$  the corresponding temporal progression, according to the applied model. The temporal part is obtained analogously to the single-point case (equations 2.23 and 2.27 for the parallel and sequential cases, respectively), but

instead of summation<sup>46</sup> of the addends they are individual rows in the matrix  $C$  and their weight factors are set to one, since the corresponding spectral amplitude is contained in  $A$ . Alternatively put, equations 2.23 and 2.27 are special cases of equation 2.30 for the fit of a single wavelength (i. e. row in matrix  $F$ ). Depending on the temporal model, the spectra  $A_{\lambda,i}$  are termed decay- or species-associated spectra (DAS or SAS) for the cases of a parallel decay (global analysis) and a sequential model (target analysis), respectively. Notably, it is possible to retrieve the spectral components  $A_{\lambda,i}$  without the application of a model or variation of additional parameters. They are obtained, under the premise that the fit matrix  $F$  converges towards the real data matrix  $D$ , via multiplication of equation 2.30 with the right inverse of  $C$ :<sup>[116]</sup>

$$A_{\lambda,i} = \sum_i^N D_{\lambda,i} \cdot C_{i,t}^{-1} \quad (2.31)$$

Thus, in each step of the optimization algorithm, the DAS for the fit parameters  $\tau_i$  or  $k_i$  are calculated using equation 2.31 yielding the fit matrix  $F$  via equation 2.30. The two-dimensional least-square sum of the difference between  $F$  and the data matrix  $D$  can then be minimized via standard optimization algorithms varying the fit parameters.<sup>[117]</sup>

It should be pointed out that in addition to the evident bias of the introduced models in global and especially target analysis, the fundamental underlying assumption is that the data can be decomposed into additive components, as implied in equation 2.30.<sup>47</sup> The same assumption is made when analyzing transient absorption data by singular value decomposition (SVD),<sup>[118,119]</sup> but without the introduced bias of exponential functions or fit parameters:

$$D = U \cdot S \cdot V^T \quad (2.32)$$

which for the case of transient absorption spectra can be written as:

$$D_{t,\lambda} = \sum_i U_{\lambda,i} S_{i,i} V_{i,t} \quad (2.33)$$

where  $U$  contains the left singular vectors (temporal components) and  $V^T$  the right singular vectors (spectral components), while the diagonal elements of the singular matrix are the corresponding weights of the components  $i$ , sorted in descending order. Hence, only the first few singular vectors will contribute to the data significantly. On the one hand, this can be exploited in order to remove noise from the data, on the other hand, the singular vectors, especially the ones carrying the temporal information can be analyzed further, if

<sup>46</sup>In case of target analysis (sequential model), summation here refers to adding multiple components  $c_l(t)$  obtained from equation 2.27 to describe a single parameter. The temporal components  $c_l(t)$  themselves usually still consist of multiple exponential functions.

<sup>47</sup>This assumption is generally valid for optical absorption spectroscopy. Nonetheless, the fact that in a fit, all components are superimposed is to be considered when interpreting individual contributions to the signal (see for example section 3.2.2).

an appropriate model can be found. SVD thus provides information of temporally correlated spectral components and their importance for the data. While it can be argued that its lower bias makes it preferable over global and target analysis methods, the introduction of exponential functions is physically justified by a priori understanding of the process, while the singular vectors not necessarily correspond to a photophysical process. Thus, there is no clearly preferred method among these and the method of choice depends on the specific investigated system. In the data analyzed within the scope of this thesis, for both methods examples have been found, in which one turned out more suitable than the other.

### **Dynamic line shape analysis**

As will be seen in chapters 3 and 4, there are scenarios where neither of the holistic methods discussed so far are satisfactory. This is because in all cases, the spectral components are temporally independent, which means only the overall amplitude of the components changes in time. Like in case of single-point kinetic fits, this does not account properly for spectral shifts in which the central wavelengths of the transient signals change. As discussed, spectral integration can mitigate this issue, but also removes information such as the central wavelength, spectral line width and absorption fine structure. Therefore, a new fit routine was developed, denoted as dynamic line shape analysis (DLSA). As the name suggests, it is based on the commonly applied line shape fit method in which an absorption spectrum is fit with one or the sum of  $N$  line shape functions (*LSF*) and an optional additive constant  $C$ :

$$Abs.^{(fit)}(\bar{\nu}) = \sum_j^N [A_j \cdot LSF_j(\bar{\nu})] + C \quad (2.34)$$

Since the line-shape functions are symmetric while the absorption spectra are asymmetric in wavelength, they are again described in terms of the spatial frequency  $\bar{\nu}$ . The novelty in this routine lies in the execution of such fits for each time delay whilst establishing a temporal correlation between the fit parameters by using the result for a given time delay as the initial values for the subsequent step. While it was not done within the scope of this thesis, the temporal behavior of the line shape parameters could itself be constraint by introducing an exponential progression, analogously to the global fit routines. However, the increased number of parameters may affect the fit consistency.

Commonly used line shape functions are Gaussian (eqn. 2.35), Lorentzian (eqn. 2.36) or Voigt profiles (eqn. 2.37). The latter is a convolution of the two former distributions and its function contains both the Gaussian width parameter  $\sigma$  and the Lorentzian parameter  $\gamma$ . It is obtained by evaluating the real part of the Faddeeva function (eqn. 2.38).<sup>[120]</sup> From a photophysics perspective, the Lorentzian distribution describes homogeneous broaden-

ing (vide supra). Inhomogeneous broadening on the other hand can be accounted for mathematically by convolution with a Gaussian, which is why the Voigt profile is most appropriate for the description of optical transitions. If otherwise a fit would contain too many independent parameters to converge, the pure Gaussian can be used as a less complex approximation.

$$LSF_j^{(Gauss)}(\bar{\nu}) = \frac{1}{\sigma_j \sqrt{2\pi}} \cdot e^{-\frac{(\bar{\nu}-b_j)^2}{2\sigma_j^2}} \quad (2.35)$$

$$LSF_j^{(Lorentz)} = \frac{1}{\pi\gamma_j} \cdot \frac{\gamma_j^2}{(\bar{\nu}-b_j)^2 + \gamma_j^2} \quad (2.36)$$

$$LSF_j^{(Voigt)} = \frac{1}{\sigma_j \sqrt{2\pi}} \cdot \text{Re} \left[ w \left( \frac{\bar{\nu}-b_j + i\gamma_j}{\sigma_j \sqrt{2}} \right) \right] \quad (2.37)$$

$$w(z) = e^{-z^2} (1 - \text{erf}(iz)) \quad (2.38)$$

The widths for the Gaussian and Lorentzian profiles are directly obtained from the corresponding parameters  $\sigma$  and  $\gamma$ , respectively.<sup>48</sup> For the Voigt profile, an approximate relationship exists between its line width at half maximum  $w_V$  and the FWHM values  $w_L$  and  $w_G$  of the corresponding Lorentzian and Gaussian functions:

$$w_V \approx \frac{C_1}{2} w_L + \sqrt{\frac{C_2}{4} w_L + w_G^2} \quad (2.39)$$

with the empirically determined parameters  $C_1 = 1.0692$  and  $C_2 = 0.86639$  for an approximation within 99.98% accuracy.<sup>[120]</sup> Which line-shape function is to be selected depends on the specific problem, especially the number of components used in the fit.

The DLSA routine has played a pivotal role in the analysis of the photochemical reaction dynamics of both spironaphthopyran in solution, aiding in the distinction between isomerization and equilibration dynamics (conf. section 3.2.2), and protonated Z-spiropyran, where it was possible to disentangle a complex transient absorption signal and extract the life times of the involved spectral species (conf. section 4.3.2).

## 2.4.7 Interactive data analysis software

All processing and analysis methods detailed in the previous sections have been integrated in a software package written in Python and embedded into an interactive graphical user interface (tkinter) enabling the inspection, processing and analysis of transient absorption spectroscopy data (see Fig. 2.14), even for users without extensive programming experience. By application during all spectroscopic analyses presented in this thesis, the software has been tested thoroughly and will be made available via GitHub<sup>[121]</sup> after a

<sup>48</sup>  $w_G = 2\sqrt{2\ln(2)}\sigma \approx 2.36\sigma$ ,  $w_L = 2\gamma$ .

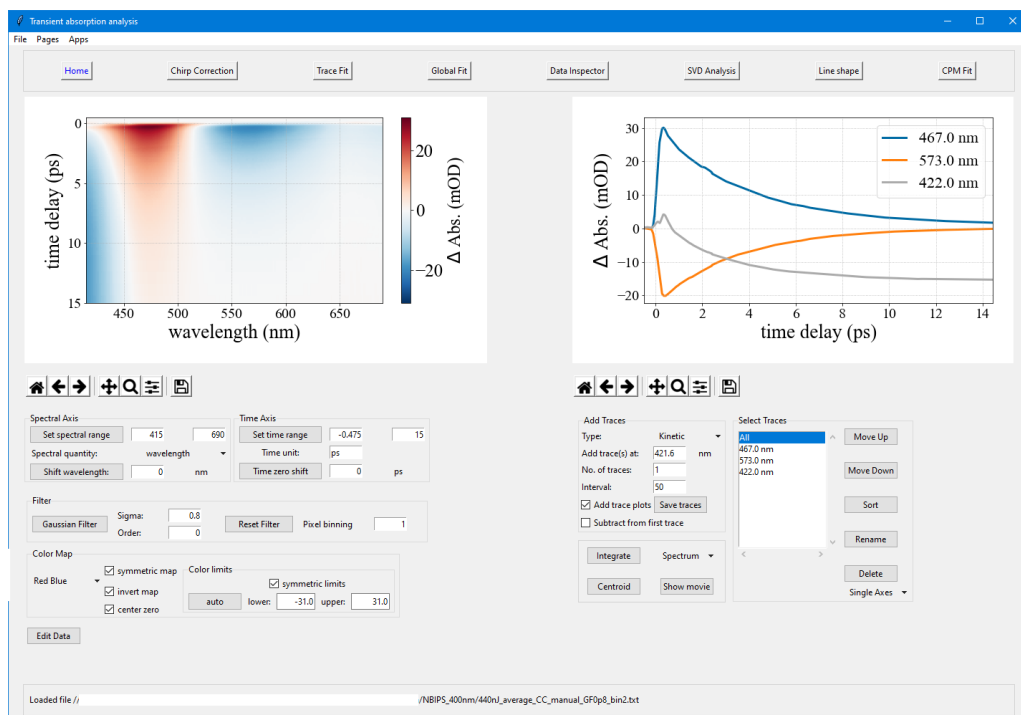


**Figure 2.14:** Main page of the developed interactive software for transient absorption data analysis. From the shown page, which offers basic tools as well as the selection of kinetic and spectral traces, several other pages or windows for the different analysis methods can be reached (see the navigation bar on top).

few envisaged improvements regarding readability and platform compatibility as well as the completion of a comprehensive user manual. The object-oriented program structure allows for the addition of further fit models or even whole analysis modules and facilitates potential collaborations. A few exemplary images from the GUI as well as essential excerpts from the source code can be found in the appendix, section A.1.

## 2.5 Ultrafast Electron Diffraction

Ultrafast electron diffraction (UED) experiments were conducted using single crystals of spironaphthopyran on the one hand, and all three of the investigated diarylethene derivatives on the other hand. These experiments should be considered preliminary, since more extensive studies will be required in order to obtain quantitatively significant data. Nonetheless, the results obtained within the scope of this thesis set the basis for and encourage execution of further UED experiments and are therefore discussed qualitatively in the respective chapters. Since extensive analyses were not carried out, a detailed theoretical background is not required. Nevertheless, a few basic concepts need to be familiar, which are laid out in the next section, followed by a description of the utilized experimental setups and parameters.

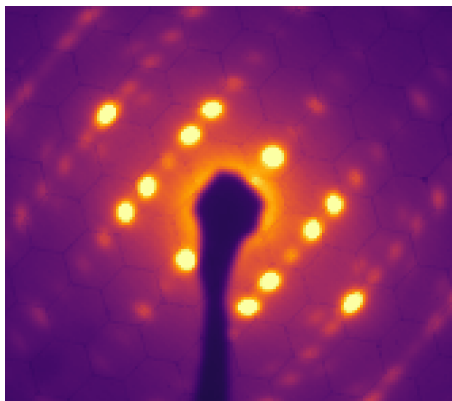


**Figure 2.15:** Example for an electron diffraction pattern. The sample was a 100 nm thin single-crystalline film of a di(benzothienyl)perfluorocyclopentene (see chapter 5) and the pattern was recorded in an ultrafast electron diffraction setup (90 keV electron energy).

### 2.5.1 Electron diffraction fundamentals

Fig. 2.15 shows the electron diffraction pattern obtained from a single-crystalline di-thienylethene derivative, one of the photochromic molecules investigated in this thesis work. As can be readily seen, it consists of regularly spaced, distinct spots with varying intensity, which are arranged center-symmetrically with respect to the main electron beam. It is the mere result of the incidence of a series of electron pulses on a thin crystalline slice and focusing the transmitted beam onto a CCD camera. While the phenomenon of diffraction patterns is well-known and understood among scientists, it is nonetheless remarkable and warrants a brief explanation how elastic interaction of electrons with a molecular crystal can produce such a result.<sup>49</sup>

#### Electron scattering and diffraction

Diffraction is the interference of a coherent wave scattered from one or multiple objects, which are of comparable size to the wavelength. As an incident plane wave is elastically scattered, a spherical wave is emitted with an amplitude denoted as the scattering amplitude  $f(\Delta\vec{k}, \vec{r})$ ,  $\Delta\vec{k}$  being the difference in wavevectors between the incident and scattered waves, thus representing the momentum transfer. For electrons, the scattering due to an arbitrary electrostatic potential  $U(\vec{r})$  can be derived by solving the corresponding Schrödinger equation for an electron with mass  $m_e$  to yield:

$$f(\Delta\vec{k}, \vec{r}) = -\frac{m_e}{2\pi\hbar^2} \int U(\vec{r}) e^{-i\Delta\vec{k}\cdot\vec{r}} dV \quad (2.40)$$

It is evident from equation 2.40 that the integral contains an oscillating component indicating that the scattering amplitude is only finite for certain angles, i.e. constructive interference of the scattered wave. However, a condition for these angles cannot be de-

<sup>49</sup>Since most of the content can be found in common textbooks, literature references will only be given in a few specific cases. The general content is based on refs. [58, 97, 122–124]

rived without further knowledge about the electrostatic potential  $U(\vec{r})$ . Considering an atomic or molecular material as the scattering object,  $U(\vec{r})$  can be approximated via the independent-atom model as the superposition of all atomic potentials  $U_m$  at position vectors  $\vec{r}_m$ , with an individual scattering amplitude  $f_m(\Delta\vec{k})$  for each atom:

$$f(\Delta\vec{k}) = \sum_m f_m(\Delta\vec{k}) e^{-i\Delta\vec{k} \cdot \vec{r}_m} \quad (2.41)$$

### The crystal lattice

Crystals in the classical sense are characterized by translation invariance, i.e. for each point  $\vec{r}$  a large number  $N$  of points  $\vec{r}'$  exists, from which the crystal appears identical. The corresponding translation vectors  $\vec{T} = \vec{r} - \vec{r}'$  are discrete points in a three-dimensional vector space spanned by the basis vectors  $\vec{a}_i, i \in \{1, 2, 3\}$ , such that:

$$\vec{r} - \vec{r}' = \vec{T}_{uvw} = u\vec{a}_1 + v\vec{a}_2 + w\vec{a}_3 \quad u, v, w \in \mathbb{Z} \quad (2.42)$$

The parallelepiped formed by the basis vectors is called the unit cell and represents the smallest symmetrical unit of the crystal lattice.<sup>50</sup> The translation operators  $\vec{T}_{uvw}$  dictate the geometry of the unit cell and thus the entire crystal. Depending on the basis, the lattice can be classified into one of 14 possible so-called Bravais lattice types.

### The shape factor and the structure factor

The introduction of the unit cell and the lattice vectors enables further elaboration of the scattering amplitude within the independent-atom approximation for the case of molecular crystals. This is achieved by separating the atomic positions  $\vec{r}_m$  into the lattice translation  $\vec{T}_{uvw}$  and the position  $\vec{r}_l$  of the so-called basis atoms within the unit cell:

$$\vec{r}_m = \vec{T}_{uvw} + \vec{r}_l = \sum_{i=1}^3 n_i \vec{a}_i + \vec{r}_l \quad (2.43)$$

Substitution of  $\vec{r}_m$  into equation 2.41 for a crystal consisting of  $N_i$  unit cells for each basis  $\vec{a}_i$  yields:

$$f(\Delta\vec{k}) = \prod_{i=1}^3 \left( \sum_{n_i=0}^{N_i-1} e^{-i\Delta k n_i \vec{a}_i} \right) \sum_l f_l(\Delta\vec{k}) e^{-i\Delta\vec{k} \cdot \vec{r}_l} \quad (2.44)$$

<sup>50</sup>Since larger symmetry units still satisfy translation invariance, the distinction between the smallest possible unit cell, the so-called primitive unit cell with corresponding primitive basis vectors, needs to be made. However, the term unit cell is commonly used to denote the specific case of the primitive unit cell, which is also adopted here.

The geometric progression in equation 2.44 can be simplified:<sup>51</sup>

$$f(\Delta\vec{k}) = \prod_{i=1}^3 \left( \frac{1 - e^{-iN_i\Delta\vec{k}\vec{a}_i}}{1 - e^{-i\Delta\vec{k}\vec{a}_i}} \right) F(\Delta\vec{k}) \quad (2.45)$$

introducing the definition of the structure factor  $F(\Delta\vec{k}) = \sum_l f_l(\Delta\vec{k}) e^{-i\Delta\vec{k}\vec{r}_l}$ . The latter depends on the position and nature of the basis atoms within the unit cell, while the product in equation 2.45 contains the information associated with the unit cell geometry and is thus referred to as the shape factor  $S(\Delta\vec{k})$ . The structure factor is the more complex and system-specific quantity encompassing not only the atomic or molecular structure but also contributions from thermal motion (Debye-Waller effect),<sup>[125,126]</sup> making it the main target for modeling of diffraction patterns. Since reconstruction of atomic positions is not the subject of this thesis work it will not be discussed in more detail.<sup>52</sup> The shape factor on the other hand can be used to derive general diffraction conditions, specific to a given Bravais lattice.

The measured diffraction intensity is the absolute square of the scattering amplitude and the contribution from the shape factor is thus obtained via substitution using Euler's equation and half-angle relations of the trigonometric functions:

$$|S(\Delta\vec{k})|^2 = \prod_{i=1}^3 \frac{\sin^2\left(\frac{1}{2}N_i\Delta\vec{k}\vec{a}_i\right)}{\sin^2\left(\frac{1}{2}\Delta\vec{k}\vec{a}_i\right)} \quad (2.46)$$

The absolute square of the shape factor is only significantly large if the arguments of the sine functions are integer multiples of  $\pi$  in all three dimensions. The resulting condition for non-zero intensities is known as the Laue diffraction condition:<sup>[127]</sup>

$$\Delta\vec{k} \cdot \vec{a}_i = 2\pi h_i \quad h_i \in \mathbb{Z} \quad (2.47)$$

This limitation for allowed momentum transfers and thereby diffraction angles is indeed the reason why, for single crystals, an intensity pattern of discrete spots such as the one shown in Fig. 2.15 is obtained.

### The reciprocal lattice

Like the translation vectors  $\vec{T}_{uvw}$ , those momentum transfer vectors  $\Delta\vec{k}$  which fulfill the Laue diffraction condition are discrete points in a three-dimensional vector space. Its basis

---

<sup>51</sup>  $\sum_{i=0}^N -1x^i = (1 - x^N)/(1 - x)$ .

<sup>52</sup> Nonetheless it is important to note that changes in the distribution of atoms within a unit cell, which includes changes in molecular structure, solely lead to a change in intensity of the diffraction signal. Neither changes in diffraction peak position nor peak widths are thus indications of a change in the structure factor, but are associated with the unit cell geometry.

vectors  $\vec{b}_j, j \in \{1, 2, 3\}$  are related reciprocally to the basis vectors of the Bravais lattice through  $\vec{a}_i \cdot \vec{b}_j = 2\pi\delta_{ij}$  and  $|\vec{b}_i| = 2\pi/|\vec{a}_i|$ . Therefore, the lattice comprised of all possible solutions  $\Delta\vec{k} = \vec{G}$  of equation 2.47 is called the reciprocal lattice and  $\vec{G} = \sum_{i=1}^3 h_i \vec{b}_i$  the reciprocal lattice vectors. The integer coefficients  $h_i$  are called the Miller indices, also written as  $h, k$  and  $l$ , and are used to identify diffraction peaks in the measured pattern. Furthermore, each reciprocal lattice vector  $\vec{G}_{hkl}$  is the plane vector of (i.e. orthogonal to) a set of parallel crystal planes in the direct lattice with distances of  $d_{hkl,n} = n \cdot 2\pi/|\vec{G}_{hkl}|, n \in \mathbb{Z}$ .<sup>53</sup> Indeed, a diffraction pattern is the two-dimensional projection of the reciprocal lattice. However, not all reciprocal lattice points are experimentally accessible since the momentum transfer  $\Delta\vec{k}$  cannot take arbitrary values. Only the scattering angle  $\theta$  is a free parameter, while the absolute value of  $\Delta\vec{k}$  is dictated by the wavelengths of the incident and scattered waves. This can be used to obtain a more intuitive diffraction condition, known as Bragg's law. For elastic scattering, the wavelength  $\lambda$  does not change and thus  $\vec{k}_{in}^2 = \vec{k}_{scat}^2$ . It can be shown,<sup>[123]</sup> that this allows to rewrite the general requirement  $\Delta\vec{k} = \vec{G}$  as:

$$\vec{G}_{hkl}^2 = 2\vec{k}_{in} \cdot \vec{G}_{hkl} = 2 \cdot \frac{2\pi}{\lambda} \cdot |\vec{G}_{hkl}| \cdot \cos \alpha \quad (2.48)$$

with  $\alpha = 90^\circ - \theta$  being the angle between  $\vec{k}_{in}$  and  $\vec{G}_{hkl}$ . Expressing equation 2.48 in terms of  $\theta$  and the distance  $d_{hkl}$  between associated crystal planes yields Bragg's diffraction condition in its familiar form:

$$2 \cdot \frac{2\pi}{\lambda} \cdot n \cdot \frac{2\pi}{d_{hkl}} \cdot \sin \theta = \left( n \cdot \frac{2\pi}{d_{hkl}} \right)^2$$

$$2d_{hkl} \sin \theta = n \cdot \lambda \quad (2.49)$$

It should be noted that the discussed diffraction conditions in this precise formulation would almost never be fulfilled in reality, requiring an exact match of reciprocal lattice vectors and momentum transfer, which is restricted by the wavelength. However, actual crystals are finite, leading to broadening of the reciprocal lattice points and the electron wavelength has a finite bandwidth, both of which make the match between  $\Delta\vec{k}$  and  $\vec{G}$  much more likely and more diffraction peaks accessible.

## 2.5.2 Electron pulse generation and propagation

In order to generate short electron pulses, the photoelectric effect is utilized by irradiating a photocathode with a laser pulse whose photon energy is similar to the effective work function, which is the work function of the material under the application of an electric field. The latter is also required to accelerate the electrons to kinetic energies close to

<sup>53</sup>For example, the planes parallel to the basis vectors  $\vec{a}_2$  and  $\vec{a}_3$  are indicated as the (100) set of planes and the corresponding diffraction peak is referred to as the (100) peak. Negative  $hkl$  values are indicated as  $(\bar{h}\bar{k}\bar{l})$ .

100 kV, which is the commonly used voltage for electron diffraction of thin crystalline slices in transmission. Under these conditions, a laser wavelength of 266 nm is sufficient for emission from a gold photocathode (see section A.7.5 in the appendix). The use of a laser pulse to control the emission bears the further advantage of readily applying a pump-probe scheme or the use of an optically triggered streak camera for time-resolved experiments.

The electron scattering cross-section, which is a measure of the scattering probability, is on the order of  $10^{-18}\text{cm}^2$  at 100 kV,<sup>[128]</sup> which is about  $10^6$  times higher than that of x-rays.<sup>[129]</sup> This means that the mean free path of electrons in organic materials, being the inverse of the product of scattering cross-section and the number density, is on the order of 200 nm or less. On the one hand this requires samples to be sufficiently thin to avoid effects from multiple scattering and an overall reduction in diffraction intensity. On the other hand, electrons are inherently well-suited for ultrathin samples. Another consequence of the high scattering cross-section is the need for an ultrahigh vacuum when using electrons as a probe since the mean free path even in air under ambient pressure is only about  $10^3$  times longer than in such crystals, i.e. on the order of 200  $\mu\text{m}$ . These considerations need to be taken into account in the design of any experimental setup using electrons as probe and UED is no exception.

Two more parameters of the electron pulses are crucial, specifically for ultrafast electron diffraction. The first, generally important for all diffraction techniques, is the transverse coherence length, which is inversely proportional to the transverse momentum spread. If the coherence length is shorter than approximately the unit cell size, diffraction can no longer be observed. For flat photocathodes and ultrashort pulses, i.e. relatively large energy bandwidths, the transverse coherence length is still on the order of a few nanometers, which is sufficient for crystals of small organic molecules. While it is still desirable to improve the transverse coherence length, the more pressing problem faced when dealing with electron pulses is their space-charge broadening during propagation, which severely affects the temporal resolution. A numerical simulation by Siwick et al. in 2002 indicated that mutual electrostatic repulsion of the electrons leads to a broad axial velocity distribution, already after a propagation distance of 2 cm, with a linear relationship between relative axial velocity of the electrons in the pulse and their axial position.<sup>[130]</sup> This means that electrons at the front of the pulse are faster than those further back causing continuous broadening of the pulse.

### **2.5.3 Experimental approaches and setups**

One way to reduce the detrimental effect of space-charge broadening on the time resolution during propagation is to limit the distance between the electron source and the sample.<sup>[20,131]</sup> These experimental setups are denoted as compact electron guns and their development as an immediate response to the findings from Siwick et al. has enabled the

first sub-ps atomic movies, only a year later.<sup>[25]</sup> However, due to a minimum required distance between photocathode and anode to maintain sufficiently high voltages, finite dimensions of the anode and some spacing required between anode and sample holder, propagation distances below 2 cm are typically not feasible. Thus, while this approach is both simple and reliable, and often provides a sufficient time resolution for sub-ps processes, more complex setups have been developed in order to resolve faster structural dynamics. These setups exploit the second insight from the aforementioned study that the velocity distribution (or chirp, in analogy to the optical phenomenon) becomes linear. By using a radiofrequency cavity, commonly applied in accelerator technology, the linear chirp can be inverted such that the electrons in the pulse front are slower than the ones in the back.<sup>[28,31,52,132,133]</sup> Thus upon propagation, the fast electrons in the back of the pulse catch up with the others resulting in a certain propagation distance where the spatial (and thus temporal) distribution of the electrons is only limited by fundamental quantum mechanical laws, i.e. the Pauli and Heisenberg principles. Adjusting this inversion such that this propagation distance coincides with the sample position can be used to optimize the time resolution. While this method entails more deviations from the ideal case, due to timing jitter of the RF cavity, synchronization methods have been developed to overcome this, making experiments with sub-100 fs time resolution possible.<sup>[32]</sup>

Either of the general experimental approaches has been applied in experiments presented in this thesis and the specific setups will be described in the following. The compact electron gun, also called DC gun for distinction from RF-based electron diffractometers, has been used for sample tests with both single crystals of SNP and the diarylethene derivatives, dealt with in chapters 3 and 5, respectively. The setup is shown schematically in Fig. 2.16, as it was used for experiments on the diarylethene ring-closing reaction, operated with the Pharos laser system (see section 2.2). It has also been described in detail elsewhere, for instance in refs. [20, 97, 134]. The electron diffractometer itself consists of two vacuum chambers with individual turbomolecular pumps (VP), separated by the anode made of stainless steel. The electron pulses are generated by irradiation of a gold photocathode<sup>54</sup> inside the first chamber using the fourth harmonic of the Nd:YAG laser. The cathode is connected to a high voltage feedthrough providing stable voltages on the order of -100 kV with respect to the grounded anode with a distance between the anode and the photocathode of about 12 mm. For pump-probe scans, the arrival time of the photocathode laser beam is controlled using a motorized delay stage (DL). The electrons pass through a small aperture in the anode onto the sample, which is mounted on a copper sample holder (SH), about 1 cm away from the anode. The sample holder is motorized and connected to a cold finger enabling the use of liquid nitrogen or helium, if cryogenic

---

<sup>54</sup>The photocathode is made of a thin gold layer ( $\approx 30$  nm thickness) deposited on a chromium coated (5 nm thickness) sapphire disk (1 mm thickness). The chromium layer acts as an adhesive between the gold layer and the substrate.

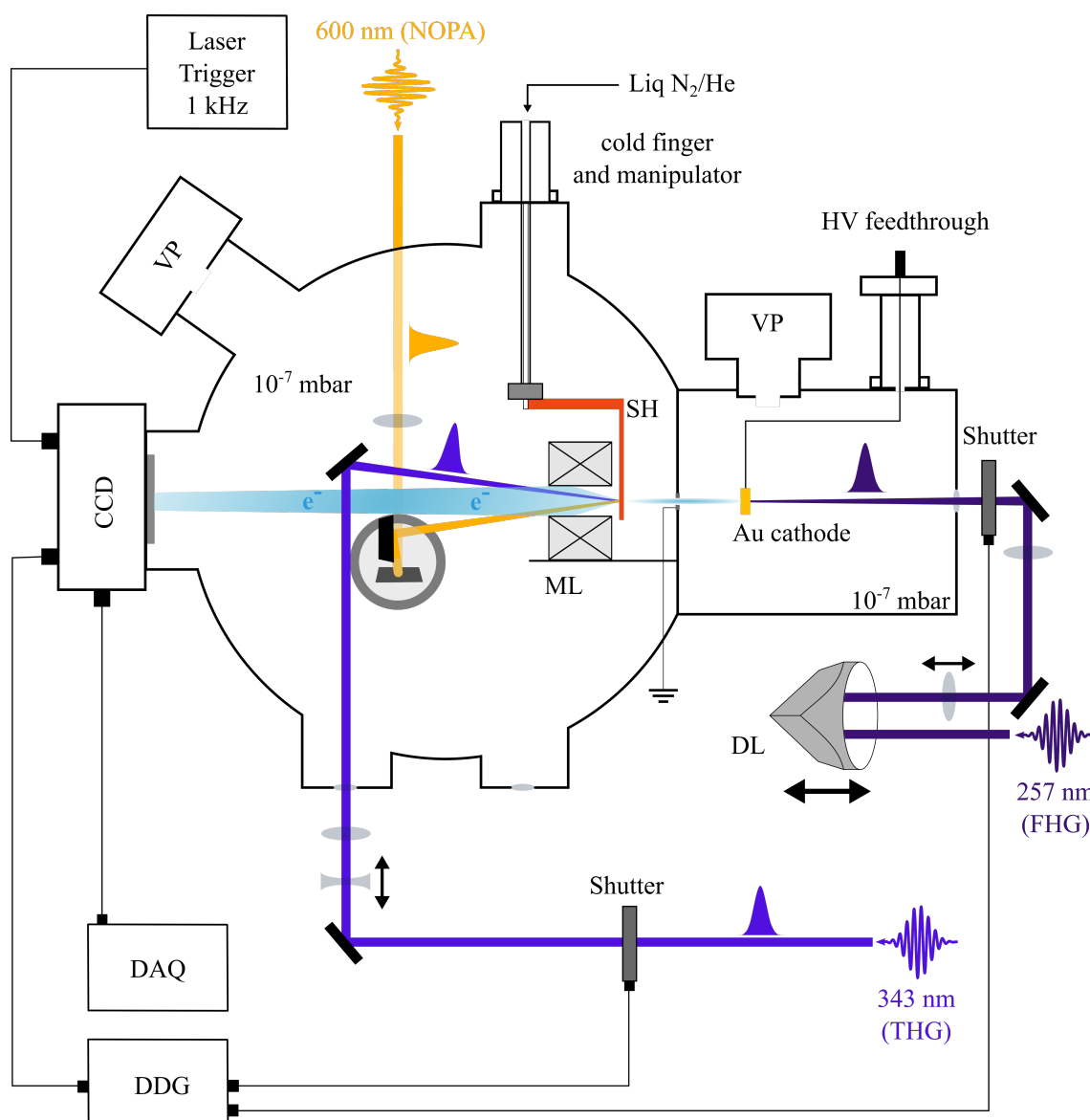


**Figure 2.16:** DC electron gun schematic as operated with the Pharos Nd:YAG laser system for preliminary time-resolved tests on the investigated diarylethene derivatives. The fourth harmonic (FHG) was used for the electron generation, while for sample excitation the third harmonic (THG) was applied. Synchronized photoreversion was carried out using a visible NOPA (600 nm central wavelength). VP = turbomolecular vacuum pump, SH = sample holder, HV = high voltage, DAQ = data acquisition unit, DDG = digital delay generator, DL = motorized delay stage, ML = magnetic lens.

temperatures are required. Behind the sample holder, a magnetic lens has been placed and is used to focus the electron beam onto the detector. The latter consists of a 2048x2048 pixel CCD camera and a phosphorous screen for electron-photon conversion, which are linked via a fiber-optical taper. The pump beam for the diarylethene experiments was the third harmonic (343 nm) and focused onto the sample using a Galilean telescope, while the photoreversion beam from the visible NOPA was focused via a convex lens. Both optics were placed outside the vacuum chamber to enable readjustment without open-

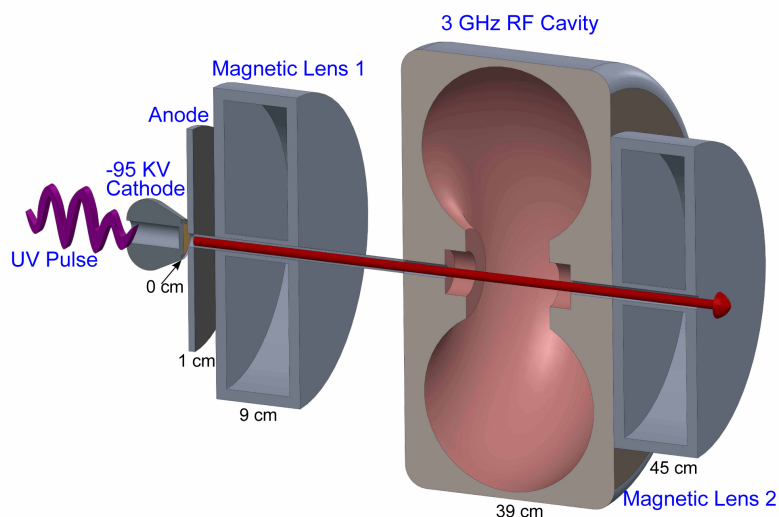


**Figure 2.17:** RF electron gun: pulse compression Scheme. Electron pulse generation was done by irradiation of the photocathode at 267 nm, before collimation of the beam with a magnetic lens. For compression, a 3 GHz RF cavity synchronized to the laser oscillator was used before focusing the beam onto the sample. The remainder of the setup was analogous to the DC gun (see Fig. 2.16). Reprinted with permission from [31] ©2012, The Optical Society.

ing the chamber. Shutters were used to control the accumulation of either probe-only or pump+probe diffraction patterns to calculate the time-resolved signal for each time delay.<sup>55</sup>

The time-resolved electron diffraction experiments on spiropyran discussed in this thesis were acquired in the RF electron gun at the university of Toronto, which has been used in the past in a multitude of projects, for instance in refs. [53, 55, 56, 135], and has been described in detail in ref. [31]. The general setup is equivalent to the DC electron gun described previously, but differs in the part between electron pulse generation and the sample holder, which contains a magnetic lens for beam collimation, the RF cavity for pulse compression and another magnetic lens to focus the beam onto the sample and the detector behind the sample holder (see Fig. 2.17). The radiofrequency amplifier is synchronized to the Ti:Sa laser system (*vide supra*) via a phase-locked loop circuit receiving the trigger from the oscillator pulses prior to entering the regenerative amplifier. In the experiments presented in this thesis, the electron pulses were generated with the third harmonic (267 nm) and the same wavelength was used for excitation of the sample.

<sup>55</sup>For more details on the data acquisition see ref. [97]

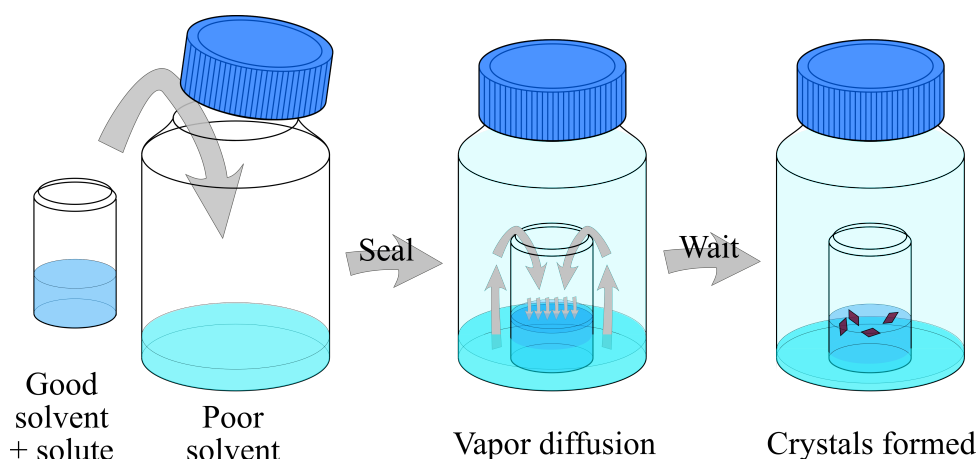


**Figure 2.18:** Crystallization via vapor diffusion. The principle is based on diffusion of the vapor of a poor solvent into the solution of the molecules to be crystallized in a better solvent, inside a sealed flask. "Poor" and "good" solvent refers to the specific solute. Wait times can be hours to weeks depending on the system and the aspired crystal size.

## 2.6 Sample Preparation

### 2.6.1 Crystallization

Crystallization of organic molecules into the highly ordered crystal structure is often no trivial task. While in principle it can be done from a solution, a liquid or a gas of the target molecule, only the first strategy was applied for this work. Nucleation of crystals in solution and their subsequent growth mostly is controlled by the solute concentration and/or changes in its solubility due to changes in temperature, pressure or solvent composition. A supersaturated solution is required, from which the molecules precipitate in a controlled manner and become part of the crystal lattice. The specific strategy to achieve this depends on the aspired results, predominantly regarding the crystal size. Requirements to the latter are dictated by the experimental methods in which the probe beam sizes are usually on the order of a few hundred  $\mu\text{m}$ , constituting a minimum lateral size of the crystal facets. On the other hand, preparation of thin slices via ultramicrotomy (vide infra) becomes infeasible if the facet to be cut exceeds edge lengths of 2-3 mm, depending on the knife dimensions.

In order to obtain single crystals of these dimensions with a low number of defects, an overall slow crystallization process becomes crucial. Two main strategies have been applied within the scope of this thesis and will be described briefly in the following.

#### Solvent Evaporation

The simplest procedure to grow single crystals involves slow evaporation of the solvent from a saturated solution, thereby gradually increasing the solute concentration, and thereby the level of supersaturation, until crystals start to form. The evaporation speed

is the most important parameter in this process and can be adjusted by the choice of solvent as well as the type of vessel regarding its permeability for the solvent vapor. While offering little room for optimization, for many small organic molecules this strategy is already sufficient to meet the experimental requirements and it was applied successfully to yield large single crystals of the diarylethene derivatives dealt with in chapter 5. Although solvent evaporation is a good starting point for the crystallization effort, more involved methods should be considered if the results are non-ideal. One example is slow cooling of the solution in a sealed vessel, which provides significantly more control over the creation of the supersaturated phase and in principle allows adjusting the speed for nucleation and growth separately. However, this requires a dedicated cooling device with sufficient temperature control.

### **Vapor diffusion**

Other common crystallization strategies are based on diffusion of a poor solvent for the target molecule into a saturated solution of the latter in a good or better solvent. This can be done with the poor solvent either being in a separate liquid layer on top of the solution (solvent layering) or in the gas phase (vapor diffusion).<sup>[136]</sup> The latter was applied to yield high-quality single crystals of spironaphthopyran (SNP, see chapter 3).

The process is depicted schematically in Fig. 2.18. A saturated solution in the better solvent, in this case  $\text{H}_3\text{CCl}$  (Chloroform), was prepared in a vial, subsequently placed inside a larger, sealable flask containing the poorer solvent,  $(\text{C}_2\text{H}_5)_2\text{O}$ . The solvents were chosen such that the poorer solvent had a higher vapor pressure than the better solvent, causing the former to evaporate predominantly. Slow diffusion of its vapor into the solution not only decreases the effective solubility of the solvent mixture but also creates a solubility gradient. The latter is beneficial because normally when nucleation occurs from a homogeneous solution, the initial growth may take place faster than ideal due to its supersaturation. With the gradient in solubility and thereby supersaturation this effect is mitigated to an extent.

Vapor diffusion thus allows for the slow and controlled formation of large organic single crystals. Its applicability is not always given because the solvent parameters need to meet the stated requirements. If there is a mismatch regarding their vapor pressure, solvent layering is one possible alternative, but in this case, they need to be immiscible.

### **2.6.2 Ultramicrotomy**

As elaborated in the previous sections, samples for both transient absorption spectroscopy and ultrafast electron diffraction need to be sufficiently thin for transmission of the probe beams, in order to match optical penetration depths or the electron mean free path, and to avoid multiple scattering effects in case of UED. Thus, their thickness should not exceed

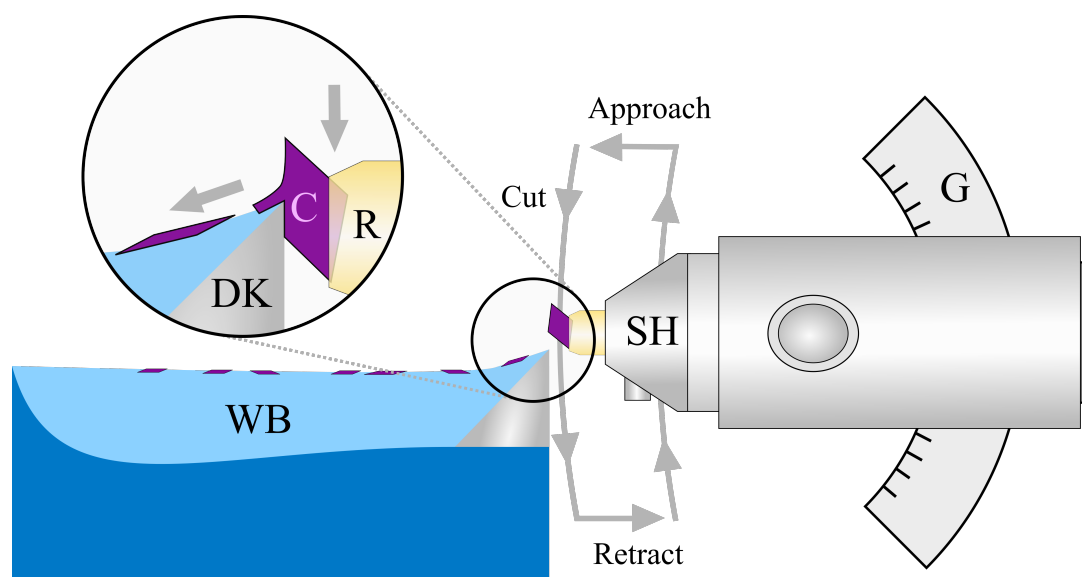


**Figure 2.19:** Ultramicrotomy working principle. A resin block onto which the crystal has been glued is fixed inside the specimen holder on the microtome arm. The crystal can be rotated axially and its tilt manipulated with the goniometer. The cutting cycle is indicated by arrows, with the difference between the retract and approach step sizes defining the crystal thickness. WB = water basin, DK = diamond knife, C = crystal, R = resin block, SH = specimen holder, G = goniometer.



**Figure 2.20:** Ultrathin samples of butyl-dithienylethene (a) for transient absorption spectroscopy on a UVFS substrate and (b) for ultrafast electron diffraction on copper TEM meshes inside the sample holder.

150 nm for UED and  $\approx 1 \mu\text{m}$  for TAS. On the other hand, their lateral size needs to be at least a few hundred  $\mu\text{m}$  wide (*vide supra*). One strategy to achieve this is the in-situ growth of crystalline or polycrystalline films onto a suitable substrate.<sup>[137]</sup> However, for many systems this is not feasible. A more general method, which has been applied for all crystalline materials investigated within the scope of this thesis, involves cutting thin slices off a macroscopic crystal using ultramicrotomy.<sup>[138,139]</sup> The working principle is shown in Fig. 2.19. The thin slices are cut by vertical movement of the crystal parallel to a diamond knife edge. The knife is placed on the edge of a small basin so that the cut slices do not stick to it but float on the surface of the liquid. By microscopic translation of

the knife towards the crystal between each cutting cycle, slices with a thickness defined by the step size are cut successively. Mounting of the crystal involves gluing it onto an epoxy substrate which is fixed in a specimen holder on the microtome arm. Both the crystal and the knife stage can be rotated in order to allow for cutting in parallel to a crystal facet, which ought to reduce abrasion of the knife and usually gives rise to a larger number of visible diffraction peaks. Once several slices have been cut, they are picked up from the water surface with a small metal loop and transferred onto either a standard TEM mesh for UED or a transparent substrate (usually UVFS or sapphire) for TAS (see Fig. 2.20).

---

# Ring-Opening Dynamics of Spiro-naphthopyran

This chapter deals with the photoisomerization dynamics of spironaphthopyran, a common representative of the spiroopyran family of photochromics. It was studied using transient absorption spectroscopy in solution and crystal, as well as ultrafast electron diffraction.<sup>1</sup> The chapter begins by giving a brief introduction into the photochromism of spiroopyrans in general and the scientific question behind their investigation in this work. The following sections deal with the transient absorption studies in solution and crystal, respectively, before reporting on the insights gained in the UED experiments.

## 3.1 Spiroopyran Photochemistry

The spiroopyran family is among the most prominent representatives of photochromic molecules in contemporary research.<sup>[140–142]</sup> While photochromism itself is defined simply by a color change upon light irradiation, this effect is generally caused by a reversible photoisomerization reaction, changing the molecule's structural, chemical and physical properties, which can be exploited in a variety of applications as photoswitches,<sup>[143–145]</sup> all-optical memories,<sup>[64,146,147]</sup> as markers in biological imaging<sup>[148]</sup> and as building blocks for photoactive smart materials,<sup>[142]</sup> to name only a few examples. Manipulating the properties of the different forms via chemical functionalization not only allows for optimization of the photochromic reaction in terms of increased quantum yields and robustness against photodegradation, but also enables the creation of highly complex, multi-responsive systems. In the introductory chapter of this thesis, it was outlined that photochromics are excellent subjects for the fundamental research of photochemical reactions. On the one hand, this is due to the ubiquity of the involved reaction motifs such as electrocyclization, cycloreversion or cis-trans-isomerization. On the other hand, the

---

<sup>1</sup>The results from the TAS study in solution have been published in ref. [68], along with result from numerical simulations carried out by Dr. Raison Dsouza. Publication of the TAS results from crystal is currently in preparation. Ultrafast electron diffraction results are preliminary and will likely be extended by a follow-up study.

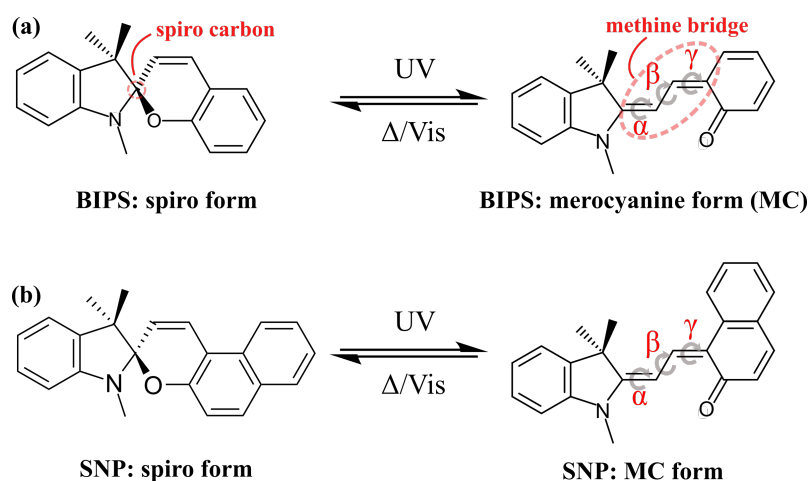


**Figure 3.1:** Reaction scheme of the spiropyran photoisomerization, shown exemplarily for (a) indolinobenzospiropyran (BIPS) and (b) indolinonaphthospiropyran (SNP), with the merocyanine forms in *trans-trans-cis* (TTC) configuration. The dihedral angles ( $\alpha$ ,  $\beta$ ,  $\gamma$ ) of the methine bridge in the MC forms are indicated. Reprinted with permission from [68], ©2019, Royal Society of Chemistry.

distinct absorption properties of their different isomers allow for their selective excitation (*vide supra*). Beyond their photochromic properties, spiropyrans in particular have been shown to be suitable for multi-responsive systems since certain derivatives also react to changes in the solvent (solvatochromism),<sup>[149]</sup> pH (acidochromism),<sup>[149–151]</sup> electrochemical stimuli,<sup>[152,153]</sup> or mechanical stimuli (mechanochromism).<sup>[154]</sup>

The photoisomerization reactions of benzo- and naphthospiropyran (BIPS and SNP) are depicted schematically in Fig. 3.1. Being indolino-spiropyran,<sup>2</sup> in their closed forms they consist of an indoline and a pyran moiety, which are linked by a common,  $sp^3$ -hybridized spiro-carbon. For this reason, these respective isomers are commonly referred to as their spiro forms. Upon photoexcitation, the bond between the spiro-carbon and the oxygen in the pyran subunit is broken, inducing a change in hybridization of the former to  $sp^2$  and planarization of the molecule via conformational isomerization. This planar, open-ring isomer is called the merocyanine form (MC) as it consists of two aromatic rings linked by a methine bridge. While in the spiro form, the electronic wave function overlap between the two moieties is low, planarization results in delocalization of the wave function across the entire molecule. Therefore, the spiro-form only shows absorption contributions in the ultraviolet originating from the two individual subunits, while the higher degree of delocalization in case of the MC form gives rise to an absorption band in the visible.<sup>3</sup> Due to the conformational degrees of freedom in the dihedral angles of the methine bridge, eight different planar conformers are possible in principle, though it has been argued that

<sup>2</sup>When discussing spiropyran in modern day research, the vast majority of studies deals with the subset of indolino-spiropyran. Usually, spiropyran is used synonymously for this subset, which will also be done throughout this thesis (unless noted otherwise).

<sup>3</sup>While the absorption ranges here explicitly refer to the cases of BIPS and SNP and the particular optical transition energies vary for different derivatives, this bathochromic shift is a general characteristic of the spiropyran photochromism.

the *trans-trans-cis* (TTC) or *cis-trans-cis* (CTC) conformations ought to be the most stable from a steric perspective.<sup>[155]</sup> Additionally, possible dependences on the particular spiropyran derivative or the solvent environment have been reported.<sup>[156,157]</sup> The photochromic reaction is generally reversible by irradiation of the MC form, but in case of the derivatives discussed here also thermally at room temperature.

Since the discovery and initial characterization of their photochromic properties by Fischer and Hirshberg in 1952,<sup>[158–160]</sup> spiropyran reactions have been investigated regarding their dynamics,<sup>[161]</sup> involved states and structural changes as well as the quantum yield.<sup>[162,163]</sup> The first time-resolved experiments were reported by Ernsting et al. in the early 90's for BIPS and SNP.<sup>[155,164,165]</sup> The authors concluded formation of the MC isomers to occur with time constants of 0.9 ps and 1.4 ps, respectively, with equilibration of the product being reached within 30 ps. However, in a later study using transient IR-absorption spectroscopy, the product formation was argued by Rini et al. to occur significantly more slowly, with a time constant of 28 ps, via an unidentified reaction intermediate.<sup>[166]</sup> This intermediate was assumed to have an absorption band similar to the MC product, in order to explain the discrepancy to the previously reported experiments. On the other hand, a more recent study on a different, but sufficiently similar BIPS derivative concluded the reaction to occur within a picosecond,<sup>[167]</sup> more in line with Ernsting's findings.

Evidently, the reaction dynamics have remained unresolved to date, in part owing to the limited detail of reported data from the early transient absorption studies due to the experimental and analytical limitations of the time. This motivated further investigation of the spiropyran dynamics in solution encompassing a careful comparison of the dynamics in different solvents in order to identify relaxation processes and distinguish them from the isomerization dynamics. The experimental results, combined with extensive molecular dynamics simulations by Dr. Raison Dsouza, have been published (ref. [68]) and are presented in section 3.2.

As stated in the introductory chapter, the primary research focus of this PhD project lies in photoisomerization dynamics in the crystalline phase, in order to allow for the direct observation of structural changes during the reaction via diffraction techniques, with enhanced signal-to-noise ratio due to the periodic nature of crystals. However, involving significant structural changes, the photochromic reaction in single crystals of most derivatives is inhibited due to the spatial confinement.<sup>[142]</sup> Nonetheless, signs of MC formation even in the crystalline phase have been found by Suzuki and coworkers for SNP.<sup>[67]</sup> Therefore, this particular spiropyran derivative was selected for investigation by means of transient absorption and preliminary electron diffraction experiments (see sections 3.3 and 3.4). For consistency, this particular derivative was also chosen for the solution experiments. Based on its high structural similarity to BIPS as well as the reports by Ernsting

et al., the dynamics of both molecules in solution can be considered equivalent besides minor differences in the time constants.<sup>4</sup>

## 3.2 Transient Absorption Spectroscopy of Spiroanthopyran in Solution

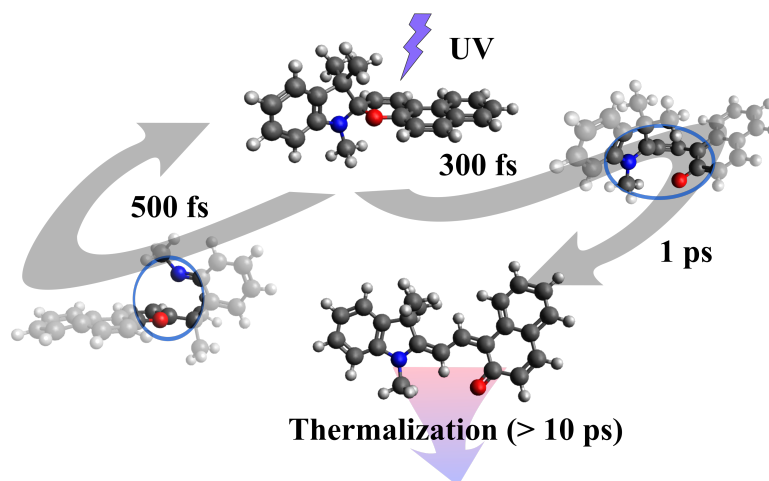


**Figure 3.2:** Summary of the dynamics of SNP in solution based on the combined experimental and theoretical efforts (see ref. [68]). Internal conversion back to the closed form involves C-N bond elongation and occurs within approximately 500 fs. Reaction to the planar MC form entails the formation of an excited-state intermediate with a time constant of 300 fs, from which the product is reached with a lifetime of  $\approx 1$  ps. All subsequent spectral dynamics were assigned to thermalization of the MC form. Adapted with permission from ref. [68], ©2019 Royal Society of Chemistry.

The key findings from the combined experimental and theoretical study of the spiroanthopyran photoisomerization dynamics in solution are shown in Fig. 3.2. This section details the experimental part, consisting in transient absorption measurements of SNP in three different solvents – non-polar aprotic, polar aprotic and protic, and provides a brief summary of the theoretical results by Dr. Raison Dsouza. Extensive data analysis utilizing various methods as well as comparison to the simulations allowed for the separation of isomerization and product equilibration dynamics, resolving the apparent mismatch between previously reported studies.

<sup>4</sup>The transient absorption data for BIPS in solution was acquired subsequently as a reference for a subset of experiments dealt with in the following chapter. Although the data was not analyzed in such detail as the present SNP data and no solvent dependence was investigated, the sub-to-few-ps dynamics indeed show a sufficient agreement to conclude that the conclusions made for SNP in this chapter also apply to BIPS.

### 3.2.1 Solution preparation and steady-state absorption

1,3,3,-Trimethylindolino- $\beta$ -naphthopyrylospiran (spironaphthopyran, SNP) powder from TCI Chemicals, Japan,<sup>[168]</sup> was dissolved without further purification in spectroscopy-grade acetonitrile, ethanol and *n*-hexane, respectively, to yield 1.5 mM sample solutions. Static absorption spectra in the ultraviolet and visible range were recorded using a home-built microspectrometer<sup>5</sup> and are shown in Fig. 3.3 (a). In order to obtain the absorption spectra of the merocyanine form, the solutions were irradiated with a 266 nm beam from the transient absorption setup until the photostationary state (PSS) was reached. Since both forms absorb in the ultraviolet, the absorption difference between PSS and thermal equilibrium is more relevant for the interpretation of transient absorption data in this wavelength range. Since the obtained difference spectra were similar for all three solvents, the one for ethanol is shown representatively in Fig. 3.3 (b).

For the closed forms, the absorption edge in the UV was found to be around 375 nm and three main absorption bands are identifiable, centered at approximately 250 nm, 300 nm and 350 nm. The positions, amplitudes and fine structures of these bands do not exhibit any significant solvent dependence. On the other hand, in case of the merocyanine absorption spectra in the visible, all of these characteristics vary with the type of solvent being used, warranting closer inspection.

The obtained absorption spectra of the merocyanine forms in the visible are shown in Fig. 3.3 (c). In order to allow for a better visual comparison, the spectra for hexane and acetonitrile have been multiplied by factors of 5 and 3, respectively. These ratios approximately reflect the difference in overall absorption amplitudes between the three solvents. The same order from non-polar aprotic to polar protic solvent is found for the central position of the absorption bands as well as the absorption edges, exhibiting an increasing bathochromic shift of the spectra. These observations can be quantified by calculating the integrals and spectral centers of mass (centroids), which are collated in Table 3.1, together with the estimated absorption edge positions. Accordingly, the centroid at 522 nm for hexane is at a shorter wavelength than the centroids of acetonitrile and ethanol at 543 and 551 nm, and the spectral integrals increase with hexane taking the lowest and ethanol the highest value.

A commonality among the three MC absorption spectra is that each consists of three distinguishable bands, albeit with varying relative amplitudes. The band positions and (non-weighted) amplitudes are shown in Fig. 3.3 (d). In case of ethanol and acetonitrile, their relative amplitudes decrease towards shorter wavelengths, with an almost linear relationship for ethanol. Hence, the highest-energy bands are relatively small in amplitude manifesting as mere shoulders in these spectra. For hexane on the other hand, the amplitude of the middle band is largest with a maximum of 41 mOD while those of the neighboring bands are more similar (29 and 35 mOD), compared to the other two sol-

<sup>5</sup>Constructed by Dr. Corthey, design based on [169].

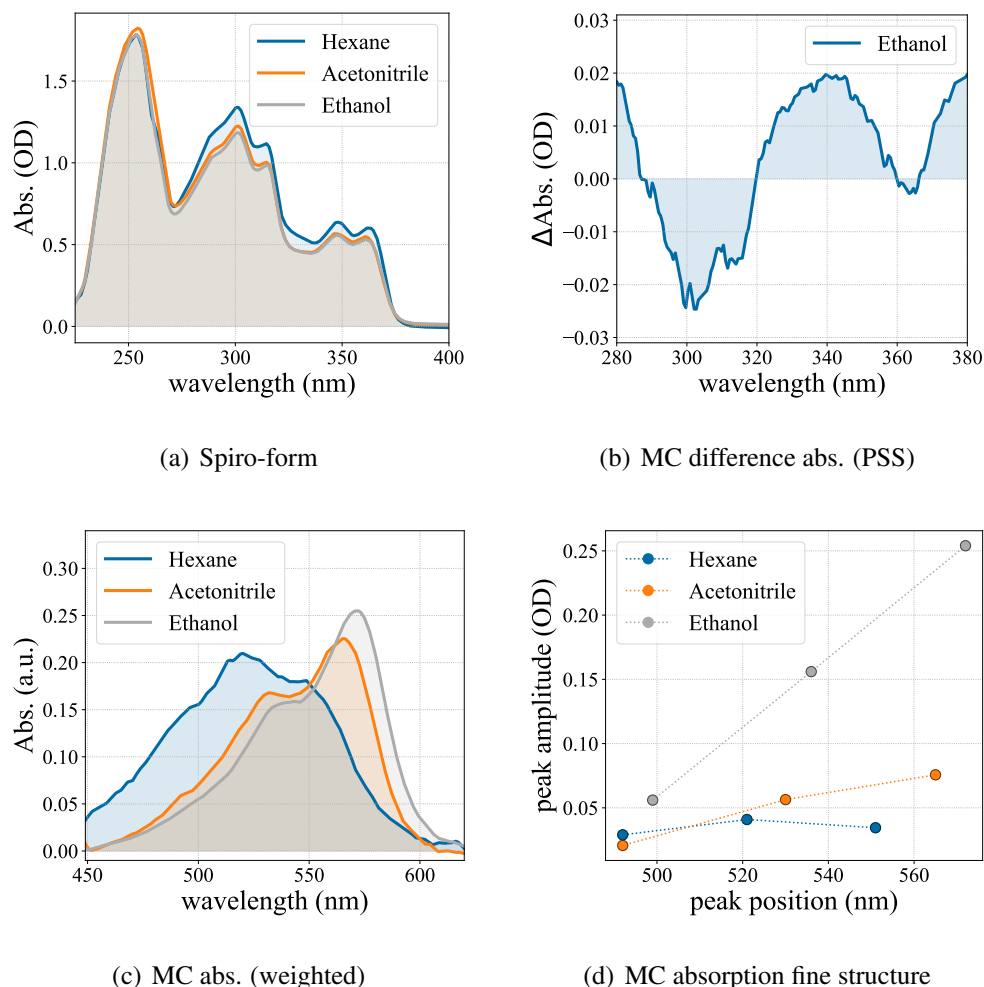


**Figure 3.3:** Steady-state absorption spectra of SNP in acetonitrile, ethanol and *n*-hexane. (a) UV absorption of the closed form (no absorption in the visible), (b) Differential UV absorption of the MC form with respect to the spiro-form in the photostationary state (PSS), (c) visible absorption of the MC form, (d) sub-peak analysis of the spectra shown in (c).

vents.

Based on these observations and analyses, solvent effects on the electronic structure of the open-ring form can be characterized in a semi-quantitative way, shown in Fig. 3.4. Since for all three solvents the absorption coefficient of the closed form at 266 nm is identical within the margin of error of the measurement, it can be concluded that the transition dipole moment is unaffected by the type of solvent. As a consequence, under identical excitation conditions the same fraction of SNP is excited. Therefore, the differences in integral values can be explained by an increased energetical stabilization  $\Delta_1$  of the product ground state in acetonitrile compared to hexane and even more in ethanol ( $\Delta_1 + \Delta_2$  with respect to hexane).<sup>6</sup> The polar solvents increasing the thermal stability of the MC form implies that its ground state is also polar to a degree, which is in agreement with the

<sup>6</sup>This conclusion is made under the assumption that the quantum yield of the reaction is not notably affected by the type of solvent, which can be verified using transient absorption (see section 3.2.2).

**Table 3.1:** Spectral integrals and centroids as well as edge positions of the absorption spectra for open-ring SNP in the three solvents (photostationary state). Integral values are normalized to the number of pixels and the respective wavelength ranges adjusted to ensure complete coverage of the spectra.

	Integral (OD)	Centroid (nm)	Abs. Edge (nm)	Abs. Edge (eV)
Hexane	6.5	522	570	2.18
Acetonitrile	8.7	543	581	2.13
Ethanol	24	551	586	2.12

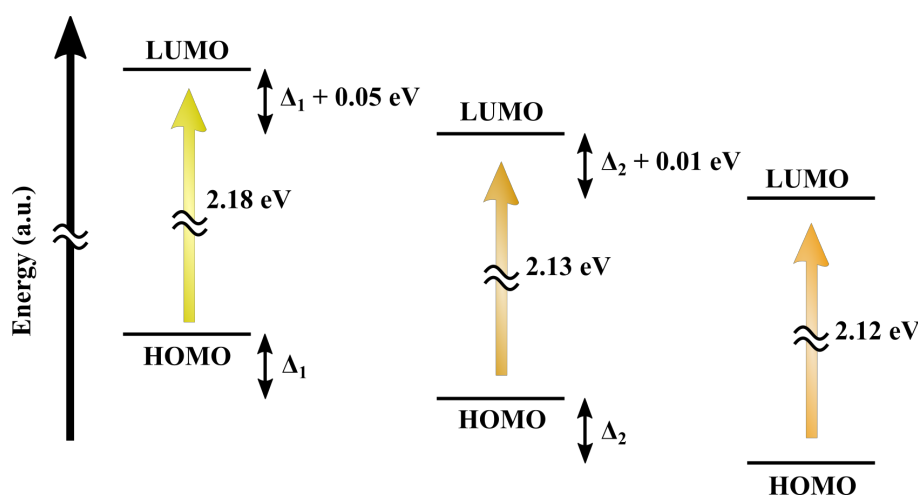


**Figure 3.4:** Semi-quantitative energy diagram of MC for hexane, acetonitrile and ethanol as solvents (from left to right), based on the acquired photostationary state absorption spectra.  $\Delta_1$  and  $\Delta_2$  are the differences in ground state energy of the MC forms between hexane and acetonitrile as well as between acetonitrile and ethanol, respectively.

phenoxy group being of electron withdrawing nature and the existence of a zwitterionic resonant structure for MC, in which the oxygen carries a negative charge. Furthermore, the negative partial charge allows for the formation of hydrogen bonds between the phenoxy group and polar protic solvents. Indeed, the spectral integral is increased even more for ethanol compared to acetonitrile, by almost a factor of three. Besides ethanol being slightly more polar than acetonitrile, the capability of forming hydrogen bonds is the most prominent difference between the two solvents. Hence, it can be concluded tentatively that this type of interaction significantly contributes to the stabilization of MC in the ground state.

If solely the ground state energy was affected by the solvent environment, there should be an increase in transition energies to the excited states with higher degree of stabilization. This would result in a hypsochromic shift of the absorption edge corresponding to the HOMO-LUMO gap, as well as the spectral centroid, which additionally takes into account higher-lying excited states. However, the opposite is observed suggesting that en-

ergetical stabilization effects for polar and especially polar protic solvents are even more pronounced for the excited states.

Inspecting the fine-structures of the visible absorption bands suggests that interaction between the molecule and the solvent environment induces a shift in potential of the first excited electronic state ( $S_1$ ) with respect to the ground state, which changes the vibronic wave function overlap and thereby the Franck-Condon factors and transition dipole moments (see section 2.4.1). In the polar solvents, especially in the protic ethanol, the lowest vibrational state on the  $S_1$  potential energy surface has the highest transition dipole moment, while for the non-polar hexane, the fine-structure indicates the second-lowest vibrational state having the highest overlap with the ground-state wave function. Even though the assignment of the observed fine-structure to a vibrational progression is not unambiguous due to the limitations of static absorption spectroscopy, the hypothesis was tested and ultimately corroborated in the analysis of the conducted transient absorption experiments, which will be discussed in more detail in section 3.2.2.

In summary, the absorption spectra of both the closed and open-ring forms exhibit no significant solvent dependence in the ultraviolet range. On the other hand, visible absorption of the merocyanine form is influenced by the solvent environment indicating a significant interaction with both the ground and first excited states, which demands further investigation via time-resolved experiments. Since the selection of solvents for these experiments was limited due to the main focus of the study being the chemical reaction dynamics, these conclusions, though consistent with the chemical properties of the MC form, are mostly qualitative in nature. To further elucidate the effects of solvents on the electronic structure, more systematic studies are encouraged, utilizing a wider array of solvents of each type as well as theoretical simulations.

## 3.2.2 Transient absorption experiments

### Experimental details

Transient absorption experiments of SNP in *n*-hexane, acetonitrile and ethanol were conducted using the flow-cell based solution TA configuration of the home-built setup, described in detail in section 2.4.2. For excitation of the samples, the third harmonic of the Ti:Sa laser system was used (266 nm) at a repetition rate of 500 Hz with a fluence of  $3 \text{ mJcm}^{-2}$  (490 nJ pulse energy and  $120 \mu\text{m}$  beam diameter (FWHM)).<sup>7</sup> Both the visible (380-700 nm) and the UV (250-350 nm) probes were used under identical conditions, but applying the aforementioned dual-chopping scheme for UV probing to mitigate pump scattering around 266 nm. Furthermore, the UV absorption experiments were only con-

---

<sup>7</sup>As usual, the suitability of these parameters was ensured by performing a standard fluence dependence measurement (see section A.3 in the appendix). The fluence of  $3 \text{ mJcm}^{-2}$  corresponds to an excitation fraction of 4 %.

ducted in hexane and ethanol, since no significant solvent effects on the absorption in this particular wavelength range were expected (*vide supra*).

For all solvent and probe range combinations, transient absorption spectra at pump-probe delays up to one nanosecond were recorded and processed as detailed in section 2.4.3.

#### Observations

The acquired transient absorption scans for the respective solvents are shown in Fig. 3.5 for the visible probing range. The depictions cover pump-probe delays up to 100 ps, since no significant spectral changes beyond this point were observed within the measurement range of one nanosecond.

In the visible, the spectral dynamics within the first 5 ps exhibit the same characteristics for all three solvents except for the central wavelengths of the respective absorption bands. Therefore, they are representatively described in the following using the example of acetonitrile (Fig. 3.5 (c) and (d)), for which the spectral features are the most distinguishable. Following the cross-phase modulation (CPM) signal at time zero, a broad absorption band, initially covering the entire probe range and with a distinct maximum around 450 nm, appears at  $\approx 0.3$  ps after excitation. Within 1-2 ps, the absorption band narrows and shifts towards longer wavelengths reaching a center wavelength of around 550 nm. This evolution is accompanied by a slight decrease in intensity within the first picosecond and followed by an increase, reaching a value of 9.5 mOD at 5 ps. Beyond this point, no significant changes in amplitude of this band are observed in either case, but the band is narrowed further within the depicted 100 ps.

In addition to narrowing of the band, the spectral fine-structure and central wavelengths of the band evolve to match the steady-state spectra of the respective solvents. Like the equilibrium spectra themselves, these dynamics differ between the three solvents. In case of hexane, the spectral dynamics consist mostly in a refinement of the fine-structure bands without any notable changes in relative amplitudes and with the second-lowest energy band possessing the largest amplitude. However, an overall decrease of the absorption band at 100 ps compared to 15 ps can be identified. For the polar solvents, this is not observed, but the respective relative amplitudes exhibit dynamics beyond the initial rise of the band. While at 5 ps in case of acetonitrile and at 10 ps in case of ethanol, the amplitudes of the lowest and second-lowest energy bands are similar, the lowest energy bands subsequently gain in amplitude at the expense of the other bands. This process appears to be slower in ethanol compared to acetonitrile. Regarding the central wavelength, the transient absorbance of SNP in acetonitrile does not show any noticeable shift barring further analysis. However, in case of ethanol there is a shift of the spectrum towards longer wavelengths at 100 ps compared to the one at 10 ps. These qualitative observations necessitate further analysis of the sub-band dynamics, which are described in the next section.

The transient UV absorption scan of SNP is shown in Fig. 3.6 for ethanol as solvent. The

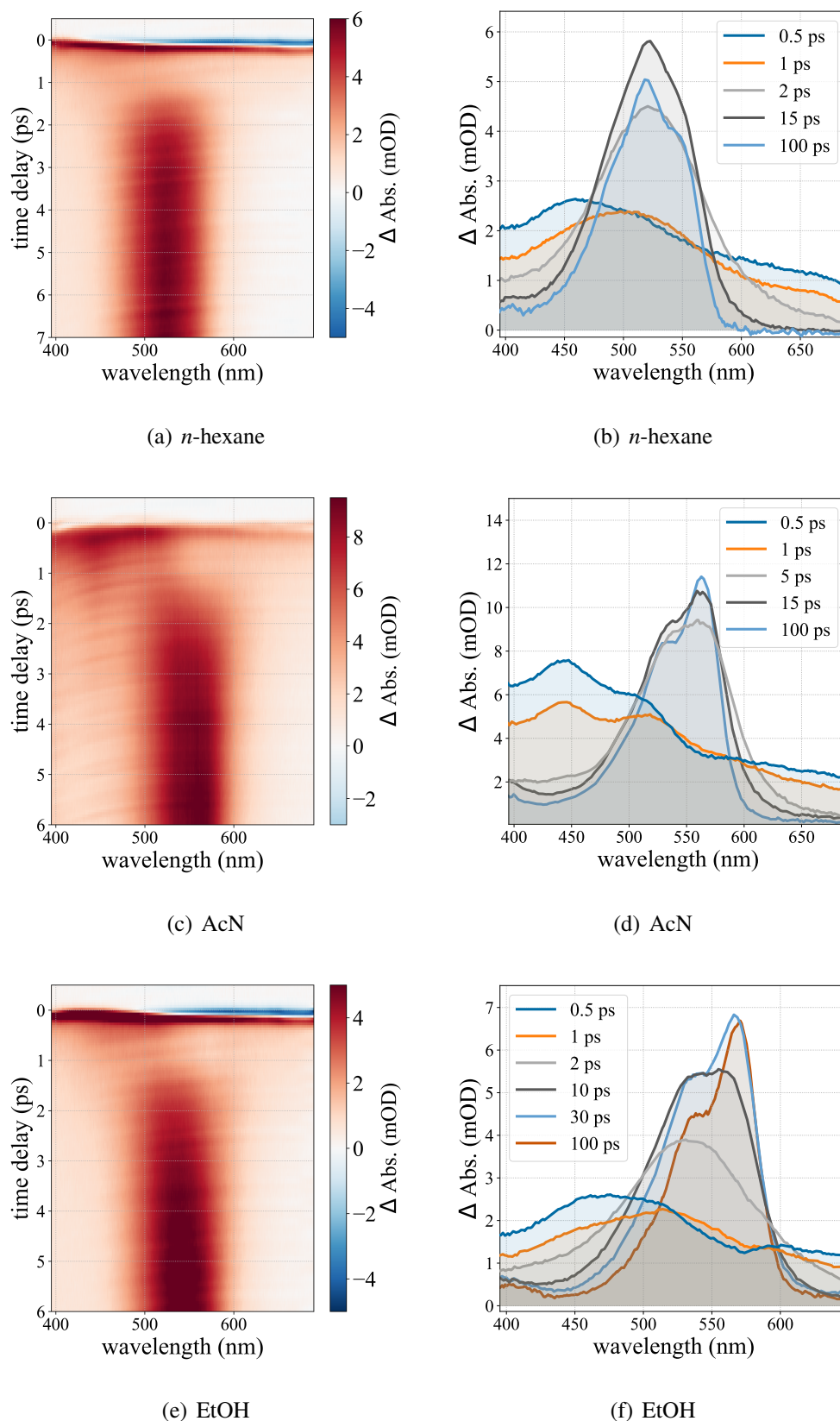


**Figure 3.5:** Transient absorption spectra of SNP in the visible range. Figures (a), (c) and (e) show TA maps of the first few ps for hexane, acetonitrile and ethanol, respectively. Figures (b), (d) and (f) depict corresponding spectral traces for select time delays within 100 ps after excitation. No significant differences between the respective spectra at 100 ps and 1 ns were observed.

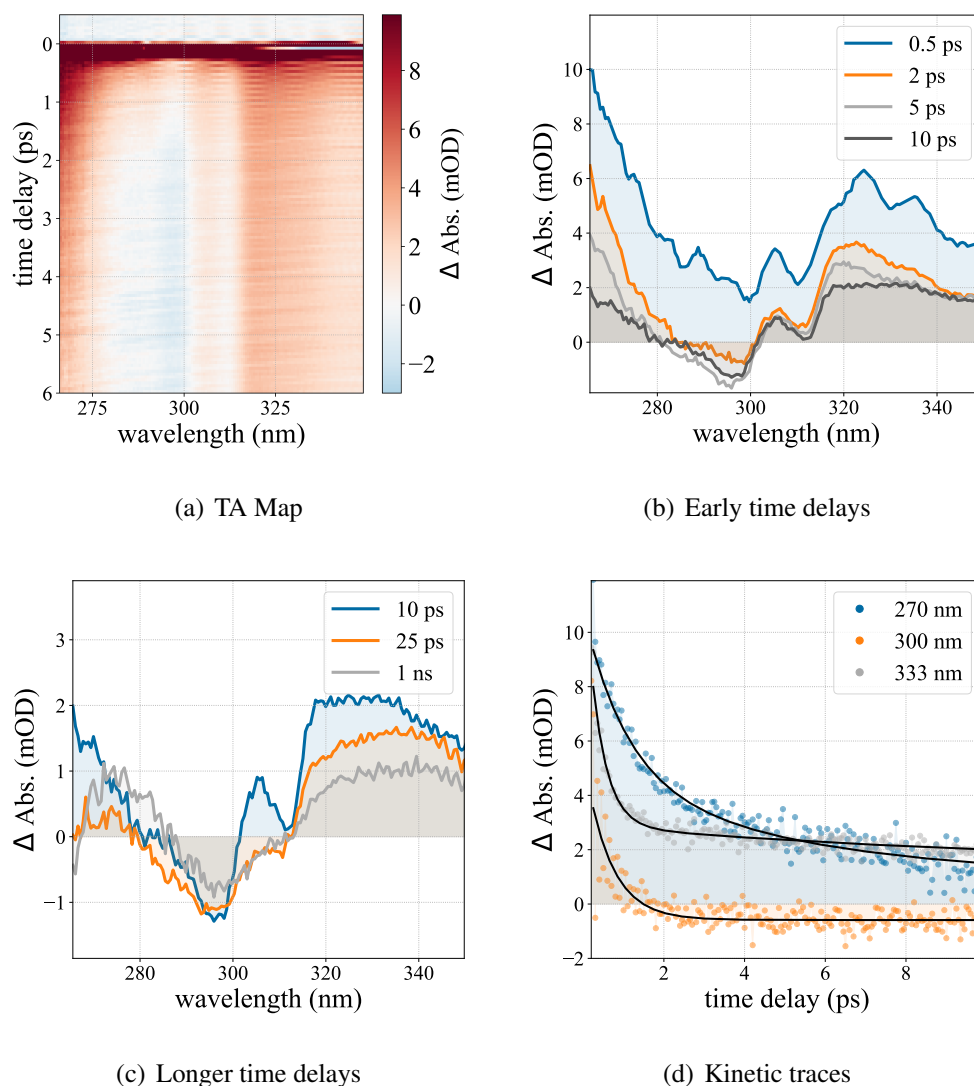


**Figure 3.6:** Transient UV absorption spectra of SNP in ethanol. (a) Transient absorption map of the first 6 ps, (b) selected spectral cuts of the first 10 ps, (c) selected spectral traces of time delays up to 1 ns, (d) selected kinetic traces including exponential fits (black lines).

data for hexane exhibits no notable differences and can be found in section A.4.1 in the appendix. The TA data consists of an intense broad absorption band appearing around time zero, which decays for the most part within 2 ps, giving way to a difference absorption spectrum, which besides some minor changes in spectral fine-structure lasts for the remainder of the measurement window (1 ns). Said spectrum consists of a negative region between 280 and 305 nm and a positive band between 305 and 350 nm. It closely resembles the calculated MC-SNP difference spectrum depicted in Fig. 3.3 (d).

### Global and target analysis

In order to quantitatively interpret the obtained data, two of the developed analysis routines were applied. Different global fit models were tested focusing on the early, sub-5 ps dynamics, while the spectral refinement of the long-lived absorption band was analyzed

by means of a dynamic line shape fit (*vide infra*).

The decay-associated difference spectra (DAS) obtained from a global fit of the data in the time delay range from 0.3 to 14 ps are shown in Fig. 3.7 for each solvent. A parallel decay model using four exponential components was applied, out of which one was set to be constant in time. The first components describe a fast decay (200-300 fs) of a spectrum with positive values across the spectral range and a pronounced positive feature in the region of the long-lived absorption band, approximately between 500 and 600 nm depending on the solvent. The second component in each case is the approximate mirror image of the first (with respect to  $\Delta Abs.$ ), but with an offset resulting in positive values below  $\approx 475$  nm and above  $\approx 600$  nm, and negative values in the region of the MC product absorption. The lifetimes of this component range between 1.1 and 1.3 ps. Intermediate components with time constants between 4.3 and 7.2 ps was required, exhibiting a low amplitude overall and several local maxima and minima, which vary in position and quantity depending on the solvent. The long-lived absorption band is accounted for by a fourth, constant component, which is equal to the spectrum at the end of the fit range.

For the interpretation of these results, it needs to be borne in mind that individual fit components only obtain physical meaning when added together with the others. Generally, a negative DAS amplitude is interpreted as either a rise of a positive signal or the decay of a negative signal and vice versa for positive DAS amplitudes. However, especially if spectral features overlap in wavelength, the validity of this interpretation becomes compromised. This is the case considering the first component in the present analysis, as it can be readily verified by inspecting the data that the broad positive feature in the region of the MC absorption neither corresponds to a decaying absorption spectrum nor to the rise of a negative feature. It can only be understood by interpreting the remaining components. Based on the observations described in the previous section and comparison to the steady-state absorption measurements, the constant component can be assigned to a photoproduct, either the MC form or a structurally similar precursor. The negative spectral region of the second component thus corresponds to a rise of said photoproduct absorption spectrum with a time constant of 1.1-1.3 ps and a simultaneous decay of the broad excited state absorption with the distinct maximum around 450 nm. However, at 2 ps, when most of this rise is complete, the spectral shape does not yet match the one at 14 ps, let alone the one at equilibrium. Therefore, the third component is needed to describe the spectral refinements and shifts within this time window. The early dynamics however, appear to be more complicated, which is where the first component comes into play. It can be understood as the sum of a broad, positive baseline, the positive band in the product absorption region and a negative band between 400 and 500 nm. This is most evident from the DAS for acetonitrile, but distinguishable in case of the other solvents as well. The baseline is a contribution to the decay of the broad excited state absorption. On top of this, the maximum at 450 nm rises with this time constant, resulting in a dip in the decay-associated spectrum. The part of the first component, which mirrors the prod-

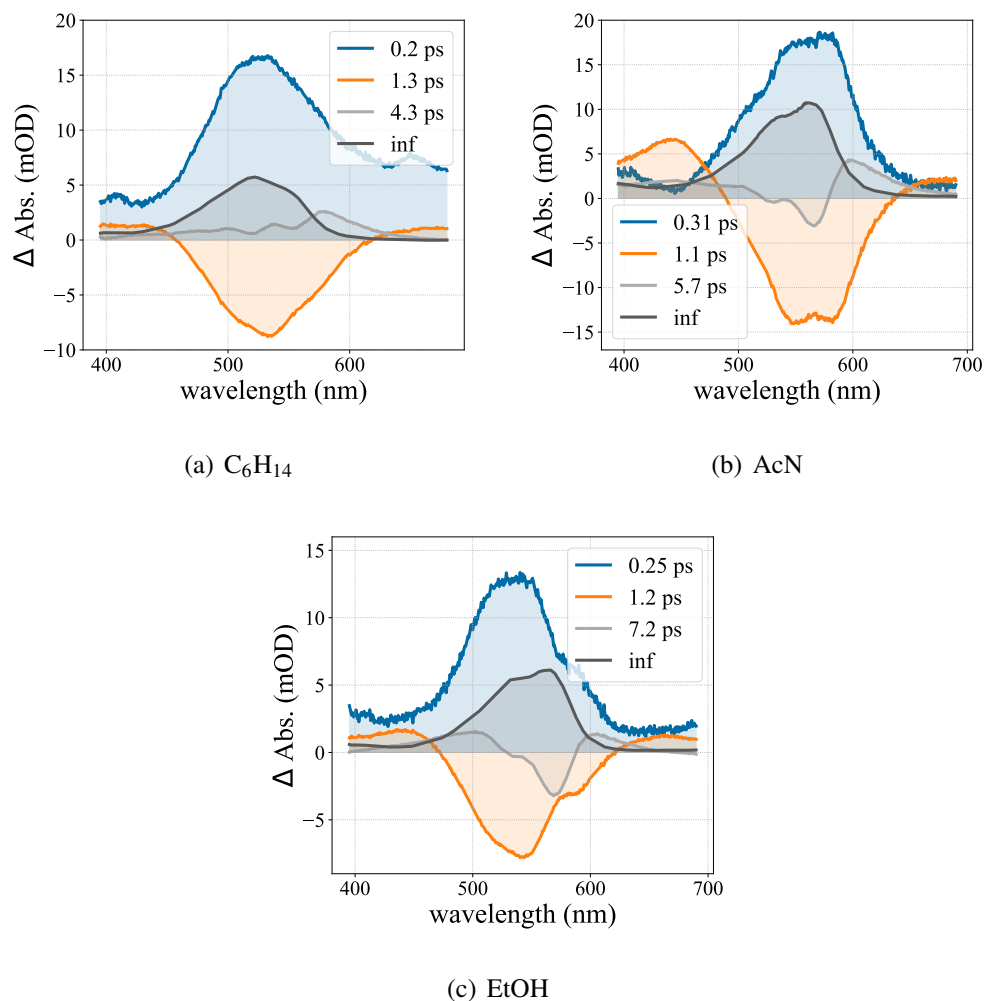


**Figure 3.7:** Decay-associated difference spectra from global analysis of photoexcited SNP in the visible range for (a) hexane, (b) acetonitrile and (c) ethanol as solvent. Four components were used in each case, with one set as constant (inf).

uct absorption, causes a delayed onset in the rise of the latter. This is because, within a parallel decay model, all exponential decays start at the same time. If the formation of a species and thereby the rise of its characteristic absorption effectively starts at a later time delay, another component is needed to initially suppress the rise.

The fact that this suppression and the formation of another absorption band can be adequately fitted with a single time constant suggests the applicability of a kinetic sequential model, in which a species absorbing at 450 nm is formed with a time constant of 200-300 fs in the first step (rise at 450 nm), which in turn reacts to the product in a second step (decay at 450 nm and delayed rise around 550 nm). Such a model was successfully applied to the data and the obtained species-associated spectra (SAS) are shown in Fig. 3.8 (a) for acetonitrile. Assuming a unidirectional chain of four species (A-D), the temporal functions were calculated using equation 2.25. The SAS as well as the corresponding time constants are in agreement with the interpretation of the parallel model. In the first step, with a time constant of approximately 300 fs, the transient absorption spec-

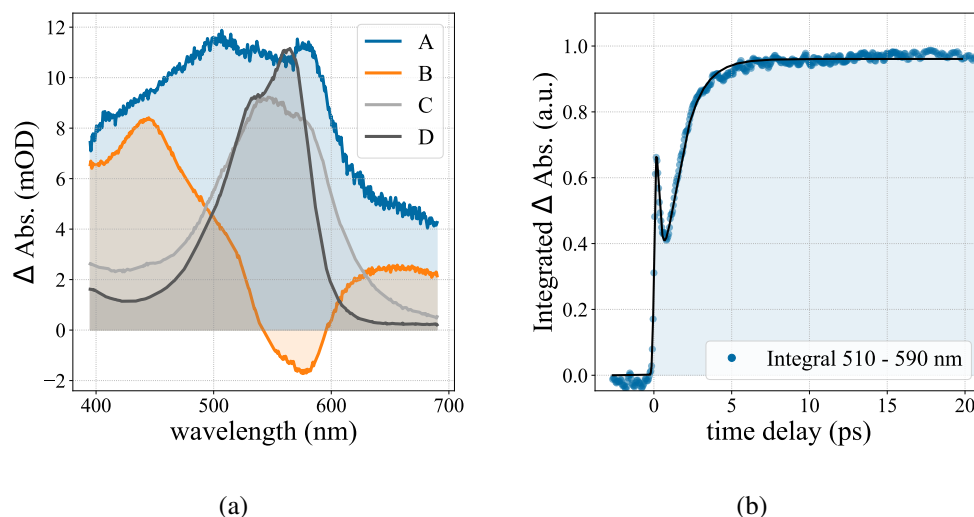


**Figure 3.8:** Kinetic models of the SNP dynamics in acetonitrile. (a) Target analysis using a sequential model with three reaction steps. Corresponding time constants:  $\tau_{AB} = 0.31$  ps,  $\tau_{BC} = 1.2$  ps and  $\tau_{CD} = 8.0$  ps. (b) Integrated product absorption band, fit with a sum of the first and third components from a two-step sequential chain model ( $\tau_{AB} = 0.35$  ps,  $\tau_{BC} = 1.2$  ps).

trum evolves from a broad intensity distribution in the excited state (species A) towards a spectrally more defined species B with the maximum at 450 nm. For the second step, in which this absorption band decays and the product absorption rises, a time constant of 1.2 ps was found. The transformation of species C into species D represents the spectral refinements, described by the third component in the parallel model and has a similar time constant of 8 ps.<sup>8</sup>

The presence of spectral narrowing and shifts in the data poses problems for the validity of these global analysis models, since their temporal components by definition are wavelength-independent and therefore unable to properly deal with this type of spectral evolution. As can be seen from the parallel model fits, a supporting component without direct correspondence in the data, can help to mitigate this. In case of the target analysis, this problem is reflected in the presence of a negative artifact in the spectrum of species B between 500 and 600 nm. To ensure that these artifacts in the fits do not significantly impair the validity of the obtained time scales, the spectra in this wavelength range were integrated and separately fit with a sum of exponential functions (see Fig. 3.8 (b)). Both a parallel decay model, i.e. the sum of independent exponentials, and a kinetic sequential model were tested. Since small spectral shifts and refinements are mostly eliminated by integration, it was possible to adequately fit the data with a sum of only two exponentials and an additive constant in either case, effectively eliminating one component with

<sup>8</sup>Since the spectral species C and D exhibit only small differences in fine structure and band widths, it can be assumed that they are the same chemical species, but with a different population of the vibrational states. This assumption is explored further in the discussion of the longer time delays in the following section.

respect to the global and target analyses. For the parallel model, this resulted in time constants of 0.3 ps with a positive amplitude and 1.3 ps with a negative amplitude, which is in agreement with the previous interpretation of a product band rise with a delayed onset. The kinetic model was tested by applying a two-step chain model and fitting the integrated differential absorption  $\Delta Abs_{\text{int}}$  with a sum of the first and third component:<sup>9</sup>

$$\Delta Abs_{\text{int}}(t) = a \cdot A(t) + c \cdot C(t) \quad (3.1)$$

wherein  $A(t)$  and  $C(t)$  are the time dependent concentrations of species A and C, calculated according to equation 2.25, while  $a$  and  $c$  are independently varied weights corresponding to the respective absorption coefficients. Like in case of the parallel model, the obtained time constants of  $\tau_{\text{AB}} = 0.35$  ps and  $\tau_{\text{BC}} = 1.2$  ps agree with the results from global fitting. Furthermore, the validity to fit the region of the product absorption band with this model as opposed to a sum of all three components supports the existence of an intermediate species with only negligible absorption inside the integrated spectral range, which validates the previous assignment of the absorption band around 450 nm to said intermediate species. The fact that the decays of this band and the broad excited state absorption are described by a single component implies that this intermediate species is in the excited state rather than the ground state.

The UV transient absorption results are less conclusive compared to the visible, which is due to the high amplitude of the initial excited state absorption compared to the long-lived difference absorption spectrum. While the latter corresponds to the PSS absorption difference (see Fig. 3.3 (b)), its formation time cannot be retrieved since it is expected to match the 1.2 ps obtained in the visible and this time range is dominated by the decay of the ESA. Hence, global analysis yields only three components, one describing the ESA decay with time constants of 0.6 and 0.4 ps for hexane and ethanol, respectively, an intermediate component (25 and 21 ps) which reflects slight spectral shifts and residual ESA decay, as well as a constant component matching the steady-state difference absorption. The DAS shown in Fig. 3.9 and the corresponding time constants were obtained fitting the entire measurement window of one nanosecond. The intermediate time constants of 21-25 ps agree with the ones from global fits of the visible when using the same time range (see Fig. A.11 in the appendix) and are therefore ascribed to product equilibration, as discussed in the following section. The ESA decay on the other hand was found to be faster compared to the visible. This can be explained by a lower influence of the additional dynamics of distinct intermediate and product absorption bands in the visible, which are absent in the UV. Hence, global analysis in the visible is dominated by the product formation pathway, while the ESA decay in the UV carries contributions from both the product formation and internal conversion back to the reactant. Since the resulting effective time

<sup>9</sup>Omission of the second component was not a premise for, but an outcome of the fit. Including it resulted in only a small amplitude of the component and overall higher parameter uncertainties.

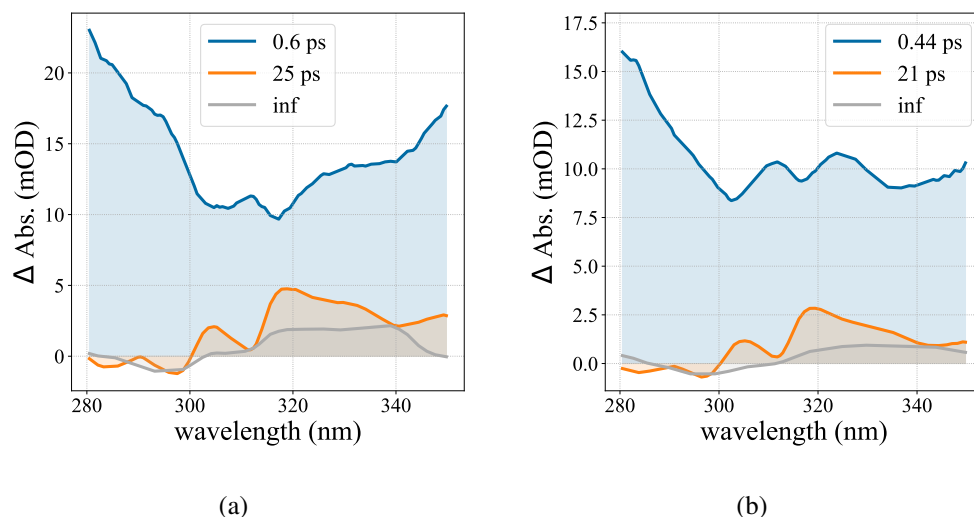


**Figure 3.9:** Decay-associated difference spectra of SNP in (a) hexane and (b) ethanol, probed in the UV. The fits consist of three components, out of which one was set as constant (inf).

constant is faster than the product formation, it can be concluded that internal conversion to the reactant molecule occurs faster than 0.6 ps.

In summary, independent global and target analyses in the visible led to the same conclusion regarding the early reaction dynamics of photoexcited spironaphthopyran. After excitation, rapid internal conversion into the  $S_1$  state is assumed to occur, since it is expected for large organic molecules and no evidence for the contrary was found. Subsequently, the wave packet propagates on the  $S_1$  potential energy surface towards an excited-state intermediate (ESI) with a time constant of  $\approx 300$  fs. From the ESI, within  $\approx 1$  ps, the product is formed, whose absorption undergoes solvent-dependent spectral refinements within the following 100 ps. Considering the UV transient absorption yields evidence that the competing pathway back to the reactant molecule via internal conversion occurs within less than 600 fs.

### Dynamic line shape analysis

As mentioned in section 3.1, it has been argued that the long-lived absorption band in the visible may not necessarily belong to the product as previously assigned.<sup>[166]</sup> Instead, the product formation time was postulated to be 28 ps for the closely-related BIPS. In order to resolve this disagreement, further analysis of the spectral dynamics beyond 1 ps is required to differentiate between product formation and equilibration. While it was concluded in the previous section that the observed spectral shifts do not falsify kinetic analysis of the early time dynamics and formation of the product band, quantitative analysis of these spectral refinements from the preliminary product absorption band to the steady-state absorption spectrum is not possible by means of global analysis. This mo-

**Table 3.2:** Time constants from exponential fits of the Gaussian peak positions (overall peak position  $\tau_{pos}$  and peak spacing  $\tau_{spac}$ ) and line widths ( $\tau_{\sigma}$ ) from the dynamic line shape analysis (Key: r – rise; d – decay).

	$\tau_{pos}$ (ps)	$\tau_{spac}$ (ps)	$\tau_{\sigma}$ (ps)
Hexane	$13 \pm 0.3$ (r)	$11.7 \pm 0.2$ (r)	$15 \pm 0.6$ (d)
Acetonitrile	$11.8 \pm 0.1$ (r)	$13.2 \pm 0.6$ (r)	$14.7 \pm 0.3$ (d)
Ethanol	$51 \pm 2$ (d)	$10.3 \pm 2.2$ (r)	$13.1 \pm 0.1$ (d)
		$70 \pm 60$ (d)	

tivated the development of the dynamic line shape analysis routine (DLSA) described in section 2.4.6, to allow for the appropriate characterization of these spectral shifts as well as the distinct spectral fine-structure dynamics found for the different solvents.

As outlined previously, this method involves fitting the transient absorption spectra for each time delay consecutively using a sum of Gaussian functions (see equations 2.34 and 2.35)<sup>10</sup>, and the resulting parameters as initial values for the next time step. To ensure appropriate starting parameters, the fit was done in reverse time steps, as the spectral fine structure at later time delays was better defined. For the analyzed time window between 4 and 100 ps, various fit settings were tested including different numbers of Gaussian functions and parameter constraints. After systematic evaluation of the fit results regarding the residual matrix and a consistent temporal evolution of the Gaussian parameters, the most appropriate conditions were determined. The best results in this regard were achieved for all three solvents when constraining the center positions  $b_i$  and peak widths  $\sigma_i$  for a Gaussian component number  $i$ , going from lowest energy to highest, such that the spacing  $\delta$  between neighboring Gaussians was equal for all components (equation 3.2) and the widths increased linearly with the component number (equation 3.3):

$$b_i = b_1 + (i - 1) \cdot \delta \quad (3.2)$$

$$\sigma_i = i \cdot \sigma_1 \quad (3.3)$$

For ethanol and acetonitrile, a sum of three and for hexane a sum of four Gaussians was used, since in case of the former two solvents, the relative amplitudes of the fourth band were too small to yield stable fit results. A non-zero offset was required in all cases due to residual excited state absorption and minor probe fluctuations.

The applicability of equidistant energy levels for the optical transitions indicates that the fine structure of this absorption band can be ascribed to a vibrational progression, ap-

<sup>10</sup>In order to match the results presented in the corresponding publication (ref. [68]), non-normalized Gaussian functions were used, omitting the normalization factors  $(\sigma_j \sqrt{2\pi})^{-1}$  in equation 2.35.

proximated by a harmonic potential, as postulated discussing the steady-state absorption spectra. Increased peak broadening for transitions to higher-energy states suits this picture as well, assuming that broadening is governed by fluctuations of the harmonic potential, resulting in broader energy distributions for higher-lying vibrational levels. Hence, the individual components will be interpreted as transitions to vibrational states on the  $S_1$  potential energy surface.<sup>11</sup>

The results of the DLSA using the selected model of a vibrational progression with linearly increasing line widths are depicted in Fig. 3.10. The introduced parameter constraints reduced the number of independent parameters significantly, allowing for complete representation of the fit by a total of four different quantities: The positions  $b_1$  and line widths  $\sigma_1$  of the lowest energy transitions, the equidistant spacing  $\delta$  between neighboring transitions and the weight factors  $A_i$  of each individual Gaussian component  $i$ . Since non-normalized Gaussians were used, the weight factors are equal to the maximum values of the respective Gaussian functions rather than the line integrals. Since the latter are the physically more meaningful quantity, they are shown instead. All of these parameters were fit using mono- or biexponential functions starting at  $\approx 9$  ps and the retrieved time constants for the fits of  $b_1$ ,  $\delta$  and  $\sigma_1$  are collated in Tab. 3.2. The line integral dynamics will only be discussed qualitatively, but the corresponding exponential parameters can be found in Tab. A.2 in the appendix.

The temporal evolutions of the Gaussian line widths  $\sigma_i$  are nearly identical for all three solvents showing monoexponential decays with time constants between 13 and 15 ps, which is equivalent to a narrowing of the bands. All other parameters however exhibit significant differences, especially when comparing ethanol to the other two solvents. While within the fit window, the positions  $b_1$  of the first peak undergo a blue-shift of about  $150 \text{ cm}^{-1}$  for both acetonitrile and hexane, with time constants of 12 and 13 ps, respectively, the one for ethanol exhibits a red-shift of  $50 \text{ cm}^{-1}$  with a time constant of 51 ps. The peak spacings  $\delta$  show high similarities between acetonitrile and hexane as well, with monoexponential rises (time constants of 13 and 12 ps) towards constant values of 990 and  $950 \text{ cm}^{-1}$ , respectively. While the spacing in case of ethanol also increases initially (10 ps time constant), a subsequent decrease on the time scale of tens of picoseconds can be noted.<sup>12</sup> Regarding the peak integrals, the temporal progressions show a similar, effectively monoexponential rise for all three solvents for the lowest energy peaks. The behavior of the second peaks on the other hand are different for all cases. For Hexane, an initial rise is followed by a slow decrease, whose time constant exceeds the measurement

---

<sup>11</sup>As discussed previously, a better approximation is given by the Voigt profile (see section 2.4.6), but due to the higher parameter correlation no consistent fit results were obtained. The systematic error introduced by using a Gaussian to approximate the spectra however was found to be marginal, based on inspection of the fit residuals. Furthermore, only relative changes in the peak widths are analyzed further, which justifies using one common parameter for both types of line broadening.

<sup>12</sup>The retrieved time constant of 70 ps for the second exponential component has a large confidence interval, since it is too close to the upper limit of the fit range and is therefore not suited for quantitative interpretation.

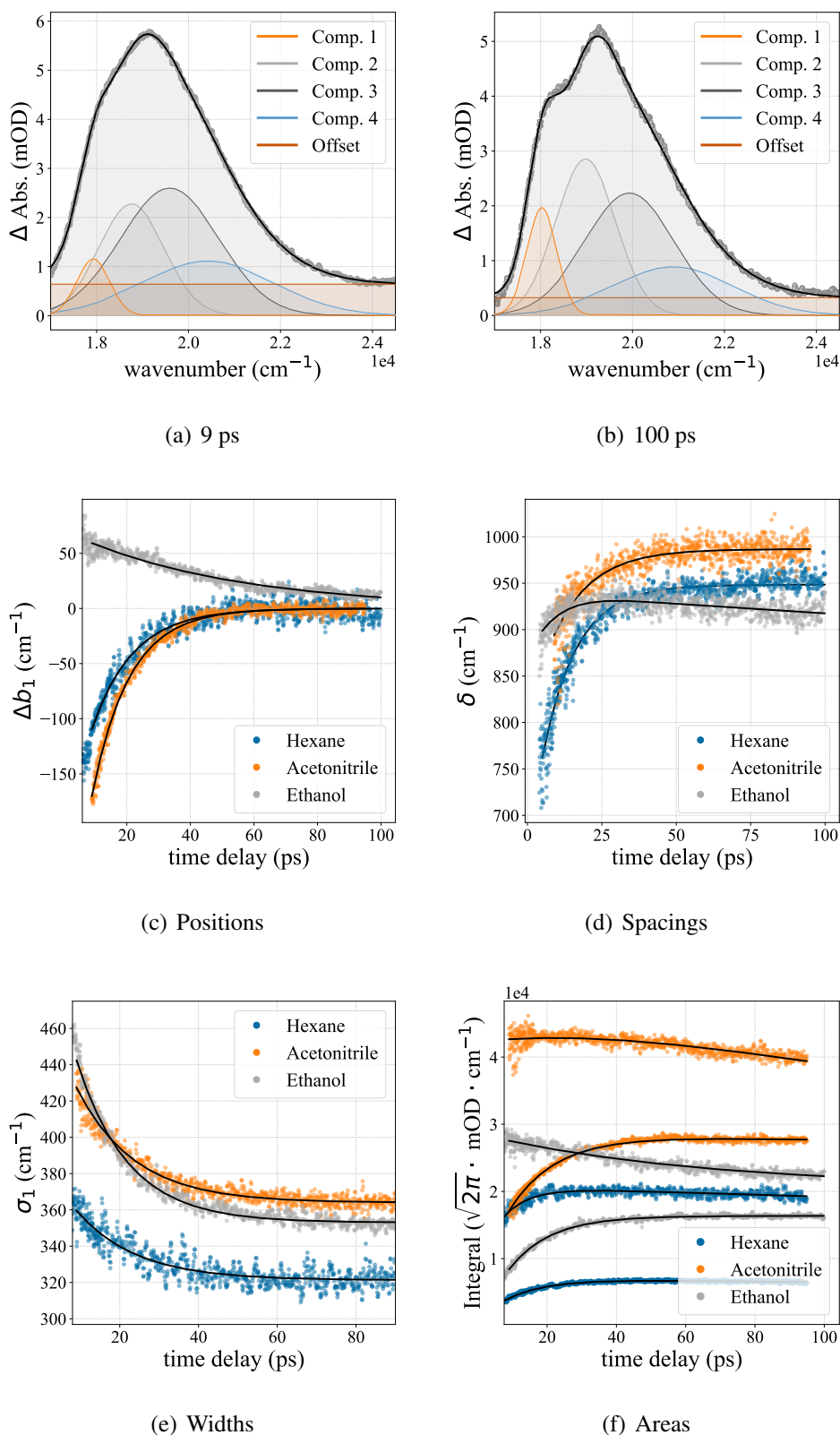


**Figure 3.10:** Dynamic line shape analysis of photoexcited SNP in solution. Figs. (a) and (b) show exemplary line shape fits for either end of the covered time range. Temporal evolution and exponential fits of the Gaussian parameters: (c) position  $\Delta b_1$  of the lowest energy peaks with respect to equilibrium, (d) equidistant spacing  $\delta$  between transitions, (e) line widths  $\sigma_1$  of the first components and (f) Gaussian integrals for the first two components (smaller integral = lower energy peak in all cases).

window. In case of acetonitrile, the initial rise is less pronounced while the subsequent decrease is more notable compared to hexane. SNP in ethanol again shows an entirely different temporal evolution with a monoexponential decay towards a constant value.

The peak narrowing within 15 ps is readily explained by dissipation of excess energy from the molecule to the solvent environment. Initially after excitation, distribution of the electronic energy into vibrational modes of the molecule (internal conversion, *vide supra*) leaves it in a vibrationally hot state, with higher-lying vibrational states populated and a broader energy distribution. This consequently leads to an overall decrease in transition energy and broadening in its distribution. As subsequently thermalization occurs via energy dissipation to the environment (vibrational cooling), a narrowing and decrease in expectation value of the transition energy distribution is expected. Hence, vibrational cooling would also induce a blue-shift in peak positions  $b_1$  of the lowest energy peak, which is equivalent to the HOMO-LUMO-gap, when including the vibrational part of the wave function. However, this only holds true if the ground and excited state energy levels are not significantly altered by other factors. For acetonitrile and hexane, vibrational cooling appears to dominate the dynamics in HOMO-LUMO transition energy, which is supported by the matching time scales between the hypsochromic shift of  $b_1$  and the peak narrowing. For ethanol however, a decrease in this transition energy is observed. Since the time scale for peak narrowing matches the other two solvents nonetheless, it can be assumed that thermalization of the molecule occurs similarly. The origin of the bathochromic shift can be explained by considering the interpretation of the steady-state absorption measurements, that the first singlet excited state  $S_1$  appears to be energetically more stabilized in ethanol with respect to the aprotic solvents. Thus, the DLSA results give insight into the dynamics of this stabilization, even though the obtained time constant of 51 ps is likely impaired by the underlying hypsochromic shift.

Further qualitative information as to how the solvents affect the  $S_1$  PES can be gained from inspection of the line integrals and peak spacings  $\delta$ . Describing the equidistant energy differences between the lowest vibrational states on the  $S_1$  PES in a harmonic approximation,  $\delta$  is linked to the shape of the electronic potentials. For all solvents an initial increase is notable, indicating an increasing spring constant of the harmonic potential, which happens during the same time as narrowing of the transition energy distribution. Exclusively for ethanol, a subsequent decrease is observed, giving further confirmation for a characteristic interaction with the  $S_1$  potential in the sub-100 ps window being absent in case of the other two solvents.

A comprehensive interpretation of the line integral dynamics by means of spectroscopy alone is not possible, since within the picture of a vibrational progression, the integrals are proportional to the transition probabilities and thereby the Franck-Condon factors, which are linked to the vibronic wave function overlaps between the ground and excited states. Thus, qualitative evaluation of both the peak spacing and integrals indicates that interaction between ethanol and the solvate molecule affects the  $S_1$  potential energy surface

in terms of spring constant and equilibrium position along the reaction coordinate. The distinct dynamics of these effects imply that the nature of the interaction differs from the other two solvents.

As pointed out during discussion of the steady-state spectra, the main difference between ethanol and the other two solvents is its capability of forming hydrogen bonds. Comparing the absolute peak positions,<sup>13</sup> it is evident that the hypsochromic shift of the equilibrium absorption spectrum for hexane with respect to the polar solvents is already established at the beginning of the analyzed time window ( $\approx 9$  ps). Therefore, there is no indication that the dipole interaction between the solvent and the merocyanine form plays a significant role in the observed dynamics on a time scale of 10 ps or more. Notably, ethanol has been reported to exhibit more complex and longer-lived relaxation dynamics compared to acetonitrile and non-polar solvents.<sup>[170,171]</sup> However, the distinctive effect of ethanol on the merocyanine species is also manifested in the equilibrium absorption spectra, energetically stabilizing both the ground and excited states with respect to the other solvents, which cannot be explained by solvent relaxation. These considerations leave the formation of hydrogen bonds as the most likely explanation for the distinct spectral dynamics of open-ring SNP in ethanol in the sub-100 ps regime. Nonetheless, a comparison of the data for ethanol to other polar protic solvents capable of forming hydrogen bonds would be helpful to clarify this question further.

In conclusion, application of the dynamic line shape analysis routine indicates that the spectral dynamics beyond the few-ps time window can be described using a simplified model in agreement with the physical picture of a vibrational progression of a single isomer. This isomer was found to undergo vibrational cooling with similar time constants in all three solvents of  $\approx 12$ -15 ps. More complex dynamics beyond this point, but on a sub-100 ps time scale, were found in ethanol, which can be explained by hydrogen bond formation.

### 3.2.3 Theoretical studies

The complementary theoretical studies of photoexcited SNP were carried out by Dr. Raison Dsouza within the scope of his PhD thesis.<sup>[69]</sup> Since the results were analyzed, interpreted and published together with the experimental results, the details and findings are laid out briefly in the following.

#### Methods

A surface-hopping molecular dynamics simulation utilizing time-dependent density functional theory (TDDFT) was carried out for a total of 30 trajectories for the first 1.1 ps after excitation. The initial conditions were based on a vibrational Wigner distribution in the

---

<sup>13</sup>See section A.4.1 in the appendix for a plot of the individual components for AcN and EtOH to compare to hexane.

ground state and vertical excitation at 266 nm, which led to population of either the  $S_2$  or the  $S_3$  state. Subsequent propagation was simulated by calculating the energy gradients on the fly using TDDFT and allowing transition between states if their energy gap went below a threshold value. Motivated by the evidence for an excited-state reaction intermediate found during analysis of the transient absorption data, a TDDFT-based geometry optimization on the  $S_1$  potential energy surface was carried out in addition.

### Population dynamics

The total populations of the respective electronic states were averaged over all trajectories and fit with a unidirectional sequential model in order to obtain the rate constants. Since  $S_2$  and  $S_3$  were close in energy, their initial population approximately equal and transitions between the states in either direction were not inhibited, it was possible to treat them as one superposition state  $S_n$  in a two-step model:



The resulting differential equations and their solutions can be determined in analogy to the unidirectional sequential model introduced in the context of target analysis (see section 2.4.6). A fit of the populations yielded rate constants of  $k_{n1} = 1.13 \cdot 10^{13} \text{ s}^{-1}$  and  $k_{10} = 7.93 \cdot 10^{11} \text{ s}^{-1}$ , corresponding to time constants of 88.4 fs and 1.26 ps, respectively. A plot of the population fit can be found in ref. [68] or Fig. A.16 in the appendix.

### Trajectory analysis

In 14 of the 30 simulated trajectories, rupture of the C-O bond in the spiroopyran molecule was observed. Out of these 14 trajectories, 13 yielded the planar merocyanine and only one returned to the closed-ring form. In order to obtain a ring-opening time constant to compare to the experimental results, a threshold for the C-O distance was set, after which the bond was considered broken. This allowed to calculate the number of molecules in the open-ring state as a function of time, which was fit with the third component of a two-step kinetic model. This was carried out for various threshold values between 0.1 and 1.2 Å yielding a minimum required threshold of 0.4 Å above which the retrieved time constants were unaffected by fluctuations of the C-O bond length around its equilibrium value.

Fig. 3.11 shows a representative fit of the ring-open species population determined in this way. Since bond breaking in these trajectories occurred exclusively in the  $S_1$  state, the first step in the kinetic model was ascribed to the transition to  $S_1$ , while the second step was ascribed to the actual bond-breaking on the  $S_1$  PES. Parameter correlation between the two rate constants, likely due to the relatively low number of trajectories and the low dimensionality of the optimization problem, was mitigated by imposing additional con-

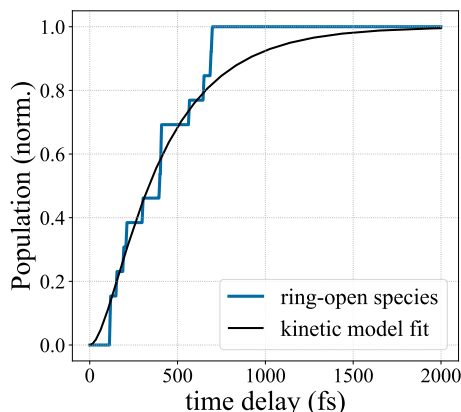


**Figure 3.11:** Bond breaking time in the MD simulations, depicted in terms of the population of open-ring species, which was fit with a kinetic sequential model.  $\tau_{AB} = 87$  fs (internal conversion) and  $\tau_{BC} = 300$  fs (cycloreversion)

straints. As the time constant for internal conversion to  $S_1$  was previously determined to be 88 fs, upper and lower bounds for the corresponding parameter were set to 80 and 95 fs, and 90 fs was used as an initial value. This resulted in time constants of  $\tau_{AB} = 87$  fs for internal conversion and  $\tau_{BC} = 300$  fs for the bond breaking. Since the limited time resolution in the transient absorption experiments did not enable to resolve the internal conversion to  $S_1$ , only an effective ring-opening time could be used for comparison. Therefore, a monoexponential fit of the same population data was applied disregarding the delayed onset, which resulted in a rise time of 340 fs.<sup>14</sup>

The remaining trajectories were all found to relax back to the ground state of the closed-ring form. In analogy to the ring-opening time, the relaxation time back to the ground state was determined to be  $\approx 500$  fs. All of these trajectories exhibited a notable bond elongation between the spiro-carbon and the nitrogen atom in the indoline moiety of  $1.1 \pm 0.1 \text{ \AA}$  for a duration of  $100 \pm 30$  fs, which was found to coincide with the transfer from  $S_1$  to  $S_0$ . The C-N stretch mode has previously been proposed in a theoretical study to be the key driving mode for the internal conversion back to the spiro-form.<sup>[172,173]</sup> Evidently, this is corroborated in the surface-hopping MD simulations.

### Excited-state intermediate

During the geometry optimization of photoexcited SNP in the  $S_1$  state, a stable configuration was found, further supporting the existence of a minimum on the potential energy surface, postulated in the analysis of the transient absorption data. The corresponding equilibrium structure can be described as an open-ring, non-planar isomer (see Fig. 3.12),

<sup>14</sup>This time constant is in agreement with the kinetic model, as the effective ring-opening lifetime is expected to be greater than  $\tau_{BC}$  and on the order of the sum of the two time constants (linear approximation of the exponential function).

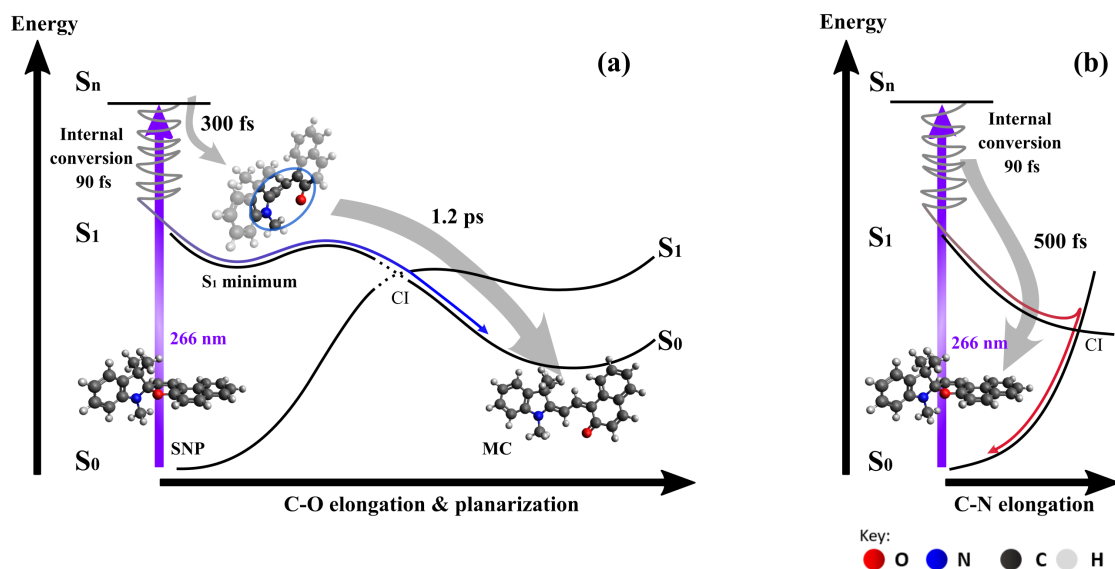


**Figure 3.12:** Schematic illustration of the two relevant reaction pathways of photoexcited SNP. Following excitation and internal conversion into  $S_1$ , bifurcation into two main pathways occurs, (a) ring opening and isomerization and (b) internal conversion back to SNP in the ground state. Reaction to merocyanine involves formation of a non-planar excited-state intermediate with a formation time of 300 fs, from which the planar isomer is formed within 1.2 ps after excitation. Conversion to SNP occurs via C-N-bond elongation with a time constant of  $\approx 500$  fs. Adapted with permission from ref. [68], ©2019 Royal Society of Chemistry.

rendering it likely as an intermediate of the chemical reaction between bond-breaking and planarization.

### 3.2.4 Concluding discussion

Combination of the insights gained from analysis of the experimental studies as well as the theoretical simulations allows for the proposal of a mechanistic picture, shown in Fig. 3.12. Following excitation at 266 nm into high-lying excited states  $S_n$ , internal conversion to the  $S_1$  state occurs with a lifetime of 90 fs according to the simulations. Internal conversion back to the spiro-form involves C-N-bond elongation and occurs with a time scale of  $\approx 500$  fs, which is in agreement with the excited state absorption decay found in the transient UV absorption experiments. The ring opening on the  $S_1$  potential energy surface pathway involves propagation towards an excited state minimum, during which the bond is broken, leading to an open-ring excited-state intermediate (ESI) with an approximately orthogonal orientation of the moieties. This intermediate manifests in the transient absorption experiments with an absorption maximum around 450 nm. Its formation time was found to be  $\approx 300$  fs which is in agreement with the bond-breaking time of 340 fs determined from the simulations.

Subsequently, propagation towards the planar merocyanine form involves overcoming an

energy barrier on the  $S_1$  PES and passing through a conical intersection (CI) into the ground state ( $S_0$ ), associated with bond rotation along the methine bridge. Planarization induces an increased delocalization of the electronic wave function consistent with the observed red-shift of  $\approx 100$  nm between 300 fs and 2 ps after excitation. Global and target analysis indicate that isomerization from the orthogonal open-ring ESI to the planar MC occurs with a time constant of 1.1-1.3 ps. All subsequent spectral shifts are at least an order of magnitude smaller than the initial bathochromic shift, indicating that no further planarization takes place.

This claim is supported by the in-depth analysis of the spectral dynamics beyond 2 ps, the results of which are consistent with vibrational cooling of a single species in the electronic ground state. The successful application of a simplified vibrational progression model indicates that the spectral dynamics are not associated with any significant structural changes of the solute. Furthermore, a notable solvent dependence was found in this time regime, with unique equilibration dynamics of the open-ring isomer in ethanol. While ethanol in general exhibits more complex relaxation dynamics than the other two applied solvents hexane and acetonitrile, its distinct effects on the merocyanine form are corroborated in the analysis of the steady-state spectra, which are unaffected by relaxation dynamics. Therefore, barring further studies, the observed spectral evolution in the sub-100 ps regime can be assigned to the formation of hydrogen bonds.

### 3.3 Transient Absorption Spectroscopy of Spiroanthopyran in Crystal

#### 3.3.1 Sample preparation

Single crystals of 1,3,3'-Trimethylindolino- $\beta$ -naphthopyrylospiran (SNP, TCI Chemicals, Japan)<sup>[168]</sup> were grown via vapor diffusion using chloroform as solvent and diethyl ether as vapor (see section 2.6). This method yielded relatively large single crystals ( $>2$  mm, see Fig. 3.13 (a)), from which 100-300 nm thin slices for time-resolved experiments were cut using ultramicrotomy (see section 2.6). The quality of the crystal cuts was assessed by inspection of static electron diffraction patterns from 150 nm thin samples, taken in the ultrafast electron diffraction setup (DC electron gun, see section 2.5.3). In comparison to other molecular crystals<sup>[56,96,97]</sup> as well as SNP crystals grown by solvent evaporation (see Fig. A.27 in the appendix) the diffraction pattern is of high quality exhibiting many intense and well-defined peaks even for higher diffraction orders, confirming a high degree of crystallinity achieved by the applied crystallization procedure.

The steady-state absorption spectrum of a 150 nm thin crystal slice and the excitation fraction curve calculated from the obtained absorption coefficient and reported crystal structure<sup>[174]</sup> are shown in Fig. 3.14. Since the absorption spectrum contains a non-negligible

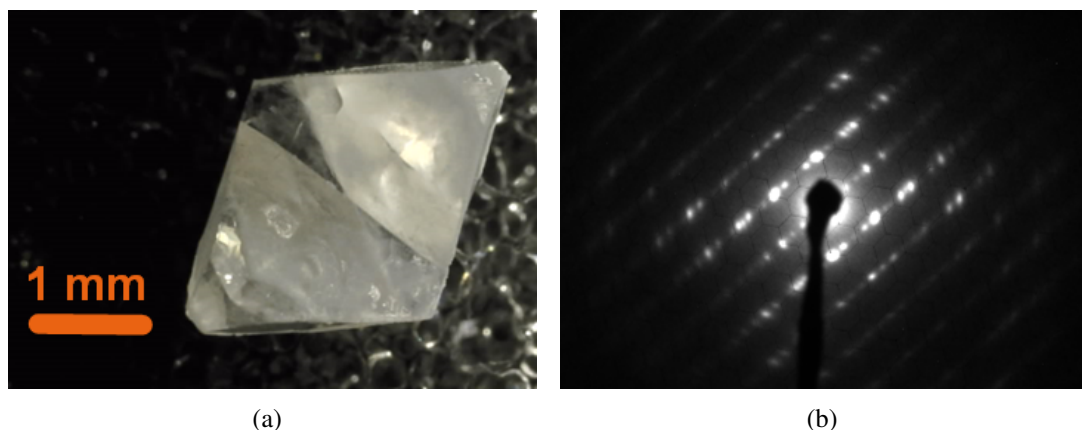


**Figure 3.13:** Single crystals of spiroanthopyran, grown via vapor diffusion. (a) Image of an example crystal, (b) static electron diffraction pattern of a 100 nm thin crystal slice.

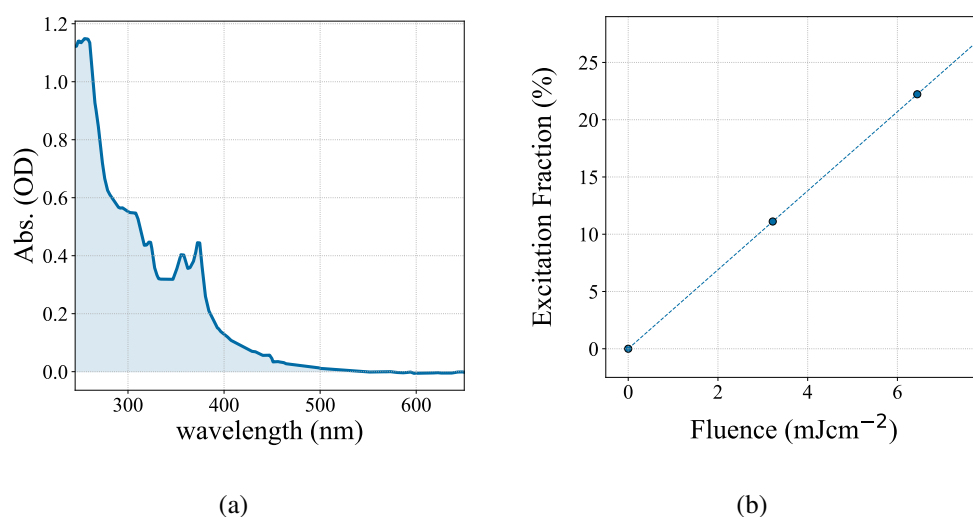


**Figure 3.14:** Steady-state absorption of crystalline spiroanthopyran. (a) absorption spectrum of a 150 nm thin crystal slice, (b) excitation fraction plot for a wavelength of 266 nm calculated from the measured spectrum.

contribution from scattering and reflection, the excitation fraction values can only serve as an upper limit. However, qualitative comparison of the solid-state spectrum to the spectra in solution suggests that the contribution to the extinction from these effects is on the order of 50 %.

### 3.3.2 Experimental details

Single crystalline samples of spiroanthopyran with a thickness of 250 nm were used for transient absorption experiments using the previously described setup in solid-state configuration with the visible supercontinuum as probe and the third harmonic of the funda-

mental (266 nm) as pump at a repetition rate of 20.83 Hz and a fluence of  $2.3 \text{ mJcm}^{-2}$ .<sup>1516</sup> The pump beam was circularly polarized by using a  $\lambda/4$ -plate to reduce potential polarization effects on the excitation density. Unlike in case of the closely related spiroanthoxazine,<sup>[63]</sup> the sample was found to be reversible under these conditions without the need for photoreversion with a visible laser. Since the experiments were conducted prior to the implementation of increasing time delay steps in the acquisition software, separate scan sets were recorded covering different time ranges with appropriate time step sizes. In order to retrieve a dataset of the entire available time range of 1.4 ns, three scan sets with different time steps for each sample were recorded and concatenated. Complementary experiments with varying thicknesses (100 to 300 nm) were carried out and compared to verify the linearity of the observed signals.

#### 3.3.3 Observations

The transient absorption data from single crystalline spiroanthopyran with a thickness of 250 nm, excited at 266 nm and probed in the visible is shown in Fig. 3.15. The initial signal after excitation is a broad absorption band with two maxima, one around 450 nm and the other between 500 and 500 nm. This spectrum evolves within the first picosecond, exhibiting a slight overall decay in intensity and a relative increase of the sub-band at 450 nm while the other initial maximum decays developing into a shoulder of the former. This absorption signal decays on the few ps time scale giving way to a longer-lived absorption spectrum with a maximum around 570 nm and a residual band at 450 nm at 10 ps. The data shown in Fig. 3.15 (c) is taken from a different sample of the same thickness and a scan with longer time steps, but comparable signal intensity. It reveals that the signal appearing to be long-lived with respect to a 10 ps window, actually decreases on the sub-ns time scale, leaving only a small residual absorption signal ( $\approx 2 \text{ mOD}$ ) between 550 and 600 nm and negative band between 450 and 550 nm, with an amplitude of  $\approx -5 \text{ mOD}$  at the end of the measurement window (1.4 ns). In addition to this decay, a positive absorption band between 400 and 450 nm rises within 50 ps before decaying partially, reaching a constant magnitude around 1 ns. Further decay of this band within a few milliseconds can be assumed since no accumulation of this absorption signal was observed while running multiple pump-probe scans on the same sample region. Furthermore, the sub-ns dynamics exhibit small oscillations with periods around 100 ps, which will be subject to further analysis in the following section.

Comparing scans from different samples of the same thickness showed some variation in signal intensity. However, compared between different scans on the same sample, the dynamics were consistent. Thus, these variations can be traced back to damage during ultramicrotomy and transfer to the sample substrate. A scan from a sample with a thickness

---

<sup>15</sup>Additionally, several scans using the broadband UV laser around 330 nm were conducted but did not exhibit any significant differences.

<sup>16</sup>The fluence corresponds to a calculated excitation fraction of 8 % (upper limit, *vide supra*).

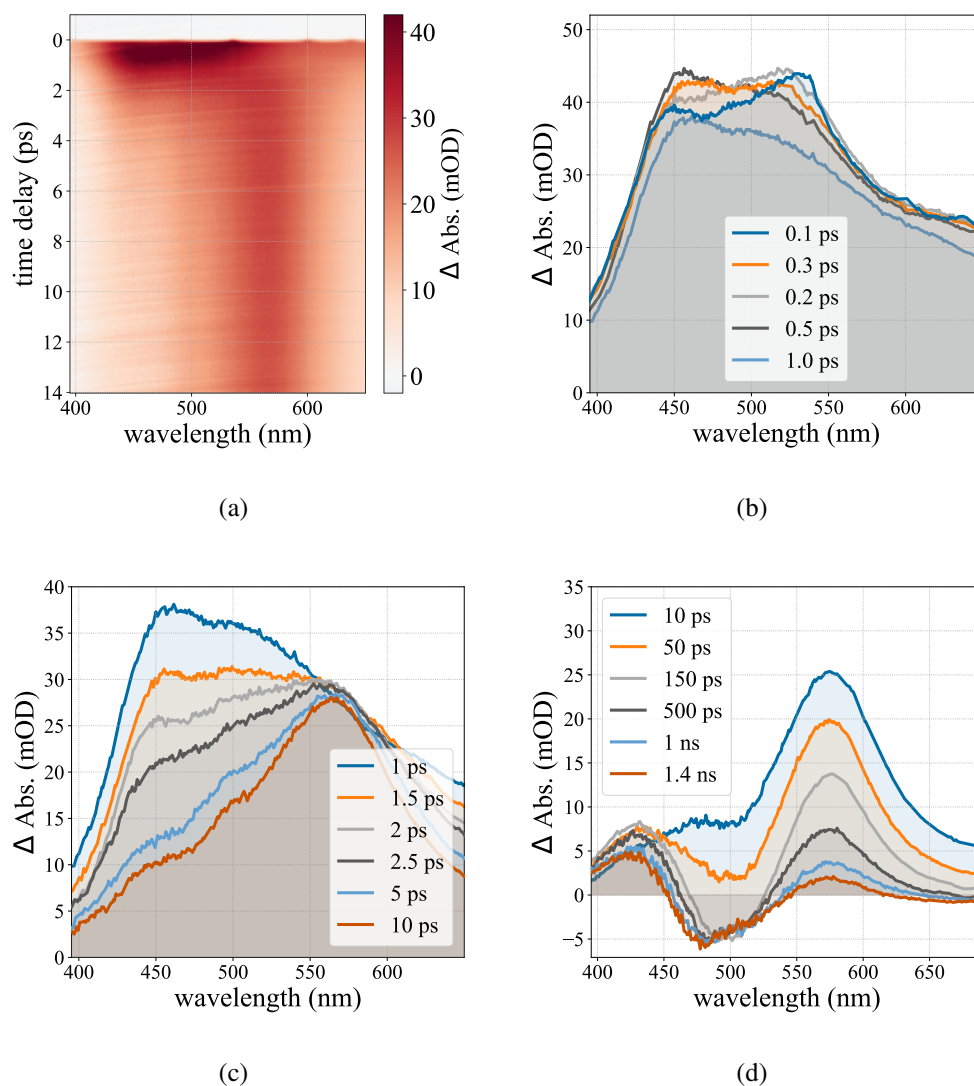


**Figure 3.15:** Transient absorption data of crystalline spironaphthopyran (250 nm thickness), excited at 266 nm and probed in the visible. Shown are (a) the TA map for the first 14 ps along with selected spectral traces to cover (b) sub-ps dynamics, (c) few-ps dynamics and (d) dynamics up to 1.4 ns.

of 150 nm is shown in the appendix, demonstrating that reducing the thickness to 60 % corresponds to a reduction in absorbance of approximately the same ratio. This indicates that the observed dynamics can be attributed to molecules in the bulk crystal and are not merely due to surface effects.

### 3.3.4 Analysis and discussion

By comparison, a high similarity in the few-ps dynamics between the present data and the one obtained from SNP solutions is readily noticed, entailing the formation of an intermediate absorption signal with a maximum around 450 nm, its subsequent decay and a simultaneous rise of a long-lived band between 500 and 600 nm. The latter signal in this case however is weaker than the intermediate band and its rise becomes masked by the

decay of the former. These similarities suggest that in crystal, not only the formation of a planar photoproduct is possible, but also following the same or a highly similar reaction mechanism. In the following, the few-ps dynamics are analyzed in order to test this hypothesis and characterize the commonalities and differences to the solution data, before discussing the dynamics beyond 10 ps, where the crystalline case deviates significantly from solution.

#### **Sub-10-ps dynamics**

Due to the lower repetition rate and limited number of pump-probe cycles compared to the solution experiments, the crystal data contains significantly higher noise both from the detector and probe fluctuations. In order to mitigate this, singular value decomposition (SVD) was carried out for all scans, shown exemplarily for the 15 ps window in Fig. 3.16. From the singular values, it was determined that the sum of the first five components could be used as a denoised dataset for further analysis. Furthermore, the second component reveals the independent rise and decay of the intermediate band around 450 nm and that indeed its subsequent decay is correlated with the rise of the photoproduct band. The first component on the other hand contains both the decay of the broad ESA signal, but also the beginning decay of the photoproduct band and is therefore too convoluted to be interpreted.

Quantitative comparison to the solution data was instead carried out on the basis of global and target analysis. The decay-associated spectra of a four-component global fit are shown in Fig. 3.17 (a) next to the species-associated spectra from an equivalent, three-step unidirectional model. The retrieved time-constants for both models were identical and therefore global and target analysis can be used interchangeably. When this is the case, the systematic error in the time constants introduced by global analysis due to all exponential decays starting at the point of excitation becomes negligible, while the advantage of a differential decomposition of the data remains. Hence, it is used for further discussion. The first component describes the formation of the intermediate absorption signal from the initial excited state absorption band, with a time constant of 300 fs. The second component consists in the simultaneous decay of the absorption maximum at 450 nm, decay of the overall excited state absorption background and, relative to the latter, the rise of the photoproduct spectrum, assigning a time constant of 1.3 ps. The third component mostly accounts for a second component in the decay of the excited-state- and intermediate absorption bands, but also slight spectral narrowing of the photoproduct band, while the fourth component represents the transient absorption spectrum at 14 ps.

Thus, in analogy to the discussion of the solution dynamics, the short-lived absorption around 450 nm can be attributed to an excited-state intermediate, from which the photoproduct is formed. Remarkably, the formation times of these two species are virtually identical to the case of solution, supporting the claim that the main ring-opening and

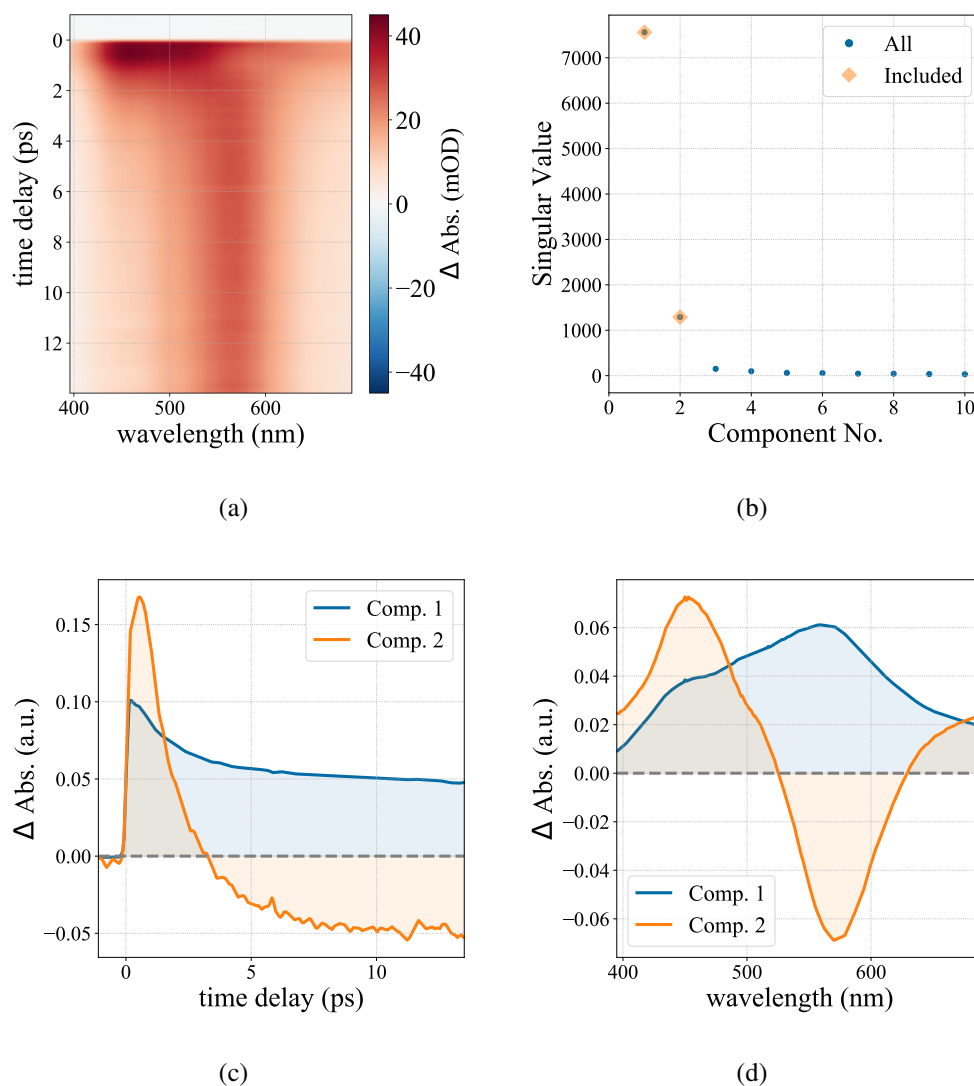


**Figure 3.16:** Singular value decomposition of the TA data from photoexcited, single-crystalline SNP. (a) reduced data using the first two SVD components, (b) first ten singular values, (c) first two left singular vectors, (d) first two right singular vectors.

planarization pathway is not significantly impaired by the crystalline environment. However, the third decay component and the overall slower decay of the broad excited state absorption suggest that in crystal alternative relaxation channels exist, which do not lead to the planar merocyanine isomer. In the solution experiments, no evidence for such pathways was found and the theoretical simulations suggested that nearly all created ring-open species subsequently underwent planarization. Furthermore, the absorbance of the product band relative to the intermediate in crystal is reduced by approximately 50%, while the amplitudes in solution are of similar magnitude. Although this ratio would also be affected by a potential change in the out-of-plane component of the transition dipole moment, this observation at least corroborates the hypothesis of a reduced photoproduct quantum yield in crystal.

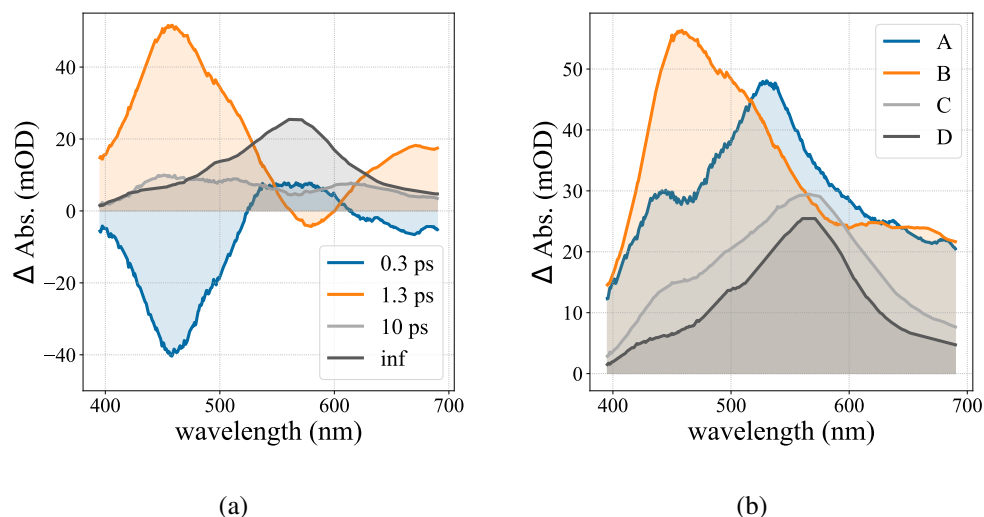


**Figure 3.17:** Global fitting results for crystalline SNP in the time window between 0 and 15 ps, using (a) global analysis and (b) target analysis. The last component in both cases was set as constant (inf). The time constants from target analysis were identical to the ones of the first three components from global analysis.

### Sub-ns dynamics

The spectral dynamics of photoexcited SNP in crystal exhibit significant differences from the solution case in the time regime beyond 15 ps. While in solution the photoproduct absorption remains constant within the measurement window, it almost entirely decays in the case of crystal. The rise of a long-lived absorption between 400 and 450 nm as well as the negative signal red-shifted with respect to the former are also absent in the solution TA.

In order to interpret these observations and find potential correlations, global and target analyses were carried out for this time window as well (see Fig. 3.18). Two decay components and a constant component were required for an appropriate fit of the data, with the latter representing the spectrum at 1.4 ns and consisting of the long-lived positive and negative bands as well as a residual of the decaying photoproduct absorption. The rise of these two long-lived bands as well as a residual decay of the excited state absorption is described by the first component, with a time constant of 45 ps. The second component (640 ps) accounts for the photoproduct decay as well as the slight decay of the long-lived absorption band before it reaches a constant level around 1 ns.

From the decay-associated spectra, two main insights can be gained. Firstly, the rise of the long-lived positive and negative bands as well as the main decay of the broad ESA can be summarized in a single component. Secondly, that component contains no signature of the product absorption band signifying that its decay occurs independently. Interpretation of the second component is less straightforward, since it describes three different processes: Decay of the photoproduct, whose absorption is assumed to be non-zero in the entire probing range, decay of the long-lived absorption band towards a constant amplitude,

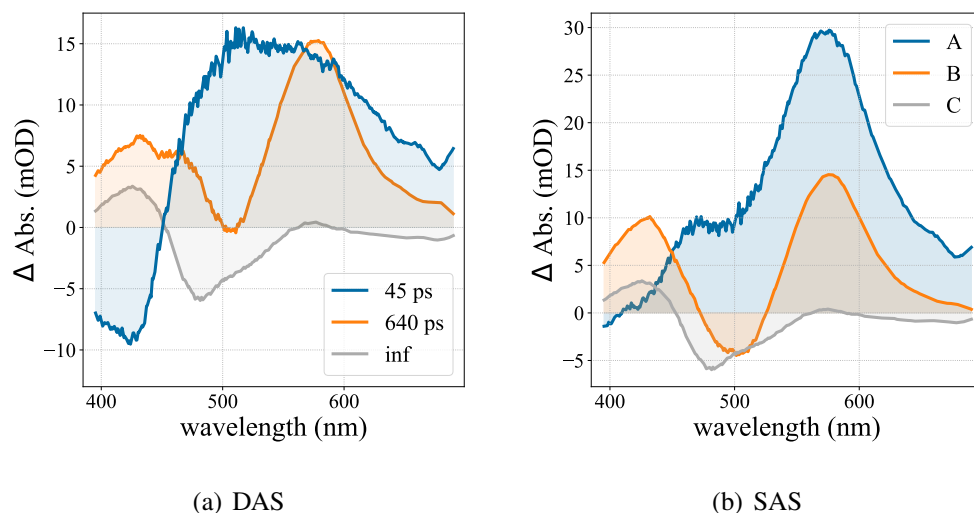


**Figure 3.18:** Global and target analysis of crystalline SNP TA in the sub-ns range. (a) DAS from global analysis, (b) SAS from target analysis. The obtained time constants of 45 and 640 ps were identical for both methods.

which in itself may be caused purely by the photoproduct decay, and a shift of the edge between the long-lived positive and negative signals.<sup>17</sup> While it can be concluded that all of these processes occur in the sub-ns time domain, their convolution sheds some doubt on their temporal correlation and thereby the reliability of their common time constant. Furthermore, the aforementioned oscillations on the 100 ps time scale are not accounted for by the exponential fits. Since they are on a similar time scale as the decay components, Fourier analysis of the residual was not carried out.

In order to complement the global fits and to overcome their shortcomings, kinetic trace fits were carried out in addition both including and excluding oscillating components. Instead of single wavelengths, spectral regions representative for the respective signals were integrated, in order to improve the signal-to-noise ratio. These integral traces including mono- or biexponential fits are shown in Fig. 3.19 (a) and the corresponding fit parameters can be found in Tab. 3.3. In general, the time constants from the independent fits of the bands are consistent with the results from global analysis. However, the shorter-lived exponential components in the trace fits are found to be slightly slower than the 45 ps from global fit in the regions close to the product absorption and faster in the regions where the ESA dominates (below 440 and above 660 nm). On the other hand, the second exponential components of the long-lived absorption and product bands are in agreement with each other as well as the second global fit component. The second time constant of the ESA decay above 660 nm deviates from this, but its small amplitude and large confidence interval prohibit any quantitative conclusions. The fit of the negative band confirms the previous observation that it undergoes no significant changes in amplitude after the initial

<sup>17</sup>These processes may be more easily recognized by comparison of the corresponding species-associated spectra B and C in Fig. 3.18 (b).

**Table 3.3:** SNP crystal sub-ns dynamics: Integrated band exponential fits.  $\tau$  = lifetimes,  $A$  = amplitudes and  $C$  = offset of the respective exponential functions.

Integ. range	$\tau_1$ (ps)	$\tau_2$ (ps)	$A_1$ (mOD)	$A_2$ (mOD)	$C$ (mOD)
405-440 nm	$36 \pm 3$	$620 \pm 70$	$-0.42 \pm 0.02$	$0.30 \pm 0.01$	$0.20 \pm 0.01$
475-520 nm	$49 \pm 1$	–	$0.35 \pm 0.01$	–	$-0.10 \pm 0.001$
560-590 nm	$48 \pm 4$	$650 \pm 60$	$0.49 \pm 0.02$	$0.54 \pm 0.01$	$0.002 \pm 0.02$
660-695 nm	$39 \pm 2$	$860 \pm 160$	$0.36 \pm 0.01$	$0.12 \pm 0.01$	$-0.06 \pm 0.01$

decay. Exponential fits with dual-frequency sine modulations were carried out for the negative band as well as the photoproduct band for the first 400 ps. While also present in the other bands, the oscillation amplitudes were too small compared to the noise level. The main oscillatory components in the respective bands were found to have periods of 140 ps for the product absorption band and 150 ps for the negative band. The latter band required a second frequency component with a period of 360 ps. Beyond 400 ps, the oscillations were dampened too much to be fit. Comparing the time scale and amplitude of these oscillations to other organic crystals, they can be attributed to intermolecular acoustic phonons.<sup>[108,175–177]</sup>

Combining the insights gained from global analysis and independent fits of the transient absorption features in the time domain between 15 ps and 1.4 ns, the following interpretation of the data can be made. The planar ground-state merocyanine, although being formed initially, appears to be only metastable in the crystalline environment and reacts back to the closed-ring form with a time constant of approximately 650 ps. Relaxation channels not involving formation of the photoproduct are slower than the main reaction path, causing a longer-lived decay of the broad excited state absorption signal of  $\approx 45$  ps compared to 1-2 ps in solution. Simultaneously, the long-lived positive absorption band is formed with a time constant of  $\approx 40$  ps. As this was found to occur independently from the merocyanine decay and because of the temporal correlation, the species responsible for this signal is likely formed from the excited state and thus a long-lived reaction byproduct in the ground state. The sufficient reversibility of the experiment without the need for photoreversion implies that this byproduct is only metastable as well and reacts back to the spiro-form within a few milliseconds at the most. Although transient absorption is not directly sensitive to the molecular structure, a comparison to the absorption spectra of the closed-ring and the open-ring planar form allows for a general classification of the byproduct species, assuming it to be in the ground-state: The fact that its absorption is red-shifted with respect to the closed-ring form implies that the wave function overlap between the two spiropyran moieties is slightly increased making the

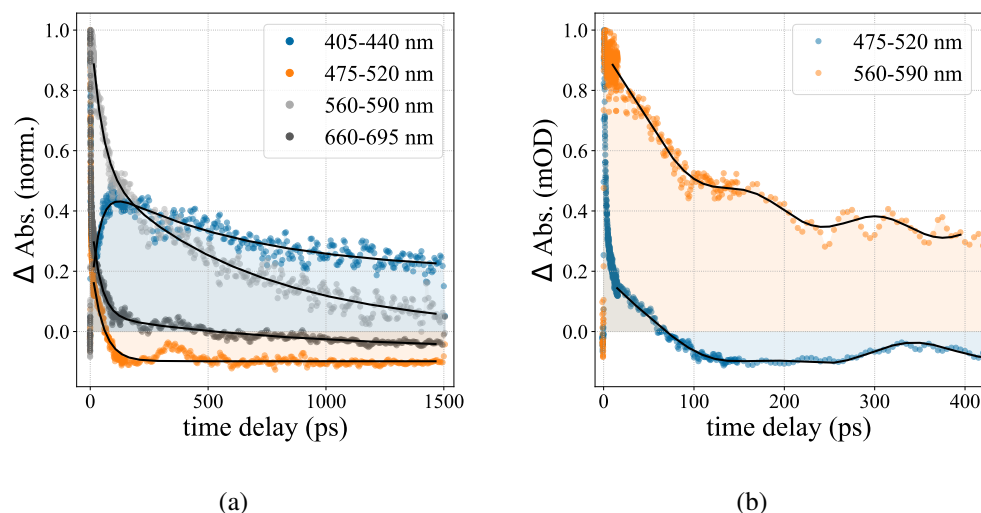


**Figure 3.19:** Exponential fits of the integrated absorption bands in the sub-ns time regime, using (a) mono- or biexponential functions, (b) sine-modulated exponential functions.

spiro-carbon at least partially  $sp^3$ -hybridized. However, complete planarization and  $sp^3$ -hybridization of the spiro-carbon can be excluded by comparing the absorption signal to the merocyanine absorption. Thus, this byproduct can be postulated to be an open-ring, non-planar conformer, likely similar in structure to the open-ring intermediate, whose structure was previously determined by numerical simulations (*vide supra*). The partial decay of the byproduct absorption band has multiple possible explanations. The match of the time scales suggests that the decay in absorption is attributed to the merocyanine re-cyclization, since the latter has a non-zero absorbance in this spectral region as well. On the other hand, part of the initially created byproduct may react back to the closed-ring form themselves before reaching the metastable state.

The dynamics of the negative band may shed some light in regard to this question, but they are not entirely unambiguous themselves. Since the closed-ring form does not absorb in this region and no accumulative effects over multiple pump-probe cycles were observed, this signal can be excluded to be associated with a ground-state bleach. This leaves either emission due to a radiative decay or an overall increased transmission, possibly due to reduced reflectivity or scattering. While both neighboring bands exhibit a decay on the order of 600 ps, the amplitude of the negative band remains constant. If the negative band itself had a constant amplitude, an overall decrease in absorbance would be expected due to its overlap with the other, partially decaying absorption features. An effectively constant level indicates a counteracting decrease in absolute absorbance of this band. Assuming the negative band to be linked to the byproduct would be consistent with this, as the partial decay of the absorption below 450 nm was found to be on a similar time scale of the merocyanine band decay, thus leading to offsetting effects. However, assuming the negative signal to be linked to transient changes in the lattice, a decrease in its magnitude may also be linked to the return towards its initial state as the photo- and

byproducts react back to the closed-ring form.

Even though these details cannot be clarified unambiguously based on the present data, analysis of the sub-ns dynamics reinforces the hypothesis that alternative reaction pathways in crystal exist and the formation of one or multiple metastable byproducts was found to occur with a time constant of  $\approx 40$  ps, independent of the main reaction channel. While the latter pathway appears to be largely unaffected by the crystal environment based on comparison to solution, the formed planar merocyanine was found to be energetically unstable and its population to decay with a time constant of 650 ps.

### 3.3.5 Summary

Analysis of the transient absorption data from photoexcited spironaphthopyran in single crystalline slices shows that the formation of an open-ring excited-state intermediate occurs with virtually the same time constant as in solution (300 fs), indicating that the bond-breaking is not affected by the surrounding crystal lattice. From this intermediate, two relaxation pathways exist, one of which yields the planar merocyanine form with a time constant of 1.3 ps, again closely matching the results from the SNP solutions. The other pathway results in the formation of a long-lived byproduct with an absorption maximum between 400 and 450 nm, which is not observed in solution. The merocyanine is only metastable in the crystalline phase and its population decays with a time constant of 650 ps, while the byproduct decays on a time scale longer than one nanosecond, but fast enough to provide reversibility in the few-ms regime. A permanent negative signal between these two bands was found in addition which presumably is associated with crystal strain, but warrants further investigation, possibly with the aid of numerical simulations.

## 3.4 Ultrafast Electron Diffraction

Time-resolved electron diffraction experiments on single-crystalline slices of spironaphthopyran were conducted using both the DC compact electron gun and the RF compression gun, described in section 2.5.3. While no clear evidence was found for a differential signal unambiguously and directly ascribable to the photoisomerization reaction, a consistent post-excitation signal was observed, which encompassed significant diffraction peak broadening, especially visible in the brightest diffraction orders. These findings are presented and characterized in this section and possible physical explanations are discussed. Although similar observations were made using either electron diffractometer, the results dealt with here will be limited to the ones obtained with the RF gun due to its inherently higher signal-to-noise ratio.

### 3.4.1 Experimental details

UED experiments were carried out using the RF compression electron diffractometer at the University of Toronto (see section 2.5.3), with the third harmonic of the Ti:Sa regenerative amplifier at 266 nm for both generation of the electron pulses and excitation of the sample. Various pump fluences and repetition rates were tested, up to  $3.4 \text{ mJcm}^{-2}$  and 100 Hz, respectively. The standard setting based on the transient absorption experiments consisted in a pump fluence of  $1.4 \text{ mJcm}^{-2}$  and 25 Hz, and was applied for the measurements discussed in the following, unless noted otherwise.<sup>18</sup> The laser and electron beam sizes on the sample were determined by scanning them with a pinhole in the sample holder and set to diameters of 130 and 330  $\mu\text{m}$ , respectively. The electron pulse duration and timing jitters were measured to be approximately 400 and 300 fs, respectively, for the utilized bunch charges of  $\approx 23 \text{ fC}$  ( $1.4 \cdot 10^5$  electrons). The pump pulse duration was estimated to be  $\approx 200 \text{ fs}$  based on the laser specifications and effects of GVD from passing through optical elements as well as the vacuum chamber window. All scans were carried out cooling the sample to 270 K using a cold finger (liquid nitrogen), to prevent sample evaporation.

Time zero determination was carried out each day prior to the sample scans using single crystalline silicon in order to set the time windows for the scans. Since the time resolution of the instrument did not allow for resolution of the reaction intermediate, the emphasis of the measurement was set on signatures from the planar MC product, few ps after excitation and thus time steps on the order of one picosecond were chosen for the measurement.

### 3.4.2 Results

Processing of all data from the utilized RF compression diffractometer at the University of Toronto was carried out based on Matlab functions written by Dr. Lai Chung Liu in the course of his thesis work.<sup>[58]</sup> Fig. 3.20 shows a static diffraction pattern acquired during a time-resolved scan. The indices noted in the figure were determined coarsely using the CrystalMaker<sup>[178]</sup> software suite (see A.5.1 in the appendix for further details) and the reported crystal structure obtained from powder diffraction measurements.<sup>[179]</sup> Evidently, the thin crystal slices had been cut approximately orthogonally to the (100) crystal direction and the brightest peaks ((004), (012), (01 $\bar{2}$ ), (015), (01 $\bar{5}$ ) and their corresponding peaks) form two equivalent rhomboids, which are mirror-symmetric with respect to each other and reflect the symmetry of the monoclinic crystal system. The depicted pattern being an average of the acquired pump-off spectra during the scan indicates the overall conservation of crystallinity during the scan. However, for fresh samples a decrease of

---

<sup>18</sup>The fluence of  $1.4 \text{ mJcm}^{-2}$  corresponds to an excitation fraction of 4.8 % according to the steady-state absorption spectra. As noted, effects of scattering and reflection in solid-state samples (especially in the far ultraviolet) contribute significantly to the latter, rendering this only an upper limit.



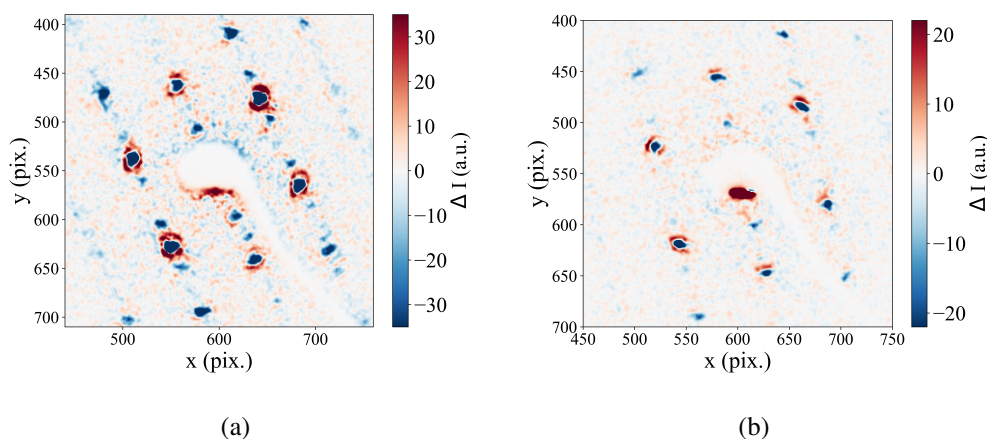


**Figure 3.21:** Differential electron diffraction pattern of photoexcited SNP, averaged over the first 10 ps after excitation.

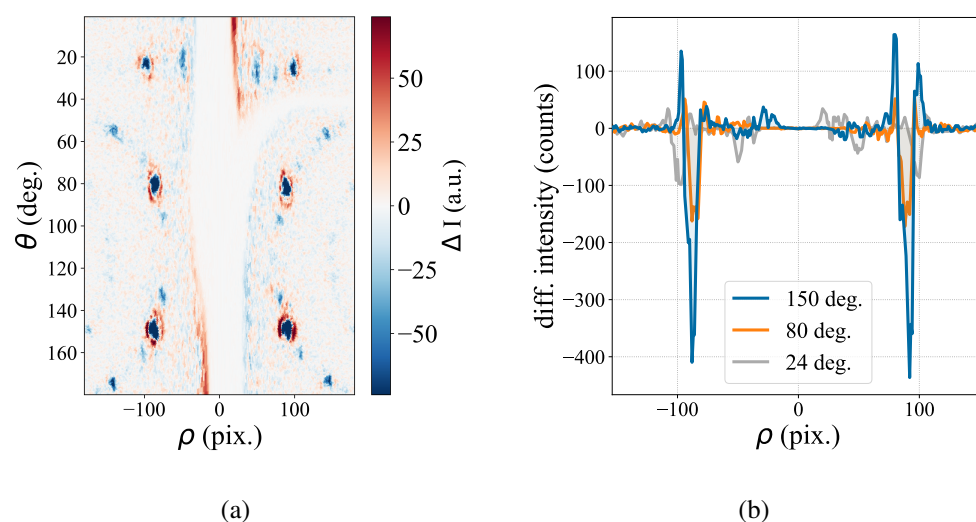


**Figure 3.22:** UED difference signal of photoexcited SNP, projected onto polar coordinates (Radius  $\rho$  and angle  $\theta$ ). (a) map for all angles, (b) line plot for the most important angles.

dent that the approach is only a first approximation,<sup>19</sup> the results from these fits reflect the general observations. For the investigated scans at various angles, dynamic increases in peak width between 20 and 30 % were obtained. The amplitude ratio between the positive and negative Gaussian components ranged between 60 and 70 % confirming the overall decrease in intensity, but also indicating that the main part of the peak intensity change can indeed be caused by the broadening process.

<sup>19</sup>A more accurate analysis should at least model and compare the respective shape factors (conf. equation 2.46 in section 2.5.1), but ideally simulate the entire diffraction pattern for different hypotheses, which exceeds the scope of this thesis.

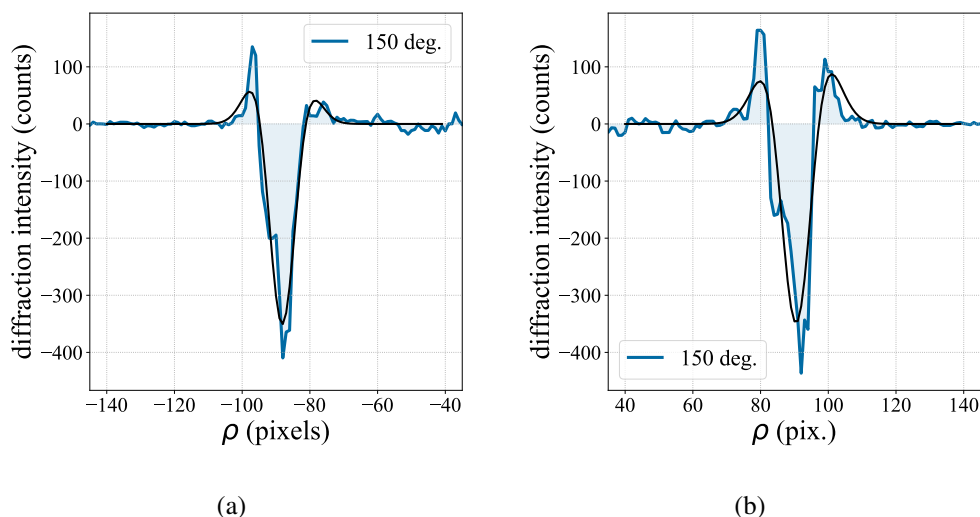


**Figure 3.23:** Coarse fit of the diffraction peak broadening, observed in photoexcited SNP, for an angle of  $150^\circ$ , using two Gaussian functions, indicating a width increase of  $\approx 30\%$  and an intensity decrease of  $\approx 30\text{-}40\%$ .

### 3.4.3 Discussion

A more in-depth analysis of the present data, ideally extended by additional measurements, is required in order to provide a full interpretation of the observed phenomena, which exceeds the scope of this thesis. Nevertheless, based on the observations and characterizations, a few interpretive approaches can be discussed. At equilibrium, the width of the diffraction peaks depends on the periodicity of the sample on the one hand and the transverse coherence length of the electron beam on the other hand. Both of these dependences originate from the superposition of interfering scattered beams from multiple scattering centers. Since the coherence of the beam is unaffected by sample excitation, the origin of the peak broadening has to lie within the sample. As stated in section 2.5.1, changes in peak width or position are attributed to the shape factor, which depends on the unit cell dimensions as well as the number of unit cells contributing to the signal. Indeed, the observed signal is different from the commonly observed Debye-Waller effect, which is attributed to (temporary) heating of the lattice and whose contribution is encompassed in the structure factor (see section 2.5.1). While this effect may be the cause of the overall decrease in intensity, it does not explain changes in peak width. Permanent damage of the sample may also induce peak broadening, but it can be excluded as the main cause of the observed phenomenon due to two reasons: Crystal damage will also entail a drastic loss of intensity in increase in incoherently scattered background, neither of which are observed in the time-resolved signal. Secondly, even though for a fresh sample an initial drop in total diffraction intensity of about  $3\%$  was observed, suggesting a loss of crystallinity to some degree, the experiment was reversible and the signal reproducible over multiple consecutive scans.

Collective changes in the unit cell dimensions via expansion or contraction due to photoinduced phase transitions have been shown to induce dynamic peak shifts in time-resolved diffraction experiments,<sup>20</sup> which is consistent with the correlation between reciprocal and direct lattice described in section 2.5.1. The observed signals can be interpreted equivalently as non-directional changes in the lattice constants, that is transient distortions of the crystal lattice. Regarding the large structural change encompassed by the photoisomerization reaction of SNP, it can be expected that formation of the planar merocyanine, as it was shown to occur based on the transient absorption experiments (*vide supra*), leads to deformation of the crystal lattice. Such distortions can also explain the observed transience of the product, which decays with a time constant of 650 ps according to the TA experiments. The restoring force from the crystal lattice, as discussed in the previous section, is thus the likely cause for the decreased stability of the merocyanine form relative to solution.

As noted, no obvious signs for changes in the structure factor other than overall decreases were found, pending appropriate modelling of the diffraction pattern including transient lattice deformation. In principle, the integrals for one or more pairs of diffraction peaks should net increases in intensity. The potential reason why this is not observed is an insufficient excitation fraction, estimated to be around 5 % at the most,<sup>21</sup> while the target value usually lies around 10 %.<sup>[6]</sup> However, increasing the fluence under the present conditions led to rapid sample deterioration. Potentially, reducing the temperature further can mitigate this in part allowing for higher excitation fractions.<sup>[96]</sup> While the product itself is only metastable at room temperature, it needs to be verified that the sample is still reversible at cryogenic temperatures. Especially the longer-lived byproduct, found in the transient absorption measurements and with an absorption maximum around 425 nm, needs to be considered. While it does not appear to affect the reversibility at temperatures above 200 K, reducing the temperature further may lead to accumulation of this species and rapid crystal damage. Nonetheless, both of these potential causes of irreversibility can be overcome in principle by applying synchronized (or continuous-wave) photoreversion at the appropriate wavelengths, i.e. 575 nm for the merocyanine form and 425 nm for the byproduct.<sup>22</sup>

---

<sup>20</sup>See for instance refs. [53, 55].

<sup>21</sup>As noted above, the calculated excitation fraction can only be viewed as an upper limit and thus a value of 5 % for a fluence of  $3.4 \text{ mJcm}^{-2}$  is more reasonable than the calculated 10 %. Most of the experiments were carried out at even lower fluences (*vide supra*) to avoid sample damage.

<sup>22</sup>The byproduct may also be photoreverted by using 400 nm for convenience if using a Ti:Sa laser system. However, it remains to be tested whether photoexcitation of the byproduct leads to ring-closing and if so, how efficiently.

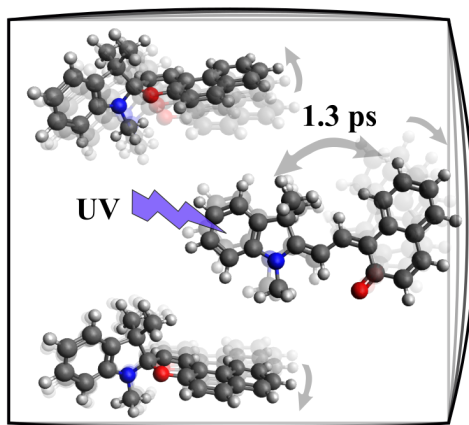


**Figure 3.24:** Summary of the findings for the photoisomerization dynamics of spiroanthopyran in crystal. The planar merocyanine form is created via the same mechanism as in solution, within 1.3 ps after excitation. Formation of the MC form leads to significant lattice deformation, observable in the UED experiments. Restoring forces from the crystal lattice lead to the decreased stability of the MC form, which is reverted back to the closed-ring form with a time constant of 650 ps.

### 3.5 Summary and Outlook

About 30 years after the first reported transient absorption experiments on spiropyrans, their complex photoisomerization dynamics still warrant investigation and novel insights can be gained by systematic studies and their careful evaluation. Together with state-of-the-art numerical simulations, it was possible to clarify the (seemingly) contradictory interpretations in the reported literature inferring reaction times of  $\approx 1$  ps vs. 28 ps. Indeed, neither claim turned out to be false, merely two different viewpoints on the reaction process. The ring opening was found to occur within 300 fs followed by planarization of the molecule resulting in an effective photoisomerization time constant of 1.2 ps. While this confirms the findings by Ernsting, relaxation of the merocyanine form towards equilibrium via vibrational cooling was observed and characterized on a longer time scale, more in line with the findings of Rini et al. Furthermore, it was shown how specific interactions with the solvent, especially the formation of hydrogen bonds, can affect the spectral dynamics and need to be considered in this type of experiments.

The most striking finding in this chapter certainly is the high similarity of the reaction dynamics between solution and crystal. Not only have clear indications been found that the merocyanine form can be photochemically created in the crystalline state, but also the reaction dynamics are virtually unaffected by confinements of the lattice. The latter does however strongly affect the longevity of the product causing its decay within approximately one nanosecond. This system thus represents an example of how electronic excitation can create a strong mechanical force able to distort the crystal far out of equilib-

rium before the molecules are pushed back into the more compact closed-ring isomer by restoring forces. While the crystal shows signs of byproduct formation as well as strain in the transient absorption data, it remarkably remains intact under the given excitation conditions ( $\approx 5\%$  excitation fraction). Formation of the byproduct was tentatively concluded to occur from the open-ring excited-state intermediate, which suggests – together with its absorption maximum being in the visible – that the byproduct is a non-planar, open-ring isomer. It was found to be reverted thermally at the tested temperatures between 250 and 298 K, since its formation did not affect the reversibility of the experiments, even at 100 Hz repetition rate.

The lattice distortion induced by the product formation was corroborated in preliminary time-resolved electron diffraction experiments. While in these experiments, the isomerization was witnessed indirectly via its effects on the crystal lattice, the goal of atomically resolving the photoisomerization reaction itself still remains as a target for future projects.

# Isomerization Dynamics of pH-gated Spiropyrans

Protonation of spiropyran derivatives with a strong acid leads to the formation of new thermally stable isomers with distinct spectral properties and a photochromic switching cycle, different from the behavior investigated in the previous chapter. In the following chapter, the photoswitching dynamics of protonated spiropyrans entailing bidirectional Z-E-isomerization are investigated, analyzed and discussed.

## 4.1 Acidochromism in Spiropyrans

In addition to their extensively studied and applied photochromic properties, most spiropyrans undergo an acidochromic reaction in solution, manifesting in a distinct color change upon addition of a sufficiently strong acid.<sup>[141,142,149,150]</sup> Beyond the general interest in such systems for pH-sensing or detection of acidic vapours,<sup>[180–183]</sup> the combination of photo- and acidochromism gives rise to a variety of possible applications as multi-responsive molecular switches in polymers,<sup>[182–184]</sup> surfactants,<sup>[185,186]</sup> smart materials,<sup>[153,187–192]</sup> and biological systems,<sup>[193,194]</sup> as well as photoacids for light-controlled proton transfer and pH-tuning.<sup>[195–200]</sup>

As discussed in the previous chapter, at thermal equilibrium spiropyrans reside in their closed-ring spiro-form and undergo ring opening and planarization upon light irradiation

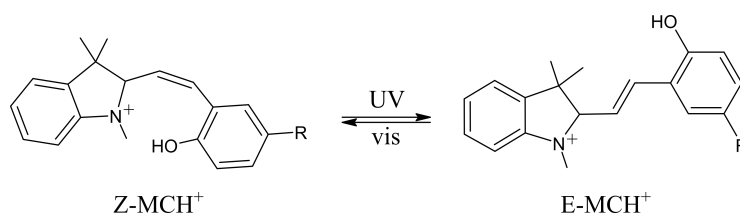


**Figure 4.1:** Z-E-Photoisomerization of protonated spiropyran in the presence of a strong acid. The non-planar, open-ring Z-MCH<sup>+</sup> form can be isomerized to its planar isomer E-MCH<sup>+</sup> via excitation in the UV. The reaction is reversible by visible light irradiation.

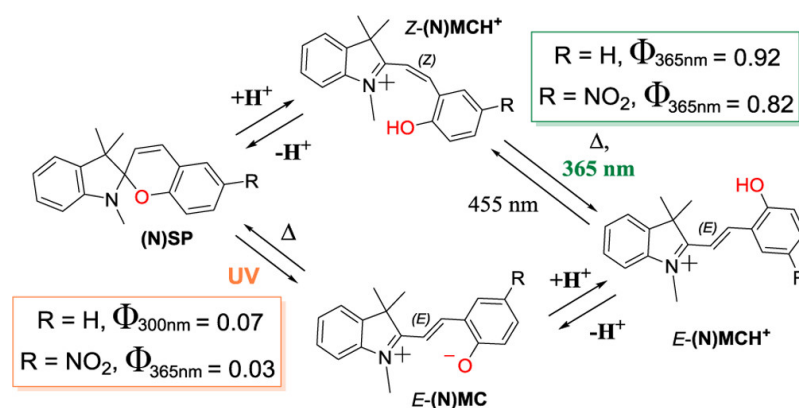


**Figure 4.2:** Photo-acidochromic switching cycle of spiropyran in presence of a strong acid, as deduced by Kortekaas et al. Adapted from [151], licensed under CC-BY-NC-ND.

in the ultraviolet, giving rise to an absorption band in the visible. Alternatively, ring opening of spiropyran can be induced through the addition of a sufficiently strong acid to the solution yielding an open-ring form with a protonated phenoxy group. This form has several stable isomers, that can be distinguished from the non-protonated merocyanine and each other by their absorption properties.<sup>[151]</sup> Early studies of this mechanism in spirobenzopyrans (BIPS) proposed the involvement of a protonated closed-ring transition state via bond formation between the added proton and the oxygen in the pyran moiety leading to rupture of the oxygen-spiro-carbon bond and the formation of an open-ring, but non-planar cis-merocyanine ( $Z\text{-MCH}^+$ ).<sup>[150,201,202]</sup> This metastable isomer was concluded to be in thermal equilibrium with the planar trans-merocyanine ( $E\text{-MCH}^+$ ).<sup>[150,201]</sup> In analogy to a previously published study of protonated merocyanine dyes not derived from spiropyrans,<sup>[203]</sup> Shiozaki et al. additionally indicated the possibility to yield the planar  $E\text{-MCH}^+$  via UV irradiation of the  $Z$ -isomer, based on molecular orbital calculations complemented with spectroscopic results.<sup>[202]</sup> They postulated the initial protonation to occur at the oxygen atom rather than the nitrogen atom of the indoline moiety or, as proposed elsewhere,<sup>[204]</sup> a transient, open-ring intermediate species.

Despite the general consistency of these studies, during an investigation of a spiropyran functionalized polymer Fissi et al. assumed a different photoswitching mechanism, in which light irradiation of the protonated merocyanine form yields an N-protonated form of the closed-ring spiropyran ( $\text{SPH}^+$ ), in thermal equilibrium with the non-protonated spiro-form.<sup>[205]</sup> Such an equilibrium was also proposed by Wojtyk et al. when investigating the nitro-substituted BIPS analog, but with the formation of the N-protonated  $\text{SPH}^+$  in competition to the acidochromic formation of  $E\text{-MCH}^+$ .<sup>[206]</sup> Raymo and Giordani adopted the idea of being able to switch from the protonated merocyanine form directly to the non-protonated closed-ring form by visible light irradiation, presumably via the N-protonated  $\text{SPH}^+$ ,<sup>[187,188]</sup> and other subsequent studies based their interpretation on this proposed mechanism.<sup>[180,181]</sup> Notably, in none of these reports, formation of the non-planar  $Z\text{-MCH}^+$  isomer was discussed. It was only approximately ten years after

the first mechanistic studies, that the latter idea was taken up once more in an investigation of the photoisomerization of protonated BIPS in the gas phase.<sup>[207]</sup> The possibility of an N-protonated SPH<sup>+</sup> closed-ring isomer formed from Z-MCH<sup>+</sup> via collisions was still considered but its assignment uncertain. In more recent studies, the hypothesis of an involvement of SPH<sup>+</sup> in the photoswitching cycles became less prominent,<sup>[182]</sup> or was no longer considered altogether,<sup>[189]</sup> with the mechanistic interpretations being more in line with the initial studies. However, the amount of contradictory interpretations present in the literature still warranted clarification.

In 2018, Kortekaas et al. published a comprehensive investigation of the photoswitching cycle of BIPS and Nitro-BIPS in various acids based on optical and NMR spectroscopy as well as theoretical calculations.<sup>[151]</sup> Largely in agreement with Shiozaki et al., they found evidence that addition of a strong acid led to the formation of Z-MCH<sup>+</sup>, presumably via the protonated closed-ring form as a non-observable intermediate or transition state. Irradiation of the Z-isomer with UV light yielded the planar isomer, which was also obtainable via direct protonation of the open-ring merocyanine. Since the latter itself could be created via UV irradiation of the non-protonated spiro-form, it was possible to describe a full photo-acidochromic switching cycle between these species (see Fig. 4.2). In addition to elucidating this mechanism, the influence of the p*K*<sub>a</sub> values of the utilized acids was investigated. It was found that when choosing an acid with an appropriate p*K*<sub>a</sub> value between those of the E- and Z-isomers of MCH<sup>+</sup> (in case of BIPS phosphoric acid), a photo-controlled protonation and deprotonation mechanism was accessible (see Fig. 4.3). This was because only one of the protonated isomers was stable under these conditions, while the other would become deprotonated after creation via irradiation and subsequently react back to the closed-ring form. Manipulating the p*K*<sub>a</sub> of the two different forms can thus enable tailored, photo-activated photoacids in specific environments,<sup>[142]</sup> or in turn allow for pH-switching of material properties via chemical functionalization with a spiropyran compound as a photoswitchable proton-acceptor.

However, while some of the more recent studies adopted the mechanism deduced by Kortekaas et al.,<sup>[191,200]</sup> these insights were not or only to a limited extent taken into account in most of them.<sup>[184,186,192,198,199]</sup> Furthermore, in contrast to the well-studied photochromic reaction in non-acidic environments, no reported time-resolved experiments of the pH-gated photochromism exist, despite the potential to provide further clarification regarding the switching mechanism and the species involved. Only one time-resolved study was reported very recently, but dealt with the use of different MCH<sup>+</sup> derivatives as a photoacid via excited-state proton transfer in a protic solvent and the possibility of a photoinduced isomerization reaction as a competing channel was not discussed.<sup>[199]</sup>

Thus, in order to elucidate the E/Z-isomerization mechanism regarding their time scales and possible intermediate species and to further consolidate or – if applicable – extend the mechanistic picture proposed by Kortekaas et al., transient absorption experiments of the same two spiropyrans (BIPS and Nitro-BIPS) were carried out investigating both

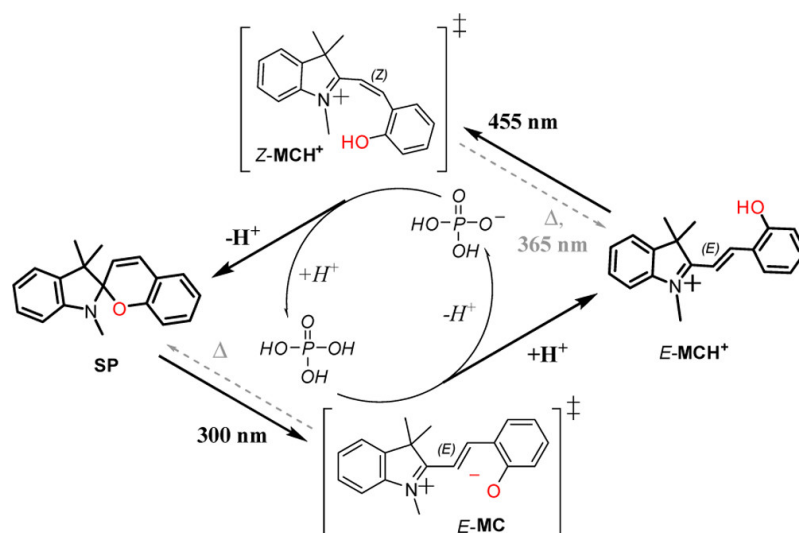


**Figure 4.3:** Light-induced protonation cycle of BIPS in  $\text{H}_3\text{PO}_4$ . Adapted from [151], licensed under CC-BY-NC-ND.

isomerization pathways by use of the respective excitation wavelengths. In addition, the  $\text{p}K_{\text{a}}$ -specific de- and re-protonation cycle proposed in their study was tested by comparison of the transient absorption data of BIPS in a phosphoric acid solution to the non-acidic case. In order to avoid the influence from proton-transfer to the solvent, especially from molecules in the excited state, the aprotic solvent acetonitrile was used for all experiments presented in this chapter. As will be demonstrated by aid of an extensive analysis, the results are in line with the proposed mechanisms in either case, and not only provide further proof, but also additional insight in the reaction dynamics and relevant intermediates involved in the switching process.

## 4.2 Solution Preparation and Steady-State Absorption

The chemicals used for preparation of the solutions were purchased from TCI Chemicals, Japan and use without further purification.<sup>[168]</sup> 1.5 mM solutions of spirobenzopyran<sup>1</sup> (BIPS) as well as nitrospirobenzopyran<sup>2</sup> (Nitro-BIPS) in acetonitrile (spectroscopy grade) were prepared and used in all experiments in this chapter. For protonation of the spiroyrans, 98 % sulfuric acid ( $\text{H}_2\text{SO}_4$ ) was added to the sample solutions in equimolar quantity. Steady-state absorption spectra of these solutions before and after addition of the acid as well as the spectral changes upon UV light irradiation were recorded using a commercial spectrophotometer,<sup>3</sup> and are shown in Fig. 4.4. For irradiation, a UV LED lamp was used with an emission wavelength of 365 nm.

Like in case of the closely related spironaphthopyran, dealt with in the previous chapter, the closed-ring spiro-forms of BIPS and Nitro-BIPS only absorb in the ultraviolet with

<sup>1</sup> 1',3',3'-Trimethylspiro-[2H-1-benzopyran-2,2'-indoline].

<sup>2</sup> 6-nitro-1',3',3'-trimethylspiro[2H-1-benzopyran-2,2'-indoline].

<sup>3</sup> UV-VIS spectrophotometer by Shimadzu [208].

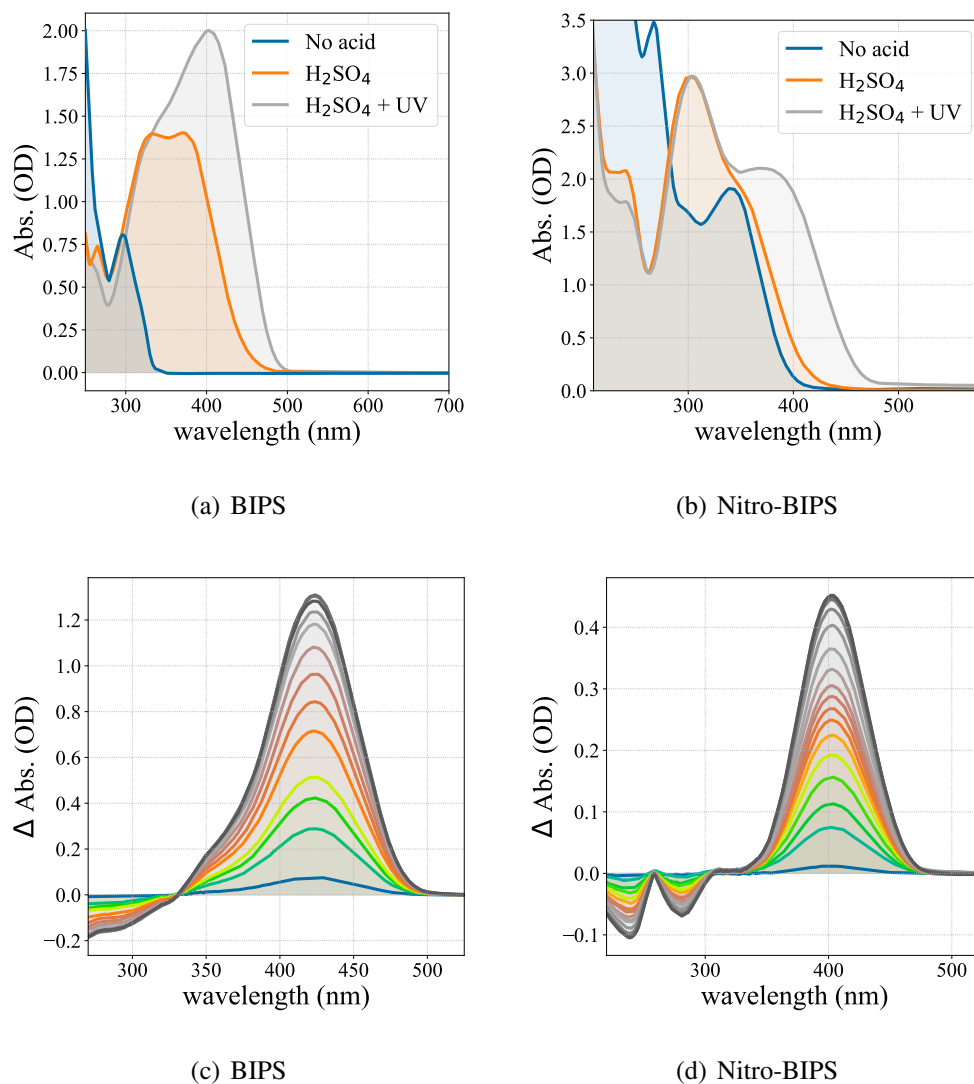


**Figure 4.4:** Steady-state absorption spectra of BIPS and Nitro-BIPS in an acetonitrile solution of  $\text{H}_2\text{SO}_4$ . Figs. (a) and (b) show the respective spiropyran absorption spectra before and after addition of the acid, as well as the photostationary state (PSS) after UV irradiation. Formation of the PSS was monitored and is shown as differential absorption spectra for both derivatives in Figs. (c) and (d), respectively.

absorption edges around 320 nm and 370 nm (see Figs. 4.4(a) and (b), respectively). As previously reported,<sup>[151]</sup> addition of a strong acid such as  $\text{H}_2\text{SO}_4$  gives rise to an absorption band that is red-shifted with respect to the absorption edge of the native species and extends into the visible. Thus, protonation is observable by eye as the initially colorless solutions turn yellow. In either case, the increase in absorption in the near-UV and visible is accompanied by a decrease in UV absorption below 300 nm. Additionally, absorption spectra of the sample solutions in the photostationary state upon 365 nm light irradiation are shown (grey curves). However, they are more easily characterized by taking the difference spectra between the PSS and thermal equilibrium, shown in Figs. 4.4 (c) and (d). For both BIPS and Nitro-BIPS a positive difference absorption band with respective maxima

at  $\approx 425$  nm and  $\approx 400$  nm can be discerned, whose amplitude increases with irradiation time until the photostationary state (PSS) is reached. Isosbestic points, where the absorption shows no significant changes and below which the difference absorption spectrum in the PSS becomes negative are found at 331 nm in case of BIPS and 305 nm in case of its nitro-substituted form.<sup>4</sup>

Since the steady-state properties of these molecules in their protonated forms and in the PSS during UV light irradiation have been investigated extensively, the main purpose of these measurements was to reproduce the previously reported data, which can be readily verified (see ref. [151]). Accordingly, the spectra at thermal equilibrium can be ascribed to the open-ring, but non-planar Z-isomers of MCH<sup>+</sup> (BIPS) and Nitro-MCH<sup>+</sup> (Nitro-BIPS), respectively, while the photostationary state consists of a mixture of both the Z- and the corresponding planar E-isomers. Similarly to the non-protonated case, absorption maxima of the planar forms are shifted towards longer wavelengths compared to the non-planar forms.

The difference absorption spectra indicate which signals to expect in the transient absorption experiments. When exciting the sample solution in thermal equilibrium with a UV laser, a long-lived product absorption band should be formed around 425 nm for BIPS and around 400 nm for Nitro-BIPS. Consequently, upon visible excitation of the sample solution in the photostationary state, corresponding ground state bleach signals in these spectral regions are to be expected. Furthermore, the non-zero difference spectra at shorter wavelengths motivate conducting complementary transient UV absorption experiments, even though the difference in absorption in the attainable wavelength range above 250 nm is significantly smaller than in the visible.

### 4.3 Z-to-E-Isomerization Dynamics

The experimental findings dealt with in this section are summarized in a graphical representation in Fig. 4.5, which is meant to provide visual guidance throughout the presentation, analysis and discussion of the results. It will be rationalized in the course of the section, how the depicted model was deduced and how the involved states, transitions and population transfer times are reflected in the measured transient absorption data. The most important insights culminating in this picture resulted from an observed biexponential progression of the E-isomer formation. As will be argued in the discussion of the analysis, this observation could only conclusively be explained by the involvement of two different reaction intermediates, formed from a rapidly decaying excited-state species.

---

<sup>4</sup>In case of the Nitro-BIPS, around 257 nm, another point where there is little difference in absorption appears to exist, but closer inspection revealed that there is a slight decrease in absorption in the PSS relative to the thermal equilibrium.

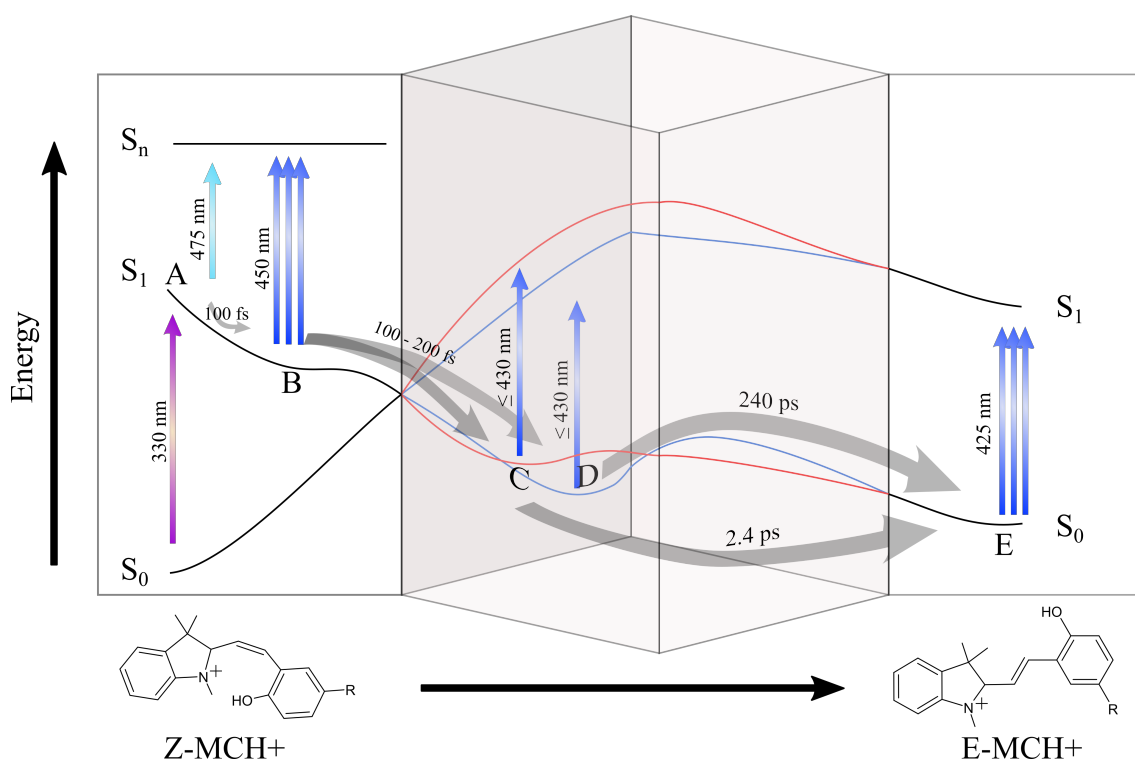


**Figure 4.5:** Summary of the Z-to-E-isomerization dynamics of protonated, open-ring spiropyran, based on the experiments presented in this section, and shown representatively for  $\text{MCH}^+$ .

### 4.3.1 Experimental details

For the transient absorption experiments, the home-built setup described in section 2.4.2 was used in the flow-cell based solution configuration. Since both isomers had been reported to be thermally stable at room temperature, reversion of the accumulated photoproduct was ensured by continuous illumination of the solution reservoir with a conventional visible lamp. The molecules were excited at a repetition rate of 500 Hz using the broadband UV laser pulses with a central wavelength of  $\approx 330\text{ nm}$ , obtained via sum-frequency mixing of a visible NOPA and the fundamental output from the Ti:Sa laser (see section 2.3.2), and probed with the visible super-continuum beam covering time delays up to one nanosecond. Since the high repetition rate and improved signal-to-noise ratio from the implemented probe referencing allowed for fast data acquisition, it was feasible to record entire scansets at multiple fluences. The scans selected for analysis and presented here were acquired using fluences of  $2.4\text{ mJcm}^{-2}$  for BIPS and  $1.7\text{ mJcm}^{-2}$  for Nitro-BIPS,<sup>5</sup> while the remaining scans were used to ensure the selected fluences were within the linear absorption regime (see section A.3 in the appendix).

<sup>5</sup>These fluences correspond to excitation fractions of 4% and 3%, respectively (see section A.2.2 in the appendix).

### 4.3.2 Results and analysis

#### Observations

Transient absorption maps of photoexcited, protonated BIPS ( $\text{MCH}^+$ ) as well as selected spectral traces are depicted in Fig. 4.6. Upon excitation, after  $\approx 100$  fs a broad, asymmetric absorption feature appears with a maximum between 450 and 500 nm, an extended tail towards the infrared and a comparatively steep edge towards the ultraviolet, crossing 0 mOD around 400 nm. Subsequently, this spectrum continuously narrows, becoming more symmetric. Simultaneously, the maximum differential absorbance increases at first, reaching 12 mOD at 300 fs, before it starts to decay towards a local minimum of  $\approx 8$  mOD at a time delay of 700 fs. This spectral evolution is complicated further by a gradual shift of the maximum position from the initial value of  $\approx 475$  nm to  $\approx 430$  nm. From the local minimum, the absorption band starts to slowly rise, reaching a constant maximum of  $\approx 30$  mOD around 750 ps. A continuation of the spectral narrowing and the blue-shift of the maximum can still be observed during the earlier part of this rise, both being completed around 20 ps, after which the band only increases in intensity.

The transient absorption data of the nitro-substituted derivative (Fig. 4.7) shows nearly identical sub-ps dynamics with only minor differences in the time scales on the order of 100 fs or less and an overall hypsochromic shift of the absorption bands. Even though the local minimum in differential absorbance is reached around the same time delay of 700 fs, the subsequent rise of the equilibrium absorption band is faster in case of Nitro- $\text{MCH}^+$  compared to  $\text{MCH}^+$ , with the maximum at 200 ps already close to the final value of  $\approx 24$  mOD at 1 ns. Furthermore, an additional shoulder between 450 and 500 nm starts to appear after 20 ps, which is absent in case of  $\text{MCH}^+$ . This feature reaches its maximum around 100 ps before it starts to decay, becoming indistinguishable from the tail of the main absorption band towards the end of the measurement window.

For both molecules, the transient absorption spectra at 1 ns are identical to the respective PSS difference spectra in shape and position (see Fig. 4.4). Thus, for convenience it is sensible to assign these spectra to the photoproduct, which is the planar E-isomer. This hypothesis will be re-evaluated based on the outcome of the analyses described in the following section.

#### Analysis approach

The early dynamics are dominated by a significant blue-shift of the absorption maximum as well as spectral narrowing. In case of the spironaphthopyran photoisomerization dynamics in the previous chapter, where similar phenomena were observed, this was mitigated in the analysis by the fact that the spectral maxima were well separated (by  $\approx 100$  nm) and a significant decay of the initial spectrum accompanied by the rise of the

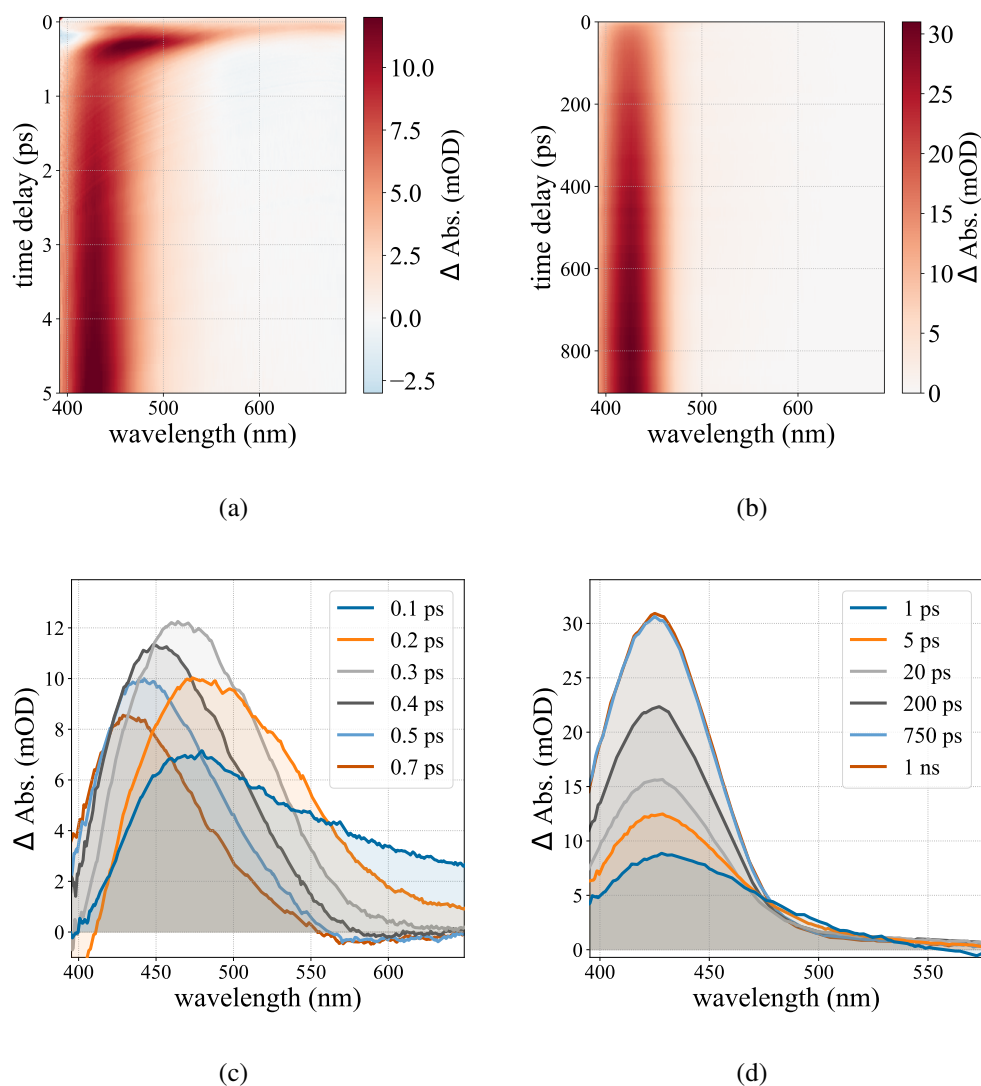


**Figure 4.6:** Transient absorption data of the Z-to-E-isomerization of MCH<sup>+</sup>. Depicted are TA maps for the time range of (a) 5 ps and (b) 900 ps, as well as selected spectral traces up to 1 ns ((c) and (d)).

final spectrum was observed. This enabled the approximation of the sub-5 ps dynamics by exponential decay and rise functions in global and target analysis with only minor artifacts in the obtained results. However, in case of the present data, neither of these conditions are sufficiently met, rendering all matrix-based analysis methods, such as global analysis and SVD, as well as single-point kinetic fits inappropriate for quantitative characterization of the first  $\approx 2$  ps. In principle, the effects of spectral shifts can be eliminated by integration of the band, while the shifts themselves can be described by the spectral center of mass. However, the product absorption bands in either case are not covered entirely by the probe range ( $>390$  nm), especially in case of Nitro-MCH<sup>+</sup> where the maximum lies around 400 nm. Both fits of the integrals and the centroids are therefore expected to yield time constants shorter than the actual dynamics. Instead, the dynamic line shape analysis method (DLSA) was applied, which had originally been developed for the mero-

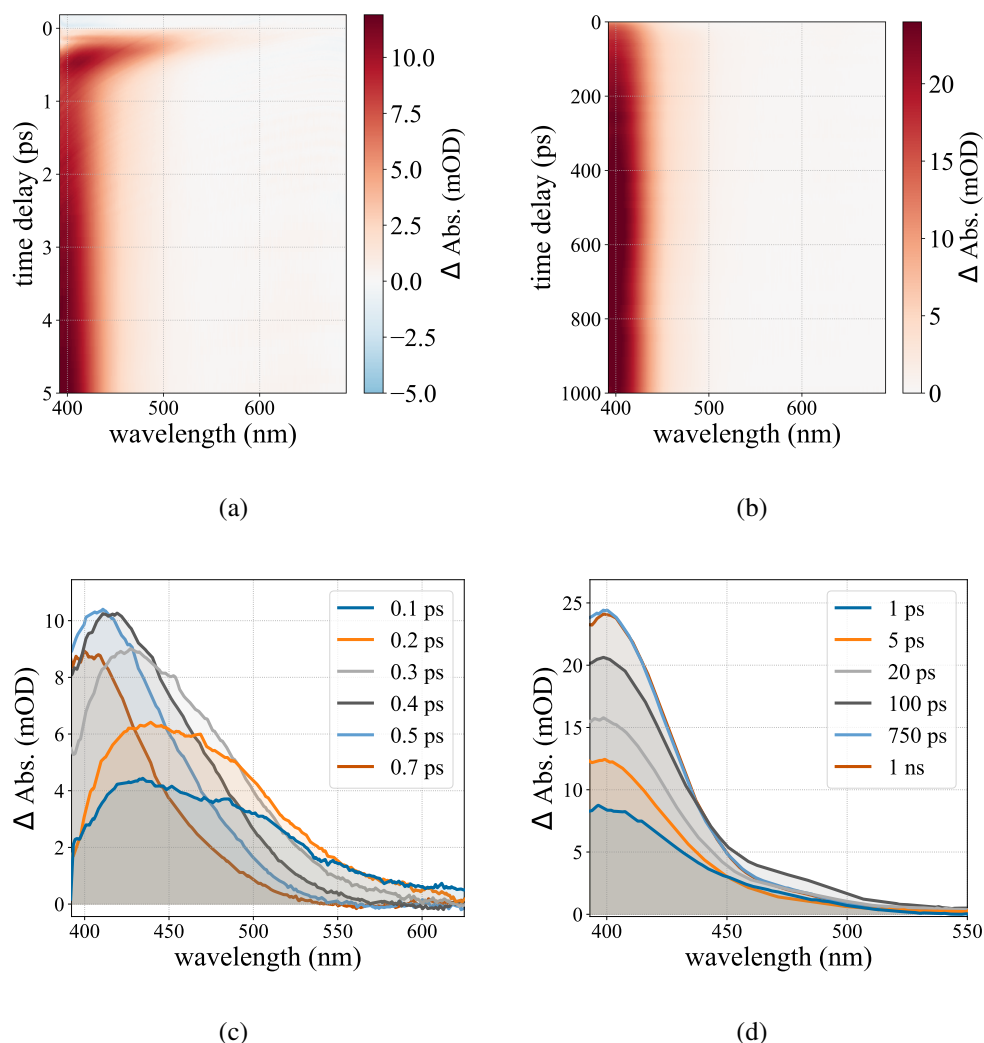


**Figure 4.7:** Transient absorption data of the Z-to-E-isomerization of Nitro-MCH+. TA maps for the time range of (a) 5 ps and (b) 1 ns, as well as selected spectral traces are shown ((c) and (d)).

cyanine equilibration dynamics of photoexcited SNP. These line shape fits do not require the whole spectrum of an absorption band, as long as a clearly defined maximum and at least one absorption edge are distinguishable.

Based on the long-lived product absorption spectra it was determined that neither a pure Gaussian nor a pure Lorentzian line shape function was sufficient, but the aforementioned Voigt profile was required being a convolution of the two distribution functions and the physically more appropriate model.<sup>[120]</sup> In contrast to the case of photoexcited spironaphthopyran, no vibrational fine-structure of the band was observed, which allowed for the use of a single component, mitigating the introduction of an additional line width parameter compared to a Gaussian or Lorentzian curve. Besides a lower bound of zero for the width parameters and an upper bound of  $25300 \text{ cm}^{-1}$  for the center position  $b_1$  to keep the latter within the probe range, no further parameter constraints were introduced. The fits were carried out for time delays between 0.0 and 900 ps, in reverse time steps starting at

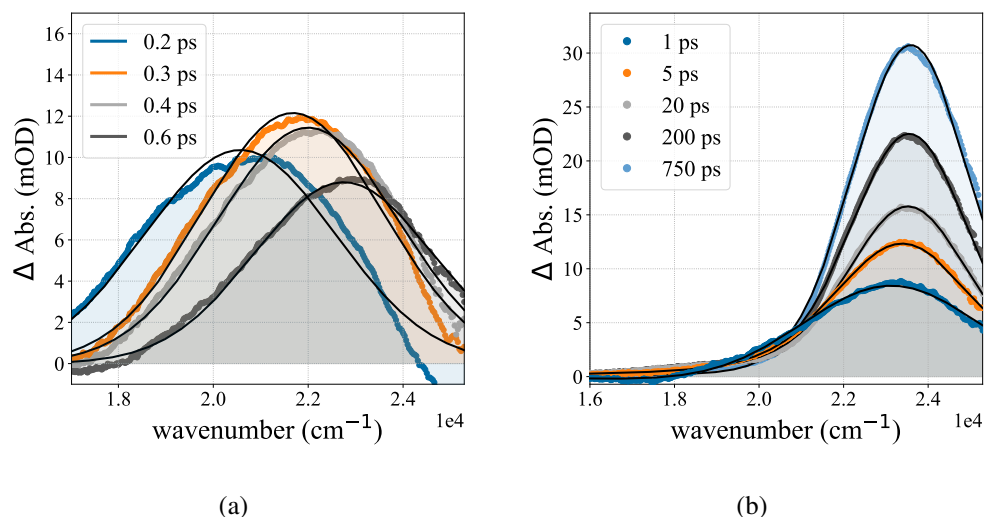


**Figure 4.8:** Spectral traces and fits (black lines) from the dynamic line shape fit of Z-MCH<sup>+</sup>, excited at 330 nm and probed in the visible. The data was fit with a single Voigt profile for each time step.

the latest time point. Due to the observed differences in the ps-dynamics between MCH<sup>+</sup> and its nitro-substituted analog, results of the DLSA will be discussed separately for the two compounds starting with the simpler case of the non-substituted MCH<sup>+</sup>.

#### Dynamic line-shape analysis of Z-MCH<sup>+</sup>

In Fig. 4.8, selected spectral traces from the entire fit range and the corresponding line shape fits are shown, in order to visualize the evolution of the Voigt profiles. A plot of the entire fit range and the residual can be found in Fig. A.18 in the appendix. For time delays less than 100 fs after excitation, the absorption spectra became too broad to be properly fit with a single line shape function and thus, only time delays above were considered for further analysis. As previously noted, the initial absorption band shows a significant asymmetry, leading to a deviation on the higher-energy edge of the spectrum. Since the lower-energy side of the spectrum is fit well by the used line shape function, this is probably not due to an inherent asymmetry of the band but rather to a contribution from a second, negative signal. This second band is most likely a ground-state bleach in accordance with the steady-state absorption spectrum (conf. Fig. 4.4 (c)). However, its influence is only marginal for time delays greater than 500 fs, which prohibits the addition of a second component for the entire fit window, and inspection of the spectral traces and corresponding fits suggests, that the error due to this deviation from a perfectly symmetric shape is only marginal, especially when considering the line integrals.

The parameter traces for the center positions and line widths are depicted in Fig. 4.9. The line widths are the values at half maximum calculated from the Gaussian and Lorentzian parameters  $\sigma$  and  $\gamma$  (see equation 2.39), separate plots of which can be found in the

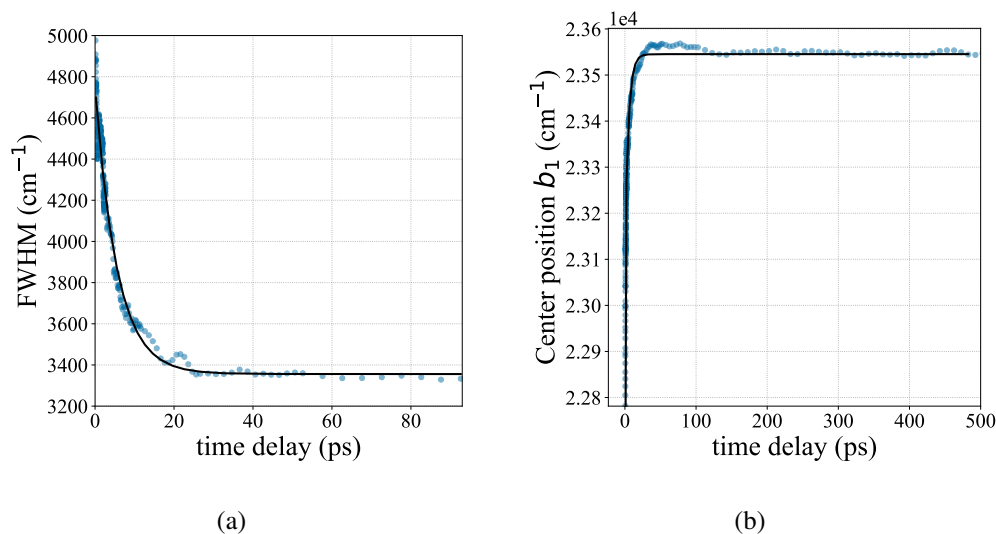


**Figure 4.9:** Parameter traces and fits of (a) FWHM value and (b) center position of the Voigt profile used for the dynamic line shape fit of Z-MCH<sup>+</sup>, excited at 330 nm. The parameter traces were fit between 0.2 and 800 ps with a mono- and a biexponential function, respectively (black lines).

appendix (Fig. A.20). The full-width at half-maximum (FWHM) values exhibit an essentially monoexponential decay within the first 100 ps with a time constant of  $5.6 \pm 0.2$  ps and an amplitude of  $1410 \pm 10$  cm<sup>-1</sup>.<sup>6</sup> Beyond 100 ps, a slight decrease is still observable, but with a much smaller amplitude (around 100 cm<sup>-1</sup> within 700 ps) and a time constant significantly larger than the measurement window. The center positions undergo a biexponential blue-shift with rise constants of  $230 \pm 2$  fs and  $5.8 \pm 0.3$  ps and corresponding amplitudes of  $-4260 \pm 30$  cm<sup>-1</sup> and  $-400 \pm 8$  cm<sup>-1</sup>.<sup>7</sup> The equilibrium center position was determined to be at  $23550 \pm 4$  cm<sup>-1</sup>.

The parameter trace of the Voigt profile amplitude, which due to its normalization is equivalent to the line integral, is depicted in Fig. 4.10. In addition to a mere superposition of exponential functions, various kinetic fit models were tested, out of which the two most relevant are shown in the figure. Both models encompass five species, out of which all but the first were included in the weighted sum to fit the parameter trace.<sup>8</sup> The first model (Figs. (a) and (b)) is a unidirectional sequential model (see equation 2.25) and the second a sequential branched model (equation 4.1):

<sup>6</sup>N.B.: Errors indicated here and throughout the thesis refer to the fit parameter confidence intervals and provide a measure for the goodness of the fit and possible parameter correlations. Quantitative conclusions from these fits have to be made considering the temporal and spectral resolution as well as sensitivity of the setup (see section 2.4.4). The spectral resolution converted to wavenumbers was on the order of 10 cm<sup>-1</sup>.

<sup>7</sup>As can be seen in Fig. 4.9 (b), a small deviation from the biexponential behavior within 100 ps after excitation was observed, whose amplitude was too small in comparison to yield stable fit results. Based on the timescale it is likely associated with the rise of the long-lived band.

<sup>8</sup>The omission of the first species was necessary because the first observable process consisted in a rise in amplitude.

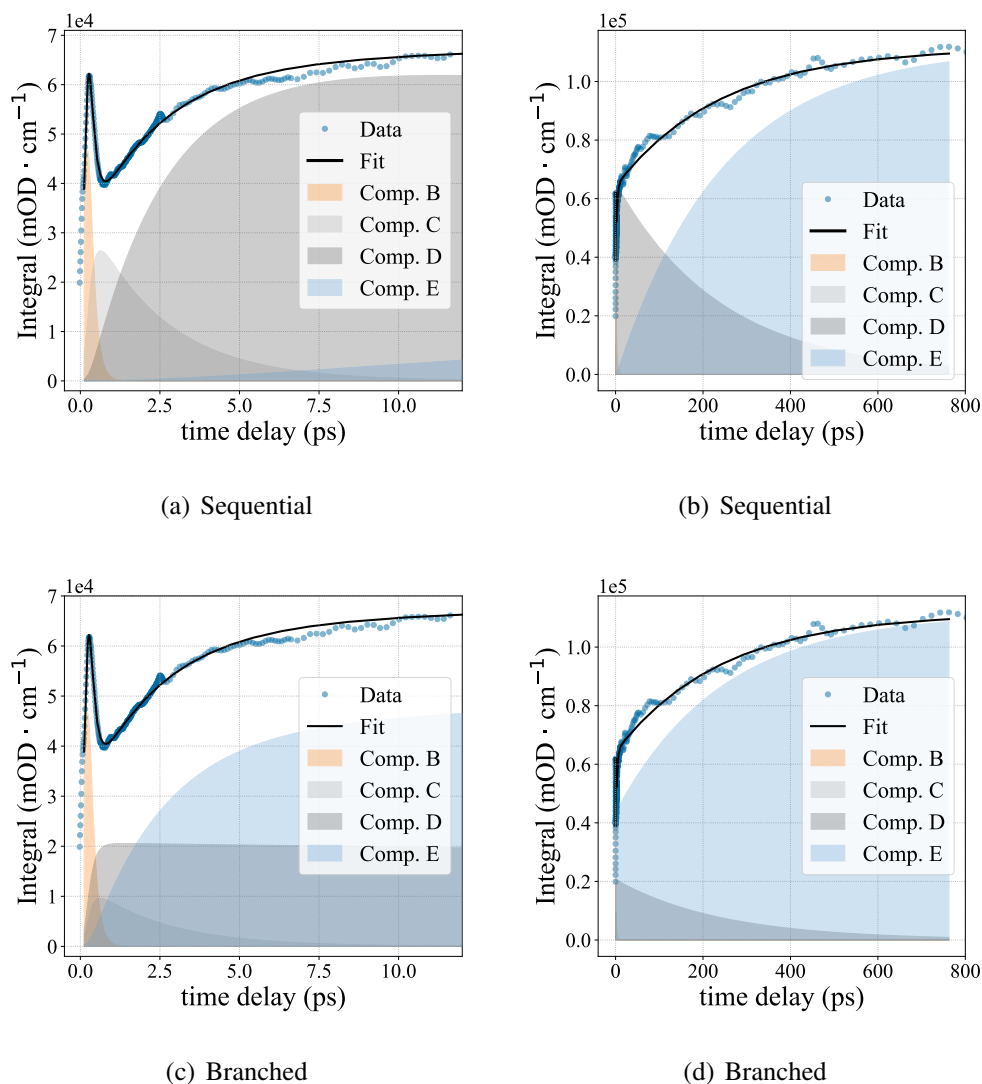
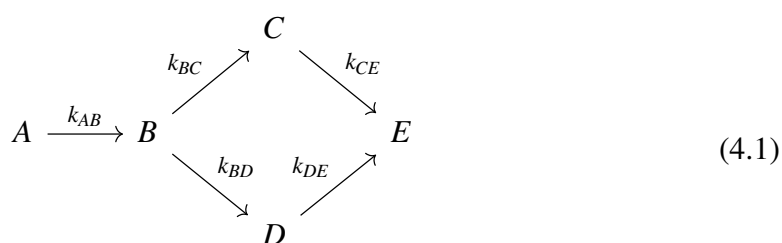


**Figure 4.10:** Voigt profile integral parameter trace from DLSA of Z-MCH<sup>+</sup>, excited at 330 nm and probed in the visible. The parameter trace was fit with a kinetic sequential ((a) and (b)) and a kinetic branched model ((c) and (d), see equation 4.1).



Commonalities between these two kinetic models are the following. Species B is attributed to the absorption band which rises between 100 and 300 fs after excitation and subsequently decays until reaching the local minimum around 700 fs. Species A consequently is a precursor species representing the broad distribution of occupied excited states and molecular configurations immediately after excitation. The decay of species

**Table 4.1:** Time constants from the applied kinetic models for the line integrals from DLSA of photoexcited Z-MCH<sup>+</sup>.  $\tau_D$  indicates the formation rate of species D, i.e.  $\tau_{CD}$  for the unidirectional model and  $\tau_{BD}$  in case of the branched models.

	Unidirectional	Branched	Branched*	Branched**
$\tau_{AB}$ (ps)	$0.07 \pm 0.03$	$0.09 \pm 1.2$	$0.1 \pm 0.1$	$0.12 \pm 0.03$
$\tau_{BC}$ (ps)	$0.12 \pm 0.03$	$0.2 \pm 10^4$	$0.1 \pm 0.4$	$0.12 \pm 0.05$
$\tau_D$ (ps)	$2.4 \pm 0.07$	$0.2 \pm 10^4$	$0.1 \pm 0.2$	$0.17 \pm 0.07$
$\tau_{CE}$ (ps)	–	$2.4 \pm 0.07$	$2.4 \pm 0.07$	$2.4 \pm 0.07$
$\tau_{DE}$ (ps)	$240 \pm 6$	$244 \pm 7$	$244 \pm 7$	$242 \pm 6$

B results in the formation of one or multiple intermediates with absorption coefficients smaller than the one of species B. For simplicity, these intermediates will be referred to as spectrally dark intermediates in the following, even though this is meant only in comparison to species B and E and their absorption coefficients in this spectral range may in fact be finite. The slow rise of the product absorption band, associated with species E, is biexponential, which can be readily verified in a separate fit. The difference between the models lies in the treatment of this biexponential behavior. In case of the unidirectional model, there is only one dark intermediate C, which reacts to species E via another intermediate D. In the branched model on the other hand, the dark intermediate is postulated to consist of two different species C and D, which both react to the product, but with different rate constants.

The obtained time constants for the different models are shown in Tabs. 4.1.<sup>9</sup> In case of the branched kinetic model, high parameter correlation, especially for the decay of species B into C and D, led to large fit parameter confidence intervals. For this reason, in addition to the sum of all species but A, variations were tested where the contribution of either species C (Branched\*) or species D (Branched\*\*) was left out of the sum, significantly reducing the fit error. The applicability of the different models will be discussed together with the other line shape parameters in the following interpretation of the results.

As previously demonstrated for the case of photoexcited spironaphthopyran, the DLSA has the potential to differentiate between reaction dynamics and thermalization, which is indeed possible in the present case of the isomerization dynamics of Z-MCH<sup>+</sup>. The consistent, monoexponential narrowing of the line width with a time constant of 5.6 ps can be attributed to vibrational cooling using the same reasoning as for the case of SNP in section 3.2.2. Albeit faster for MCH<sup>+</sup>, the time scale of several ps is similar to the

<sup>9</sup>The associated amplitudes can be found in Tab. A.3 in the appendix.

13-15 ps found for SNP in the various solvents. The slow component of the biexponential blue-shift of the center position with a time constant of 5.8 ps is thus readily attributed to vibrational cooling.<sup>10</sup> Furthermore, the amplitude of this slow component of  $400\text{ cm}^{-1}$  matches the order of magnitude of the observed hypsochromic shift in case of the SNP reaction in acetonitrile and hexane.

The fast component of this blue-shift on the other hand is an order of magnitude larger while the time constant of 230 fs is faster than typical vibrational cooling times<sup>11</sup> and not reflected in the spectral narrowing. Instead, this component can be attributed to the observed fast spectral shift of the short-lived absorption band, which accompanies its rise and subsequent decay. In terms of the kinetic models, it is associated with the dynamics of the intermediate species B and an indication for significant changes in the electronic structure. For the interpretation of the line integrals (*vide infra*), it is important to note that beyond  $\approx 20$  ps only marginal changes in spectral line width and central wavelength occur. This implies that beyond this point, the biexponential rise of the absorption band can be assigned to the formation of a single chemical species or, hypothetically, a mixture of conformers with nearly identical electronic structure. There are however slight changes in the ratio between the Gaussian and Lorentzian line width parameters on the scale of hundreds of picoseconds, with a slight increase in the Gaussian contribution. While this observation cannot be interpreted unambiguously, a possible explanation are small adjustments of the solvent environment, slightly changing its influence on the absorption spectrum via inhomogeneous broadening. This underlines the advantage that a DLSA fit has over single-point and global fits, since these phenomena will skew the obtained time constants in those methods, while not actually associated with structural dynamics.

As previously stated, the different kinetic fit models of the line integrals treat the early dynamics in the same way, assigning the short-lived absorption band to the second species B in a sequential chain, which is formed with a time constant of  $\approx 100$  fs and subsequently decays to either one or two intermediates with lower absorption coefficients in the respective wavelength range. Based on the time scales it is feasible to assign this species B to the excited state and its formation time to internal conversion from a broader distribution of vibronic configurations created upon excitation into the Franck-Condon state. Its rapid decay as well as the continuous hypsochromic shift of the band implies that there is no or only a small barrier on the excited-state potential energy surface and its energy continuously decreases with respect to higher lying excited states during propagation along the reaction coordinate. The decay constant of this species is suitably described by the unidirectional model and thus a decay time of 120 fs.

The two time constants for the biexponential rise of the product band are identical for all

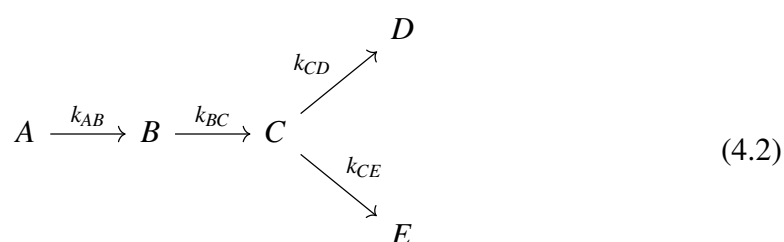
---

<sup>10</sup>As discussed in the previous chapter, vibrational cooling usually entails a blue-shift of the spectrum, since the transition energies increase when lower vibrational levels are populated, unless (higher) excited states are altered simultaneously, as in case of merocyanine in ethanol.

<sup>11</sup>See chapter 3 and e.g. refs. [209, 210].

of the applied models, with values of 2.4 and 240 ps. The fact that the product formation is orders of magnitude slower than the excited state decay indicates that at least one intermediate species must exist. While the unidirectional model results in the best fit in terms of parameter confidence intervals, its general suitability to explain the biexponential rise is questionable. Assuming it is accurate would entail an intermediate species D being formed, whose absorption in the visible is approximately identical in shape and central wavelength to the product but with a transition dipole moment only half the one of the final product. While this possibility cannot be ruled out entirely, it is unlikely that an alternative conformer exists for which all of the above applies, since the distance between the positive charge, predominantly located around the nitrogen of the indoline moiety, and the negative partial charge of the hydroxy group changes significantly when comparing stable conformers such as CTC, TTC and TTT.

An alternative model was tested containing two different E-MCH<sup>+</sup> conformers, in which the excited-state species B also reacts to a single intermediate C is the following:



Assuming species D and E to have near identical spectral properties like in the sequential model, but without relying on a significant difference in transition dipole moments, this model could explain the lack of changes in spectral shape and position beyond 20 ps while the line integral still increases. However, the difference in the two time constants of the biexponential rise of two orders of magnitude causes such a model to effectively describe the rise of both species as monoexponential, because the population of species C is depleted much faster via the 2.4 ps pathway than the slower reaction path. Evidently, this model is not appropriate to account for the biexponential rise of the product absorption band. Thus, the interplay of two different photoproducts with approximately the same transition energies from S<sub>0</sub> to S<sub>1</sub> can be ruled out, either by chemical considerations or applicability of the fit model.

The branched models according to equation 4.1 are therefore the only appropriate among the tested kinetic models. While the high parameter correlation between the time constants and amplitudes of the parallel decay channels of species B impedes their quantitative consideration, the fit residual is not larger than in case of the other models and small compared to the data. Furthermore, the high parameter uncertainty in this model is to be expected due to the temporal coincidence of these decay processes, the large time range covered by the fit in comparison to the time constants in question, the lack of knowledge

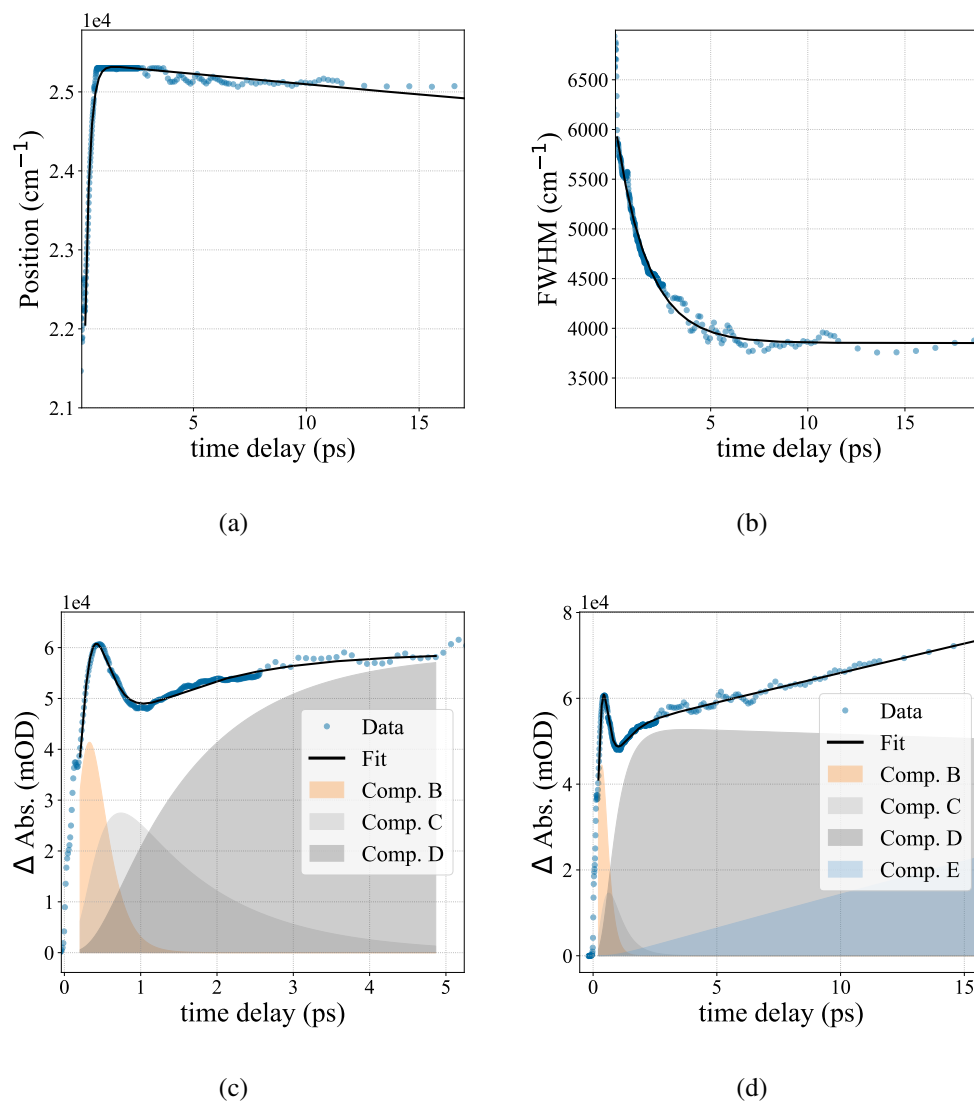


**Figure 4.11:** DLSA results from photoexcited Z-Nitro-MCH<sup>+</sup> transient absorption for the first 20 ps. Parameter traces of the single Voigt profile fits and exponential fits are depicted for (a) center position, (b) FWHM values as well as the Integrals, fit with two different unidirectional models including (c) three steps and (d) four steps.

of the absorption contribution of the two intermediate species C and D, as well as the low dimensionality of the data. This assessment is supported further by the fact that omitting the contribution to the line integral by one of the species, in case of the slower reaction channel via species D, leads to a significant reduction in the parameter confidence interval. Nevertheless, the high uncertainty of the parameter values prohibits the assignment of individual time constants to the formation of species C and D, respectively, and their formation will only be characterized in terms of the decay time of the preceding species.

**Table 4.2:** Time constants  $\tau$  from the kinetic sequential fits of the DLSA line integrals of photoexcited Z-Nitro-MCH<sup>+</sup> using unidirectional chains with three steps (Model I) and four steps (Model II), respectively.

Model	$\tau_{AB}$ (ps)	$\tau_{BC}$ (ps)	$\tau_{CD}$ (ps)	$\tau_{DE}$ (ps)
I	$0.12 \pm 0.07$	$0.16 \pm 0.09$	$2.5 \pm 0.2$	–
II	$0.15 \pm 0.18$	$0.18 \pm 0.23$	$0.51 \pm 0.14$	$300 \pm 800$

### Dynamic line-shape analysis of Z-Nitro-MCH<sup>+</sup>

The rise and decay of a second absorption band on the time scale of a few 100 ps in case of the nitro-substituted MCH<sup>+</sup> complicate a DLSA of the entire transient absorption scan range. The absence of significant spectral shifts in the time range above 10 ps however enable the separate treatment of these dynamics using more conventional methods and thus, a DLSA was carried out only for the first 20 ps.

Fig. 4.11 shows an overview of these results. The parameter traces of (a) center position and (b) FWHM of the Voigt profile are similar to the ones obtained for the non-nitro-substituted merocyanine for time delays below 1-2 ps, with a fast blue-shift in position and narrowing of the line width. While the blue-shift can be fit with an exponential rise function with a time constant of  $200 \pm 3$  fs, the slower rise component present in case of MCH<sup>+</sup> is missing and replaced by a slow red-shift with a time constant significantly larger than the fit window, which can be considered an artifact caused by the beginning rise of the satellite peak. In the time window between 0.74 and 2.8 ps, the center position was fixed at the measurement window, due to the applied boundary condition. While this does not significantly affect the fast rise component, a hypothetical second rise component on the same order as the one found for MCH<sup>+</sup> was impossible to determine. Narrowing of the line width was fit by a monoexponential decay with a time constant of  $1.7 \pm 0.02$  ps, which is notably faster than the 5.6 ps for MCH<sup>+</sup>. It is possible that vibrational cooling indeed occurs faster in case of Nitro-MCH<sup>+</sup> due to increased interaction with the solvent. Furthermore, part of the reason may again lie in the rise of the satellite band, which can not only cause the peak center to shift but also a widening of the Voigt profile, thereby partially masking the band narrowing due to vibrational cooling.

The Voigt profile amplitudes, fit with two different kinetic sequential models are shown in Figs. 4.11 (c) and (d). The first model is a three-step unidirectional chain, applied to the first 5 ps after excitation and including all species except the first one. The second model is identical to the first, except for adding another step at the end and increasing the fit window to 20 ps. The obtained exponential time constants are shown in Tabs. 4.2.<sup>12</sup> As can be seen from the fit of the first model, it adequately describes the first  $\approx 5$  ps, but its

<sup>12</sup>See Tab. A.4 in the appendix for the corresponding amplitudes

monoexponential rise of the final species is not suitable for a fit beyond this point. Thus, the second model was introduced, artificially accounting for the biexponential rise, as in case of  $\text{MCH}^+$ . The obtained time constant for the slow component of the rise not only exceeds the measurement window, leading to a large parameter confidence interval, but also extends well into the regime where the line shape fit validity is compromised by the rise of the satellite band. Since the branched model introduced for  $\text{MCH}^+$  entails the same problems and the inherently higher parameter correlation completely prohibits quantitative results, it was not applied in this case either. Nevertheless, by comparison to the analysis of  $\text{MCH}^+$  the qualitatively identical temporal development of the Voigt integral suggests that the DLSA results for Nitro- $\text{MCH}^+$  can mechanistically be interpreted in the same way, only differing in the time scales. Furthermore, the obtained time constants for the few-ps dynamics are valid as they are unaffected by both the slower component of the product band rise and the additional rise of the satellite band. In analogy to the previous discussion of  $\text{MCH}^+$  they can be assigned to wave packet propagation on the excited-state potential energy surface towards one or more meta-stable intermediate species, from which the product is formed subsequently. This last reaction step as well as the additional ps-dynamics of the satellite band for Nitro- $\text{MCH}^+$  will be discussed further by means of conventional analysis methods in the following section.

### Complementary analyses

Since effects of spectral shifts and narrowing are absent in the dynamics beyond  $\approx 10$  ps for both  $\text{MCH}^+$  and Nitro- $\text{MCH}^+$ , the stated issues of single-point- and matrix-based analysis for the earlier time window do not apply in this case. Thus, in order to complement and add to the DLSA results, global fits of the data in this time range were carried out. Fig. 4.12 shows the results of target and global analysis for both molecules using a three-step, unidirectional kinetic model and a three-component parallel decay, respectively, with the final decay times set to infinity in either case. The corresponding time constants are collated in Tab. 4.3 exhibiting no difference between the respective target and global analysis results, due to their separation of at least an order of magnitude and the simplicity of the spectral dynamics within this time window.

As was pointed out in the discussion of the DLSA results for  $\text{MCH}^+$ , there are some changes in the spectral shape on the time scale of hundreds of picoseconds, which are not linked to population dynamics since they do not manifest in the line integrals. Therefore, the obtained time constants from the DLSA, while deviating from the global fit results, are more reliable for discussion of the chemical dynamics. The global fits of this data are only shown for comparison with the ones for Nitro- $\text{MCH}^+$  for which the DLSA of the dynamics beyond 10 ps was inconclusive.

Since the decay constant of the last component in all cases was set to infinity, the respective SAS and DAS are identical with the equilibrium absorption spectra and thus

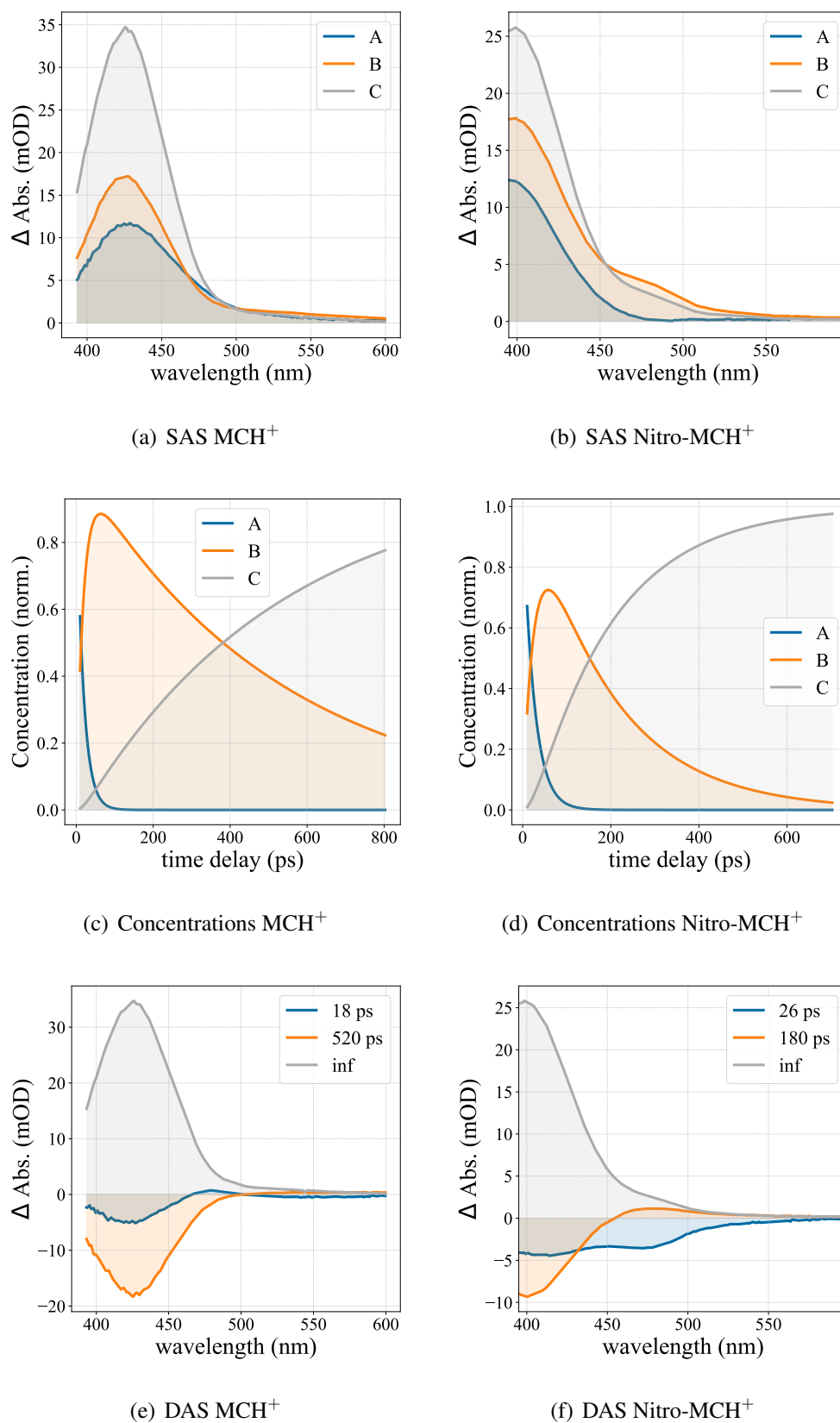


**Figure 4.12:** Global and target analysis of the photoinduced Z-to-E-isomerization of protonated BIPS and Nitro-BIPS. (a) and (b): Species-associated difference spectra of MCH<sup>+</sup> and Nitro-MCH<sup>+</sup>, respectively, using a three-step unidirectional model. (c) and (d): corresponding concentrations. (e) and (f): Decay-associated difference spectra.

**Table 4.3:** Time constants  $\tau$  obtained from global fits of the Z-to-E-isomerization transient absorption data of MCH<sup>+</sup> (BIPS) and Nitro-MCH<sup>+</sup> (Nitro-BIPS) using a three-step unidirectional kinetic model (alphabetical subscripts) and a three-component parallel decay model (numerical subscripts). In either case, the decay constant of the last component was set to infinity.

	$\tau_{AB}$ (ps)	$\tau_{BC}$ (ps)	$\tau_1$ (ps)	$\tau_2$ (ps)
MCH <sup>+</sup>	18.3 ± 0.1	520 ± 1.6	18.3 ± 0.1	520 ± 1.6
Nitro-MCH <sup>+</sup>	25.5 ± 0.2	181 ± 0.7	25.5 ± 0.2	181 ± 0.7

the product absorption of the planar E-isomers. For MCH<sup>+</sup>, the first step with a time constant of 18 ps contains the faster component of the biexponential rise of the product absorption spectrum and a residual contribution from the spectral narrowing observed in the earlier time window. This is corroborated in the decay associated spectrum of the first component, with a negative part between 400 and 450 nm and a small positive part at the absorption edge, which accounts for the narrowing. The second step in the kinetic model and the second component in the parallel model with time constants of 520 ps can be ascribed to the slow component of the biexponential product absorption rise.

In case of the nitro-substituted derivative, the analysis results are qualitatively identical near the maximum of the product absorption around 400 nm but differ in the region between 425 and 550 nm due to the effects of the satellite absorption band. The three species-associated spectra reflect characteristic points of this spectral evolution, but the dynamics are better visualized based on the decay-associated spectra. The rise of the satellite band is reflected in the first DAS, with negative values in the corresponding spectral region and a time constant of 26 ps. The second component with a lifetime of 180 ps consequently accounts for its slow decay, which is not entirely complete at 1 ns as a small shoulder of  $\approx 3$  mOD in the third component remains at this time. Since it is not present in the steady-state absorption spectrum, it can be concluded that its decay continues on a longer time scale.

While the kinetic and parallel models are consistent, the dynamics of the main band and the satellite feature are forced into the same time component due to the methodology. Therefore, independent single-point kinetic fits were carried out in order to confirm or correct the obtained time constants (see Fig. 4.13). The models were selected based on the outcome of the target analysis. Hence, for 400 nm a weighted sum of all three components in a two-step unidirectional chain was used. Since the absorbance at 470 nm was close to zero in the steady-state difference spectrum, which is equivalent to species C in this model, only the first two components were used for the fit at this wavelength.<sup>13</sup> The

<sup>13</sup>A sum of all three components was tested in addition, but resulted in an amplitude of zero for the last component and larger confidence intervals for the other parameters.

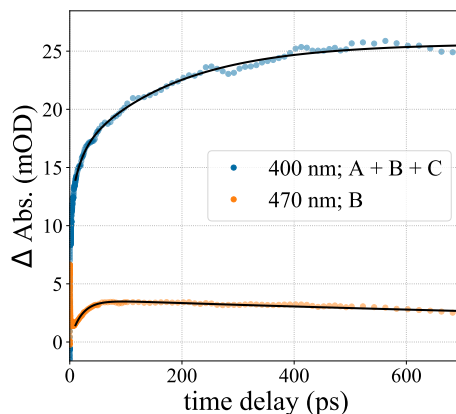


**Figure 4.13:** Single-point kinetic fits of the transient absorption from photoexcited Z-Nitro-MCH<sup>+</sup>. The fit parameters can be found in Tab. 4.4.

**Table 4.4:** Time constants obtained from single-point kinetic fits of the Z-to-E-isomerization transient absorption data of Nitro-MCH<sup>+</sup> (Nitro-BIPS) using a three-step unidirectional kinetic model. In case of 400 nm, the weighted sum of all three species was used for the fit, in case of 470 nm only the first two species.

	$\tau_{AB}$ (ps)	$\tau_{BC}$ (ps)	$a$ (mOD)	$b$ (mOD)	$c$ (mOD)
400 nm	$16.4 \pm 3$	$175 \pm 10$	$11.3 \pm 0.5$	$16.8 \pm 0.4$	$25.7 \pm 0.1$
470 nm	$24.6 \pm 1$	$2200 \pm 100$	$0.54 \pm 0.07$	$3.65 \pm 0.04$	–

obtained time constants are shown in Tab. 4.4.

A comparison of these rate constants to those from the target analysis shows which processes dominate the time scale of the global fit. The rate of the first steps in global fit and single-point fit of 470 nm are in good agreement, while the one at 400 nm has a slightly lower value of  $\approx 16$  ps. This is likely due to residual spectral narrowing of the main band around 400 nm causing an additional increase in maximum absorbance. This was observed in the global fit of the non-nitro-substituted form but is masked in this case by the rise of the satellite feature. The time constant of the second step obtained in the global fits on the other hand is evidently dominated by the rise of the main band with nearly identical time scales. The fact that the final species does not contribute to the kinetic fit at 470 nm and the obtained time constant of  $\approx 2$  ns are in accordance with the postulated continuation of the decay beyond the measurement window.

For MCH<sup>+</sup> without the nitro substituent, a single-point kinetic fit of the maximum absorbance yielded time constant identical to those from global fit, further validating the independent dynamics of the satellite band in Nitro-MCH<sup>+</sup> as a cause for the deviations between global and single-point fits.

### 4.3.3 Concluding discussion

In Fig. 4.14, the schematic representation of the Z-to-E isomerization reaction mechanism of  $\text{MCH}^+$  deduced from analyses above and shown at the beginning of this section is depicted once more for convenience. Following excitation into the Franck-Condon state (A) with an initial absorption maximum around 475 nm, propagation on the  $S_1$  potential energy surface yields an excited-state species (B) with an absorption maximum around 450 nm. An effectively barrierless relaxation, likely via the same or two separate conical intersections leads to the creation of two reaction intermediates C and D, which show no or only little absorbance between 390 and 430 nm and none at longer wavelengths.<sup>14</sup> Both species can be presumed to be in the ground state, since the overall excited-state absorption decays significantly faster ( $\approx 100$ -200 fs) than the following reaction steps. These encompass thermal barrier crossing on the  $S_0$  PES towards the energetically more stable E-isomer, with time constants of 2.4 ps and 240 ps, respectively.

While the identity of these intermediates cannot be determined without the aid of theoretical methods or a structural probe, a few educated propositions can be made. Due to its relatively short lifetime, the intermediate C may be more similar to a transition state than a stable planar isomer, which would explain its lack of absorbance in the visible. On the other hand, the longer-lived intermediate appears to be energetically more stable pointing towards a conformational isomer of the E-form.<sup>15</sup>

In case of Nitro- $\text{MCH}^+$ , the main reaction pathways only differ in the rate constants, with faster barrier crossing times for both intermediates (500 fs and 180 ps). The decay time of species C being even faster suggests an almost barrierless relaxation, further supporting the assignment to a transition-state-like structure. However, it also makes its assignment to a ground-state species less reliable altogether, as the difference between its decay time and the overall excited-state absorption decay becomes less significant.

Clarification regarding the identity of these intermediate species bears further importance for the interpretation of the long-lived satellite band around 470 nm. Its rise time of 25 ps being two orders of magnitude slower than the ESA decay renders a direct formation from the initially populated  $S_1$  (species B) highly unlikely. Thus, the species associated with the satellite band needs to be created from one of the identified intermediates in competition to formation of the E-isomer or an additional intermediate species. The main difference between the photoisomerization dynamics of BIPS and Nitro-BIPS in

---

<sup>14</sup>The apparent lack of absorbance in the visible suggests carrying out transient absorption experiments in the ultraviolet, which indeed was attempted. However, strong scattering signals from the pump obscured the wavelength range above 300 nm and below and no significant signal was found after subtraction. A possible remedy for this would be excitation with a narrower bandwidth pulse and possibly at a shorter wavelength. For the sake of consistency and because analysis of the visible data in itself was conclusive in terms of the reaction dynamics, this was not attempted here, but may be an approach of future studies regarding the identity of the proposed reaction intermediates.

<sup>15</sup>Since the TTT isomer was reported to be the most stable configuration for the protonated merocyanines,<sup>[151]</sup> the CTC or TTC conformers are the most likely for such a metastable configuration.

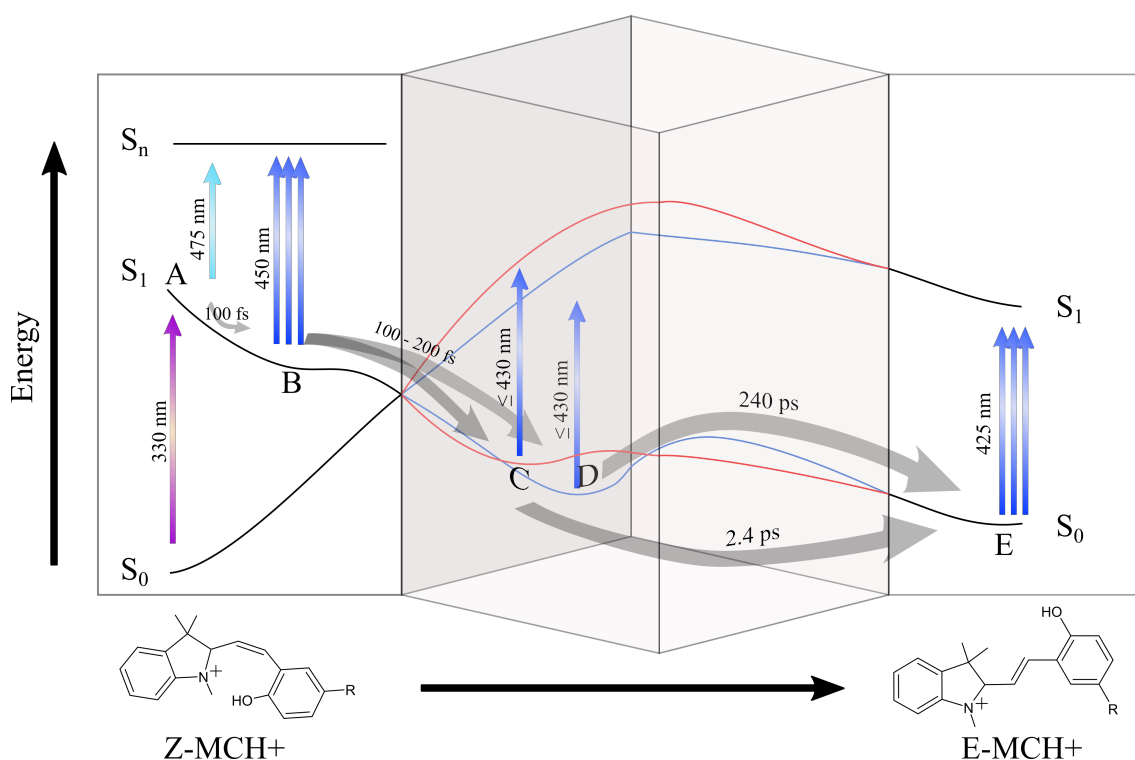


**Figure 4.14:** Schematic energy diagram of the E-to-Z-isomerization of protonated, opening spiropyran. The indicated transfer time constants and absorption wavelengths are based on the analysis of the non-substituted spirobenzopyran. Relaxation of the molecule from the Franck-Condon state (A) towards the E-isomer occurs via a short-lived excited-state intermediate (B) which decays into two distinct intermediates (C and D), presumably in the ground state. Both of these intermediates subsequently react to the product.

their non-protonated forms lies in the involvement of a long-lived excited triplet state for the latter.<sup>[211–213]</sup> Although this immediately suggests an analogous process to occur for the protonated forms, since the number of electrons is independent of protonation, this hypothesis would require intersystem crossing from the  $S_1$ , which due to the aforementioned mismatch in time scales appears unlikely. The more probable explanation thus consists in the formation of a different, reactive ground-state conformer, which due to its bathochromic shift with respect to the other isomers is very likely a planar form, such as TTC or CTC, and reacts to the TTT conformer on the sub-to-few- $\mu\text{s}$  time scale.

To emphasize, an unambiguous assignment of these species by means of transient absorption spectroscopy alone is not possible. Complementary theoretical methods are envisioned to elucidate the identity of the multitude of species apparently involved. Possible endeavors entail an extensive molecular dynamics simulation using the same methodology as conducted for SNP and outlined in the previous chapter. It would suffice to simulate time delays up to 1 ps in order to capture the formation of possible reaction intermediates and their electronic states. Computationally less expensive calculations can be done for static structures to find possible metastable configurations and link them to certain absorption signals either via their excited-state energies or by calculation of their

absorption spectra (see for instance the supporting information of ref. [68]). Furthermore, optimization on the  $S_1$  PES can be carried out analogously to SNP to test if there are any potential excited-state intermediate structures.

## 4.4 E-to-Z-Isomerization Dynamics

This section deals with the photo-isomerization dynamics of protonated spiropyran from the planar E-isomer to the non-planar Z-isomer on the basis of transient absorption experiments exciting at a wavelength of 400 nm. Due to the overlap in absorption between the two isomers in case of the non-nitro-substituted BIPS at this wavelength, the discussion is mostly focused on the nitro-substituted derivative, with only a comparative discussion of the results for the former. Fig. 4.15 shows a summary of the findings presented in the following, which will be revisited and explained in more detail at the end of the section.

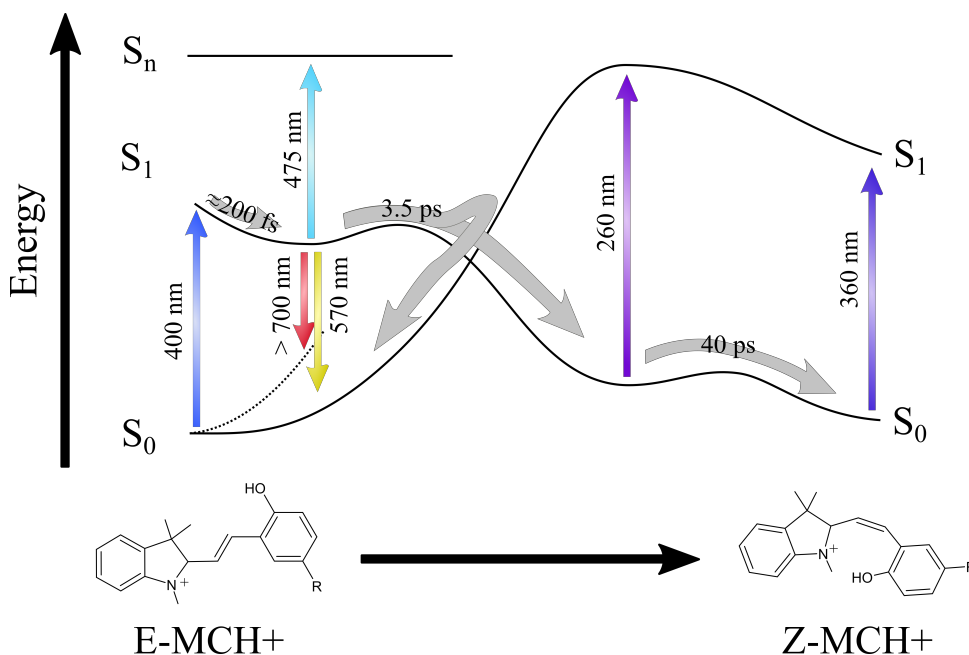


**Figure 4.15:** Summary of the E-to-Z-isomerization of protonated spiropyran on the basis of the conducted experiments. Excitation leads to the creation of an excited-state intermediate, which has a lifetime of 3.5 ps. Subsequent formation of the Z isomer occurs via an unidentified ground-state intermediate with a time constant of 40 ps.

### 4.4.1 Experimental details

The solutions were prepared following the same procedure as previously described in section 4.2. Transient absorption experiments were carried out in the same manner as for the Z-to-E reaction (see 4.3.1), but with an excitation wavelength of 400 nm and instead of irradiating the reservoir with a visible light bulb, a UV LED lamp emitting at 365 nm was

used to create the photostationary state mixtures of the respective E and Z isomers. Since the latter was known to mostly absorb below 390 nm, both the visible (390-700 nm) and the UV supercontinuum (250-350 nm) were used as probe. Several fluences were tested, which were ensured to be in the linear excitation regime by a separate fluence dependence (see Fig. A.8 in the appendix). The data presented in the following was recorded using a peak fluence of  $3.9 \text{ mJcm}^{-2}$  for the visible and  $2.4 \text{ mJcm}^{-2}$  for the UV probing range in case of Nitro-MCH<sup>+</sup> and  $2.4 \text{ mJcm}^{-2}$  in case of MCH<sup>+</sup> in both the visible and the UV.<sup>16</sup>

#### 4.4.2 E-Nitro-MCH<sup>+</sup> TA

##### Observations

The transient visible absorption maps and select spectral traces for E-Nitro-MCH<sup>+</sup> excited at 400 nm are shown in Fig. 4.16. The data essentially consists of four signals; one long-lived negative band around 400 nm and three decaying features, out of which one has a positive amplitude with a maximum at  $\approx 475 \text{ nm}$  and two have negative amplitudes with minima at  $\approx 570 \text{ nm}$  and  $>700 \text{ nm}$ , respectively. While the negative bands decay entirely within  $\approx 10 \text{ ps}$ , a small positive absorption band remains until the end of the measurement window with a maximum of  $\approx 1.7 \text{ mOD}$  at  $480 \text{ nm}$ .

The early dynamics below 400 fs are governed by the formation of the two subsequently decaying bands, while the long-lived signals are mostly covered by the strong positive absorption around  $470 \text{ nm}$ . Notably, the rise of the two main bands is accompanied by a slight hypsochromic shift in both their central wavelengths and position of the edge between them. After reaching their maximum amplitude around 400 fs after excitation, these bands decay continuously within  $\approx 10 \text{ ps}$  making the two long-lived bands increasingly distinguishable. During the decay, no further spectral shifts occur. The spectrum at 15 ps is largely identical with the one at 1 ns, with only a slight decrease in magnitude of the negative band.

The corresponding data using the ultraviolet probe is depicted in Fig. 4.17 in terms of select spectral and kinetic traces. The spectrum at 60 ps exhibits a high similarity to the photostationary-state difference absorption (see Fig. 4.4 in section 4.2), with a positive difference absorption below  $295 \text{ nm}$  with a maximum around  $275 \text{ nm}$ , a local minimum close to 0 mOD at  $255 \text{ nm}$  and a small negative contribution ( $\approx 0.2 \text{ mOD}$ ) above  $295 \text{ nm}$ . The edge of the second difference absorption maximum found in the PSS difference spectrum can be recognized as well. Superimposed with this approximately constant spectrum is a decaying spectrum with qualitatively similar features, but higher overall amplitude and different maximum positions. As this spectrum decays, the maximum of the positive part undergoes a slight red-shift while the minimum of the negative part blue-shifts towards the spectrum at the end of the covered time delay range. The shifts are reflected in the

<sup>16</sup>The fluences for the visible data correspond to excitation fractions of 8 % in both cases. The UV data was recorded exciting 5 % of the molecules (see section A.2.2 in the appendix).

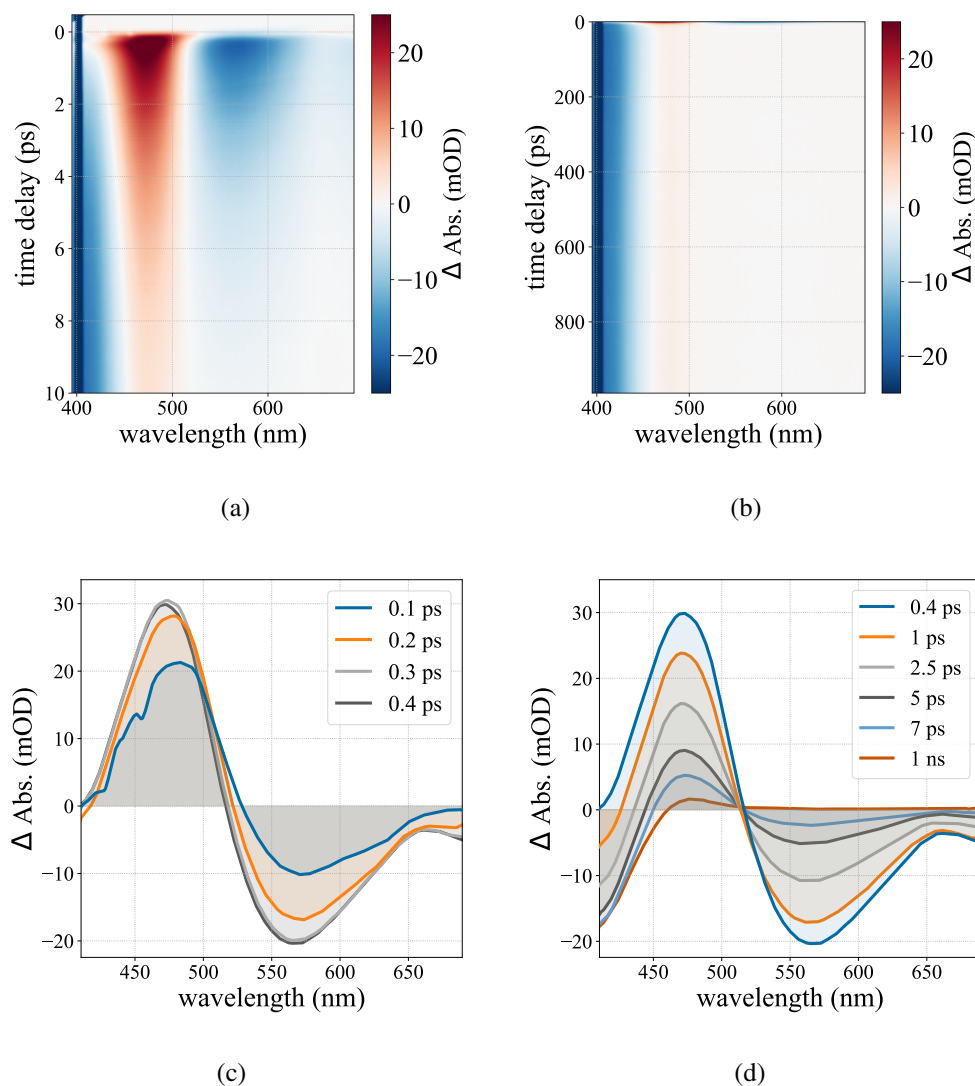


**Figure 4.16:** Transient visible absorption of photoexcited E-Nitro-MCH<sup>+</sup>. TA maps for the time range of (a) 10 ps and (b) 1 ns are shown along with plots of corresponding spectral traces ((c) and (d)).

different temporal behavior of the kinetic traces at different wavelengths within the negative and the positive band (Fig. 4.17 (b)). These observations suggest that the spectrum consists of multiple components with similar absorption characteristics, which will be investigated further in the analysis.

#### Analysis of E-Nitro-MCH<sup>+</sup> TA in the visible

In order to facilitate the following discussion, a preliminary assignment of the transient absorption bands in the visible will be made. Based on the steady-state absorption spectra and their temporal evolution, the long-lived negative band can be attributed to a depletion of the ground-state population of the E-isomer (ground-state bleach, GSB). Since no steady-state absorbance was found for any of the isomers in the region of the other two

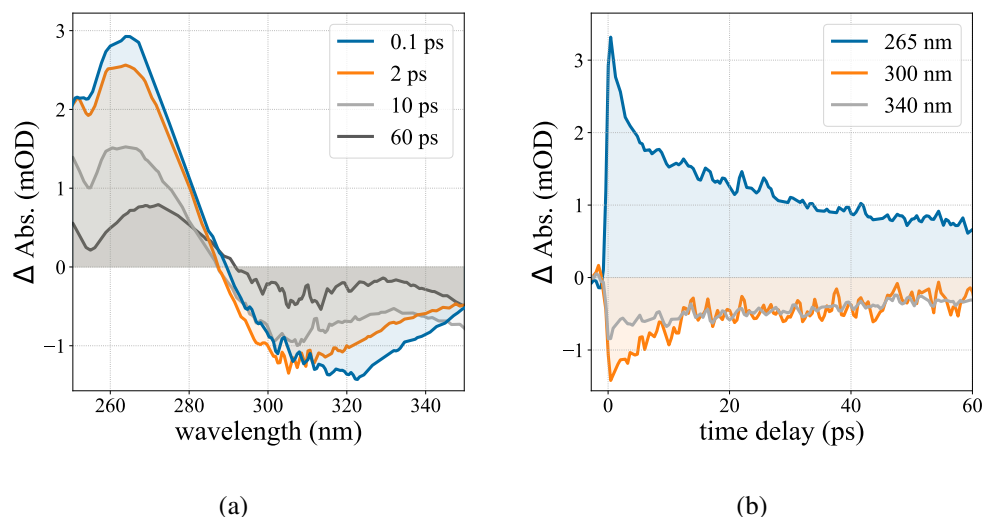


**Figure 4.17:** Transient ultraviolet absorption of photoexcited E-Nitro-MCH<sup>+</sup>, depicted in terms of (a) spectral and (b) kinetic traces.

negative signals and because of their relatively fast decay, a GSB can be ruled out as their origin. Thus, these signals must be due to a radiative decay of excited states and based on their dynamics and intensities can be assigned as stimulated emission bands (SE). The positive decaying band around 475 nm decays approximately with the same lifetime as the SE band centered around 570 nm. This suggests that these two signals are associated with the same excited state. While this correlation needs to and will be verified in the following analysis, a preliminary assignment of the positive band as an excited-state absorption signal (ESA) is justified. As the steady-state spectra do not exhibit any signal corresponding to the long-lived positive band, its assignment is not possible without further analysis. Since besides the comparatively small blue-shift in the first 400 fs, no significant changes in center positions were found, analysis of the data by means of single-point exponential fits and matrix-based methods is feasible. For each of the four main bands, a kinetic trace at or as close as possible to the band maximum was fit with a sum of parallel exponential functions (see Fig. 4.18) and the resulting fit parameters are shown in Tab. 4.5. Unlike the ESA band, the SE bands do not overlap significantly with either of the long-lived absorption bands, making the kinetic trace fit less ambiguous. In both cases, a sum of two exponentials was sufficient to respectively fit the fast rise (100-200 fs) and the subsequent decay ( $\approx 3.5$  ps), with nearly identical time constants. The decay of the ESA band on the other hand was found to be biexponential with the faster component significantly smaller in amplitude (300 fs and 5 mOD) than the slower component (4 ps and 29 mOD). The additional fast component compared to the SE decay inhibited fitting the rise of the ESA band with a third exponential function, since the expected rise time of 100-200 fs was too close to both the fast decay component and the instrument-response-function ( $\approx 100$  fs). Both decay components of the ESA band are reflected in the decay in absorbance at 415 nm, in the region of the GSB. Since depletion of the ground-state population occurs

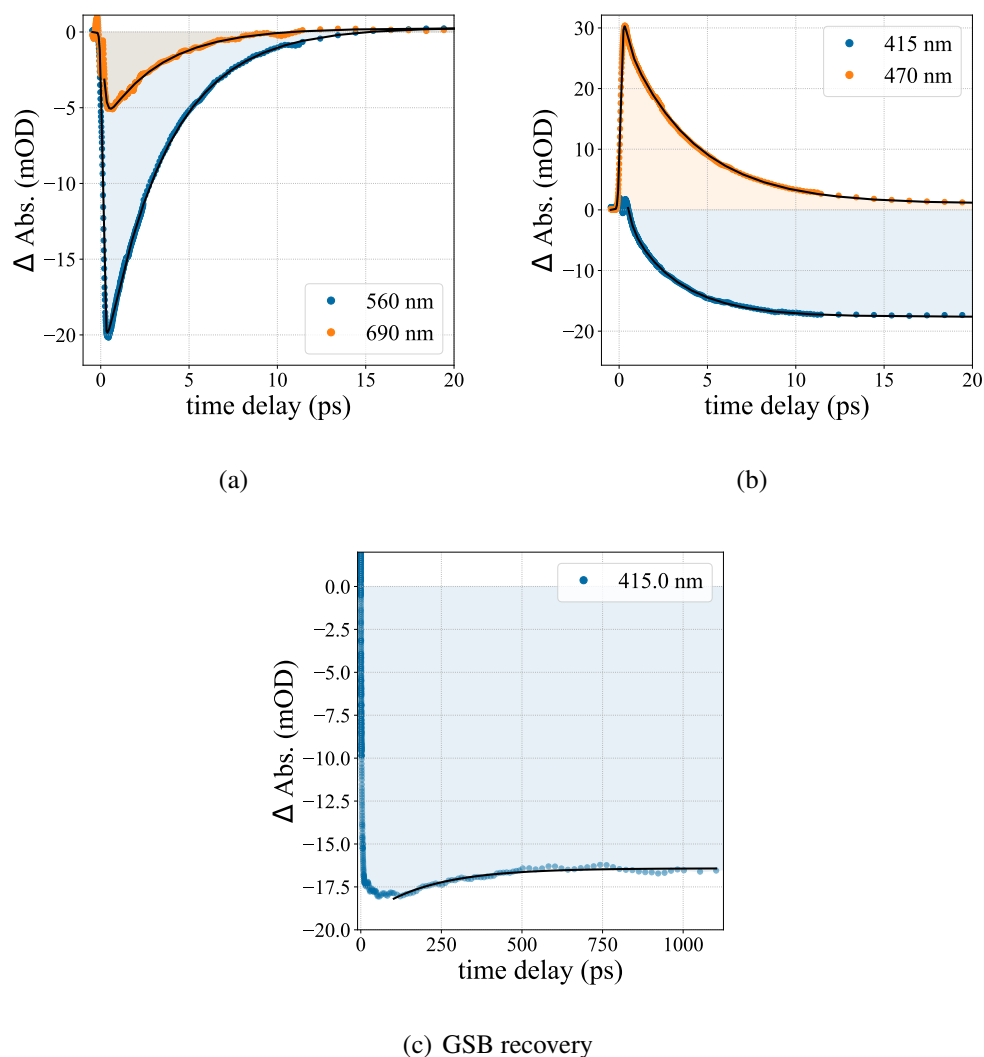


**Figure 4.18:** Single-point kinetic fits of photoexcited E-Nitro-MCH<sup>+</sup> in the visible for selected wavelengths and time domains. The corresponding parameters can be found in Tab. 4.5.

immediately after excitation, this decay can be attributed entirely to the overlapping ESA band. On a longer time scale, the trace at 415 nm shows a slight increase towards an equilibrium value. This time range between 100 ps and 1 ns was fit with a single exponential yielding a time constant of  $190 \pm 15$  ps and an amplitude of  $-3 \pm 0.1$  mOD, which can be understood as a slight recovery of the ground-state E-isomer population. The existence of a potential, faster component of this recovery is possible and could explain the difference in the time constants of the main decays between the traces at 415 nm and 470 nm (3 and 4 ps, respectively). However, due to the band overlap, this component of the bleach recovery cannot be quantified by means of single-point kinetics.

Data decomposition via SVD and global analysis is in principle capable of dealing with these overlapping bands if their dynamics are sufficiently different. The results of the SVD are summarized in Fig. 4.19. The singular values indicate that the first three components are required to reproduce the data and their singular values have a ratio of approxi-

**Table 4.5:** Parameters obtained from single-point kinetic fits of the E-to-Z-isomerization transient absorption data of Nitro-MCH<sup>+</sup> (Nitro-BIPS) using a sum of two exponential functions with time constants  $\tau$  and amplitudes  $A$  as well as an additive constant  $C$ .

wavelength (nm)	$\tau_1$ (ps)	$A_1$ (mOD)	$\tau_2$ (ps)	$A_2$ (mOD)	$C$ (mOD)
415	$0.31 \pm 0.02$	$0.1 \pm 0.02$	$2.9 \pm 0.02$	$10.7 \pm 0.03$	$-17.6 \pm 0.02$
470	$0.33 \pm 0.02$	$5.1 \pm 0.2$	$3.9 \pm 0.03$	$28.6 \pm 0.09$	$0.96 \pm 0.04$
560	$0.18 \pm 0.03$	$2.9 \pm 0.3$	$3.5 \pm 0.04$	$-22.7 \pm 0.1$	$0.31 \pm 0.06$
690	$0.14 \pm 0.01$	$12 \pm 0.7$	$3.3 \pm 0.04$	$-6.6 \pm 0.04$	$0.25 \pm 0.02$

mately 12:4:1. The main component includes the ESA and SE bands with a small negative offset and its temporal evolution exhibits a fast rise and subsequent decay. The second component on the other hand encompasses the two long-lived bands. For early times below 10 ps its left singular vector qualitatively mirrors the one of the first component, but with a finite baseline. The slight recovery of the GSB band on the time scale of  $\approx 100$  ps is reflected in it as well (see Fig. A.21 in the appendix). In the right singular vector of the second component, a small dip between 500 and 550 nm can be distinguished but ascribed to the non-zero baseline of the third component. The latter plays a role mostly around the point of excitation and therefore contains contributions from the cross-phase modulation signal as well as the spectral shift of the first component. Because of this and its low singular value in comparison to the other two components it will be neglected in the discussion of the dynamics.

The main SVD component was fit with a sum of the first two species in a two-step sequential model (see Fig. 4.19 (d)). This was motivated by the fact that the fast rise was slower than the instrument-response function of around 100 fs. Thus, a first species A created with an IRF-limited rise was introduced, with a different amplitude than the main decaying species B. For this transfer from species A to B a time constant of  $270 \pm 10$  fs was found and a time constant of  $3.69 \pm 0.01$  ps for the subsequent decay to zero. Since both species in this model are associated with the same right singular vector, this transfer does not correspond to a change in chemical species but effectively describes the rise of the absorption and emission bands. Due to the relatively slow decay of species B, it is likely associated with a local minimum on the excited-state potential energy surface and can be considered an excited-state intermediate, while species A represents the distribution of configurations immediately after excitation into the Franck-Condon state.

As evident from the early dynamics of the second SVD component, it was not possible to mitigate the band overlap entirely. Because of their ratio in singular values, this does not invalidate the interpretation of the first component, but the first  $\approx 1$  ps of the second left

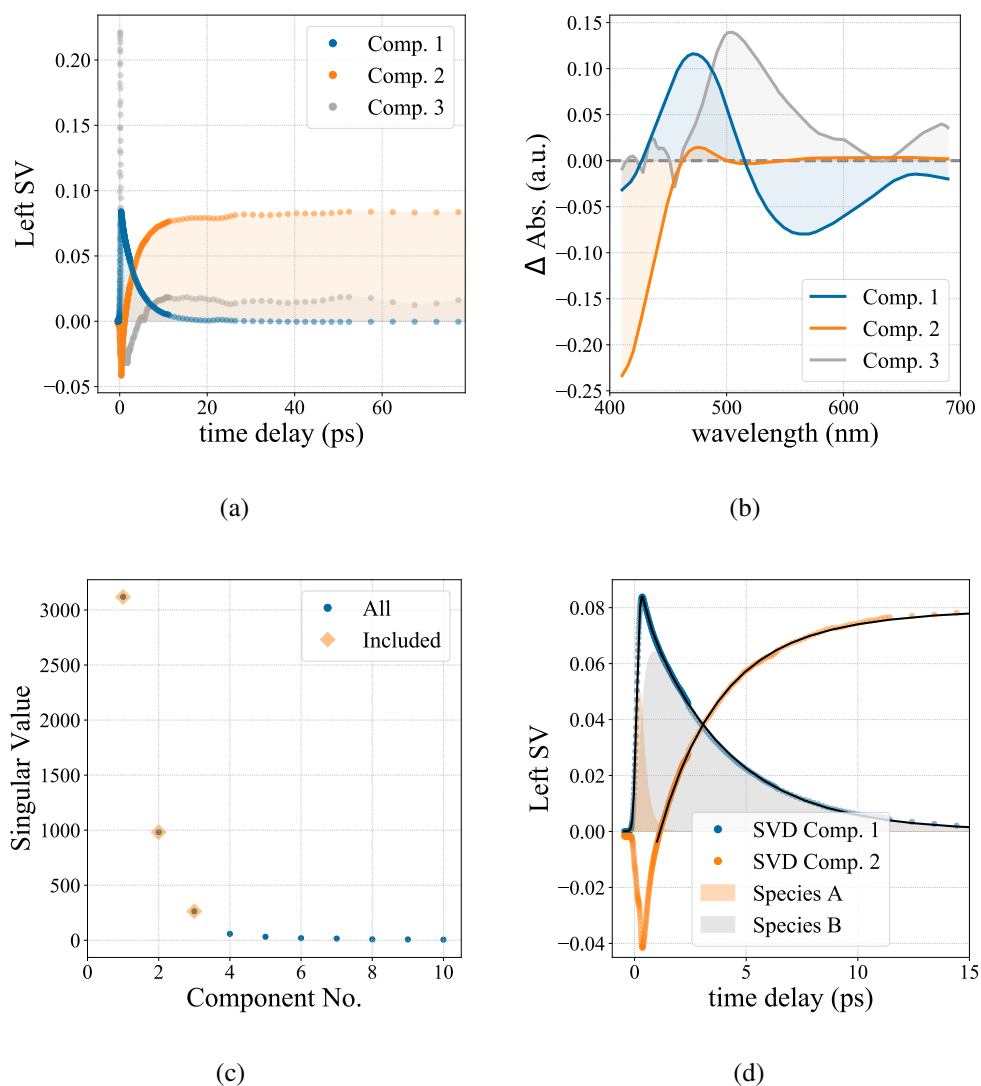


**Figure 4.19:** Singular value decomposition of the TA data from photoexcited E-Nitro-MCH<sup>+</sup>, probed in the visible. (a) and (b) first three left and right singular vectors, respectively, (c) singular values, (d) exponential fits of the first two left singular vectors. For the fit of the first component, a two-step kinetic model was used (see text) of which the fit components are plotted in addition (filled curves). The second component was fit with a regular exponential function.

singular vector cannot be interpreted by means of a kinetic model. In order to compare the dynamics beyond this point to the first component, it was instead fit with a sum of two exponential functions and a constant in the time window between 1 and 150 ps. The faster of these exponential functions has a lifetime of  $2.8 \pm 0.02$  ps, which matches the ground-state-bleach single-point kinetics at 415 nm. However, an additional rise constant of  $21 \pm 2$  ps was found, which is absent in the single-point kinetics. Thus, these dynamics can be attributed to the satellite absorption band. The decomposition therefore enables to mitigate the overlap of this band with the ESA, since the latter is correlated with the decay of the SE bands and therefore its left singular vector decays to zero. The GSB recovery on a longer time scale is reflected in the second left singular vector as well. However,

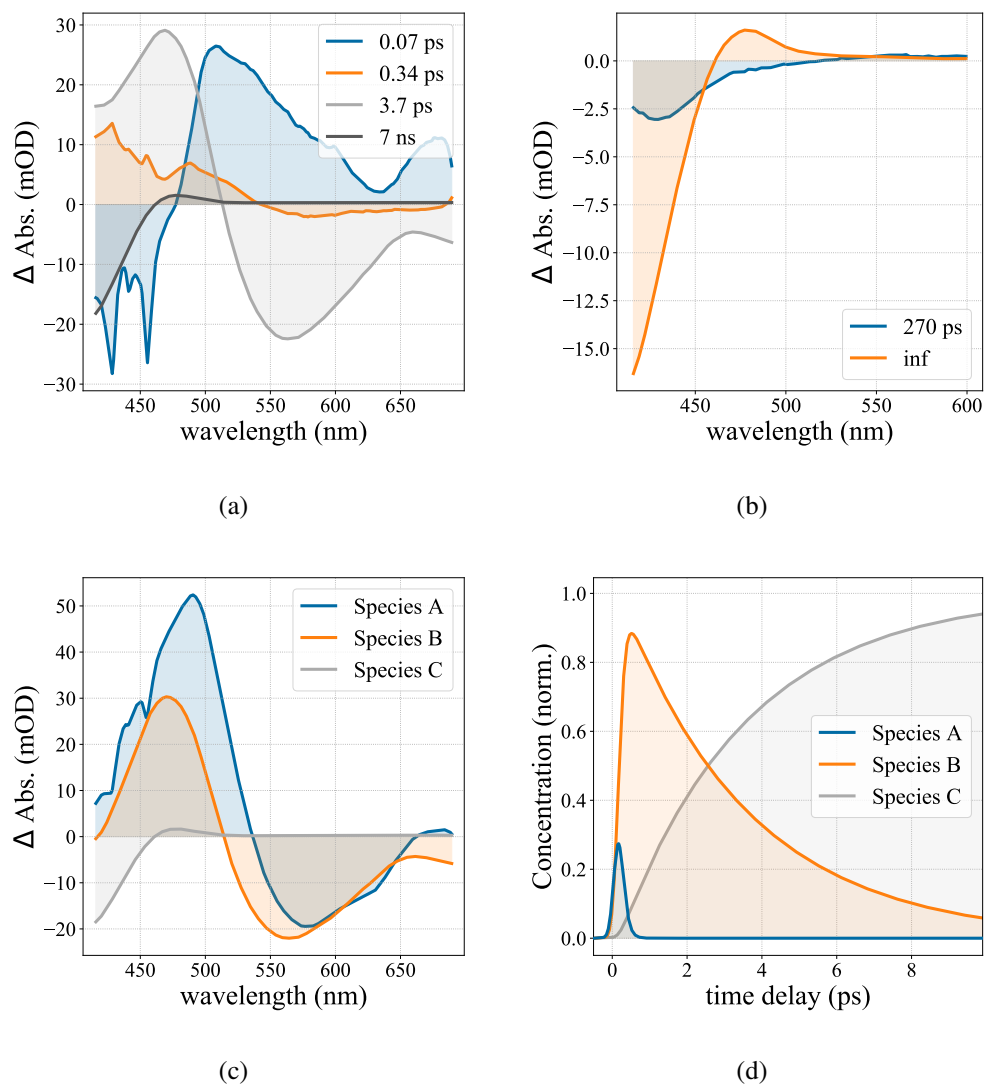


**Figure 4.20:** Global and target analysis of the TA data from photoexcited E-Nitro-MCH<sup>+</sup> in the visible range for time delays up to 1 ns. (a) DAS for the entire window, (b) DAS from a two-component fit starting at 150 ps, (c) SAS from target analysis, (d) corresponding concentrations. Time constants from target analysis:  $\tau_{AB} = 100$  fs,  $\tau_{BC} = 3.4$  ps.

the single-point kinetics of the GSB and satellite bands on this time scale appear to be different, while the SVD forces a common temporal progression governed by the GSB dynamics with a significantly higher contribution to the SVD component and the data in general. Therefore, the long-term dynamics should not be discussed on the basis of the SVD analysis.

The results from global fits of the data using both a parallel decay and a unidirectional sequential model are shown in Fig. 4.20. The parallel model required four decay components when fitting the entire data with IRF-convoluted exponential functions with the fourth component having a decay time of  $\approx 7$  ns and containing the long-lived bands. The finite decay constant is due to the observed partial recovery of the ground state bleach within the measurement window. The third component with a time constant of 3.7 ps de-

scribes the decay of the ESA and SE bands. Since the first two components are affected by the cross-phase modulation (CPM) between the pump and probe pulses, they are more ambiguous. The first component contains spectral features that match the decaying bands, thereby reproducing their rise. However, its lifetime is slightly below the instrument-response function, impeding quantitative interpretation. The second component (0.34 ps) mostly describes a hypsochromic shift of the spectrum, with negative amplitudes above 550 nm and positive amplitudes below. Additionally, it entails a spike structure below 500 nm, which can be considered an artifact from the residual decay of the first component, as its decay is slower than the CPM signal these features originate from. Since it is known from the previous analysis that a single long-lived decay is not accurate in order to describe the sub-ns dynamics, the window between 150 ps and 1.1 ns was treated with a separate, two-component fit. One of these components is a constant, thus representing the equilibrium difference spectrum, and the other one a rising component with a time constant of 270 ps, which represents the ground-state bleach recovery.

Since analysis of the SVD results suggested the applicability of a kinetic model, target analysis of the data was carried out in addition. Fig. 4.20 (c) and (d) show the species-associated spectra and the corresponding concentrations when applying a two-step model with a finite lifetime for the last species. The time constants for the transfer between species were found to be  $\tau_{AB} = 100 \pm 1$  fs and  $\tau_{BC} = 3.4 \pm 0.001$  ps. As in case of the global analysis, a long-lived decay of species C ( $\tau_C \gg 1$  ns) was required due to the ground-state bleach recovery. According to the SAS, Population transfer from species A to species B involves the observed spectral blue-shift in the early time window, but also a rise in amplitude, since the maximum concentration of species A is significantly lower than that of species B. Thus, the obtained time constant is a convolution of the two processes, unlike in case of the SVD and parallel fit, where they are attributed to separate components. Transfer from species B to C on the other hand agrees well with the decay time of the ESA and SE bands obtained via the other methods. Both global and target analysis qualitatively reproduce the results from the SVD analysis, but the obtained lifetimes are more ambiguous. This is mostly due to influence of the CPM in case of the parallel fit and the spectral shift in case of the kinetic model, which in the SVD are contained in a separate component. Nevertheless, the global analysis enables quantification of the ground-state bleach recovery and both methods validate the interpretation of the SVD results.

#### **Analysis of Nitro-MCH<sup>+</sup> TA in the UV**

The highly convoluted nature of the transient absorption bands in the UV requires a decomposition of the data via SVD or global analysis. The left singular vectors of the first SVD components did not exhibit a temporal development suitable for conclusive exponential fits. Thus, postulating the temporal behavior to consist of exponential decays a

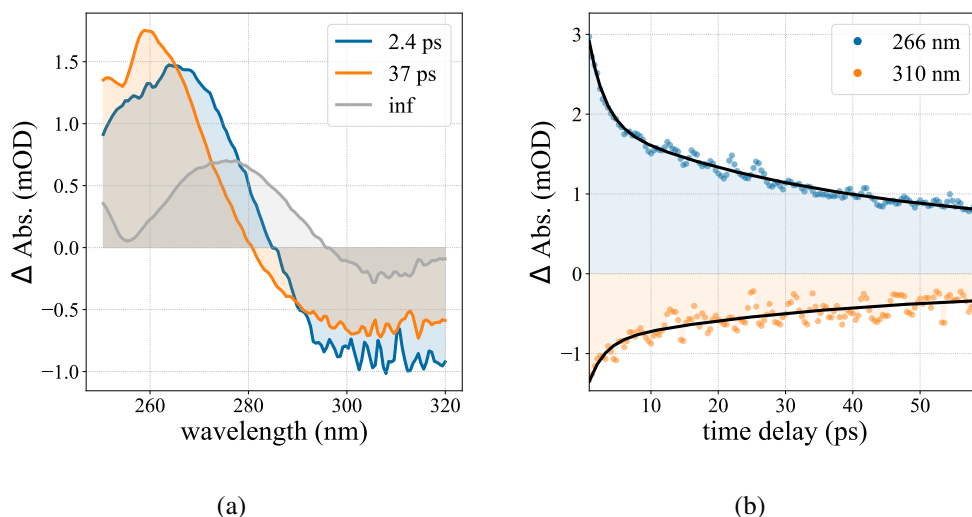


**Figure 4.21:** Global fit of the UV transient absorption data from photoexcited E-Nitro-MCH<sup>+</sup>. (a) DAS, (b) exemplary kinetic traces including the global fit (black lines) at the respective wavelengths.

priori as in case of global analysis was necessary. The results from global fits using two decaying and one constant component are shown in Fig. 4.21.

The decay of the absorption bands towards the steady-state difference spectrum was found to be biexponential in all of the tested models. According to global analysis, the fast component has a lifetime of  $2.4 \pm 0.06$  ps, with a positive amplitude below 285 nm and a negative amplitude above. The second component with a lifetime of  $37 \pm 1$  ps has a similar decay-associated spectrum, although the edge is slightly blue-shifted with respect to the first component, crossing 0 mOD around 280 nm. Furthermore, it has a more distinct absorption fine-structure in the far UV with a local maximum around 260 nm, a shoulder around 265 nm and a local minimum around 255 nm. The constant component represents the equilibrium difference spectrum at 60 ps and is thereby equivalent to the photostationary-state difference absorption (see Fig. 4.4 in section 4.2).

Hence, global analysis allows for the separation of these overlapping bands by their different decay times. Several kinetic models were tested on the UV transient absorption data in addition, in which the second component was interpreted as an intermediate in either a unidirectional chain or a three-component branched chain according to equation 4.3, of which the results can be found in the appendix (Fig. A.22).



The retrieved time scales in these models matched the ones obtained from global analysis, suggesting that the second component can indeed be interpreted as an intermediate species in either model. However, target analysis lacks the capability of deconvoluting the overlapping bands in the same way as global analysis, rendering the latter more appropriate in this specific case.

Interpretation of the UV TA results is more ambiguous than the visible because not only are both isomers known to absorb in this wavelength region, but also most intermediates are expected to, especially if in the excited state. Thus, they will be interpreted holistically along with the results obtained in the visible probing range in the concluding discussion (section 4.4.4).

### 4.4.3 E-MCH<sup>+</sup> TA

The transient absorption results of the photostationary state mixture of protonated BIPS excited at 400 nm are shown in Fig. 4.22. Qualitatively, the data consists of the same type of signals as in case of the nitro-substituted variant, with two negative decaying bands, one centered between 550 and 600 nm, the other above 700 nm, a positive absorption band with a maximum around 475 nm and a long-lived negative band with a maximum in absolute amplitude around 425 nm. Thus, these signals can be preliminarily assigned in analogy to the E-Nitro-MCH<sup>+</sup> data. The ESA band appears to be smaller in amplitude and narrower compared to the case of Nitro-MCH<sup>+</sup>, but this is likely an effect of the MCH<sup>+</sup> GSB band being red-shifted by  $\approx 25$  nm with respect to Nitro-MCH<sup>+</sup>. Like in case of the latter, the ESA and SE bands initially rise within the first few 100 fs before a subsequent decay on the few-ps time scale (see Fig. 4.22 (c)). However, the sub-ns dynamics exhibit two main differences to the nitro-substituted derivative, the absence of a positive absorption feature on the one hand and a more noticeable recovery of the ground-state bleach band on the other hand (about 40 % at 1 ns compared to the spectrum at 5 ps). Inspection of the kinetic traces in the bleach region (see Fig. 4.22 (d)) furthermore suggest this recovery to follow a biexponential progression. As mentioned, transient UV absorption experiments were carried out in addition. However, these did not exhibit any signals above noise level in the probing range of 270-350 nm.

It was noted previously, that these experimental results are impaired by the fact that both the E- and the Z-isomer have a non-negligible absorption cross-section at the excitation wavelength of 400 nm. These superimposed dynamics are likely the reason why no signal above noise level was observed in the UV range, where both species absorb with only small differences in absorbance (see Fig. 4.4 (c)). In the visible on the other hand, the contribution of the Z-isomer can be inferred qualitatively from the TA data of the Z-to-E-isomerization (*vide supra*), in order to estimate which spectral and temporal regions of the data are less affected by superposition of the two reaction pathways. Furthermore, since the photostationary state absorbance of MCH<sup>+</sup> at 400 nm under irradiation

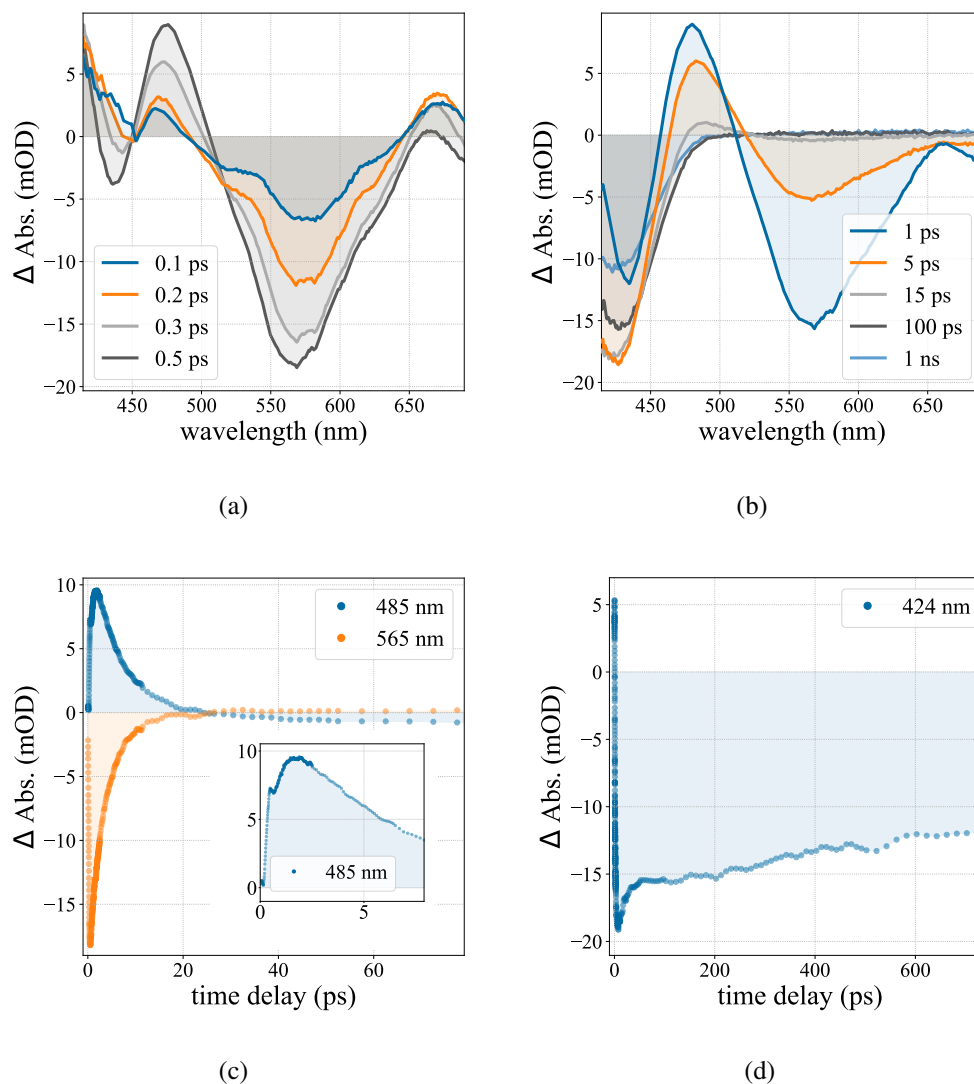


**Figure 4.22:** Transient absorption of photoexcited E-MCH<sup>+</sup>, excited at 400 nm and probed in the visible. Shown are representative spectral traces (Figs. (a) and (b)) as well as selected kinetic traces (Figs. (c) and (d)).

at 365 nm is approximately two times the absorbance of the initial thermal equilibrium, attributed purely to the Z-isomer, the excitation fraction of the E-isomer can be assumed to be significantly higher than the one of the former, and thus the data to be dominated by dynamics of the photoexcited E-isomer. Based on these considerations as well as the high qualitative similarity to the TA data obtained for E-Nitro-MCH<sup>+</sup>, a few conclusions can be drawn.

The sub-ps dynamics are assumed to be influenced by the short-lived positive absorption signal of the Z-isomer in the entire probing range, leading to a delayed rise of the negative bands and a signature of its excited-state absorption dynamics in the positive band, shown in the inset of Fig. 4.22 (c). However, the Z-to-E-isomerization data does not exhibit any significant spectral dynamics on the few-ps time scale above  $\approx 550$  nm. While holistic analysis methods such as SVD or global fit are compromised by the superimposed

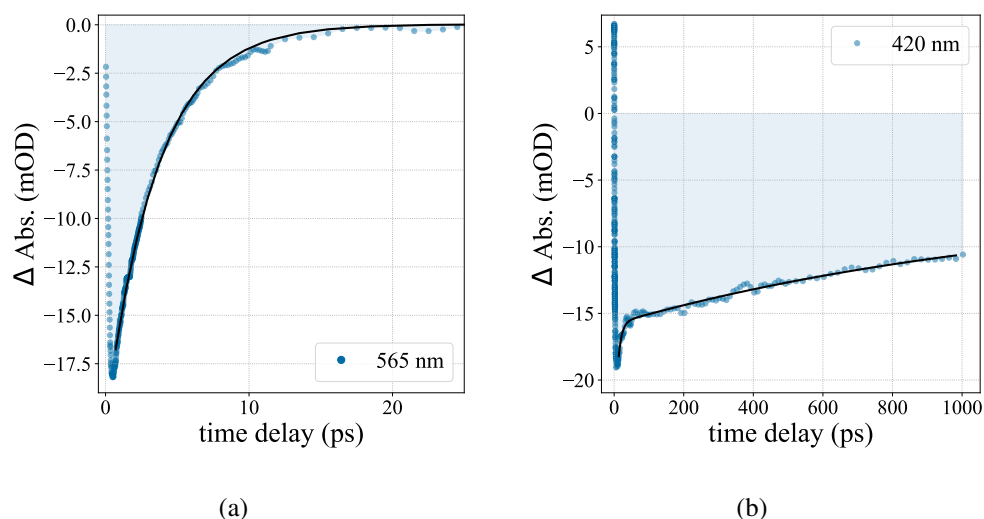


**Figure 4.23:** Single-point exponential fits of photoexcited E-MCH<sup>+</sup> in the regions of (a) the stimulated emission and (b) the ground-state bleach bands. The trace in (a) shows a monoexponential ( $\tau = 3.6$  ps), the one in (b) a biexponential behavior ( $\tau_1 = 10$  ps,  $\tau_2 = 1.2$  ns).

dynamics of the two isomers, this part of the data can still be analyzed by means of single-point kinetics. The kinetic trace at 565 nm representing the stimulated emission band was fit in the time window between 0.7 ps and 1 ns and found to follow a monoexponential decay with a time constant of  $3.6 \pm 0.02$  ps and an amplitude of  $-20.5 \pm 0.05$  mOD (see Fig. 4.23 (a)). In order to quantify the recovery of the ground-state bleach, the kinetic trace at 485 nm was fit in the time window between 13 ps and 1 ns with a sum of two exponential functions yielding time constants of  $10 \pm 1$  ps ( $-11 \pm 2$  mOD) and  $1.2 \pm 0.2$  ns ( $-9 \pm 1$  mOD) and an offset of  $-6 \pm 1$  mOD. This recovery is readily attributed to the formation of the E-isomer, largely due to the isomerization of the photoexcited Z-isomer, which was also found to exhibit a biexponential behavior (see section 4.3.2). However, repopulation of the ground state of photoexcited E-isomers via internal conversion has to be assumed to influence these dynamics as well, making these time constants purely descriptive.

Nonetheless, two main insights can be gained from these observations and rudimentary analyses by comparison to the results for Nitro-MCH<sup>+</sup>. Firstly, in addition to the general similarity of the signals, the lifetimes of the stimulated emission bands obtained from single-point kinetic fits are in good agreement (conf. Tab. 4.5). This implies that no significant differences in the excited-state dynamics between these two compounds exist. Secondly, like in case of the Z-to-E reaction, the low-amplitude, long-lived absorption band around 480 nm found for Nitro-MCH<sup>+</sup> is absent in case of the non-substituted variant.

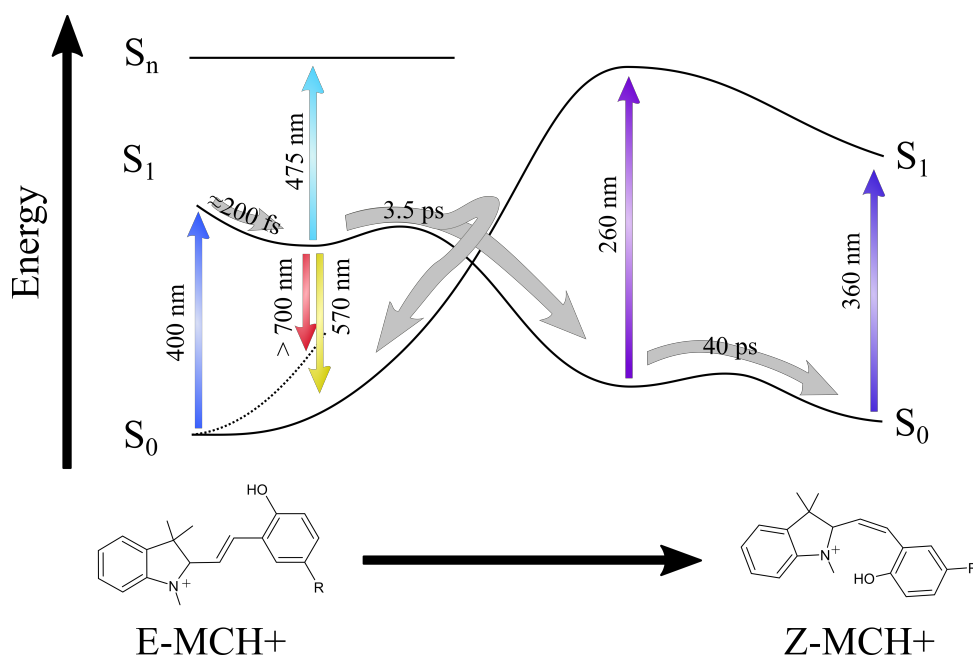


**Figure 4.24:** Schematic energy diagram of the E-to-Z-isomerization of protonated spirobenzopyran. The time constants and transition wavelengths are based on analysis of the TA data from the nitro-substituted derivative. Excitation leads to the formation of an excited-state intermediate with a lifetime of 3.5 ps exhibiting both excited-state absorption and stimulated emission signals. Subsequent reaction to the Z-isomer occurs via a ground-state intermediate (40 ps lifetime).

#### 4.4.4 Concluding discussion

In analogy to the the Z-to-E reaction mechanism, the reverse process is depicted schematically in Fig. 4.24. From the Franck-Condon state, the wave packet propagates towards a local minimum on the  $S_1$  potential energy surface manifesting in a hypsochromic shift of the absorption spectrum within  $\approx 200$  fs after excitation. Stimulated emission from this excited-state intermediate was observed at 570 nm and  $\geq 700$  nm, while the absorption maximum was found at 475 nm.<sup>17</sup> The ESI decays with a lifetime of 3.5 ps either relaxing back to the E-isomer or towards the Z-isomer via a ground-state intermediate with a lifetime of 40 ps and an absorption maximum around 260 nm. While the interpretation of this isomerization pathway is less ambiguous than the forward reaction, the identities of the excited-state and ground-state intermediates remain to be unraveled. The blue-shift in the absorption of the longer-lived ground-state intermediate with respect to the Z-isomer indicates a lower wave function overlap between the two moieties and thus the difference between the two may lie within conformation of the methine bridge.

Notably, the satellite absorption band in the Nitro-MCH<sup>+</sup> data was also observed for the E-to-Z isomerization. The formation of the associated species as a competing pathway with a formation time of 21 ps may happen from the ESI which would explain the slightly slower decay of the latter (3.4 ps) compared to the formation time of the ground-state

<sup>17</sup>The indicated center wavelengths and lifetimes refer to the case of Nitro-MCH<sup>+</sup>.

intermediate (2.4 ps). On the other hand, it may be formed from the ground-state intermediate itself in competition to the product formation. The first hypothesis of formation from the excited-state would also make intersystem-crossing to a long-lived triplet state a possible explanation (*vide supra*).

To further elucidate these questions, the same suggestions for numerical simulations as in the previous section can be made. However, molecular dynamics would only be able to feasibly cover the formation of the excited-state intermediate from the FC state. Thus, it is likely sufficient to conduct optimizations on the  $S_1$  and  $S_0$  potential energy surfaces to characterize the intermediate structures and match them with the observed transient absorption signals.

## 4.5 Light-Induced Protonation of Spirobenzopyran in $H_3PO_4$ Solution

As laid out in the introduction of this chapter, a mechanism for the photoinduced protonation of BIPS in the presence of an acid with suitable  $pK_a$  value was proposed by Kortekaas et al. based on steady-state spectroscopy.<sup>[151]</sup> In this mechanism, closed-form BIPS is irradiated to yield the non-protonated merocyanine form which subsequently accepts a proton from the acidic solution, in this case  $H_3PO_4$  in acetonitrile (AcN). This process can be reverted by irradiation with visible light via isomerization to the E-isomer, which is more acidic than  $H_3PO_4$  and therefore transfers its proton, inducing ring-closure. To verify the proposed mechanism and demonstrate its reversibility, transient absorption experiments under these specific conditions were conducted and compared to the data from BIPS in a non-acidic environment. The outcome of these investigations will be presented and discussed in this section.

### 4.5.1 Experimental details

The 1.5 mM BIPS sample solutions in acetonitrile were prepared in the same way as described in section 4.2, but either without acid for the reference experiments or using phosphoric acid ( $H_3PO_4$ ) instead of sulfuric acid. Transient absorption experiments of both sample solutions exciting at 330 nm and 500 Hz with varied fluences were carried out using the flow-cell setup, while irradiating the reservoir with a visible lamp. For an *in-situ* verification of the E-MCH<sup>+</sup> formation in presence of  $H_3PO_4$ , a set of scans without solution flow was recorded in addition. The datasets presented in the following were recorded using a fluence of  $3.3 \text{ mJcm}^{-2}$  in either case.

## 4.5.2 Results and discussion

A comparison between the transient absorption data of BIPS obtained with and without the addition of equimolar phosphoric acid is given in Fig. 4.25. The first 500 fs after excitation are dominated by a broad excited-state absorption in either case, which converges towards a more defined spectrum with a maximum between 400 and 450 nm, slightly red-shifted in case of the neutral solution. In both solutions, this spectral feature subsequently decays, accompanied by the rise of a long-lived absorption spectrum with a maximum between 550 and 600 nm as well as a second band below 450 nm, which is smaller in amplitude. In case of the non-acidic solution, this spectrum does not exhibit any drastic evolution beyond 10 ps, except a slight spectral narrowing and blue-shift of the maximum of the main band and a small increase of the smaller band. In contrast, the sample containing phosphoric acid undergoes further spectral changes on the sub-ns time scale, consisting in a continuous decay of the main band in the region between 500 and 640 nm and an increase in absorbance between 400 and 450 nm.

The dynamics of BIPS in the non-acidic environment are readily interpreted by reference to the reported literature<sup>[155,164,165]</sup> as well as the results for the closely related spiro-naphthopyran presented in chapter 3. Thus, the long-lived absorption band is attributed to the open-ring, planar merocyanine form, and the short-lived absorption feature peaking around 450 nm to an excited-state intermediate. In analogy to SNP, refinement and blue-shift of the product absorption band on the ps time scale can be ascribed to vibrational cooling. The BIPS solution containing H<sub>3</sub>PO<sub>4</sub> exhibits highly similar dynamics in the sub-10 ps time window which will be subject to further analysis in the following. The only notable difference in the early time window consists in the maximum position of the excited-state intermediate absorption. The edges of these absorption bands however span from 450 to 500 nm in both cases. It is possible that the drop in absorbance towards 400 nm for the non-acidic solution is an artifact due to spatial dispersion of the probe and thus diminished pump-probe overlap for shorter wavelengths. The different dynamics on the sub-ns time scale on the other hand suggest that in case of the acidic solution further reaction of the photoproduct takes place on this time scale.

All of these observations qualitatively agree with the postulated model by Kortekaas et al. for BIPS in a H<sub>3</sub>PO<sub>4</sub> solution, in which the non-protonated spiropyran reacts to the open-ring merocyanine like in case of a non-acidic environment and in a second, non-photoinduced step accepts a proton from the acid, yielding the planar E-isomer of MCH<sup>+</sup>. The latter would explain the decay of the MC band with a simultaneous rise in the region of the E-MCH<sup>+</sup> absorption between 400 and 450 nm. In order to quantify and further support this interpretation, especially comparing the reaction time scales between the two solutions, global and target analysis of the data were carried out and will be discussed in the following.

The obtained time constants in all cases matched between the parallel decay models as

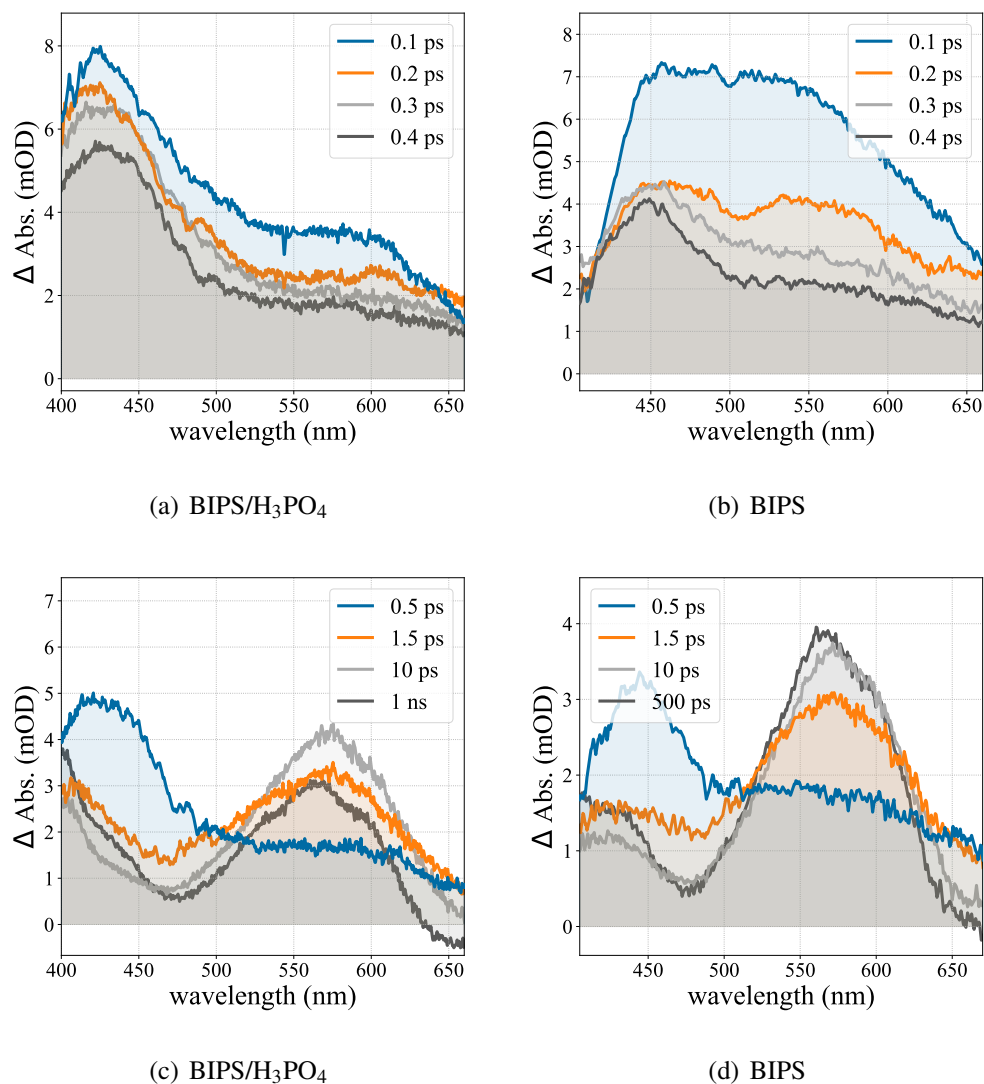


**Figure 4.25:** Transient absorption data of photoexcited BIPS in acetonitrile in the presence (left column) and absence (right column) of  $\text{H}_3\text{PO}_4$ , for the sub-ps (first row) and sub-ns (second row) time regimes.

**Table 4.6:** Population transfer time constants from TA target analysis of BIPS in the presence and absence of  $\text{H}_3\text{PO}_4$ .

	5 ps, $\text{H}_3\text{PO}_4$	5 ps, no acid	1 ns, $\text{H}_3\text{PO}_4$	1 ns, no acid
$\tau_{\text{AB}}$ (ps)	$0.23 \pm 0.001$	$0.17 \pm 4 \cdot 10^{-4}$	$0.19 \pm 4 \cdot 10^{-4}$	$0.19 \pm 0.001$
$\tau_{\text{BC}}$ (ps)	$0.55 \pm 0.001$	$0.61 \pm 0.002$	$0.73 \pm 0.001$	$0.52 \pm 0.002$
$\tau_{\text{CD}}$ (ps)	–	–	$464 \pm 4$	$6.0 \pm 0.04$

well as the kinetic sequential models when using the same number of components. Therefore, since the species-associated spectra are more readily attributed to reaction components, they will be discussed in the following without further comparison to the equivalent

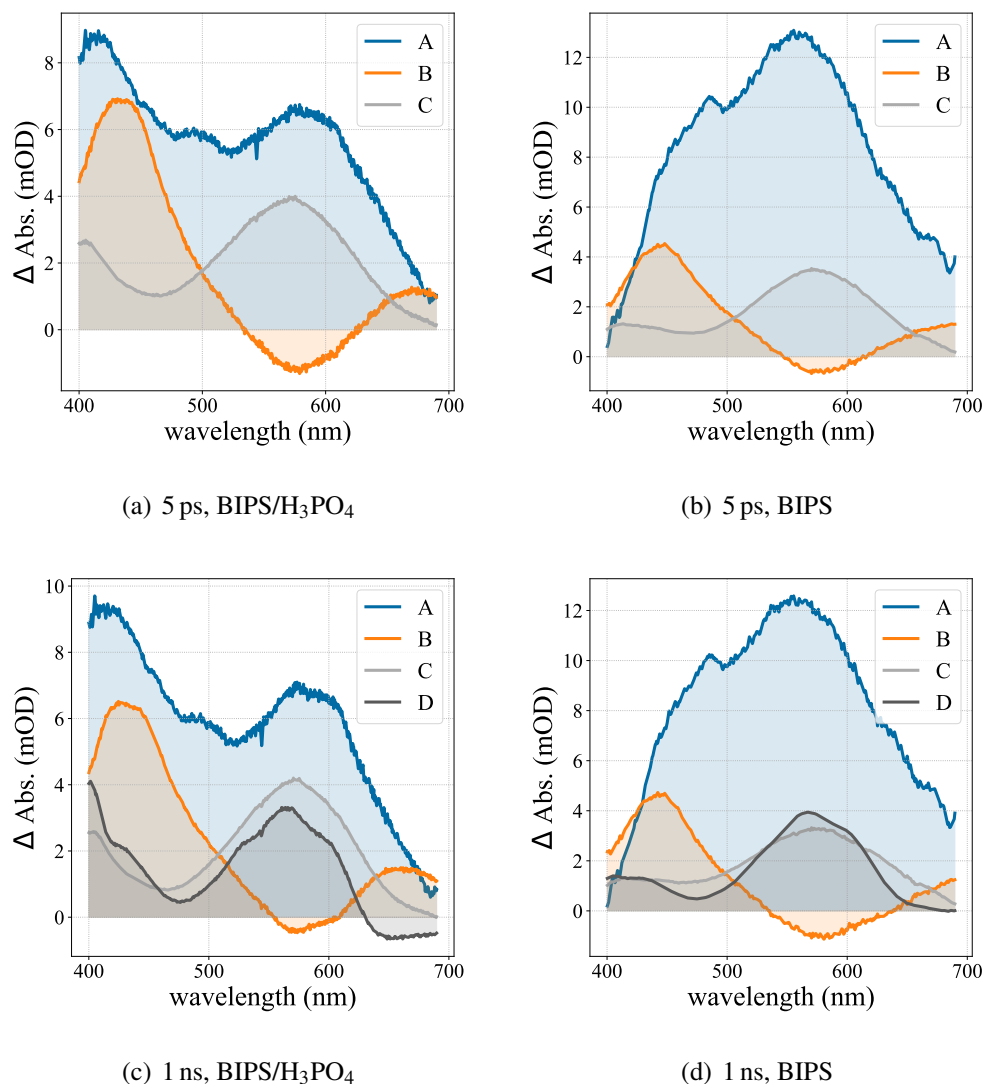


**Figure 4.26:** Target analysis results of BIPS in acetonitrile in the presence (left column) and absence (right column) of H<sub>3</sub>PO<sub>4</sub>, for time windows up to 5 ps ((a) and (b)) and up to 1 ns ((c) and (d)). The corresponding time constants are collated in Tab. 4.6

decay-associated spectra (see Fig. A.23 in the appendix). In order to compare the early dynamics between the acidic and the non-acidic environments without influence of the sub-ns spectral changes, the time window between 0.1 and 5 ps was fit using a two-step (three component) unidirectional chain for either case (Fig. 4.26 (a) and (b), respectively) in addition to a fit of the entire time window by means of a three-step model (Fig. 4.26 (c) and (d)). The SAS in both cases exhibit the same qualitative features as the ones found for SNP (see Fig. 3.8) and reflect the spectral development from the initial broad excited-state absorption (species A) via an intermediate species B towards the photoproduct absorption spectrum (species C). Similar to the case of SNP, spectral artifacts in the region of the product band are distinguishable in the SAS of both species A and B with opposite signs, suggesting a slight mismatch in the early time scales of intermediate band decay and product band rise. This mismatch is likely due to the fact that these two spectra actually

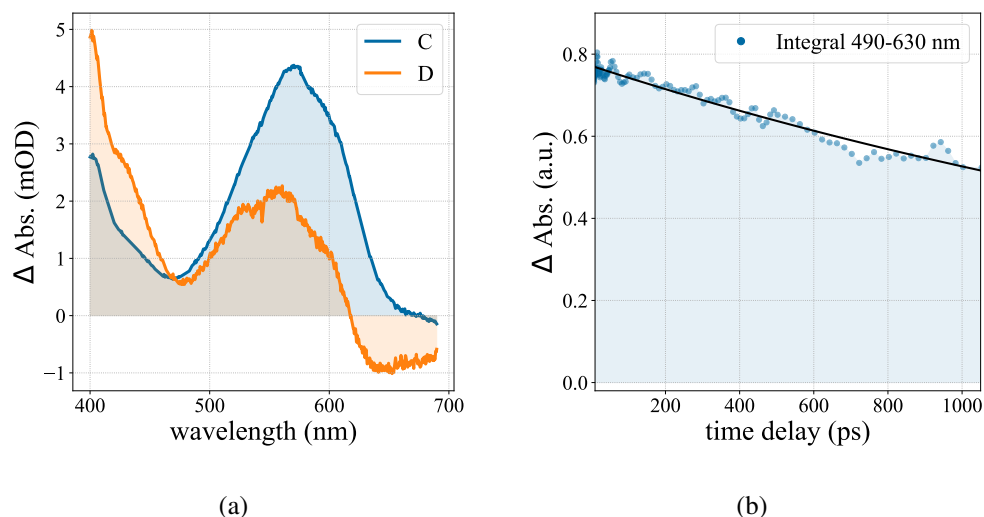


**Figure 4.27:** Spectral dynamics of photoexcited BIPS in an  $\text{H}_3\text{PO}_4/\text{AcN}$  solution in the sub-ns regime: (a) species-associated spectra from target analysis and (b) decay of the integrated merocyanine product absorption band.

transition into each other via a spectral shift instead of a parallel decay and thus considered a small systematic error well within the assumptions of the analysis method.

Like the SAS of both solutions, the corresponding time constants shown in Tab. 4.6 are in good agreement with each other, underlining the conclusion that indeed the same reaction to the planar, non-protonated merocyanine occurs in both cases. When covering the entire measurement window, the apparent differences on the sub-ns time scale are reflected in the SAS and formation time constant of the additional species D. While in case of the non-acidic solution only spectral refinement of the product band occurs (6 ps time constant), the slow decay of the product band and simultaneous rise around 425 nm in case of the  $\text{H}_3\text{PO}_4$  solution are reflected in the respective SAS and the associated time scale of  $\approx 460$  ps vastly different. Since in the latter case, spectral refinement of the product band is observed as well, the obtained time constant has to be assumed a hybrid between both of these processes. This can be mitigated in principle by adding another step in the kinetic model. Even though the sub-ns in this four-step model are accurately described, the early dynamics are compromised by increased parameter correlation. Therefore, the sub-ns dynamics were fit separately for a time window starting at 10 ps with a two-step model (see Fig. 4.27 (a)).

The outcome confirms the temporal correlation between the decay in photoproduct absorption and the rise between 400 and 450 nm, attributing a time constant of  $1260 \pm 10$  ps to both. However, the obtained SAS reveal that the decay of the product band entails a hypsochromic shift in its center position. Furthermore, the MC product absorption is known from both literature and the non-acidic solution results to absorb between 400 and 450 nm, in the region of the  $\text{E-MCH}^+$  absorption. Thus, a protonation of the MC would lead to a superposition of spectral dynamics below 450 nm. To mitigate this, the prod-

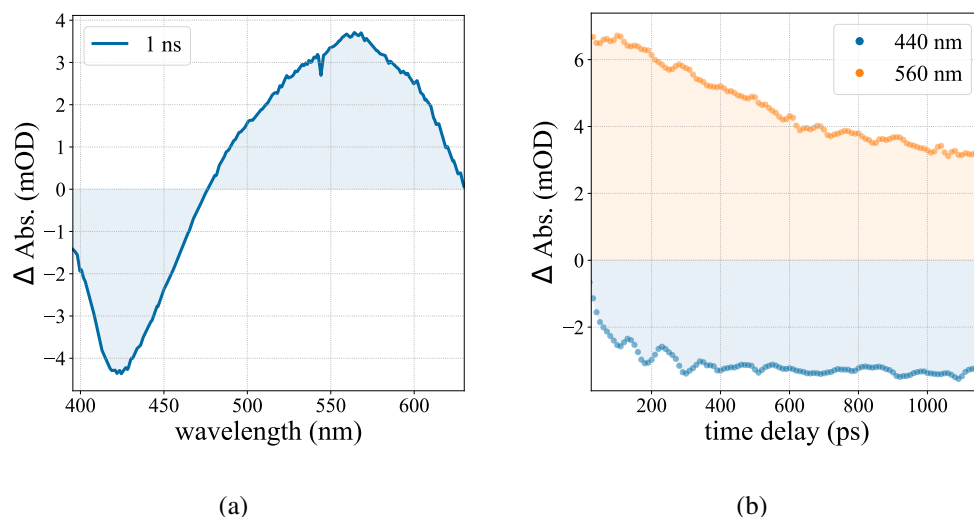


**Figure 4.28:** Transient absorption data of BIPS in  $\text{H}_3\text{PO}_4/\text{AcN}$  without solution exchange, verifying the *in-situ* formation of the protonated E-isomer. (a) transient spectrum at 1 ns, (b) selected kinetic traces.

uct band between 490 and 630 nm was integrated and fit separately with an exponential function yielding a decay constant of  $2.6 \pm 0.06$  ns. A separate integration of the spectra between 400 and 450 nm yielding a rise constant of  $400 \pm 50$  ps thus explains why the time constant obtained from target analysis is faster than the one from the integrated product band. Hence, even though the decay of the product absorption band was found to be larger than the measurement window by approximately a factor of 2.5, it can be considered the most accurate time constant for the decay of the MC band. Since the integrated product band for the non-acidic solution does not exhibit any significant decay within the observed time range and spectral signatures of the formation of  $\text{E-MCH}^+$  were found, the decay in presence of  $\text{H}_3\text{PO}_4$  can be attributed entirely to protonation of the merocyanine product.

Further proof of the creation of  $\text{E-MCH}^+$  in the TA measurements is gained from scans without solution exchange, in which accumulation of the protonated species was manifested in a permanent ground-state bleach signal which matches with the  $\text{E-MCH}^+$  steady-state absorption (compare Fig. 4.28 (a) and Fig. 4.4 (c)). This GSB signal is superimposed with the dynamics of closed-ring BIPS including the formation of the non-protonated merocyanine and the subsequent decay in its absorption due to gradual protonation, as can be seen from the respective kinetic traces in Fig. 4.28 (b).

### 4.5.3 Conclusion

The presented results and discussed analyses confirm the previously postulated model of a  $\text{p}K_a$ -gated, photoinduced protonation of BIPS. The protonation was found to occur via the planar, non-protonated merocyanine, which is formed via the same photoreaction

mechanism as BIPS and SNP in non-acidic environments, i.e. via formation of a presumably open-ring, non-planar excited-state intermediate with a time constant of  $\approx 200$  fs and subsequent planarization with a time constant of  $\approx 600$  fs.<sup>18</sup> Subsequent protonation of the merocyanine species takes place on the few-ns time scale, based on the associated decay of the merocyanine absorption band, with a time constant of 2.6 ns, which is compromised to a degree by the limited experimental time window.

## 4.6 Summary and Outlook

The results on the isomerization dynamics of protonated, open-ring spiroyrans corroborate the recently proposed switching mechanism and add a mechanistic picture for both directions of the Z-E-isomerization process. A complex mechanism with multiple pathways and intermediate species was found for the forward reaction, in which the excited state rapidly decays within 300 fs into a distribution of the reactant and two distinct intermediates. Both of these intermediates contribute to formation of the E-isomer, one with a short lifetime (2.4 ps and 500 fs for BIPS and Nitro-BIPS, respectively), the other one on the sub-ns time scale (240 ps and 180 ps). While the longer-lived intermediate is very likely a ground-state isomer, the short-lived could be either in the ground-state or an excited-state intermediate with little absorption in the red region of the spectrum compared to the Franck-Condon state.

The reverse reaction mechanism is less complex overall and entails an excited-state intermediate which decays with a time constant of 3.4 ps to form an intermediate species, subsequently reacting to the product with a time constant of 40 ps. In a reported study from 2021, Kaiser et al. investigated the dynamics of a slightly modified photoexcited E-Nitro-MCH<sup>+</sup> in an aqueous solution regarding excited-state proton transfer,<sup>[199]</sup> a process which was deliberately avoided in this work by choosing the aprotic solvent acetonitrile for all systems. The data differs mostly in the presence of a signal associated with the non-protonated merocyanine. However, isomerization to the Z-isomer as a competing channel was not discussed and all excited-state dynamics are associated with relaxation to the initial state. The results in this work on the other hand show that the isomerization pathway cannot be neglected as the long-lived transient signals match the steady-state difference spectra which have been unambiguously assigned to the different isomers by Kortekaas and coworkers using NMR spectroscopy.

Furthermore, the proposed four-step switching cycle of spiroyrans in presence of an acid whose  $pK_a$  value lies within the two protonated isomers was confirmed by means of transient absorption spectroscopy, unambiguously identifying the non-protonated, closed-ring form and its associated dynamics as well as the subsequent protonation of the merocya-

---

<sup>18</sup>These specific assignments are made by analogy to the more extensive study of the SNP photoreaction mechanism in chapter 3, but using the obtained lifetimes from the present data.

nine photoproduct. The thermal stability of the protonated open-ring form was confirmed by accumulation and its reversibility by light utilized in the experiments. Thus, all four steps have been witnessed and verified experimentally.

In the context of this entire thesis, the next step in this project is evident: Investigating potential photochromism dynamics of these compounds in the crystalline phase to eventually study the structural dynamics by means of ultrafast diffraction techniques. It has been shown by Seiler and coworkers that various protonated spiropyrans can be co-crystallized with the conjugated bases of the respective acids.<sup>[214]</sup> The next question to be answered is whether any of these crystals show steady-state photochromism, which would render them appropriate targets for further investigations. Even if that is not the case for any of them, transient photochromism like in case of SNP may still occur, which would be observable by TAS. The main obstacle for these tests lies within the fact that all of these crystals are ionic and water-soluble, which makes the standard ultramicrotomy routine not feasible. The latter however is true for many compounds of interest and general strategies are being developed to overcome this limitation. A method enabling to grow sub- $\mu\text{m}$  single crystals with 100  $\mu\text{m}$  diameters was reported recently by Hwang et al. including a demonstration of their suitability for TAS experiments.<sup>[137]</sup> If applicable to these crystals, this would suffice to test whether (transient) signatures of isomerization can be found, giving an idea as to whether the pursuit of more involved techniques is worthwhile, in order to obtain samples with suitable thicknesses for UED experiments ( $\approx 100$  nm).

From a structural dynamics perspective studying the protonated forms is particularly interesting as it effectively isolates the planarization step from the bond-breaking step, the both of which are combined in non-protonated spiropyran (*vide supra*). The results presented here indicate a significant increase in reaction time for the protonated forms, especially considering the slower pathway of the Z-to-E isomerization, compared to the non-protonated BIPS. Intuitively, this can be explained by the increased amount of energy required to break the C-O bond, which may be the driving factor and cause of the acceleration. However, photochemistry is more complex and the coupling to specific molecular modes needs to be considered when trying to understand the reaction dynamics. Thus, isolating the key modes behind the Z-to-E isomerization and comparing them to the ones responsible for the "entire" reaction in the non-protonated case would be a highly interesting question to elucidate. Either outcome of such a comparison would represent a significant contribution to our understanding of photochemical reactions. Them being the same or similar would point towards a general set of "rules" for these types of reactions and the relevant molecular motions. Significant differences in the driving modes on the other hand would pose further questions regarding the structure-function relationship of these compounds, considering the structure of the Z-isomer was found to be very similar to the formed open-ring reaction intermediate in case of non-protonated SNP.

## Ring-Closing Dynamics of Diarylethenes

The third and final project of this thesis revolves around another prominent representative of photochromic compounds, the diarylethene family. Its photoinduced ring-closing dynamics were studied and systematically compared between three structurally similar derivatives in order to investigate the influence of different substituents on the reaction. Fig. 5.1 shows a comparison between these derivatives and their cyclization rates based on the outcome of the conducted investigations. As will be detailed in this chapter, the dynamics were found to be governed by the nature of the hetero-atom in the aryl moieties, with the length of the alkyl side chains – and thereby possible steric hindrance – playing only a secondary role. In order to prepare for the envisioned ultrafast electron diffraction experiments, tests regarding the experimental feasibility and specific requirements were carried out and will be discussed in addition.

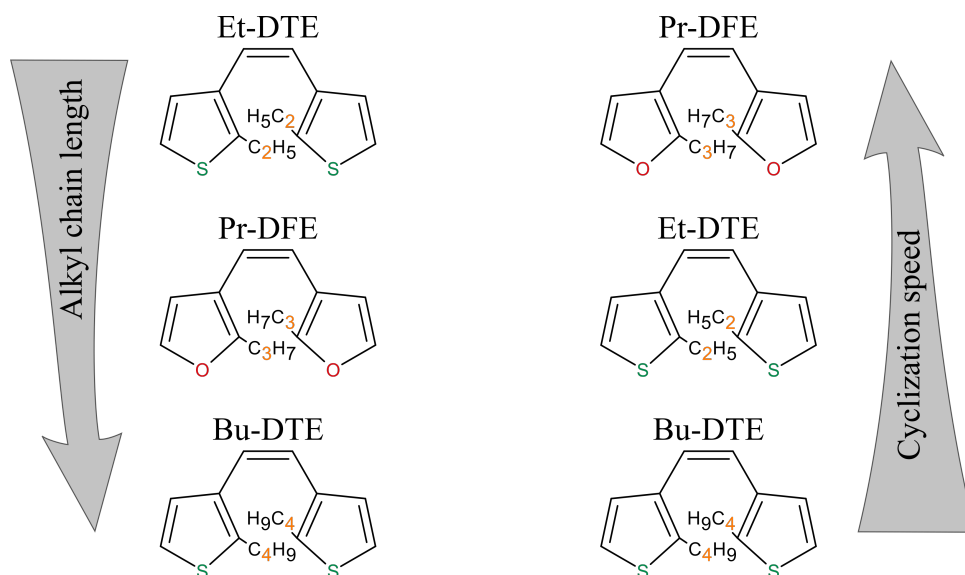


**Figure 5.1:** Summary of the findings from time-resolved studies of the three investigated diarylethene derivatives. Shown are their core units to highlight the differences; further substitution was identical for all molecules (conf. Fig. 5.2). In the left column, the derivatives are sorted by the length of the alkyl substituents at the reactive carbons, while the right column shows them ordered by the obtained cyclization time constants (both increasing from top to bottom). DTE = dithienylethene, DFE = difurylethene.

## 5.1 Ring-Closing Reaction in Diarylethene Derivatives

### 5.1.1 Diarylethene photochromism

Diarylethene compounds are among the most popular and widely used photochromic systems<sup>[64,147,215,216]</sup> and have been proposed for a variety of applications, for instance as optical memories,<sup>[217,218]</sup> switches,<sup>[143–145,219]</sup> actuators,<sup>[220]</sup> or as building blocks in photochromic polymers.<sup>[221]</sup> They are derivatives of stilbene and undergo photo-reversible ring closing (cyclization) and ring opening (cycloreversion) upon light irradiation (see Fig. 5.2). The vast amount of attention diarylethenes have gained within the last three decades in both fundamental and applied research is rooted in their outstanding properties. Many diarylethene derivatives show a high thermal stability of both photochromic isomers (estimated  $10^5$  years), coloration quantum yields close to 100 %, switching repeatability of over  $10^4$  cycles and rapid switching times in the few-ps time domain.<sup>[64]</sup> Furthermore, the relatively small structural change accompanying the photoisomerization enables reversible photochromism in the crystalline phase for various derivatives.<sup>[222]</sup>

The core unit of a diarylethene molecule consists of an ethene bridge, which links two aromatic rings. Cyclization conserves stereochemistry and molecular symmetry, entailing bond formation between two carbon atoms, one from each ring and both in ortho-position with respect to the ethene bridge. It is thus related to the well-studied electrocyclic reaction of hexatriene and its closed-ring isomer cyclohexadiene,<sup>1</sup> with the reactive carbon atoms changing hybridization from  $sp^2$  to  $sp^3$ . However, in case of diarylethenes, ring closure causes the aryl-substituents to align horizontally, increasing the planarity of the molecule and thereby extension of the  $\pi$ -conjugated system. The consequential reduction in HOMO-LUMO gap<sup>2</sup> gives rise to absorption in the visible wavelength range and a coloration of the respective diarylethene solution or crystal.

A particularly well-performing subset of diarylethenes in terms of the criteria stated above, share the following molecular properties. Their two aryl substituents are heterocycles, usually thiophene moieties or – less commonly – furan, and the ethene bridge is part of a perfluorocyclopentene ring. The heterocycles can be substituted further, typically with alkyl groups at the reactive carbons and an additional aromatic cycle, for instance a phenyl- or benzo-substitution. While the aromatic side groups mostly increase electronic wave function delocalization in the closed-ring isomer, leading to a larger photochromic shift, fluorination was found to accelerate photoswitching by an order of magnitude.<sup>[224,225]</sup>

The nature and length of the substituents at the reactive carbons on the other hand influences the effective cyclization quantum yield in solution,<sup>[64,226,227]</sup> presumably indirectly

<sup>1</sup> See for instance ref. [223]

<sup>2</sup> The energy difference between highest occupied molecular orbital (HOMO) and lowest unoccupied molecular orbital (LUMO) for a given configuration.

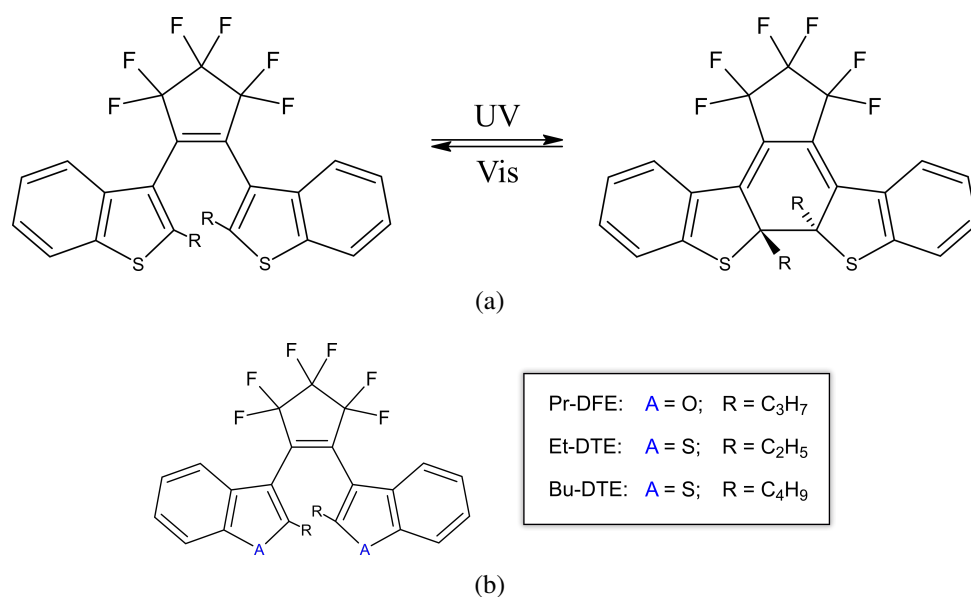


**Figure 5.2:** Diarylethene photochromism: (a) general reaction scheme (exemplary for di(benzothienyl)perfluorocyclopentenes), (b) structural formulae of the investigated derivatives.

by altering the ratio between different conformers of the open-ring isomer.<sup>[228,229]</sup> Two main conformers have been found to be stable in solution, both having C<sub>2</sub> symmetry, but either with the aryl groups in parallel or antiparallel orientation, and it has been shown that only excitation of the antiparallel conformer induces cyclization.<sup>[230]</sup> This is because only in case of the latter, the two reactive carbons are in spatial proximity and rotation of the subunits occurs several orders of magnitude more slowly than radiative or non-radiative relaxation of the excited states for either conformer. Thus, the measured quantum yields predominantly depend on the concentration ratio between these two conformers, which can be manipulated to a degree by changing the alkyl substituents,<sup>[231,232]</sup> or by further functionalization, for example introducing a second chemical bridge between the aryl subunits to limit their conformational degrees of freedom.<sup>[227,233]</sup> However, this general tendency is not found in all diarylethene derivatives, indicating that different substitution may also directly affect the quantum yield via manipulation of the excited-state potential energy surfaces and opening of relaxation pathways alternative to cyclization.<sup>[234]</sup>

Only pure single crystals of either the antiparallel or the parallel conformer are stable and only crystals of the antiparallel conformer can be photochromic due to the considerations above. Remarkably, these crystals either have a near-unity cyclization quantum yield or do not exhibit any photochromism at all, as shown by Kobatake and coworkers.<sup>[235]</sup> It was possible for them to link this observation to the equilibrium distance between the reactive carbon atoms of the open-ring isomer by means of X-ray crystallography. A critical carbon-carbon distance of 4.2 Å was determined, below which the quantum yield was close to 100 % for all investigated derivatives, while no coloration was observed for

greater spacings. An important conclusion of this study was that the photochromic reactivity was governed by the carbon-carbon distance rather than polarity or steric hindrance from substituents. However, the cyclization dynamics regarding rate constants and possible intermediates may still depend on these factors, which cannot be excluded based on the quantum yield alone.<sup>3</sup>

Further elucidating the effects of alkyl-substituents and hetero-atoms in the aryl moieties on the dynamics via systematic time-resolved studies promises to deepen the understanding of these influences and generally aid in the design and optimization of diarylethene-based photochromic materials. The study presented in this chapter represents the beginning of such an endeavor, investigating the structural and electronic cyclization dynamics of several related diarylethene derivatives by means of transient absorption spectroscopy and ultrafast electron diffraction. Since the extent of the latter exceeded the scope of this thesis, only preliminary tests using UED were carried out and will be discussed at the end of the chapter, while its main focus will lie on the discussion of TA data.

Three different diarylethene derivatives were investigated within this work: Ethyl-dithienylethene (Et-DTE), Butyl-dithienylethene (Bu-DTE) and Propyl-difurylethene (Pr-DFE). Their structural formulae are depicted in Fig. 5.2 (b) and their steady-state absorption spectra for both the respective closed and open forms in solution can be found in Fig. 5.3. These samples were recommended and provided by Prof. Masahiro Irie, specifically regarding their suitability for ultrafast experiments with single crystals.

Before presenting and discussing the obtained results from these three derivatives in crystal and solution, a brief overview of reported time-resolved studies is given, which provide important information on the used materials and are relevant for the discussion of the reaction dynamics.

### 5.1.2 Relevant reported studies

Soon after their discovery and initial characterization in 1988,<sup>[215,216]</sup> diarylethenes were investigated regarding their cyclization and cycloreversion dynamics by means of time-resolved spectroscopy.<sup>[236–241]</sup> The results from these pioneering works motivated a large number of time-resolved or at least mechanistic studies,<sup>[161]</sup> most of them using transient absorption,<sup>4</sup> but also time-resolved fluorescence spectroscopy,<sup>[244,259–262]</sup> Raman spectroscopy,<sup>[263–265]</sup> femtosecond electron diffraction,<sup>[56,57,83]</sup> and *ab-initio* or first-principles calculations.<sup>5</sup> Despite the large variety of photochromic diarylethenes, the vast

<sup>3</sup>If the reaction is faster, the quantum yield is generally increased, since the reaction pathway will out-compete alternative, slower pathways. However, other factors affect the quantum yield, for instance the inhibition of such alternative relaxation pathways due to spatial constraints.

<sup>4</sup>References [83, 224, 225, 228, 229, 233, 242–260].

<sup>5</sup>References [56, 83, 224, 225, 233, 234, 253, 266–273].

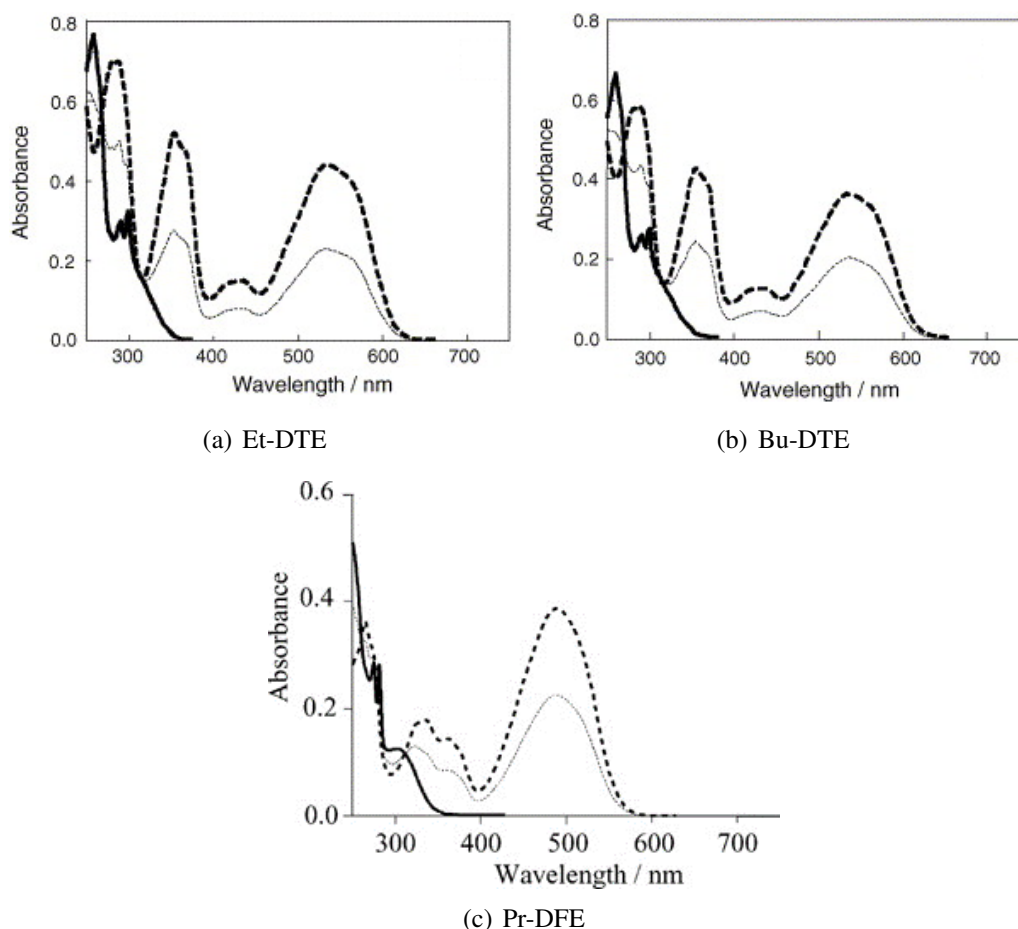


**Figure 5.3:** Reported steady-state absorption spectra of the investigated derivatives. Solid lines: open-ring forms, dotted lines: photostationary state, dashed lines: closed-ring forms. (a) and (b) reprinted with permission from ref. [231], ©2006 Elsevier S.A. (c) reprinted with permission from ref. [232], ©2006 Wiley VCH.

majority of these studies dealt with the dynamics of dithienylcyclopentenes.<sup>6</sup> Besides the general relevance of these particular derivatives, this research interest is rooted in the complexity of their spectral dynamics, which became evident early,<sup>[237]</sup> and the multitude of possible influences by chemical modifications. The fact that in solution, both the parallel and antiparallel conformers are excited and contribute to any time-resolved experiment poses further challenges, but even the dynamics attributed to the reactive conformer were found to be ambiguous, leading to contradictory interpretations in the literature (see the following section).

While there are no reported time-resolved studies dealing with the specific derivatives investigated here, a few studies exist on the cyclization<sup>7</sup> and cycloreversion<sup>[245,274,275]</sup> of Bis(benzo-methylthienyl)perfluorocyclopentene, which only differs from the present samples in terms of the alkyl substituents at the reactive carbon atoms, as well as the hetero-atoms in case of Pr-DFE. These studies will be discussed in more detail in a later

<sup>6</sup>References [56, 57, 83, 225, 228, 229, 233, 236–252, 254, 257, 258, 261, 262, 264–268, 271–275].

<sup>7</sup>References [228, 229, 254, 260, 262].

section, while key findings of the studies on the other, still chemically sufficiently similar, dithienylethene derivatives will be laid out in the following.

### Di(thienyl)perfluorocyclopentene cyclization dynamics in solution

The first published time-resolved studies on diarylethenes dealt with the cyclization of dithienylperfluorocyclopentene derivatives (DTE) and a resolution-limited time constant of 10 ps or less was determined.<sup>[236]</sup> Tamai and coworkers soon after reported a reaction time of 1.1 ps for a DTE being part of a thiophene oligomer and found evidence for the formation of a reaction intermediate prior to ring closing.<sup>[237]</sup> Additionally, they noted slower spectral components up to several ns and hypothesized their attribution to relaxation of the non-reactive parallel conformer. A later ps-time resolved Raman study of a DTE without further functionalization also determined a few-ps cyclization time constant (around 4 ps).<sup>[264]</sup> Ern et al. investigated a DTE derivative with bulky aromatic side chains supporting the existence of an intermediate excited species, in their case with a formation time of less than 1 ps, from which cyclization was concluded to occur with a time constant of 6 ps and also ascribed longer spectral dynamics to the parallel conformer.<sup>[247]</sup> Two combined experimental and theoretical studies by Hania and coworkers on phenyl-substituted DTE derivatives (Bis(phenyl-thienyl)cyclopentene, BPTE), either fluorinated or not, described the formation of such an intermediate within 150 fs via relaxation on the excited-state potential energy surface. According to their interpretation, this pre-switching step was followed by ring closure in 4.2 ps and planarization of the phenyl groups with an 8 ps time constant, for the non-fluorinated case. Cyclization was found to be accelerated to a time constant of 0.9 ps in the fluorinated derivative, while the other two processes were not altered significantly.<sup>[224,225]</sup> Bertarelli et al. on the other hand ascribed the fast dynamics below 200 fs after excitation directly to formation of the closed-ring isomer, in apparent contradiction to the other studies. However, Miyasaka and coworkers independently suggested the presence of two competing ring-closing pathways, a direct cyclization from the Franck-Condon state and an indirect, slower pathway via a longer-lived fluorescent state.<sup>[244]</sup> The existence of such a state was corroborated in a theoretical study from the same year,<sup>[234]</sup> characterizing it to be open-ring and in the 2A excited singlet state.<sup>8</sup>

In the following years, the cycloreversion reaction gained more attention from the scientific community since new approaches to increase its quantum yields had been discovered.<sup>[243]</sup> Thus, the open questions and disagreements in the literature remained unresolved for a few years before new experimental efforts were undertaken to further elucidate the reaction mechanism. In 2010, a study by Aloïse and coworkers took up the idea of two distinct cyclization channels, but for a bridged diphenylethene derivative.<sup>[253]</sup> Based on transient absorption data and TDDFT calculations, they inferred a direct pho-

<sup>8</sup>2A refers to the molecular orbital symmetry.

tocyclization channel through a conical intersection with a relaxation time constant of 120 fs and another channel via an open-ring intermediate in the first singlet excited state with a time constant of 1.5-2.5 ps, depending on solvent polarity. However, the rapid cyclization pathway was only observed for one of two studied derivatives and when exciting into higher lying excited states, at 266 nm instead of 390 nm ( $S_0$ - $S_1$  transition). While the investigated diarylethene molecules were significantly different from the DTE derivatives discussed here, a follow-up study investigating the more similar inverse dithienylperfluorocyclopentenes was published by the same group four years later, reinforcing their conclusion of two different pathways to exist, with time constants of 90 and 800 fs for the direct and indirect mechanisms, respectively, and in this case for excitation directly into  $S_1$ . In addition, a comparison between bridged and non-bridged DTE derivatives allowed them to isolate the spectral signature caused by excitation of the parallel conformer in case of the latter, which was confirmed to be absent for the bridged derivatives. The long-lived absorption band attributed to relaxation of the excited parallel conformer was determined to decay with a time constant of 120 ps.

Another comprehensive study on the dynamics of an inverse-type DTE, in this case the phenylated analog, was published recently by Sotome et al. in 2019.<sup>[259]</sup> In their study combining transient absorption and time-resolved fluorescence spectroscopy as well as TDDFT calculations, they concluded the existence of yet another non-reactive conformer with anti-parallel thiophene orientation. They based their conclusion on the existence of two different emissive spectral species as well as geometry optimization in the electronic ground-state of the open-ring isomer. For the reactive anti-parallel conformer, again a dual pathway was postulated, but due to the complex spectral dynamics only the indirect pathway via an excited-state intermediate was possible to resolve and associated with a 36 ps lifetime. From the TDDFT calculations, the intermediate was determined to have a reduced distance between the reactive carbon atoms, in agreement with previous reports.<sup>[234]</sup>

While caution needs to be taken when comparing inverse and normal type diarylethene dynamics, the coexistence of a direct and indirect cyclization pathway has evidently been concluded in several independent studies of different diarylethene derivatives and thus needs to be taken into account when discussing the results from the derivatives investigated within the scope of this thesis.

### **Bis(benzothienyl)- and Difuryl-perfluorocyclopentene cyclization**

Bis(benzo-thienyl)perfluorocyclopentenes have gained the attention of researchers more recently, predominantly due to their high cycloreversion quantum yields.<sup>[64]</sup> The reported literature on their cyclization almost exclusively deals with the same derivative, which is methylated at the reactive carbons (Me-DTE), and to which the following summary will

be limited. The first reported study on any benzothienylated diarylethenes, including Me-DTE, utilized time-resolved fluorescence spectroscopy and was published in 2007.<sup>[262]</sup> A biexponential decay of the spontaneous fluorescence was found with time constants of 1 ps and 100 ps, ascribed to alternative cyclization pathways, in agreement with the previously discussed literature. The absence of any contribution from the parallel conformer was explained by a presumably longer radiative lifetime of its excited state and thereby negligible oscillator strength.

Systematic transient absorption studies of the Me-DTE cyclization reaction were published by Ishibashi and coworkers, especially focusing on its solvent viscosity,<sup>[254]</sup> temperature<sup>[228]</sup> and solvent polarity dependences,<sup>[229]</sup> but also discussing the chemical species involved in depth. The transient spectra of Me-DTE in *n*-hexane from ref. [254] are shown in Fig. 5.4. The broad absorption spectrum after excitation was found to develop within a few ps into a transient spectrum consisting of the following features: A main absorption band around 520 nm, which was assigned to the closed-ring form (Me-DTE(c)), a shoulder at 620 nm, another band around 360 nm and a dip between the latter and the Me-DTE(c) absorption band. The bands at 360 nm and 620 nm were attributed to excited-state absorption from the S<sub>1</sub> to higher lying states, while the dip was interpreted as stimulated emission by comparison to the fluorescence spectrum. The excited-state bands were found to decay with time constants of  $\approx 450$  fs, in agreement with the rise time found for the Me-DTE(c) band, and this time constant ascribed to cyclization from the S<sub>1</sub> state. In the sub-ns time domain, the dip signal decayed, manifesting as a rise in absorbance, while the signals at 520 nm and 620 nm decreased with time constants around 150 ps. The absorbance at 620 nm did not vanish entirely within 1 ns, which implied a longer-lived decay in this spectral region towards the steady-state absorption. This was confirmed to occur in the  $\mu$ s range by separate measurements. The 150 ps decay component was supported by complementary fluorescence measurements. In contrast to the previous study, the long decay component was concluded not to contribute to cyclization, but ascribed to the parallel conformer. Residual absorbance above 600 nm was attributed to the triplet state of the latter, confirmed by oxygen deactivation.

The assignment of the slow decay component to fluorescence of the parallel conformer was corroborated in a more recent study employing time-resolved fluorescence and transient absorption by Seo et al. who also concluded that cyclization occurred within 2 ps after excitation.<sup>[260]</sup>

In contrast to dithienylcyclopentene derivatives, the dynamics of their difuryl analogs have not been studied extensively. Only recently, an investigation of a difurylperfluorocyclopentene (DFE) derivative with phenylethynyl functionalization was published applying transient absorption spectroscopy in solution and TDDFT calculations.<sup>[276]</sup> The authors reported a 420 fs ring-closing time constant and an overall similar picture of the excited-state potential energy surfaces along the C-C distance reaction coordinate. However, the transient absorption study was limited by a time resolution of around 200 fs and no time

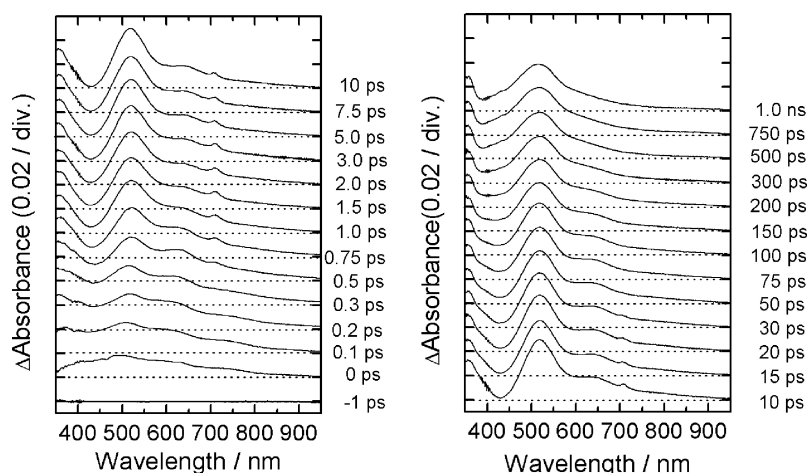


**Figure 5.4:** Transient absorption spectra of Me-DTE in *n*-hexane. Reprinted with permission from ref. [254], ©2011 American Chemical Society.

delays beyond 3 ps were shown. Since in case of the dithienyl derivatives, spectral dynamics extending into the sub-ns range or beyond have been reported, further investigations are required to obtain a more holistic picture of the photochemical dynamics.

### Diarylethene cyclization dynamics in crystal

Relative to the large body of publications dealing with diarylethene photochromism in solution, only few studies exist on the cyclization or cycloreversion dynamics in the crystalline phase,<sup>[56,83,238,249,250]</sup> despite the large variety of potential applications (*vide supra*). This can be explained by the comparatively high effort this type of study entails, especially if reaction products are thermally stable, because rapid sample exchange is not as easily provided as in case of solutions. The early studies relied on sample replacement via translation,<sup>[250]</sup> or continuous wave irradiation,<sup>[56,83]</sup> both significantly reducing feasible repetition rates. Nonetheless, already in 1997, a resolution-limited cyclization time of 10 ps was reported by Miyasaka et al. for dithienylperfluorocyclopentene.<sup>[238]</sup> Ten years later, Tani and coworkers investigated the phenyl-substituted analog (BPTE, *vide supra*) and found cyclization to occur within "a few picoseconds" (*sic!*).<sup>[250]</sup>

The most extensive study on crystalline diarylethene to date was carried out by Jean-Ruel and coworkers employing transient absorption spectroscopy, ultrafast electron diffraction and *ab-initio* methods.<sup>[56,57,83]</sup> The first article, published in 2011, was based primarily on transient absorption experiments, assisted by preliminary electron diffraction results and TDDFT calculations of electronic transitions in either isomer.<sup>[83]</sup> By analysis of their TA experiments, they were able to identify the formation of a reaction intermediate, manifested in a blue-shift of the absorption maximum towards 500 nm and with a time constant of approximately 200 fs. The decay of this spectral feature was determined to occur with a 5.3 ps time constant, simultaneously to the rise of the product band at 635 nm. A 7.3 ps time constant was found for the product band formation, but stated to be affected by resid-

ual decay of the broad excited-state absorption.<sup>9</sup> Comparing these results to the reported time constants in solution in the sub-3 ps range, a significant deceleration was noticed, which was ascribed to the higher degree of confinement of the molecular motions in the crystal lattice. Furthermore, the authors noted that the simplicity of these dynamics in comparison to solution can be explained by the absence of the parallel isomer in single crystals (*vide supra*).<sup>10</sup>

As noted, this study also employed ultrafast electron diffraction (UED), but merely as a means to verify the attribution of the long-lived absorption band to the closed-ring isomer, foreshadowing the more detailed crystallographic study published two years later.<sup>[56]</sup> The latter not only marked an important milestone towards the direct observation of chemical reactions via UED,<sup>[5,19]</sup> but also showed how the cyclization reaction was driven by only a few key vibrational modes in a vast reduction in dimensionality. This was facilitated by an improvement in time resolution compared to the previous study, allowing for the investigation of the few-ps dynamics, and an in-depth model analysis of the data. In the latter, the general structural changes towards formation of the excited-state intermediates as well as the driving modes of the cyclization were identified. The excited-state intermediate structure was determined to involve convergence of the thiophene moieties, which was corroborated in a complementary numerical optimization on the  $S_1$  potential energy surface, similar to the one discussed in section 3.2.2 and ref. [68]. It was concluded that the thiophene rotational mode was the main motion involved in the reaction, while the perfluorocyclopentene ring underwent only minimal changes, and the ring-closing time constant of around 5 ps found in the transient absorption experiments was confirmed.

Nevertheless, a few limitations of this study need to be pointed out, as they represent an essential motivation for the investigations commenced within the scope of this work. The results were mostly made possible by advancements in electron diffraction source technology regarding both source brightness and time resolution, as well as the development of an *in-situ* photoreversion scheme. However, the sample itself posed significant problems due to its lack of reversibility. Firstly, the particular diarylethene derivative suffered from a low cycloreversion quantum yield of only around 3 %, while the cyclization yield, as for most diarylethenes exhibiting photochromism in the crystalline phase, was close to 100%.<sup>[222]</sup> Hence, if hypothetically 100 open-ring molecules are excited by a single UV pulse, all of these will be converted to the closed-ring isomer. Even if exciting all of these closed-ring molecules with a single visible pulse, only 3 out of these 100 molecules can be expected to go back to the open-ring form. Consequently, a large number of ex-

---

<sup>9</sup>Another factor to be considered in these single-point kinetics would be band narrowing via vibrational cooling (conf. section 3.2.2), which can also cause a slower time constant. In any case, it is reasonable to consider the decay of the intermediate band as the true reaction time constant.

<sup>10</sup>This in turn has important implications for the interpretation of the solution data. As will be demonstrated in this chapter, analysis of the dynamics in crystal – if they are indeed less complex than in solution – can aid to reliably attribute the observed spectral dynamics in solution to the antiparallel and parallel conformers, respectively.

citation cycles for cycloreversion in-between pump-probe cycles is required for complete reversibility, drastically limiting the effective repetition rate (0.1 Hz in case of ref. [56]). Furthermore, when using a cw laser for photoreversion, crystal damage due to strain induced by the formed product molecules cannot be prevented as well as in case of a pulsed synchronized photoreversion, where a significant fraction of the molecules is reverted only a few 100 ps after excitation or less.<sup>[63]</sup> Finally, using shorter wavelengths than  $\approx 300$  nm, as in case of the reported electron diffraction experiments, has been shown to induce rapid sample fatigue,<sup>[64,83]</sup> most likely due to byproduct formation when exciting remaining closed-ring molecules into high-lying excited states.<sup>[277,278]</sup> Thus, this problem is even magnified when dealing with low cycloreversion quantum yields. For these reasons, the experimental repetition rate and the total number of cycles per crystalline sample were drastically impeded, limiting the feasible amount of datasets to average over and thereby the achievable signal-to-noise ratio. Even though these circumstances make this pioneering study all the more remarkable, an improvement in these regards promises to significantly enhance the amount of information which can be gathered directly from the data, without having to rely on, but rather complementing results from theoretical simulations.

The discussed limitations can be overcome to some extent by additions to the laser systems to enable the excitation at longer wavelengths in the UV as well as by applying the synchronized photoreversion experimental scheme in order to avoid crystal strain. However, the low cycloreversion quantum yield remains an inherent property of the specific diarylethene derivative and necessitates the use of more suitable systems, at least as long as single-cycle capabilities of ultrafast electron diffraction setups are not sufficiently developed. This is the main justification – besides their general relevance in the previously reported literature – for the choice of diarylethene derivatives in this study. Their cycloreversion quantum yields in solution have been reported to be higher by an order of magnitude compared to BPTE, and this improvement can be assumed to be similar in crystal in analogy to other, structurally similar derivatives.<sup>[64]</sup>

## 5.2 Experimental Details

### 5.2.1 Sample preparation

Ethyl-dithienylethene (Et-DTE),<sup>11</sup> Butyl-dithienylethene (Bu-DTE),<sup>12</sup> and Propyl-difurylene (Pr-DFE)<sup>13</sup> were synthesized by the group of Prof. Masahiro Irie and received as a crystalline powder.<sup>14</sup> Sample solutions for experiments were prepared using acetoni-

<sup>11</sup> 1,2-Bis(2-ethyl-1-benzothiophen-3-yl)perfluorocyclopentene.

<sup>12</sup> 1,2-Bis(2-butyl-1-benzothiophen-3-yl)perfluorocyclopentene.

<sup>13</sup> 1,2-Bis(2-propyl-1-benzofuran-3-yl)perfluorocyclopentene.

<sup>14</sup> For details on the synthesis of these compounds see refs. [232] and [231].

trile as a solvent (spectroscopy grade) with concentrations of 2 mM (Et-DTE), 1.5 mM (Bu-DTE) and 3 mM (Pr-DFE). Millimeter-sized single crystals were grown from *n*-hexane solutions of the compounds via slow evaporation of the solvent (see section 2.6). For the experiments, sufficiently thin crystal slices with thicknesses between 100 nm and 800 nm were obtained by ultramicrotomy (see section 2.6). The static absorption spectra of either forms for all of the utilized derivatives had been reported previously and are shown in Fig. 5.3. Recorded steady-state absorption spectra from the solutions were taken for comparison and calculation of the excitation fractions (see section A.2 in the appendix).<sup>15</sup>

## 5.2.2 Transient absorption

Transient absorption spectroscopy measurements were conducted for all three derivatives in both solution and crystal, using the home-built setup in the respective configurations (see section 2.4.2). The synchronized photoreversion scheme was applied for the crystalline samples due to their thermal irreversibility, using the broadband UV laser source for excitation and the visible NOPA for reversion. Sample solutions were reverted using the visible lamp as in case of the protonated spiropyran (see section 4.3.1). Pump fluences between 1 and 3 mJcm<sup>-2</sup> and repetition rates of 20-32 Hz for crystals and 500 Hz for solutions were used and the suitability of these parameters verified in fluence dependence series (see section A.3 in the appendix). Due to the still limited reversibility of the crystalline samples, separate scans from different slices, but with the same thickness and from the same crystal facet, were taken to cover different time ranges with appropriate time steps.

## 5.2.3 Electron diffraction

Electron diffraction experiments were carried out using the compact diffractometer described in section 2.5.3 (conf. Fig. 2.16). The machine was operated with the Pharos laser system using its fourth harmonic (257 nm) for electron beam generation, the third harmonic (343 nm) for excitation and a visible NOPA (580 nm central wavelength) for synchronized photoreversion. Since sample exchange necessitated venting of the vacuum chamber, the samples needed to be stable for several days under ultra-high vacuum in order to reestablish the conditions for stable operation of the electron gun at ≈90 kV. For this reason, the sample holder was cooled down to temperatures around 250 K using liquid nitrogen.

Time-resolved tests were carried out at pump fluences between 1 and 2 mJcm<sup>-2</sup> at a repetition rate of 31.25 Hz while the photoreversion fluence was varied between 5 and

---

<sup>15</sup>The estimated excitation fractions per fluence lie between 0.7 and 1%/(mJcm<sup>-2</sup>).

$10 \text{ mJcm}^{-2}$  at a repetition rate of 100 Hz.<sup>16</sup> The bunch charge of the electron pulses was determined via the pulse energy of the photocathode beam based on a separate calibration measurement. For all results discussed in this chapter, bunch charges of 5 fC ( $3.1 \cdot 10^4$  electrons) per pulse were used.

Indexing of the diffraction peaks was done based on simulated diffraction patterns from the reported crystal structures<sup>17</sup> using the CrystalMaker<sup>[178]</sup> software suite (see appendix for further information on the process).

## 5.3 Difurylene Cyclization Dynamics

The cyclization dynamics of the photoexcited antiparallel Pr-DFE conformer are summarized in Fig. 5.5, based on the findings presented in this section. It will be shown that ring closing proceeds via a single reaction pathway involving an excited-state intermediate with lifetimes of 500 fs and 300-400 fs in solution and crystal, respectively. Except for the slight acceleration in crystal, the mechanism was found to be identical in either case. It was possible to distinguish these dynamics from spectral signatures of the non-reactive parallel conformer, which will be discussed when revisiting the picture at the end of the section.

### 5.3.1 Solution TA

Transient absorption spectra of the 3 mM solution of Propyl-difurylene in acetonitrile, photoexcited at 330 nm with a peak fluence of  $2.3 \text{ mJcm}^{-2}$ , are shown in Fig. 5.6. Immediately after excitation at a pump-probe delay of 100 fs and following the cross-phase-modulation signal, a broad positive absorption band with a maximum around 550 nm becomes visible. Within the following 200 fs, an additional band rises, with a more distinct maximum around 450 nm. Both of these features decay within the next  $\approx 1$  ps and give rise to a long-lived absorption band with a maximum around 500 nm, readily assigned to the closed-ring photoproduct.<sup>[232]</sup> Closer inspection of the data reveals that decay of the intermediate features involves their shift towards the long-lived band. The few-ps to sub-ns dynamics are dominated by a residual decay of the initial absorption band. It appears that the decay at wavelengths above 550 nm occurs more slowly than the decay of the feature around 450 nm, which will be investigated further in the following section.

<sup>16</sup>The relatively high peak fluence may raise concerns regarding the peak power. However, the fundamental pulse duration of the laser being 170 fs puts these fluences in a reasonably safe range regarding multi-photon absorption processes (see section 2.4.5).

<sup>17</sup>The crystallographic files were provided in the respective supporting information sections of [231] and [232].

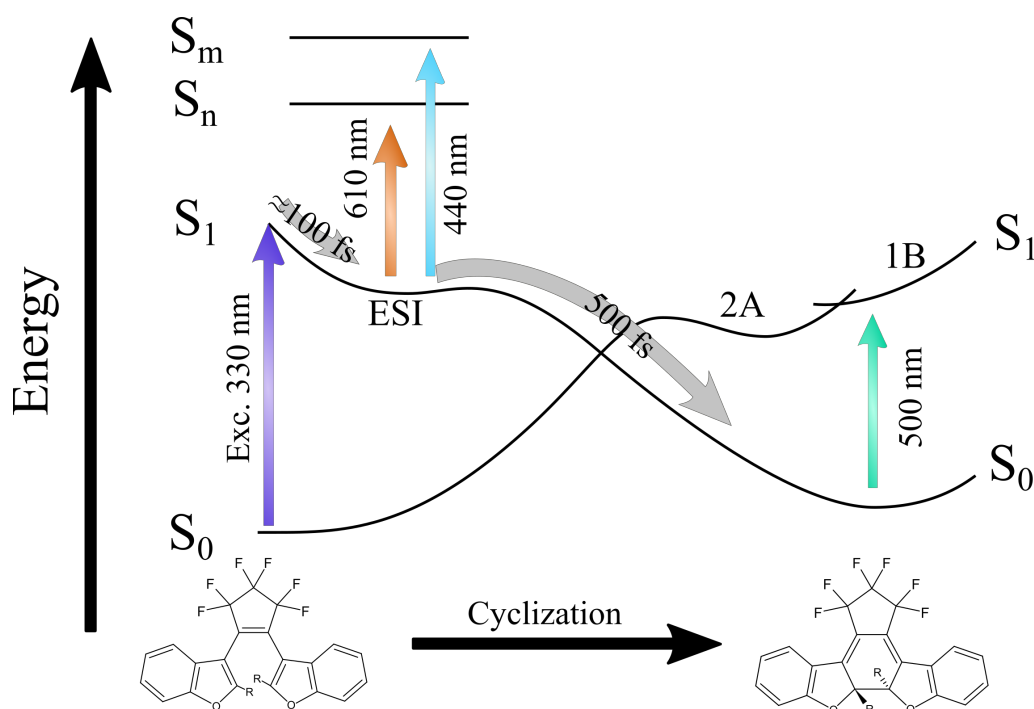


**Figure 5.5:** Summary of the Pr-DFE cyclization dynamics based on the obtained transient absorption results. Shown are the dynamics from the excited antiparallel conformer. Indicated time scales and transition wavelengths refer to the solution data. The qualitative mechanism in crystal was found to be identical.

### Analysis

Fig. 5.7 shows (a) the decay- and (b) the species-associated spectra from a parallel decay model and a unidirectional sequential model, respectively, applied to the first 100 ps after excitation. The obtained decay time constants from global analysis were identical to the corresponding transfer time constants in the sequential model and thus, the DAS and SAS can be interpreted interchangeably. The first decay component with a time constant of 70 fs describes the decay of the broad excited-state absorption signal, which carries some residues from the strong CPM signal, as well as the rise of the intermediate absorption bands with maxima around 450 nm and 600 nm. Notably, the first time constant is on the order of the estimated instrument-response function of  $\approx 50$ -100 fs. The second component entails the decay of these intermediate features as well as the rise of the product band with a time constant of 500 fs. An additional decay component was found with a positive amplitude, a maximum around 550 nm and a decay constant of 3.7 ps, which is responsible for the aforementioned slower decay of the absorption band above 500 nm. The long-lived product absorption signal is represented by the fourth component and besides the main band around 500 nm consists of a second, smaller shoulder around 600 nm. For time delays beyond 100 ps, the latter appears to decay slightly but this process is too slow to be fit within the measurement window of 1 ns.

As laid out in the beginning of this chapter, it is known from other diarylethene derivatives that solutions of the open-ring forms contain both the reactive antiparallel and the

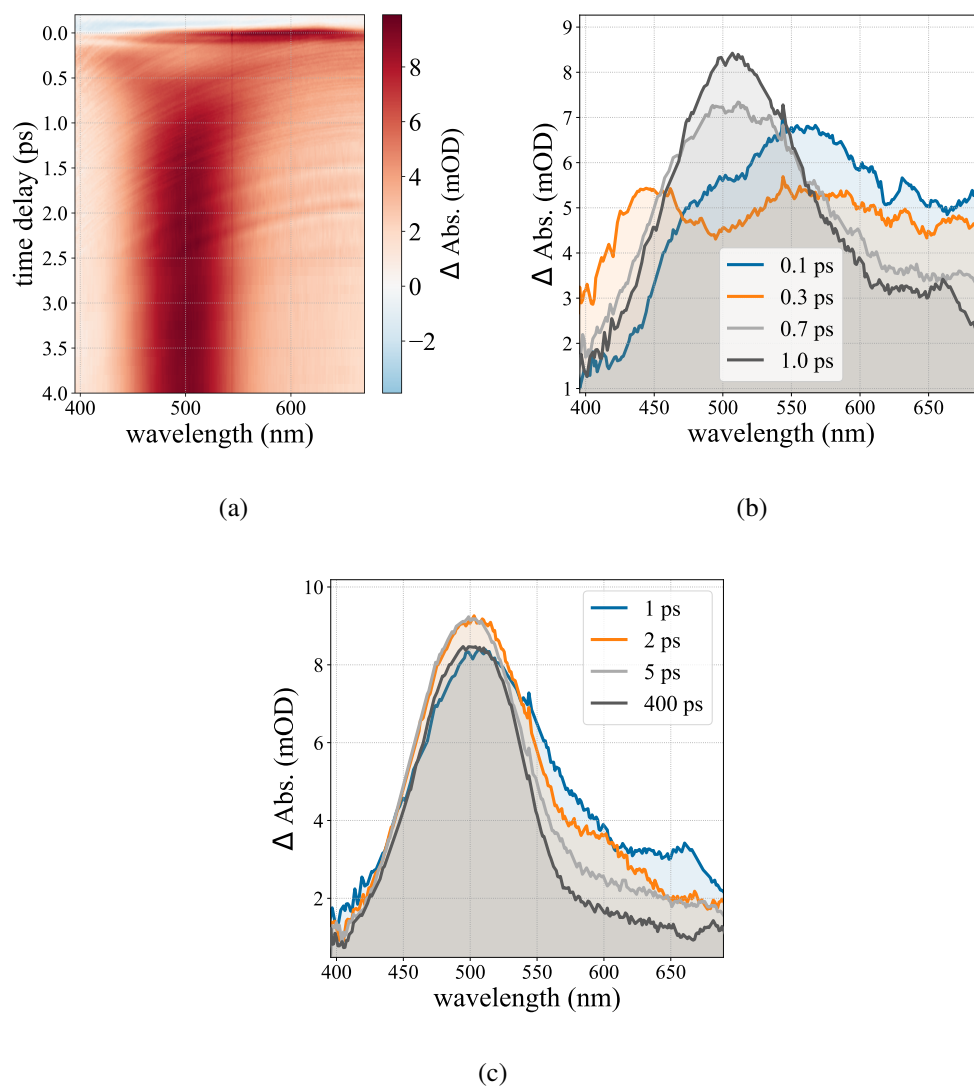


**Figure 5.6:** Transient absorption of photoexcited 1.5 mM Propyl-Difurylethene in acetonitrile. Shown are (a) the TA map for the first 4 ps as well as spectral traces for (b) the sub-ps and (c) the 400 ps range.

non-reactive parallel conformer.<sup>[230]</sup> Since excitation of the parallel conformer would thus manifest in an independent decay, a semi-sequential model was tested, in which a two-step kinetic chain was superimposed with an additional decay component (see Fig. 5.8). This resulted in a combination of the two previously applied global fits with the SAS of the sequential part (species A-C) closely resembling those from the pure sequential model and having similar time constants. The SAS of the independently decaying species D on the other hand was nearly identical to the third component from global analysis and associated with the same decay constant of 3.7 ps. The results of these models will be discussed in the following section.

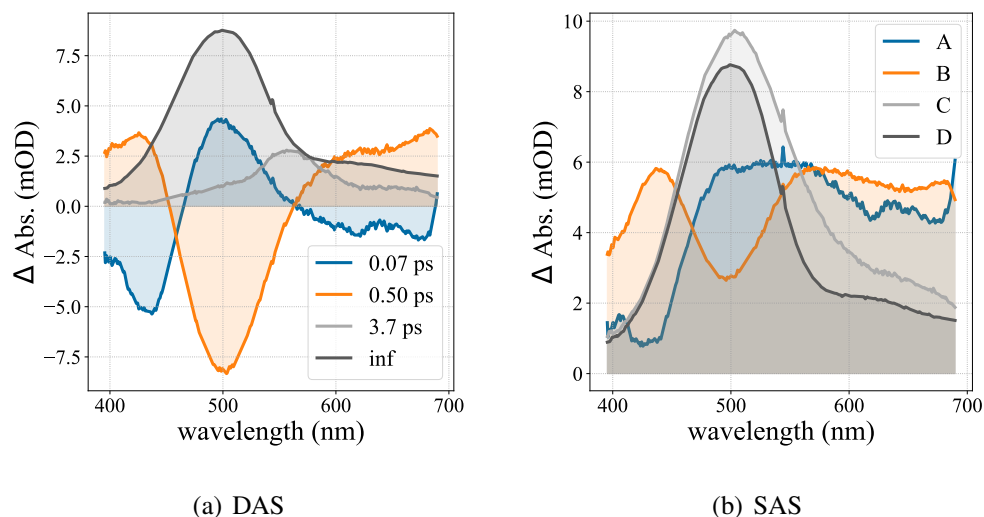


**Figure 5.7:** (a) Global and (b) target analysis (unidirectional sequential model) of photoexcited Pr-DFE in solution for 100 ps after excitation. The retrieved time constants as indicated in (a) were identical for both methods.

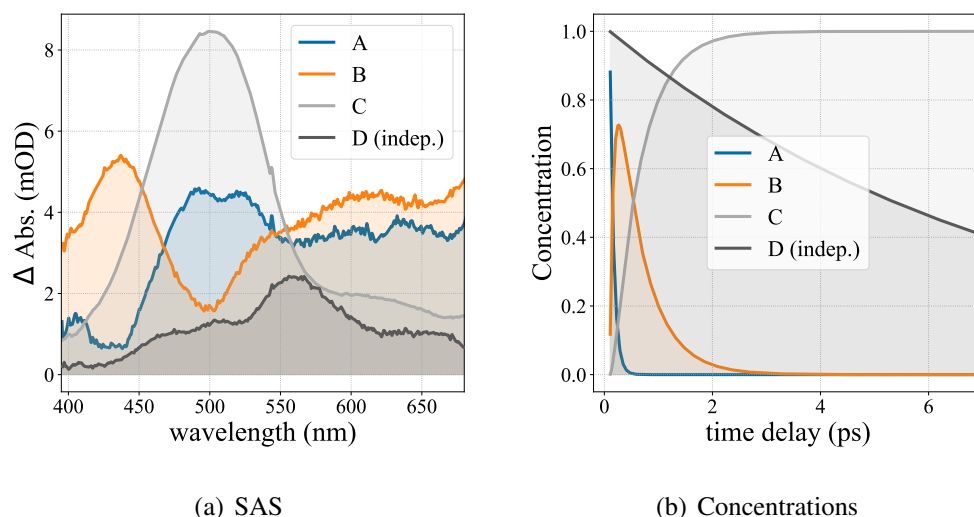


**Figure 5.8:** Semi-sequential global fit of photoexcited Pr-DFE in solution for 100 ps after excitation. (a) Species-associated spectra and (b) corresponding concentrations. Species A-C follow a sequential model with a parallel decay of species D.  $\tau_{AB} = 70$  fs,  $\tau_{BC} = 510$  fs and  $\tau_D = 3.7$  ps.

## Discussion

In analogy to previously reported time-resolved studies on the cyclization dynamics of structurally similar diarylethenes (see section 5.1.2), the sub-ps dynamics of the present Propyl-difurylene derivative are readily interpreted as the rapid formation of an excited state intermediate species with a time constant of  $\approx 100$  fs, which has two absorp-

tion bands in the visible, one around 440 nm and the other around 600 nm.<sup>18</sup> The spectral shift entailing its formation highlighted in refs. [225] and [83] is also present in this data. For other derivatives, this intermediate species was shown to be open-ring, but with the hetero-aryl moieties rotated towards each other in comparison to the open-ring ground state structure.<sup>[56,259,267]</sup> While lacking definite proof for the current system, the structural similarity of the native molecules allows for the preliminary hypothesis that the present intermediate is also an open-ring isomer in the first singlet excited state ( $S_1$ ). In the following step with a time constant of  $\approx 500$  fs, the wave packet propagates through a conical intersection into the  $S_0$  state, while undergoing closure of the cyclohexadiene ring. This assignment is made based on the formation of the long-lived absorption band closely resembling the reported ground-state absorption spectrum of the closed-ring isomer, which exhibits no significant changes on the time scale beyond 1 ps.

The ps-dynamics are more ambiguous than the cyclization dynamics. The SAS from the pure sequential model suggest that the spectral evolution with a 3.7 ps time constant mostly involves a hypsochromic shift of the product absorption band and simultaneous narrowing, which could both be attributed to vibrational cooling and cause the lack of spectral changes below 500 nm, while a noticeable decay occurs at longer wavelengths. However, the maximum position of the band does not shift by more than a few nm, failing to explain the asymmetry of the supposed spectral narrowing.

This observation is in line with the corresponding DAS from global analysis, which does not have the characteristic sigmoidal shape for a spectral shift but represents an independently decaying absorption spectrum with a distinct maximum around 560 nm. While its baseline could be attributed to the simultaneous shift and narrowing of the main band, the shape of this feature implies the contribution from an additional species. The independence of this process is corroborated by the semi-sequential model, which proves that the sub-ps dynamics can be treated independently from this decay yielding an almost exact replica of the third component for the independent species (3.7 ps lifetime). Since there is no correlated formation of another long-lived absorption band nor a contribution to the product absorption on this time scale, it can be concluded that this component describes the relaxation of a different excited-state species without contributing to the cyclization. The hypothetical internal conversion of the antiparallel conformer would be in contradiction to the reported high quantum yields of the latter for related derivatives<sup>[64]</sup> and suggests that any contribution from such pathways should be minor. Therefore, the most plausible assignment of this component is to the photoexcited, non-reactive, parallel conformer (P), in agreement with various previously reported studies on similar derivatives (*vide supra*).

As evident from the constant DAS (or SAS), the absorbance above 575 nm is still non-zero at 100 ps after excitation, which does not match the steady-state absorption of the

---

<sup>18</sup>N.B.: It is possible that the two apparent bands belong to the same transition, if the dip between them is due to stimulated emission. However, this would have no influence on the interpretation of these signals.

closed-ring isomer (see Fig. 5.3). A single-wavelength fit of the present data at 600 nm for the time window between 10 ps and 1 ns, where the aforementioned complications from earlier spectral shifts no longer play a role, yielded an additional decay component with a time constant of 110 ps.<sup>19</sup> Thus, deactivation of the excited parallel conformer appears to be biexponential in the present case with time constants of 3.7 ps and 110 ps. This means that the Franck-Condon state of the P conformer decays into a distribution of two different excited-state intermediates, since multiple decay channels of the same species ought to result in a monoexponential behavior.<sup>20</sup>

As outlined in section 5.1.2, similar independent spectral components with lifetimes on the order of 100 ps have been reported in time-resolved measurements of dithienylcyclopentene derivatives,<sup>[237,247]</sup> including the structurally similar bis(methylbenzothienyl)ethene derivative,<sup>[229,262]</sup> and assigned to an excited-state of the P conformer. In case of the latter derivative, the lifetime of this species was found to be 200 ps in acetonitrile. This decay channel was ascribed to fluorescence, which may also be the dominant relaxation mechanism in the present case, although this requires verification by direct measurements. A longer-lived absorbance in this region in analogy to the Me-DTE results observed and ascribed to intersystem crossing to the T<sub>1</sub> state of P by Ishibashi et al. (see ref. [254]) was not found in the present case.

### 5.3.2 Crystal TA

Fig. 5.9 shows the transient absorption data obtained from a 700 nm thin single crystal of the Propyl-difurylene derivative, excited at 330 nm (peak fluence of 1.6 mJcm<sup>-2</sup>) and photoreverted using a visible NOPA with a central wavelength of 530 nm. The spectral region between 490 nm and 560 nm is affected by scattering from the reversion beam and will be neglected in the following. The data shows high qualitative similarities with the solution sample, exhibiting an initial rise of a short-lived absorption spectrum within  $\approx 200$  fs after excitation, which has a local maximum around 425 nm and increased absorption in the spectral region around 600 nm. At shorter wavelengths, the signature of another absorption band is visible, though its maximum appears to lie outside the probe wavelength range. After 200 fs, these features start to decay and give rise to a long-lived band in the region where the closed-ring product is known to absorb. Despite the scattering background, its center can be estimated to lie around 500 nm. This band reaches its maximum amplitude around 2.5 ps after which point only minor spectral changes occur, mostly in the region of longer wavelengths.

<sup>19</sup>Adding another decay component and covering the entire measurement window of 1 ns did not lead to a reliable convergence of the global fit algorithm. The corresponding signal amplitude of 0.7 mOD was likely too small in comparison to the other signals.

<sup>20</sup>An alternative explanation would be the presence of a second non-reactive conformer, as it was reported for an inverse dithienylethene where a biphasic decay was observed as well. However, so far only the P and AP conformers have been shown to be stable for any of the derivatives investigated here.

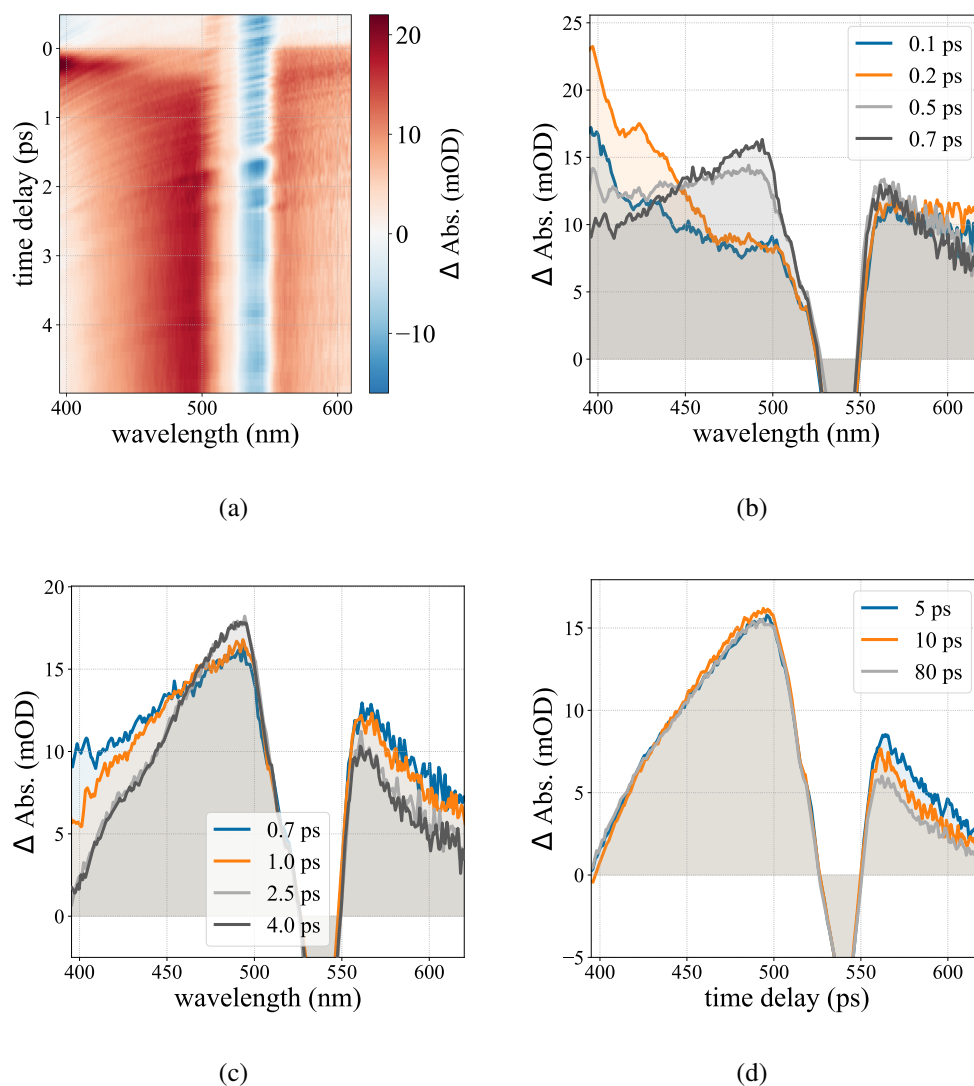


**Figure 5.9:** Transient absorption of photoexcited single-crystalline Pr-DFE (700 nm thickness). Shown are (a) the TA map for the first 5 ps as well as spectral traces for (b) the sub-ps, (c) the few-ps and (d) the 100 ps range.

### Analysis

In Fig. 5.10, the results from global and target analysis for both the 5 ps range and the 100 ps range datasets are depicted. The high similarity to the solution data stated in the previous section is reflected in the decay- and species-associated spectra as well as the corresponding time constants of 0.13 ps and 0.47 ps. The rise of the intermediate spectrum is visible in the first component and sequential step, respectively, while their subsequent decay towards the long-lived absorption spectrum is described by the second decay component. Due to the limited time window, another component for the spectral evolution on the few-ps time scale was not possible to fit for this dataset. On the other hand, an additional decay with a lifetime of 4.7 ps was found for the longer time window, which predominantly describes a spectral narrowing of the long-lived absorption band with a small, positive amplitude below 450 nm and above 560 nm as well as a negative amplitude

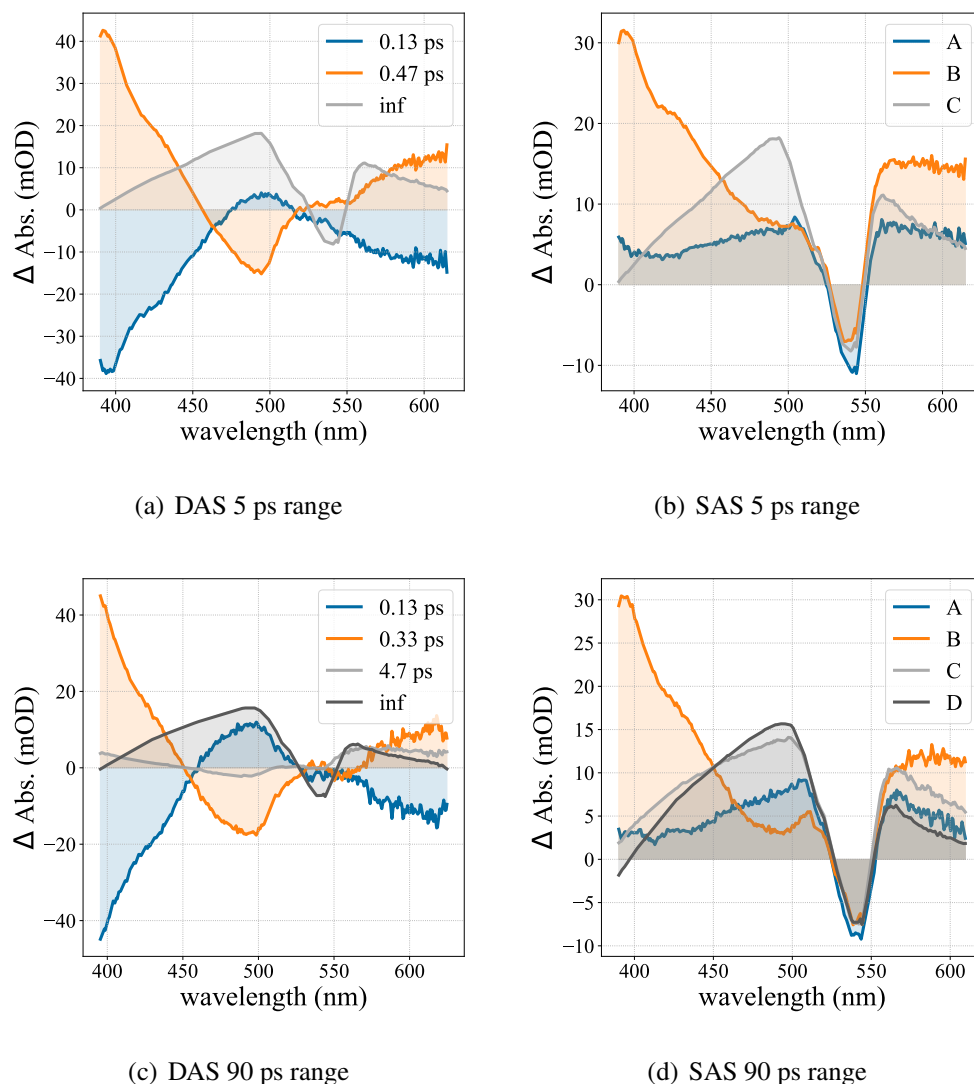


**Figure 5.10:** Global (left column) and target analysis (right column) of photoexcited PrDFE in crystal. Separate fits for the 5 ps range (first row) and the 90 ps range (second row) were carried out. The lifetimes from global analysis indicated in the figures matched the time constants from the respective kinetic models.

in the region of the product absorption. This process is likely even more comprehensible considering the difference in SAS between species C and D. Notably, while there is a residual decay at longer wavelengths than the main product band, the distinct maximum found in the analysis of the solution data is missing. Separate single-point fits of kinetic traces (see Fig. A.24 in the appendix) suggest that the decay of the spectral wings is indeed slower at 600 nm (3.3 ps) than at 400 nm (1 ps), although this may be skewed by the large amplitude of the faster decay component (470 fs) at 400 nm, which according to the DAS dominates the dynamics at this wavelength.

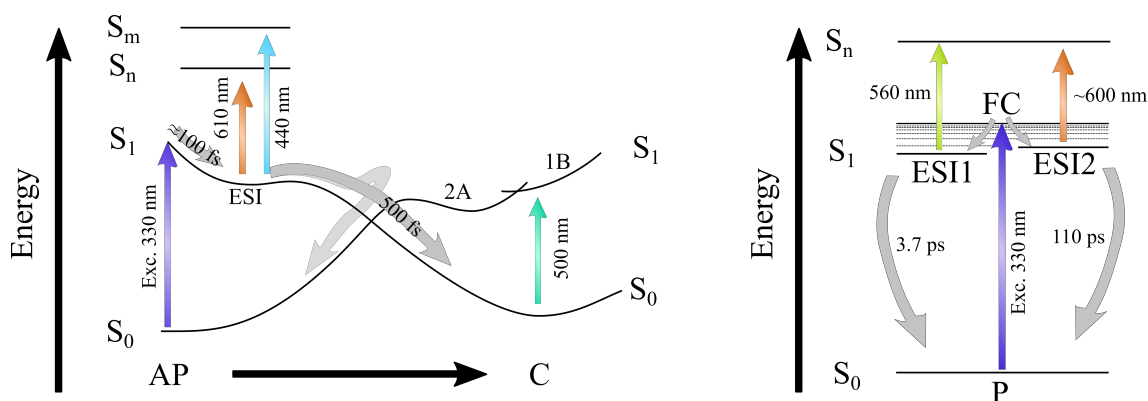


**Figure 5.11:** Schematic representation of the Pr-DFE reaction dynamics in solution. The left diagram shows the dynamics of the photoexcited antiparallel conformer, which undergoes cyclization via an excited-state intermediate with a lifetime of  $\approx 500$  fs. Excited parallel conformers (right panel) undergo biphasic relaxation from two different excited-state configurations. Cyclization of the antiparallel conformer was found to be identical in crystal except for a faster ring-closing time of 300-400 fs.

## Discussion

The ring-closing time appears to be slightly faster in crystal than in solution, with a time constant of  $\approx 300$ -400 fs.<sup>21</sup> It is possible that the confinement in the crystal lattice affects the molecular configuration in a way that favors cyclization. In particular, the equilibrium distance between the reactive carbons may be reduced with respect to solution, although in the latter case, it has not been reported as its measurement is less attainable experimentally.

The main difference between crystal and solution data lies in the separate absorption maximum on the longer wavelength edge of the product absorption spectrum, which is present in solution, but absent in crystal. Even though there is a residual decay around 600 nm with a time constant of 3.3 ps in case of the crystal, significant narrowing of the product absorption spectrum is observed on both edges of the spectrum in this time range, which is most likely the cause of these spectral dynamics. As previously pointed out, the present single crystals exclusively consist of the antiparallel conformer. Thus, the outcome of the crystal analysis confirms the conclusion drawn from the solution TA data, that the separate decay component in the latter case is most likely caused by photoexcitation of the parallel conformer in solution. This demonstrates how, despite the higher experimental effort compared to solution, studying the diarylethene dynamics in crystal can aid to interpret the more ambiguous results from solution by enabling isolation of only one of multiple possible conformers.

<sup>21</sup>The time constant from the short-range scan is presumably slightly too large due to the lack of the intermediate component.

### 5.3.3 Summary

The dynamics of photoexcited Propyl-DFE are summarized schematically in Fig. 5.11 for both conformers present in solution. Excitation of the parallel conformer does not lead to cyclization and the excited state decays biexponentially with a faster time constant of 3.7 ps and a slower one of 110 ps, which is potentially due to a radiative decay channel. The excited antiparallel conformer converges towards a local minimum on the  $S_1$  PES within 100 fs to form an excited-state intermediate, from which the closed-ring product is formed with a time constant of 500 fs. In crystal, where only antiparallel conformers are present, the same mechanism can be deduced, albeit with a slightly faster cyclization time constant of 300-400 fs. This observation is remarkable since for other diarylethene systems studied in the crystalline phase a deceleration of the reaction was observed compared to solution (*vide supra*).

## 5.4 Dithienylethene Cyclization Dynamics

This section deals with the cyclization dynamics of the two dithienylethene derivatives, investigated by transient absorption spectroscopy in solution and crystal. Due to the high similarities in the respective datasets, they will be treated conjointly, first discussing the results from solution, followed by the single crystalline samples and concluded in a combined interpretation at the end of the section. The key findings are summarized in Fig. 5.12, showing a schematic of the potential energy surface along the cyclization coordinate for the antiparallel conformers, exemplarily for the case of Ethyl-DTE in crystal. It will be shown in this section that two distinct ring-closing pathways exist, involving individual excited-state intermediates with significantly different lifetimes. Both were found to be reduced in crystal with respect to solution for either derivative.

### 5.4.1 Solution TA

#### Ethyl-Dithienylethene

The transient absorption data from a 2 mM acetonitrile solution of open-ring diethylthienylethene (Et-DTE), photoexcited at 330 nm with a peak fluence of  $2.3 \text{ mJcm}^{-2}$ , is shown in Fig. 5.13. The early dynamics qualitatively consist of the same signals as the ones from Pr-DFE presented in the previous section, but differ regarding the central wavelengths and lifetimes. From an initial, broad absorption spectrum, a short-lived positive signal arises within 500 fs after excitation, with a maximum around 425 nm and a second peak around 600 nm. The rise of the feature around 425 nm involves a slight blue-shift within the first 200 fs. Subsequently, these maxima decay, simultaneously to the formation of a long-lived absorption band, centered around 550 nm, which by comparison to the reported steady-state absorption can be assigned to the closed-ring photoproduct. While

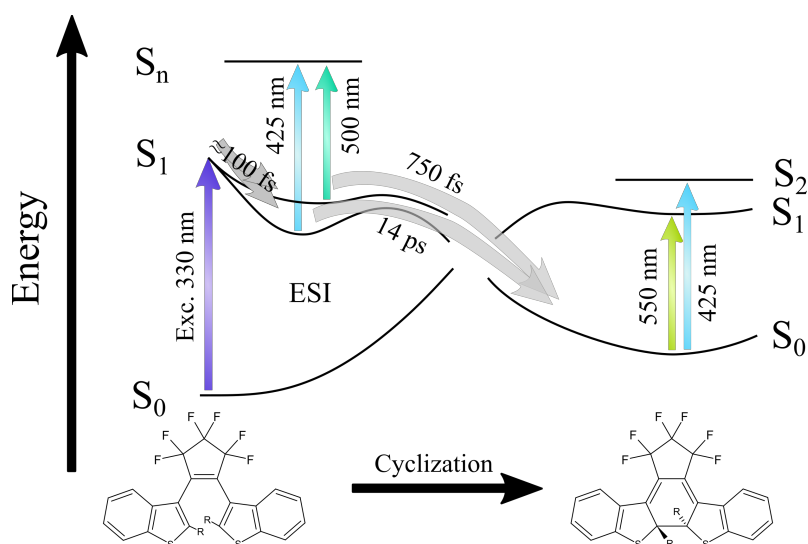


**Figure 5.12:** Summary of the DTE cyclization dynamics (antiparallel conformer). A qualitatively identical mechanism for both the ethylated and butylated species was deduced, both in crystal and solution, via two separate excited-state intermediates. Indicated lifetimes and transition wavelengths refer to the case of Et-DTE in crystal.

the decay of the maximum at 600 nm is mostly completed within 100 ps, an additional decay of the absorption band around 425 nm can be observed on the time scale of a few 100 ps as well as a small rise of the product band.

Fig. 5.14 shows the results from global and target analysis of the present data. As is common when the time constants differ by an order of magnitude or more, identical values for both models were obtained and the DAS and SAS are thus equivalent. The respective constant components are readily assigned to the closed-ring product by comparison to reported steady-state spectra (see Fig. 5.3 or ref. [231]). The first two components are qualitatively similar to those obtained from Pr-DFE, with the first describing the formation of an intermediate species from the initial excited-state absorption with a time constant of 140 fs, followed by its decay and formation of the long-lived product band with a lifetime of 2.2 ps. However, the third intermediate component exhibits significant differences to the former case. It predominantly encompasses the continued decay of the absorption band around 425 nm, but also the slight increase in intensity in the product absorption region as well as a small amplitude decay above  $\approx 625$  nm. These observations together with the significant spectral blue-shift in the data warrant further analysis beyond the global fit results.

To differentiate between different contributions to the DAS, mainly of the 140 ps component, additional kinetic trace fits were carried out at 420 and 600 nm, which are shown in Fig. 5.15. The initial rise times were found to be  $140 \pm 4$  fs at 420 nm and  $160 \pm 20$  fs at 600 nm. Deviation from the global analysis time constant in case of the latter can be explained by the strong influence of the initial CPM signal in this spectral region. The obtained time constants for the subsequent decays were  $2.3 \pm 0.1$  ps at 420 nm and  $1.2 \pm$

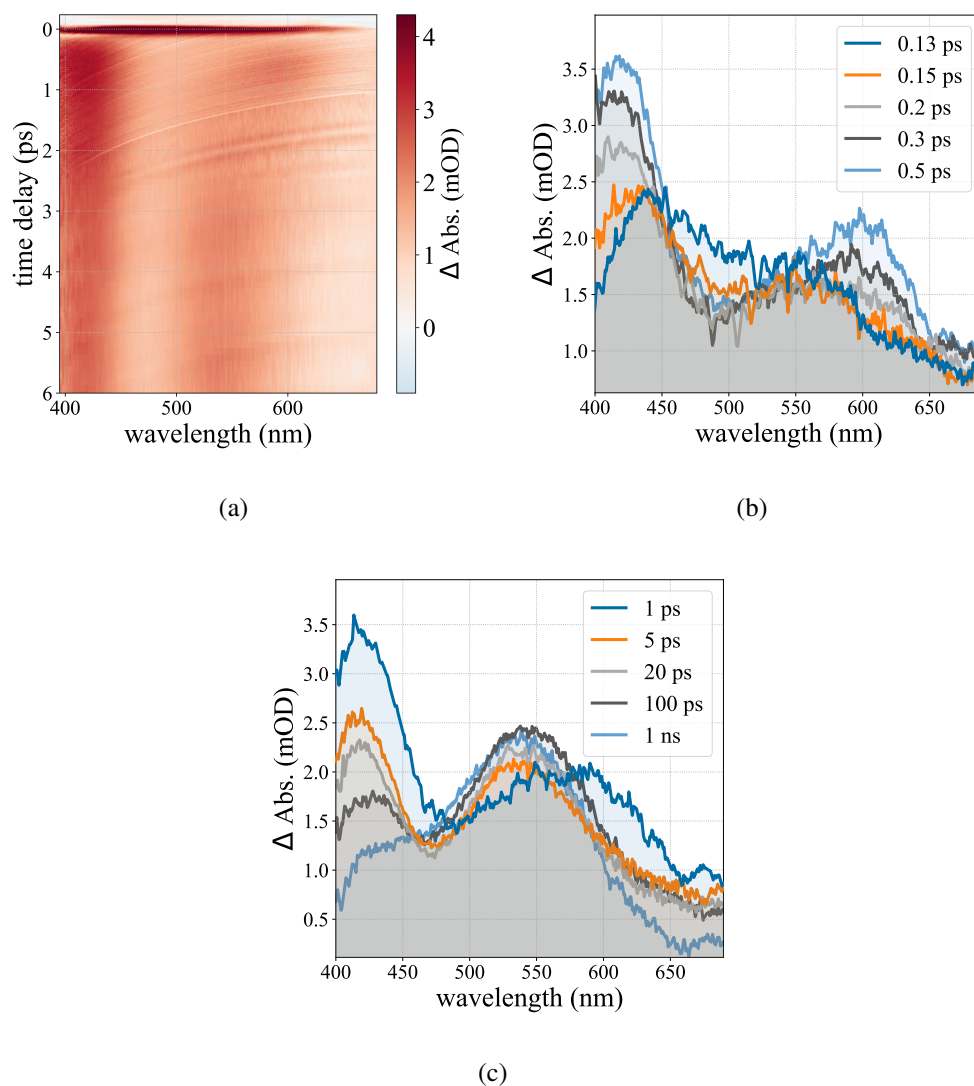


**Figure 5.13:** Transient absorption data from photoexcited 1.5 mM Ethyl-Dithienylethene in acetonitrile. (a) TA map of the first 6 ps, (b) spectral traces of the first 500 fs, (c) spectral traces up to 1 ns.

0.07 ps in case of 600 nm. While the decay at the latter wavelength was monoexponential, for the former an additional decay component was found, whose time constant of  $130 \pm 6$  ps corresponds to the third component from global analysis. The signal at 600 nm on the other hand entails an additional slow rise of the product absorption band in that time domain, which was verified by a separate single-point fit at 550 nm between 10 and 650 ps, yielding a rise time of  $130 \pm 21$  ps (see Fig. 5.15 (c)).

These comparisons indicate that the decay components from global analysis were dominated by the spectral dynamics around 420 nm, which is likely due to the spectral changes in the region of 600 nm being significantly smaller in amplitude than those around 420 nm. The shorter time scale at 600 nm compared to the global fit can be explained by the overlap with the rising product band, which has a significant contribution in the same spectral range. These superimposed dynamics result in a continuous shift of the spectral center

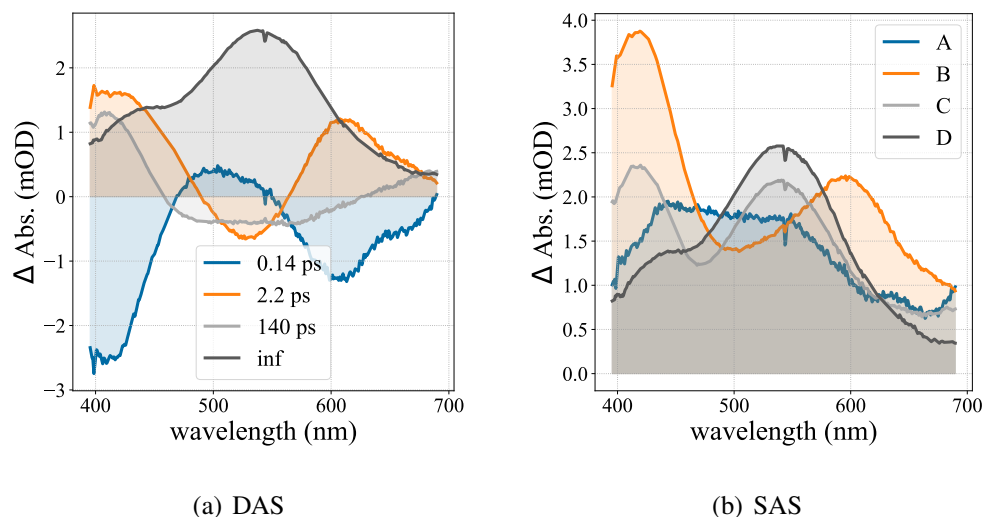


**Figure 5.14:** Global and target analysis of photoexcited Et-DTE in acetonitrile. (a) decay-associated spectra with decay constants, (b) species-associated spectra. The rate constants from target analysis were identical to the decay times from global analysis.

of mass, which was analyzed separately (see Fig. 5.15 (d)). The temporal development of the centroid between 480 and 690 nm was found to be biexponential in the time delay range between 0.7 ps and 1 ns, although the second component with a time constant of  $370 \pm 60$  ps may partially be caused by the long-lived decay of the signal around 420 nm, still having a small contribution between 480 and 500 nm. The faster decay time of  $2.1 \pm 0.1$  ps on the other hand corroborates the time constant of the product band formation found in global analysis. It remains thus to be discussed whether the bands centered at 580 and 550 nm are indeed associated with two different species as implied by the global fit or in fact the same species undergoing a dynamic hypsochromic shift upon propagation on the potential energy surface. Before looking into this question in more detail, the results from the closely related Bu-DTE will be presented to enable a combined discussion at the end of the section.

### Butyl-Dithienylethene

In Fig. 5.16, the results from transient absorption experiments of the dibutylthienylethene (Bu-DTE) derivative in solution (1.5 mM, acetonitrile) are depicted (excited at 330 nm, peak fluence of  $2.3 \text{ mJcm}^{-2}$ ). Overall, the signal intensity appears to be higher at longer wavelengths.<sup>22</sup> Besides this general observation, the relative spectral development during the first 15 ps after excitation is similar to the ethyl-substituted derivative. The initially structureless absorption signal evolves within 500 fs after excitation towards a spectrum

<sup>22</sup>In principle, this could be a systematic error caused by spatial dispersion of the probe and thereby insufficient pump-probe overlap at shorter wavelengths. However, this was ruled out by measuring different sample solutions on the same day under similar conditions, in which such an effect was not observed.

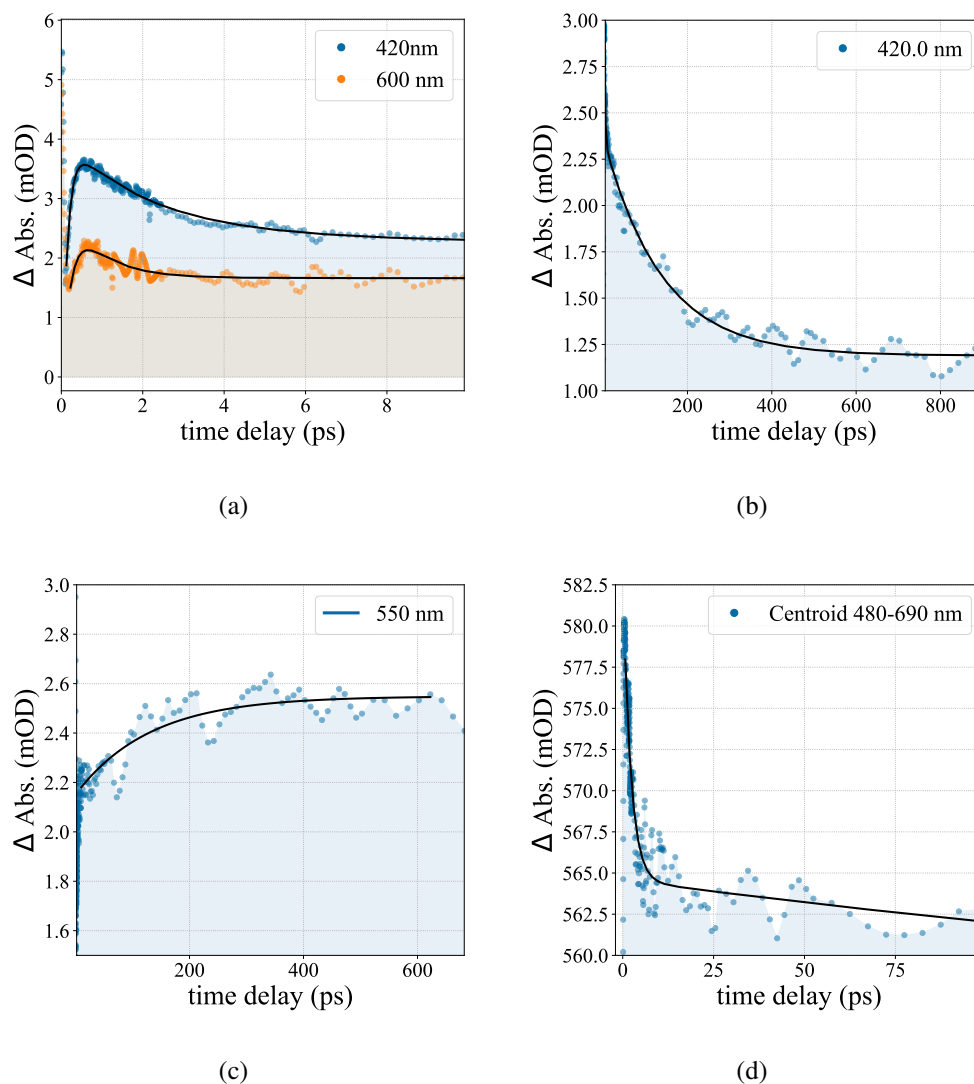


**Figure 5.15:** Et-DTE solution: Exponential fits of single-point kinetics ((a)-(c)) as well as (d) the centroid of the main absorption band.

with a local maximum at 450 nm and a global maximum at 600 nm. This intermediate spectrum subsequently decays with the simultaneous rise of a long-lived absorption band centered around 550 nm and readily ascribed to the closed-ring isomer. Beyond 15 ps, only minor developments of the spectrum were observed, entailing a slight increase in intensity of the product absorption band on the sub-ns scale. Notably, the long-lived band exhibited non-zero absorbance between 600 and 700 nm, which differs from the steady-state absorption spectrum of the closed-ring product (see Fig. 5.3 (b)).

Global and target analysis (see Fig. 5.17) quantify these observations with the first component (110 fs) consisting of an overall decay of the broad, asymmetric absorption spectrum as well as the rise of the two absorption peaks around 450 and 600 nm. Spectral evolution towards the product absorption spectrum is represented by the second component with a time constant of 3.4 ps. Although visible in the fit residual, the aforementioned sub-ns

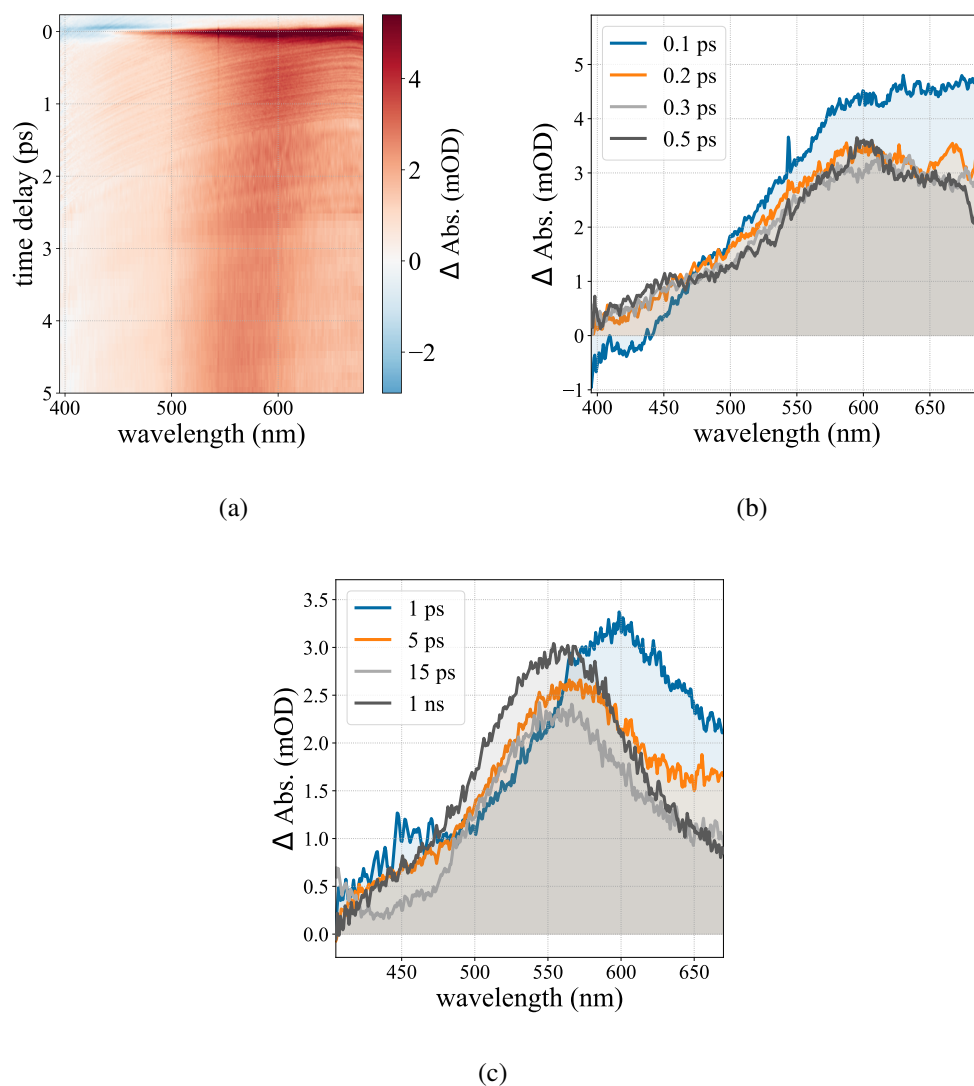


**Figure 5.16:** Transient absorption data from photoexcited 1.5 mM Butyl-Dithienylethene in acetonitrile. (a) TA map of the first 5 ps, (b) spectral traces of the first 500 fs, (c) spectral traces up to 1 ns.

increase in product absorption was not found to be sufficient for an additional component in the global fit and will be treated separately below.

Single-point exponential fits were carried out at 450 nm and 650 nm in order to avoid overlap with the product band and are shown in Fig. 5.18 (a). The kinetic trace at 450 nm consists of a rise with a time constant of  $100 \pm 10$  fs and a subsequent decay ( $2.3 \pm 0.2$  ps), while the one at 600 nm exhibits a biexponential decay with time constants of  $140 \pm 10$  fs and  $3.6 \pm 0.2$  ps. The lifetime from global fit is thus dominated by the band around 600 nm, which is in accordance with its larger amplitude compared to the one around 450 nm. The centroid of the spectrum between 500 nm and 690 nm describing the transition from the intermediate spectrum to the product absorption was calculated and fit as well as the spectral integral in the same region (see Fig. 5.18 (b) and (c)). The temporal progression of the centroid again showed a biexponential behavior with a fast

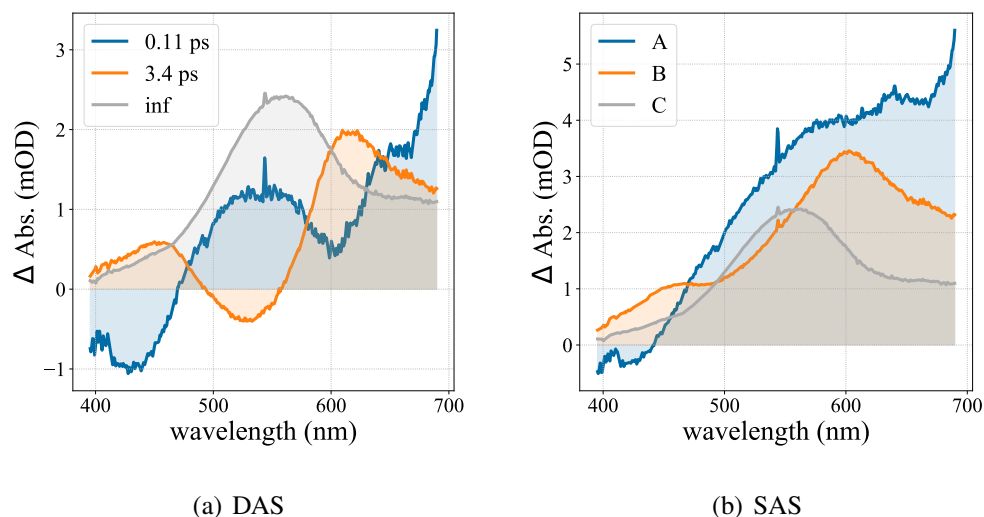


**Figure 5.17:** Bu-DTE solution TA: (a) Global and (b) target analysis. Lifetimes from global analysis agreed with the time constants from target analysis.

component of  $4.5 \pm 0.1$  ps and a slow component with a time constant larger than the measurement window. The integrated intensity in the same spectral region was fit between 0.5 and 200 ps (omitting the initial ESA decay) with a single exponential function yielding a decay constant of  $3.6 \pm 0.2$  ps which matched the decay at 600 nm. A separate fit of the integrated product band (Fig. 5.18 (d)) resulted in a lifetime of  $0.6 \pm 0.3$  ns for the observed slow rise.

## Discussion

The few-ps dynamics of both dibenzothienylethene derivatives show the same qualitative features and can be discussed conjointly. In either case, a transient spectrum with maxima around 450 and 600 nm is rapidly formed with time constants of 140 and 110 fs for Et-DTE and Bu-DTE, respectively. While the band around 450 nm is more intense than the other in case of Et-DTE, the inverse is true for Bu-DTE. Global analysis correlates the decay of both bands and the rise of the long-lived band around 550 nm, ascribed to the closed-ring isomer, resulting in ring-closing time constants of 2.2 and 3.4 ps, respectively. However, it needs to be discussed whether or not both bands are indeed associated with the same chemical species. When fitting the kinetic traces at the two maxima of the transient spectra individually, faster time constants for the red bands (600 and 650 nm) compared to the blue bands (420 and 450 nm) were obtained. At first glance, this suggests different dynamics and points towards the involvement of different reaction intermediates. The proximity of the transient band around 600 nm to the product absorption allows the hypothesis that the former is in fact a vibrationally hot closed-ring form, which undergoes vibrational cooling manifesting in a blue-shift towards the equilibrium spectrum on the few-ps scale. This would be in accordance with previous reports of a rapid cyclization

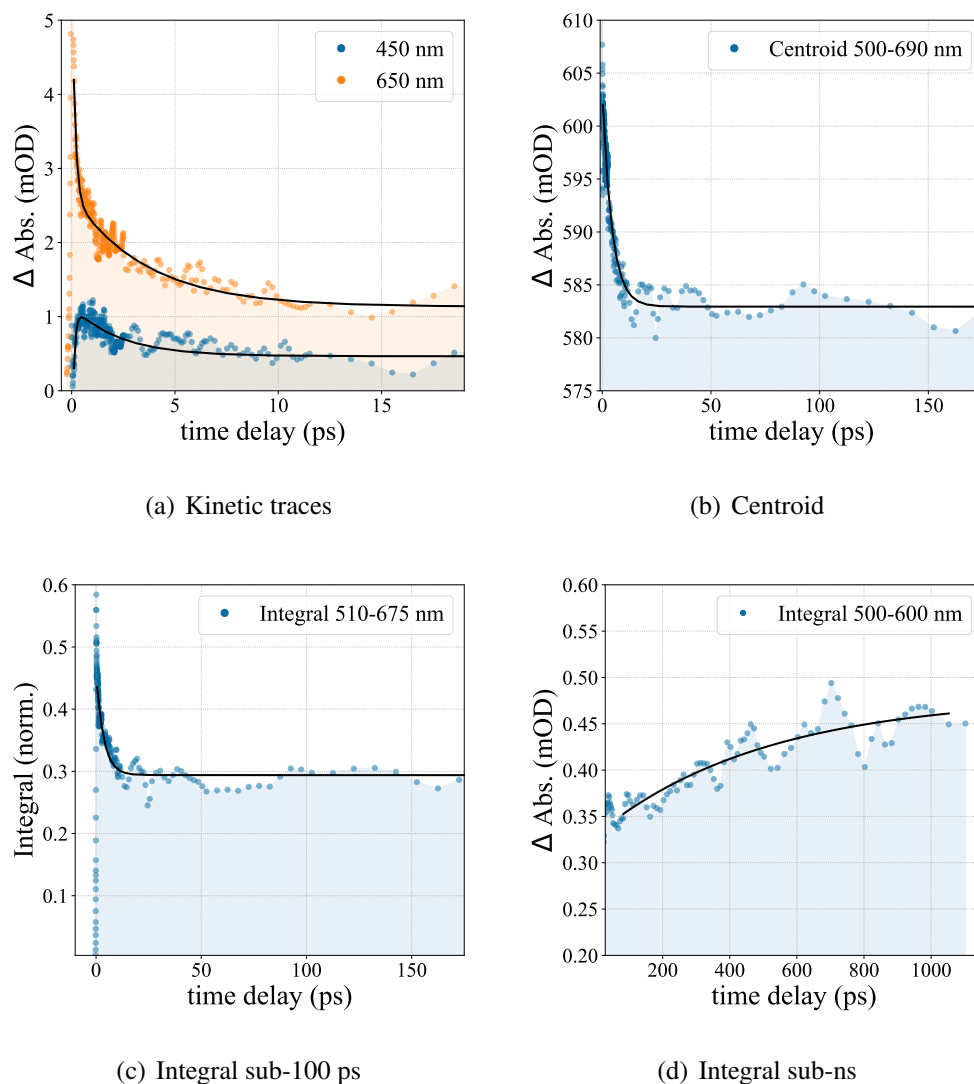


**Figure 5.18:** Bu-DTE solution TA: Kinetic fits of (a) single-wavelength traces, (b) the centroid of the product absorption and presumed ESA bands, (c) the integral of the same region in the first 100 ps, (d) the integrated product absorption band on the sub-ns time scale. Associated decay constants are collated in Tab. 5.3.

pathway for other dithienylethene derivatives (*vide supra*).

The main hypotheses to be considered are thus (a) the attribution of both transient bands to a single excited-state intermediate, (b) two individual excited-state species responsible for the respective bands or (c) one excited-state intermediate (blue band) and a vibrationally hot ground-state (red band).<sup>23</sup> To facilitate finding the most plausible interpretation, the relevant time constants obtained in the previous analysis are collated in Tab. 5.3.

Consistent correlations between the decay of the blue bands and the hypsochromic shift of the centroid as well as between the decay of the red bands and the integrals can be

<sup>23</sup>Hypothesis (a) includes the possibility of a single absorption band with a dip originating in an additional stimulated emission band, in analogy to the interpretation for Me-DTE by Ishibashi et al.<sup>[254]</sup>

**Table 5.1:** Time scale comparison between different analysis methods. Blue band: 420 nm (Et-DTE) and 450 nm (Bu-DTE). Red band: 600 nm (Et-DTE), 650 nm (Bu-DTE). Centroid and integral ranges are 500-690 nm and 510-675 nm, respectively. SPK = single-point kinetic fit.

Method	$\tau_{\text{Et-DTE}}$ (ps)	$\tau_{\text{Bu-DTE}}$ (ps)
Global (blue and red bands)	2.2	3.4
Blue band SPK	$2.3 \pm 0.1$	$2.3 \pm 0.2$
Centroid blue-shift	$2.1 \pm 0.1$	$4.5 \pm 0.1$
Red band SPK	$1.2 \pm 0.07$	$3.6 \pm 0.2$
Integral Decay	$1.1 \pm 0.1$	$3.6 \pm 0.2$

recognized.<sup>24</sup> Hypothesis (c) is in contradiction to these correlations because it would require the shift in centroid position to be correlated with the decay of the red band, and the integral not to decay but to increase with a time constant similar to the decay of the blue band.<sup>25</sup> Another argument against ascribing the apparent blue-shift of the spectral centroids for either derivative to relaxation of a single (ground-state) species is their temporal correlation with the decay of the blue bands. Instead, this correlation enables the attribution of the centroid shift to the growth of the product absorption and the decay of the excited-state absorption in analogy to various reports in the literature,<sup>[83,233,259]</sup> as well as the discussed spiropyran photochromism dynamics.

Excitation of the P conformer should be expected to contribute to the excited-state absorption and may influence the spectral region around 600 nm more than that of the blue band, like in case of Pr-DFE,<sup>26</sup> which is a possible explanation for the mismatch in time scales. Thus, there is no definite evidence for the existence of two different excited-state intermediates (hypothesis (b)) due to the possibility of other causes for the slightly different decay times. The more plausible interpretation of the data in the few-ps regime for either derivative is therefore a cyclization pathway via a single excited-state intermediate with lifetimes of  $\approx 2.2$  ps for Et-DTE and  $\approx 3.5$  ps for Bu-DTE. Furthermore, there is no indication for a direct cyclization pathway in the sub-ps time domain.

The spectral dynamics of Et-DTE on the time scale of a few hundred picoseconds on

<sup>24</sup>For Bu-DTE, the blue-shift is not as clearly correlated with the decay of the blue band as in case of Et-DTE. However, this may be due to the low amplitude of the band.

<sup>25</sup>For instance, vibrational cooling in case of spironaphthopyran in solution (see section 3.2.2), did not involve any temporally correlated changes in the band integral, only in the vibrational fine-structure and the spectral widths.

<sup>26</sup>N.B.: In contrast to the latter, no characteristic spectral signature of the excited P conformer on this time-scale was found in the analysis. As was pointed out whilst discussing the dynamics of Pr-DFE, a comparison between solution and single crystals may help to assess the influence of the parallel conformer.

the other hand suggest the presence of a second, slower cyclization pathway. While the long-lived decay of the signal around 420 nm has been reported for Me-DTE with a similar time constant, it was not attributed to cyclization, but relaxation of the non-reactive P conformer.<sup>[254]</sup> However, in case of the present data from Et-DTE, there is a correlation between this decay and an increase of the absorbance in the region of the product band (see Fig. 5.14), which was confirmed by independent single-point kinetic fits.

While less obvious due to the lack of a similar decaying signal between 400 and 450 nm, the slow increase of the product absorption band of Bu-DTE on the sub-ns time scale (0.5 ns) is analogous to Et-DTE, which implies the existence of a second pathway for this derivative as well. The fact that there is no second decay component of the blue band in case of Bu-DTE ought to be due to its overall weaker absorbance and longer lifetime compared to Et-DTE, leading to it being neglected in the applied fit.<sup>27</sup>

The residual absorbance above 600 nm for both derivatives needs to be attributed to a long-lived excited state or metastable ground state due to its absence in the steady-state spectra of the closed-ring form. For Me-DTE, the same observation was made and the band was found to decay within a few  $\mu\text{s}$ .<sup>[254]</sup> Further experimental evidence was given that the band could be ascribed to a long-lived triplet state of the P conformer by means of  $\mu\text{s}$ -time-resolved spectroscopy. Despite lacking these experimental capacities, it is reasonable to attribute the bands in the present cases analogously, considering the nearly identical chemical structures of these three derivatives.

Evidently, the butylated derivative exhibits slower ring-closure dynamics compared to the ethylated one, which in turn are slower than the reported time constant for the methylated analog. Besides possible effects on the potential energy surface by altering the frequency of relevant modes, increased steric hindrance due to longer side chains would be a chemically intuitive explanation for a decrease in reaction rates. However, electrocyclization only takes place if the reactive carbon atoms are already in spatial proximity, in contrast to the parallel conformers. The change in hybridization of the reactive carbons upon cyclization on the other hand changes the geometrical arrangement of their substituents from trigonal planar to tetrahedral, the speed of which is very likely affected by their respective mass. Nevertheless, the substituent effect can only be one of many factors, considering that the Pr-DFE ring-closing reaction was found to be significantly faster than either of the investigated DTE derivatives, as will be discussed further at the end of this chapter.

---

<sup>27</sup>Further evidence for a second cyclization channel can be gained from the spectral dynamics in the crystalline phase (see section 5.4.2), which exhibit a similar long-lived component. Since only the AP conformer was present in the investigated crystals not ascribable to the P conformer.

## 5.4.2 Crystal TA

### Ethyl-Dithienylethene

Fig. 5.19 shows the transient absorption data from 300 nm thin single crystal cuts of the di(ethylthienyl)ethene derivative, excited at 330 nm ( $0.8 \text{ mJcm}^{-2}$ ) and using synchronized photoreversion with a visible NOPA between 550 nm and 650 nm. The latter region of the spectra was affected by scattering from the reversion beam. The transient spectrum following excitation consists of two bands, one centered around 400 nm and the other one covering the entire probe wavelength range above 450 nm. Subsequently, there is a rise in the spectral region below 450 nm reaching a maximum at  $\approx 300$  fs after excitation accompanied by a bathochromic shift and narrowing of the broader absorption band above 450 nm. Both bands decay within around 100 ps with a simultaneous increase in absorbance in the region between them.

Additional experiments after improvements to the transient absorption setup were carried out, but using a different crystal from the same batch. The sample thickness was increased to 600 nm due to a generally weaker signal from these crystals. Although qualitatively, the results from both crystals matched, differences in the ratio of the two long-lived bands were found. In case of the former crystal (crystal A) the band amplitude at 400 and 550 nm were on a similar level, while the absorbance at 400 nm was found to be higher in case of the latter (crystal B). However, the data from the second crystal allowed a better resolution of the sub-ps dynamics as well as a better representation of the long-lived absorption spectrum due to the improved acquisition routine. Therefore, discussion of global and target analysis will be based on crystal B.

The DAS and SAS for the time range of 250 ps after excitation are depicted in Fig. 5.20. The first component (100 fs) describes the rise of the band at 400 nm as well as the red-shift of the initial absorption signal towards the long-lived signal centered around 550 nm. The decay of these bands was found to be biexponential, with a fast component of 0.8 ps and a slower component of 14 ps. The infinite component represents the product absorption spectrum, with both reported absorption maxima present,<sup>[231]</sup> but with an apparently higher amplitude around 425 nm (*vide supra*).

Since the present data exhibits high similarities obtained for the butyl-substituted derivative, these analysis results will again be interpreted together with those obtained from Bu-DTE.

### Butyl-Dithienylethene

Transient absorption data from two different single crystals (C and D) of the butyl-substituted dithienylethene derivative, photoexcited at 330 nm ( $1.6 \text{ mJcm}^{-2}$  peak fluence) and probed in the visible, is shown in Fig. 5.21. Although in both cases, synchronized photoreversion with a visible NOPA beam was applied, the data from the 300 nm thin slices

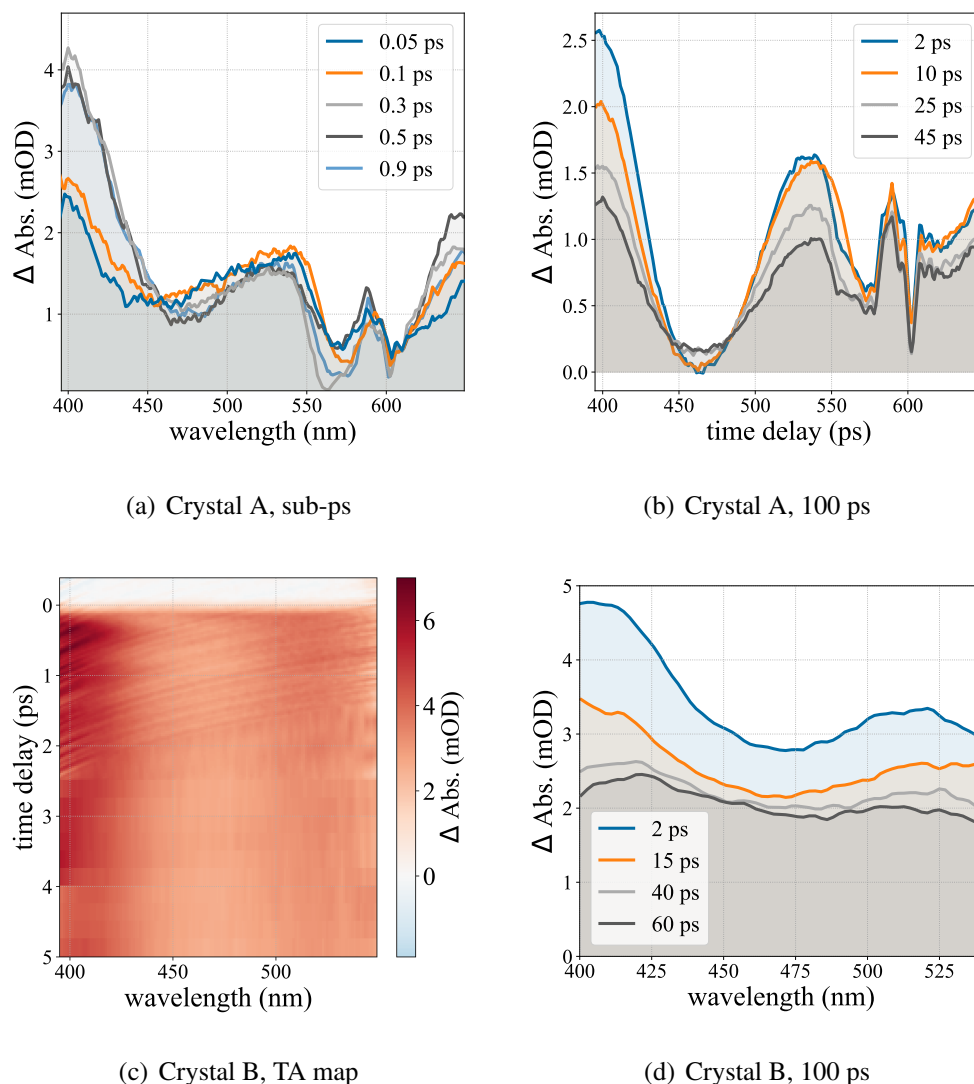


**Figure 5.19:** Transient absorption of photoexcited single-crystalline diethylthienylethene (Et-DTE) from two different crystals (A and B). (a) TA map for the first 5 ps of the data from crystal A (300 nm thickness), (b) and (c) spectral traces of the data from crystal B (600 nm thickness).

of crystal C exhibits only little influence from scattered light in the region of 550 nm (see Fig. 5.21 (a) and (b)). The transient absorption spectrum 100 fs after excitation consists of three maxima, around 410, 500 and 610 nm, respectively. Within 500 fs after excitation, the absorption bands around 410 and 600 nm increase, reaching maximum values between 4 and 5 mOD at 500 fs, while the one around 500 nm decays towards an absorbance between 1 and 2 mOD. Simultaneously, all three bands red-shift towards positions of 410, 525 and 650 nm, respectively, at a time delay of 500 fs. Subsequent equilibration dynamics entail a partial decay of the bands at 410 and 650 nm, while the middle band exhibits a slight increase.

The data from crystal D on the other hand is affected strongly by a scattering signal from the photoreversion beam, limiting its usable spectral window to wavelengths below

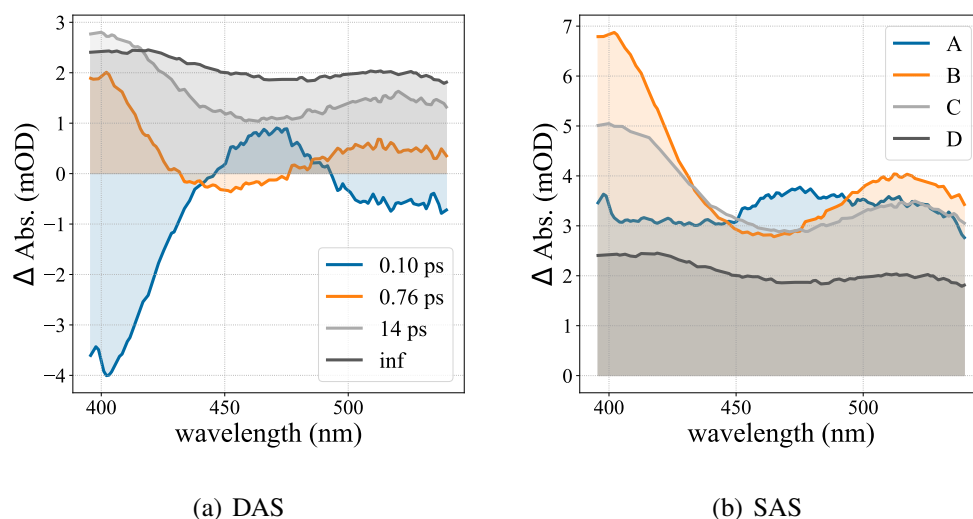


**Figure 5.20:** Et-DTE crystal TA (crystal B): (a) Global and (b) target analysis (250 ps window). Time constants from both methods were identical.

550 nm. Thus, the main transient band around 650 nm was not possible to resolve. The dynamics of the other two bands however are in agreement with the data from crystal C. Like in case of the ethyl-substituted crystals, the ratio in absorbance appears to be slightly skewed towards the blue absorption band, and a stronger absorption background between the features was observed at equilibrium.

The DAS and SAS from global and target analysis of the data from crystal C, covering the few-ps time domain up to 3 ps, can be found in Fig. 5.22. The first component and step entail the observed absorbance in- and decreases as well as the accompanying red-shifts of the spectral features in the sub-ps range and have time constants of 130 fs in either case. Due to the partial decay of the long-lived absorption band, the second component and species have a finite lifetime, longer than the fit window. The larger measurement window in case of crystal D enabled a more reliable characterization of this decay, again resulting in a biexponential behavior, with time constants of 2.6 and 63 ps towards the long-lived product absorption band (see Fig. 5.22). Despite the difference in covered wavelength range, the obtained sub-ps dynamics were equivalent for both crystals.

## Discussion

As stated above, the spectral dynamics in crystal of both the ethyl- and the butyl-substituted dithienylethene derivatives exhibit strong resemblances. The reported closed-ring absorption spectra of the DTE single crystals consist of two absorption bands, one around 420 nm and one between 550 and 600 nm.<sup>[231]</sup> For the ratio in magnitude between these two bands, a significant polarization dependence was reported leading to a change in color when rotating the crystal under polarized light. It has to be borne in mind that for the transient absorption experiments presented here, linearly polarized probe light was used,

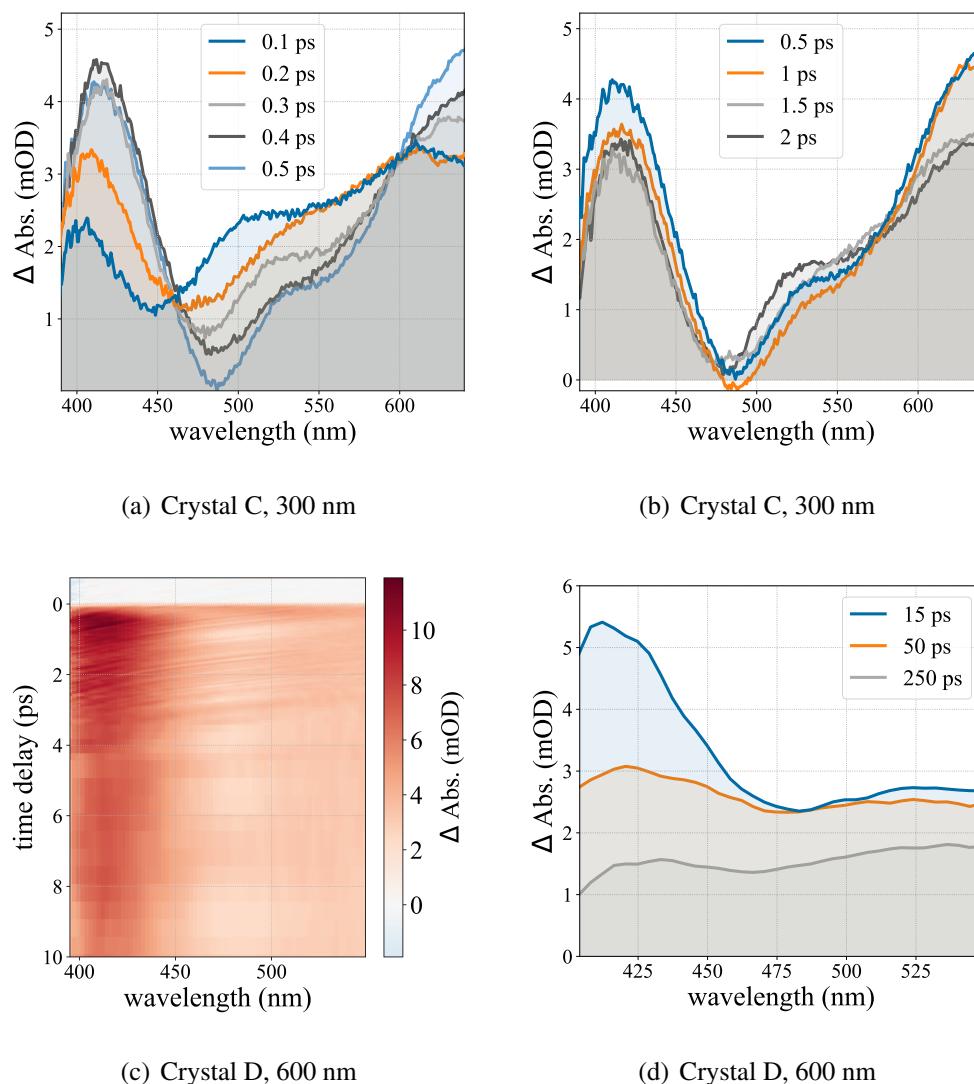


**Figure 5.21:** Transient absorption of photoexcited single-crystalline di(butylthienyl)ethene (Bu-DTE) from two different crystals (C and D) with thicknesses of 300 and 600 nm, respectively. (a) and (b) spectral traces of the data from crystal C, (c) TA map for the first 10 ps of the data from crystal D, (d) spectral traces from crystal D (250 ps range).

whose polarization was adapted for each sample in order to maximize the absorbance of the main band around 550 nm. However, since the samples represent approximately two-dimensional slices of a three-dimensional crystal, the out-of-plane components of the respective transition dipole moments were inherently fixed, limiting the capability of this optimization. Therefore, it is to be expected that, if not by chance, both absorption bands will be present in the equilibrium absorption spectrum.

While *ex-situ* verification of the product absorption spectrum in the thin crystalline cuts as opposed to the bulk material was not successful due to a limited signal intensity, accumulation of a thermally stable isomer was verified for sample cuts from the same crystal in the electron diffraction experiments presented below. Thus, it is reasonable to assign the

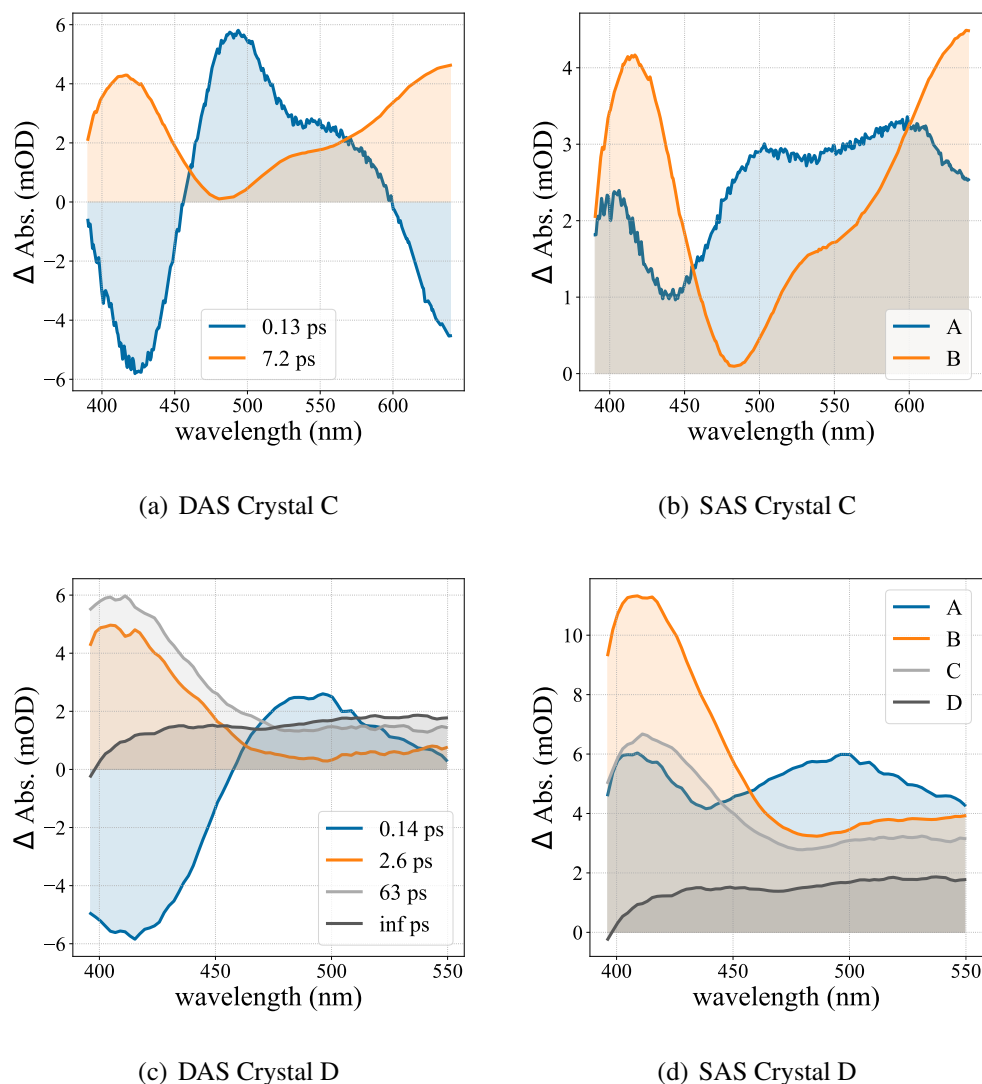


**Figure 5.22:** Bu-DTE crystal TA: Global and target analysis for the time windows up to 3 ps (crystal C) and 250 ps (crystal D) after excitation. Retrieved time constants from both methods were identical, respectively.

constant components from global fitting, which consist of both absorption bands, to the closed-ring species. These considerations together with the results from solution enable the following interpretation.

The sub-ps dynamics are analogous to the ones in solution, with the rapid formation of an intermediate spectral species within 100-140 fs. Ring closing involves a biexponential decay of this transient spectrum with time constants of 0.76 and 14 ps in case of Et-DTE and lifetimes of 2.6 and 63 ps in case of Bu-DTE. The cause of this biexponentiality needs to be discussed further. The reported near-unity quantum yield of the reaction (*vide supra*) implies that all observed spectral dynamics are related to formation of the closed-ring isomer. Hence, as both contributing DAS have significant amplitudes, corresponding to a considerable population, both decay processes must involve cyclization. This indicates that the DAS are associated with different states or species because a decay from one

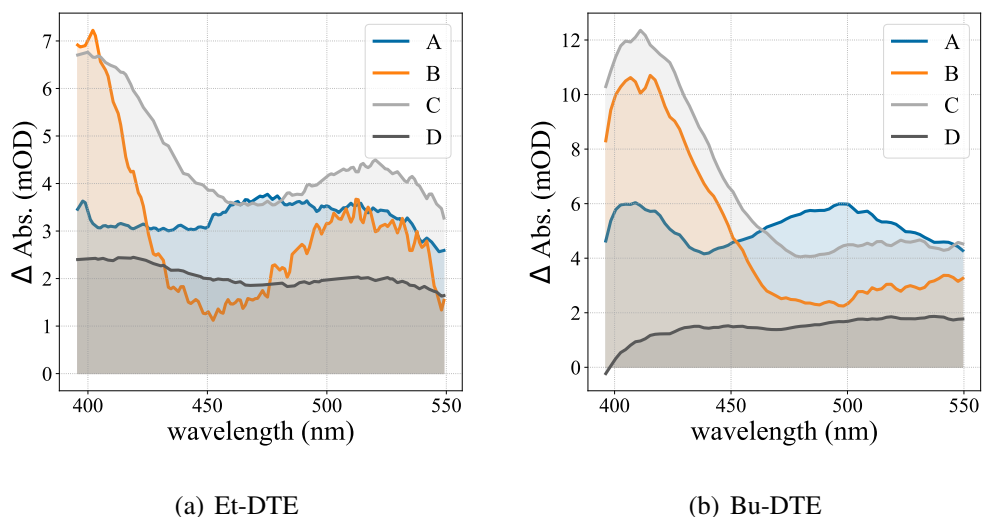


**Figure 5.23:** Crystalline DTE TA: Branched sequential models for both derivatives. Et-DTE:  $\tau_{AB} = 300$  fs,  $\tau_{AC} = 200$  fs,  $\tau_{BD} = 750$  fs,  $\tau_{CD} = 14$  ps. Bu-DTE:  $\tau_{AB} = 300$  fs,  $\tau_{AC} = 280$  fs,  $\tau_{BD} = 2.6$  ps,  $\tau_{CD} = 63$  ps.

species to another always results in a single exponential decay, regardless of the number of pathways.<sup>28</sup> Thus, the intermediate (spectral) species consists of two distinct, but in terms of their electronic structure similar chemical species. The interplay between them is more ambiguous. The applied sequential model treats the shorter-lived species as a precursor of the longer-lived one, but it is equally feasible to fit the data using a branched model, in which these two species (B and C) are both formed directly from the Franck-Condon state (A) before relaxation to the closed-ring isomer (species D, see Fig. 5.23). Within this model, the decay times of species B and C (attributed to the two cyclization pathways) were identical to the parallel and unidirectional models, while population transfer constants from A to B and A to C were found to be 300 and 200 fs for Et-DTE and 300 and 280 fs for Bu-DTE.<sup>29</sup> Even though the exact mechanism cannot be determined based on this analysis alone, the fact that no significant spectral shifts or appearances of new bands are observed when comparing the SAS of species B and C points towards the branched model with two spectroscopically similar reaction intermediates.

For Et-DTE in solution, it was possible to resolve the closed-ring product absorption band more clearly, which facilitated the assignment of the 140 ps component to a parallel cyclization pathway. The fact that a biexponential decay of the blue band was reproduced in the crystal data supports this interpretation as opposed to an alternative relaxation pathway back to the open-ring isomer or relaxation of the non-reactive conformer. The biexponentiality was also observed for Bu-DTE single crystals, which consolidates the previous

<sup>28</sup>Confirm the discussion in section 4.3.1 of the Z-E-isomerization dynamics of protonated spiropyran.

<sup>29</sup>This is not in contradiction to the results from the other models, since the first step in the unidirectional model will be a faster rate constant on the order of the sum of the two rate constants in the branched model. Note that the rate constants are the inverse of the respective time (or decay) constants, predominantly used in this discussion.

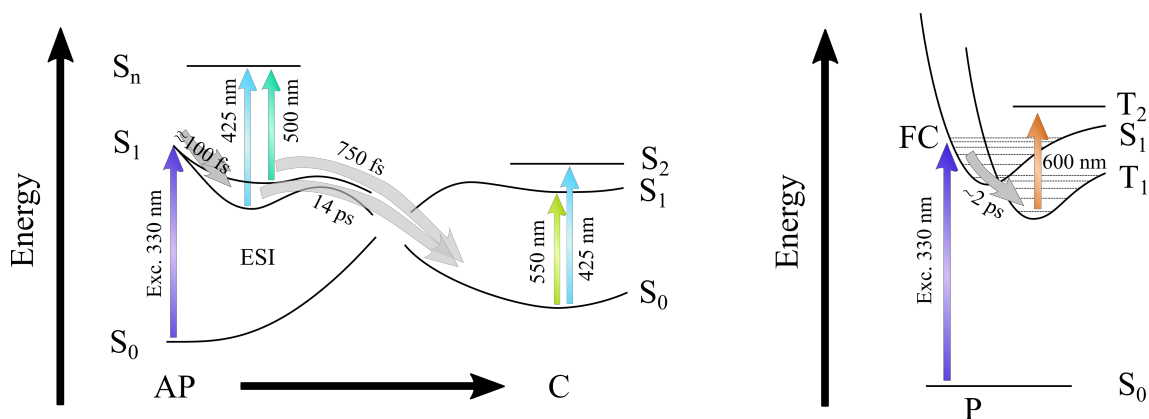


**Figure 5.24:** Summary of the deduced reaction mechanism for the investigated dithienylethene derivatives upon photoexcitation. The diagram on the left shows the cyclization dynamics of the antiparallel conformer, representatively for the case of Et-DTE in crystal. Evidence for dual cyclization pathways was found for both derivatives and both in crystal and solution. Excitation of the parallel conformer did not directly contribute to the spectral dynamics, but a long-lived absorption band was observed and assigned to a triplet state based on previous reports for a related derivative.<sup>[254]</sup>

hypothesis that the overall band amplitude in the solution experiments was merely too small to be recognized above noise level. Therefore, it can be concluded that the reaction mechanisms of both dithienylethenes in solution as well as crystal are indeed identical except for the time scales.

In turn, drawing the analogy to the solution experiments as well as the reported literature elucidates the reaction mechanism in crystal to indeed the same (or similar) two excited-state reaction intermediates. Notably, both cyclization pathways were found to be faster in crystal than in solution, unlike in previously reported dithienylethenes (see ref. [83]).

### 5.4.3 Summary

The dynamics of the two photoexcited dithienylethene derivatives discussed in this section are summarized in Fig. 5.24, for both the antiparallel and the parallel conformers. In contrast to the difuryl derivative and in line with previously investigated dithienyl systems, evidence for a dual cyclization pathway was found involving two reaction intermediates with distinct lifetimes (see Tab. 5.2 for an overview of the different lifetimes for the various cases). Investigating these dynamics in the crystalline phase and comparison to solution allowed to unambiguously assign the slower reaction pathway to cyclization, which had previously been assigned to relaxation of the unreactive conformer. Thus, like in case of Pr-DFE, a synergy between the complementary experiments in crystal and solution enabled the interpretation of one to aid interpretation of the other.

Both pathways were determined to be more rapid in crystal compared to solution. This acceleration was more notable than in case of Pr-DFE, whose cyclization time in solution was already deduced to be in the sub-ps range. A comparative discussion between all

**Table 5.2:** Lifetimes of the investigated dithienylethene derivatives in crystal and solution. Shown are the time constants  $\tau$  of the Franck-Condon states (FC) and the two excited-state intermediates (I1, I2), both of which are associated with cyclization.

Phase	Derivative	$\tau_{\text{FC}}$ (ps)	$\tau_{\text{I1}}$ (ps)	$\tau_{\text{I2}}$ (ps)
Solution (AcN)	Et-DTE	0.1	2.2	140
	Bu-DTE	0.1	3.5	600
Crystal	Et-DTE	0.1	0.8	14
	Bu-DTE	0.1	2.6	63

three investigated derivatives will be given in the concluding section at the end of this chapter.

## 5.5 Electron Diffraction Experiments

Although the conduction of systematic ultrafast electron diffraction measurements using one or multiple of the investigated systems exceeded the time frame of this PhD project, preliminary tests were conducted in order to assess the feasibility and requirements of such experiments.

Static diffraction patterns from 100 nm thin, single-crystalline slices of each diarylethene derivative are shown in Fig. 5.25. They are the result of accumulating patterns from multiple electron pulses in succession, resulting in a total number of electrons of  $10^8$  electrons per image. Overall, the diffraction quality of these samples was excellent compared to other crystals of organic molecules previously tested with the same apparatus and similar to the quality obtained with SNP samples (see section 3.4).

### 5.5.1 Photostationary state signal

Since the closed-ring product isomer is thermally stable even at room temperature, it is feasible to obtain the accumulated electron diffraction patterns of the photostationary state (PSS) in the same way as for the native crystal. The PSS was prepared by irradiation with the 343 nm excitation pulses for a time window defined via the electronic shutter and without the photoreversion beam.<sup>30</sup> Thus, this difference gives an indication of the signal to be expected in a time-resolved electron diffraction measurement after or close

<sup>30</sup>Strictly speaking, the PSS may not have been reached entirely, as the irradiation time was kept short (50 excitation pulses) in order to avoid damage to the sample. Qualitatively however, the patterns reflect the difference between the closed-ring form and the PSS, with a possibly slightly lower differential signal than in the actual photostationary state.

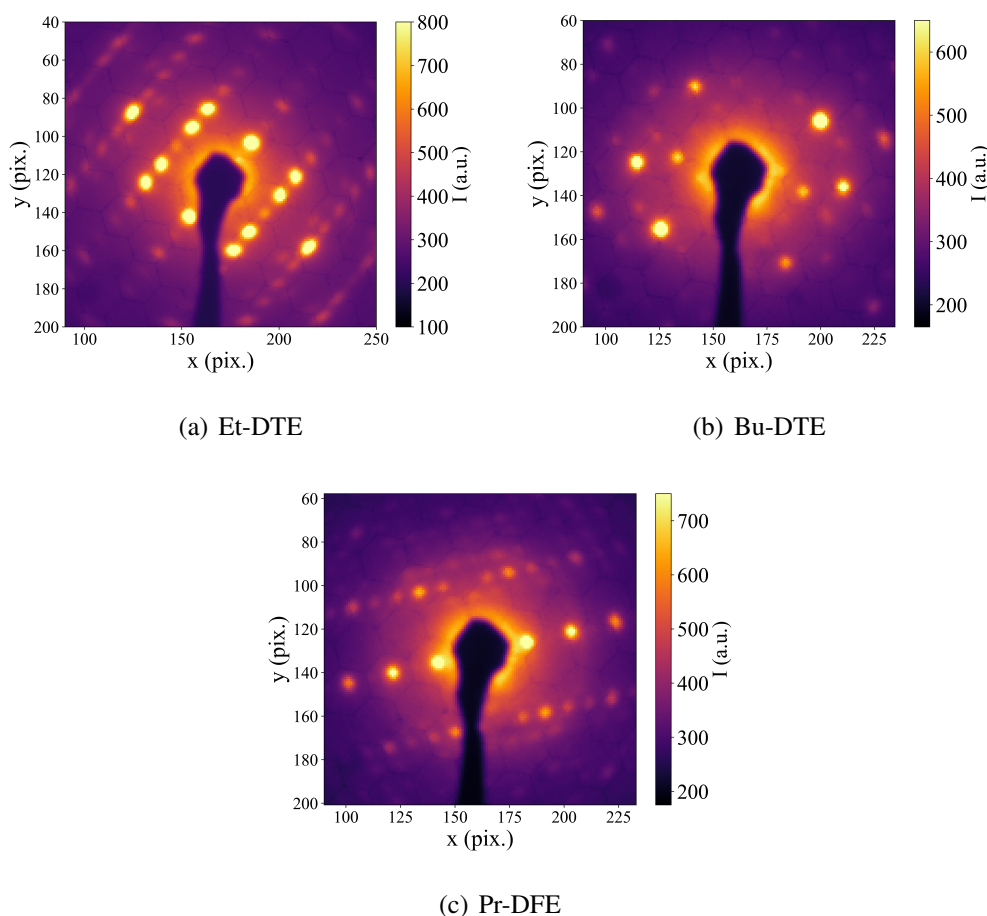


**Figure 5.25:** Static electron diffraction patterns from 100 nm thin single-crystalline samples of the three investigated diarylethene derivatives. Patterns labeled with the most important diffraction indices can be found in the appendix (Fig. A.26).

to reaching equilibrium and serves as an important verification for the feasibility of such an experiment. The obtained difference patterns are shown in Fig. 5.26 for the respective derivatives. In order to mitigate the effects of potential beam shifts, most prominently visible in case of Et-DTE (Fig. 5.26 (a)), the 25 brightest diffraction peaks from both patterns were integrated via an automated peak finding and analysis routine developed by Dr. Hayes, subsequently subtracted and are displayed alongside the difference patterns.

All three difference patterns show typical signs for a change in molecular structure within the unit cell with both increases and decreases in diffraction intensities, ascribable to changes in the respective structure factors.<sup>31</sup>

After correcting for the overall beam shift, the Et-DTE difference pattern exhibits an intensity decrease of the  $(20\bar{2})$  and the complementary  $(\bar{2}02)$  peak, while the  $(080)$  and  $(0\bar{8}0)$  peaks increase in intensity. Less prominent but still distinguishable peak changes

<sup>31</sup>The fact that in most diffraction peaks, a decrease is observed is due to the increased disorder in the lattice compared to the crystals consisting solely of the open-ring forms [279].

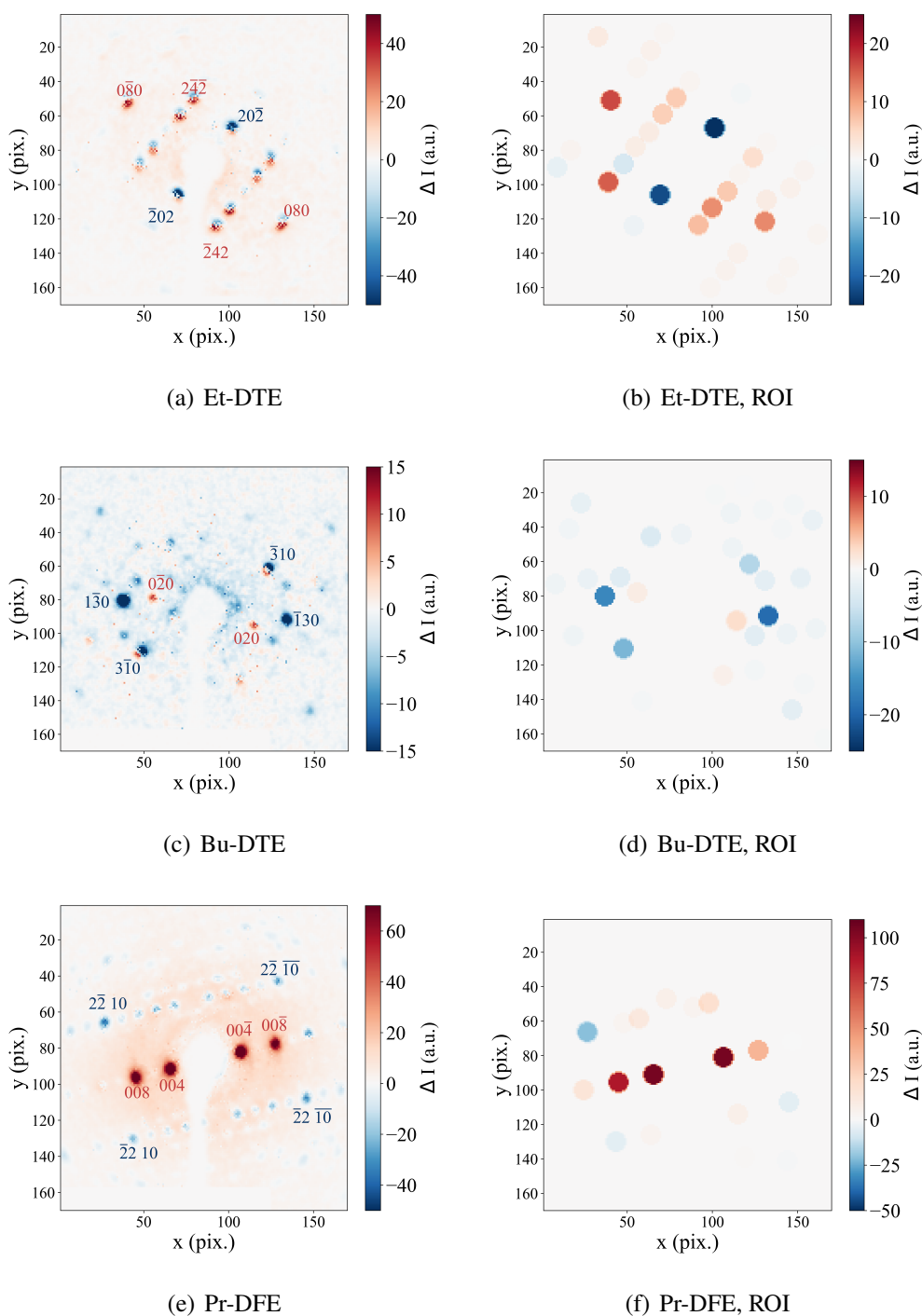


**Figure 5.26:** PSS difference diffraction patterns of the three derivatives. They were obtained by taking the difference of diffraction patterns after and before UV irradiation of the samples. Left column: subtracted diffraction patterns, right column: integrated and subsequently subtracted diffraction peaks (ROI = region of interest). Diffraction indices are preliminary (see text).

entail an increase in intensity of several  $k = 4$  and  $k = -4$  peaks.<sup>32</sup>

The Bu-DTE pattern on the other hand shows only a weak increase of the (020) peak and its counterpart, but a strong decrease in intensity of the ( $\bar{1}30$ ), ( $\bar{3}10$ ) and their respective complementary peaks.

Pr-DFE represents the pattern with the least ambiguous signs of a permanent structural change with four distinct diffraction peaks increasing in intensity ((004), (008) and their counterparts), while the intensity of the others is decreased, most prominently ( $\bar{2}2\bar{1}0$ ), ( $\bar{2}210$ ) etc. There is also a notable increase in diffuse scattering background, presumably due to beginning deterioration of the sample.

These findings render the investigated samples promising candidates for ultrafast diffraction experiments. However, static investigations have significantly lower requirements than time-resolved ones, since the excitation process only needs to be carried out a few times until the PSS has been reached, after which quasi limitless electron beam exposure can be realized. In a time-resolved experiment, the number of electron pulses per sample is fundamentally limited by fatigue of the latter. Furthermore, the number of pump-probe cycles per sample is to be distributed over multiple time points in a scan, including points before time zero. Lastly, feasible excitation fractions typically do not create populations equivalent to the photostationary state, even if quantum yields are high.

An estimation how many electrons per time point are required to obtain a signal can be made based on static diffraction experiments, not dissimilar to the ones presented above, in which the recorded frames contributing to the accumulated difference pattern are analyzed individually and a point can be defined, beyond which no further improvement is found due to the signal-to-noise ratio becoming limited by other factors. Such an analysis was carried out for a few of the DTE crystals and can be found in the appendix (section A.5.3). The recording of single frames was carried out multiple times with a defined number of excitation pulses (peak fluence of  $1 \text{ mJcm}^{-2}$ ) between measurements, to provide a coarse idea of possible improvements by increasing the excitation fraction. To summarize this analysis, with a 100 keV electron gun like the one utilized in these experiments, a number of  $10^8$ - $10^9$  electrons per time point should be targeted. Furthermore, only little improvement was gained by more than a few excitation processes, likely due to the high quantum yield rapidly leading to populations of the closed-ring isomer on the order of the photostationary state level. Thus, fluences in the regime of few  $\text{mJcm}^{-2}$  ought to be sufficient for time-resolved experiments.<sup>33</sup>

---

<sup>32</sup>Please note that all indicated indices are based on a first approximation via the commercially available CrystalMaker suite (*vide supra*) and thus pending verification by more accurate calculations of the diffraction patterns. They are used here nonetheless to ease the identification of the observed differential signals.

<sup>33</sup>As shown by the transient absorption spectroscopy, fluences up to  $4 \text{ mJcm}^{-2}$  are feasible. However, heating of the TEM mesh by the photoreversion beam, which is not absorbed by the substrate in TA experiments, needs to be taken into account for UED and thus lower fluences (e.g.  $2 \text{ mJcm}^{-2}$ ) are recommended.

### 5.5.2 Time-resolved tests and future work

The requirements pointed out in the previous section pose high challenges to be dealt with and are very likely the reason why, within the limited experimental time frame and with the available electron diffractometer, it was not possible to obtain a time-resolved signal above noise level for any of the samples. While it may be possible to achieve this by simply repeating these experiments under the same conditions or using a higher excitation density than the estimated 2-4 % in these tests, it is advisable to optimize the experimental conditions as well. A few insights from the conducted tests can aid to give a few suggestions for future time-resolved electron diffraction experiments.

As mentioned in the introduction of this thesis, source brightness is a critical factor, which is reflected in the conducted tests at relatively low bunch charges on the order of  $10^4$  electrons per pulse. Thus, a more suitable experimental setup would be (similar to) the RF electron gun used for the SNP experiments (see sections 2.5.3 and 3.4.1), in which the problem of space-charge broadening at high electron numbers per pulse is mitigated via the radiofrequency compression scheme and typically a number of electrons per pulse an order of magnitude higher is feasible whilst maintaining sub-ps time resolution. Nevertheless, fatigue of the sample demands pump-probe experiments to be carried out over a multitude of identical samples. The apparatus utilized for the tests in this work required long evacuation and cooling times, as samples could not be exchanged under vacuum and cryo conditions. A diffractometer allowing for rapid sample exchange via load-lock systems would significantly reduce effective down times between experiments and thereby the overall required time frame.

Another strategy to deal with limited cyclability lies within the use of a streak camera rather than stepwise pump-probe scans. While the experimental setup becomes more complicated and additional timing jitters introduce further uncertainties, the advantages of such a system are evident. Firstly, each excitation cycle can be used for an entire scan reducing the total number of photocycles significantly and thereby also the number of samples needed. Secondly, compression of the electron pulse is no longer necessary, since the temporal resolution no longer directly depends on its duration. The relatively slow reaction dynamics of the DTE derivatives, especially Bu-DTE, make them less suitable for this particular approach. On the other hand, the sub-ps cyclization time of the propyl-difurylene derivative as well as the lack of a second, slower pathway match the capabilities of this experimental approach very well.

## 5.6 Concluding discussion

Undertaking an extensive investigation of similar diarylethene derivatives such as the one presented in this chapter ultimately aims to answer the question how different chemical substituents affect photochemical reaction dynamics. Chemists have developed intuitive predictive models for non-equilibrium behavior inferred from steady-state structures, which often reliably predict the outcome of the reaction. However, besides not properly accounting for the quantum nature of molecular compounds,<sup>34</sup> these "arrow-pushing exercises" quickly fail when multiple concurrent influences have to be considered.<sup>35</sup>

When discussing the likelihood of a chemical reaction to occur, which is usually initiated by the formation of a transition state, steric hindrance by other substituents of the reactive atoms is often invoked for such predictions or the explanation of reaction yields. Thus, when comparing the three diarylethene derivatives investigated here, the first intuition would be to expect decreased reaction rates with increasing side-chain length. The findings of this work, as summarized schematically in Fig. 5.1 at the beginning of this chapter indicate that this prediction does not hold true. While indeed the cyclization is slower for Butyl-DTE compared to Ethyl-DTE in both crystal and solution, the Propyl-DFE derivative whose side chain length lies between the two, is significantly faster than either DTE. Comparing the cyclization dynamics from a different difurylethene derivative to reported dithienylethene studies, Khodko et al. stated a similar observation of an accelerated reaction.<sup>[276]</sup> Furthermore, when regarding the molecular structure of the anti-parallel conformer, the substituents are not in the direct way of the reactive carbons. Thus, the intuitive assertion that steric hindrance will govern the reaction can be ruled out. The same conclusion was drawn regarding the quantum yield of diarylethenes in crystal by Kobatake et al.<sup>[235]</sup> who found the C-C equilibrium distance to be the determining factor. Indeed, in crystal there is a correlation between the cyclization time and the C-C distance of the open-ring isomer, with the fastest derivative (Pr-DFE) having the shortest equilibrium distance.<sup>36</sup> However, these distances are not necessarily correlated to the respective antiparallel conformers in solution.

What, if not steric hindrance, are possible reasons for the observed behavior? The most prominent property of oxygen compared to sulfur hetero-atoms is their increased electronegativity and thus their effect on the electron density distribution, especially at neigh-

---

<sup>34</sup>For instance, as pointed out previously, a reduction in dimensionality is required to explain high efficiencies and fast dynamics of particular reaction pathways in photochemical processes, i.e. the coupling to a small set of key driving modes of the reactions. This part of the structural dynamics is not accounted for when trying to deduce dynamics from static structures.

<sup>35</sup>Even some rules derived from first principles and still being taught today often break down. For the diarylethenes, the Woodward-Hoffmann rules [280] for electrocyclic reactions predict the outcome of the reaction correctly, but the proposed one-step mechanism [216] for  $6\pi$  systems has been shown numerous times to be inaccurate, as was pointed out e.g. in ref. [224]. Excited-state intermediates have been observed in many cases, the multitude of which is being extended by the results of this work.

<sup>36</sup>C-C equilibrium distances in crystal were determined by powder diffraction to be 3.7 Å, 3.9 Å and 4.1 Å for Pr-DFE, Et-DTE and Bu-DTE, respectively [231, 232].

**Table 5.3:** Comparison of the three investigated diarylethene derivatives.

	Pr-DFE	Et-DTE	Bu-DTE
Alkyl length (No. of C atoms)	3	2	4
Hetero atom	O	S	S
Cyclization time crystal (ps)	0.3-0.4	0.76	2.6
		14	63
Dual pathway?	No	Yes	Yes
Cyc. speed crystal vs. solution	Faster	Faster	Faster
PSS ED difference signal?	Yes	Yes	Yes

boring atoms.<sup>37</sup> A reduced electron density around the reactive carbon atoms may favor their change in hybridization as well as the formation of a bond, which increases the electron density between them. Furthermore, torsional motions of the moieties which have been shown to be crucial in the cyclization (*vide supra*) may be facilitated by "softening" of the associated bonds due to a reduction in electron density.<sup>38</sup> The alkyl-chains on the other hand are electron-donating, the effect of which increases with chain length. It can be argued that this effect may be smaller than the effect by the oxygen (or sulfur) heteroatoms, but indeed unambiguous predictions are no longer possible.

This highlights the merit of the present systematic, comparative study, elucidating the effect of different substitutions and which are more significant than others. It was demonstrated that seemingly minor chemical modifications can lead to notable differences in dynamics. Nevertheless, it was possible to explain the findings by considering relatively simple and commonly known substituent effects on aromatic systems. Thus, in the grand scheme of things the present study represents a step further towards an updated chemical intuition, accurately accounting for the quantum nature of chemical systems, yet ideally still allowing to predict, design and control (photo-)chemical reactions.

Although the spectroscopic study reported here is conclusive, it would be beneficial to complement the results by other experimental or theoretical methods, especially regarding possible involved intermediate species. The very next step lies in the realization of femtosecond electron diffraction experiments under appropriate conditions and with suffi-

<sup>37</sup>The term electron-withdrawing, while not inappropriate, is deliberately avoided here because it usually denotes the effect that substituents have on an aromatic system without being a part of it themselves.

<sup>38</sup>The benefit of the electron-withdrawing fluorine substituents accelerating the reaction (*vide supra*) can be explained in a similar manner.

cient source brightness to yield reproducible results. As per the findings of this work, it is possible to create and detect the closed-ring products of all three derivatives by means of electron diffraction. Furthermore, it was shown that a significantly higher number of photocycles than in the previous diarylethene UED study can be realized with these particular derivatives and by appropriate choice of wavelengths for both excitation and photoreversion.

Altogether, the results presented in this chapter strongly encourage extensive investigations into the structural dynamics of these derivatives by means of ultrafast electron diffraction within a suitable time frame. It is highly recommended to implement one or multiple of the improvements to the utilized experimental setup suggested in section 5.5.2, in order to achieve the best data quality possible and reliably disentangle the structural dynamics.

---

## Conclusion

One of the most intriguing aspects of science is that the research is never truly finished. Oftentimes journal articles may make it seem as though the ultimate truth was unveiled beyond any doubt in order to prove worthy of publication, while in fact they are part of an iterative heuristic cycle. On the other hand, all these small steps towards a deeper scientific understanding do have their own valid results and conclusions. This is reflected in all three of the projects of which this thesis is comprised, and all of which have led to conclusive interpretations while immediately pointing towards the next steps to be taken. For spironaphthopyran (chapter 3), it was possible to settle a scientific dispute regarding the reaction time scale in solution by discriminating between excited-state, isomerization and product relaxation dynamics. The latter was found to be influenced by the type of solvent, which was characterized by careful analysis of the vibrational fine structure in the product absorption band. Yet, the nature of the specific interaction could only be theorized on, encouraging further investigation using a larger variety of solvents. Furthermore, the theoretical calculations being validated by the experimental data suggest the involvement of C-N and C-O stretch modes as the key modes for internal conversion back to the reactant and the bond-breaking, respectively. Thus, coupling to these modes specifically may be a means to manipulate the respective quantum yields in a coherent control experiment. Another essential result from chapter 3 was the observation of the photochromic reaction in the crystalline phase, closely matching the solution dynamics, which is especially remarkable considering the large structural change. Combined with the results from time-resolved electron diffraction, it is evident that product formation leads to a distortion in the crystal lattice. The latter may also explain why the sub-ns dynamics in crystal differ from solution, most prominently exhibiting a decay of the merocyanine form and the formation of a meta-stable byproduct. Again, ideas for further investigation into these dynamics can be suggested immediately. In the UED experiments, the lattice distortion signal was too strong to recover any signature of the product formation. While this might always be the case, increasing the excitation fraction to approximately 10-20 % may be a remedy for this. Since under the given conditions it was not possible to do so without damaging the sample, test experiments will need to be performed under different conditions, including

cooling of the sample and active reversion of the product. Synchronized photoreversion with the first visible pulse arriving shortly after the product formation, e.g. at a time delay of 20 ps may greatly enhance the achievable excitation fraction by reverting most of the product before the crystal is permanently damaged ("recovery before destruction").<sup>[63]</sup>

The results presented in chapter 4 not only confirmed the proposed acido-photochromic switching cycles of spiropyran in presence of different types of acids, but extended the picture by elucidating the reaction dynamics. Besides the lifetimes of excited-states and product formation, evidence for multiple involved intermediates and their respective lifetimes were deduced from the transient absorption data. The complexity of these isomerization reactions compared to the case of non-protonated spiropyran in which case the planarization is preceded by a bond-breaking step was surprising but emphasized how seemingly small modifications can alter the dynamics of these reactions. All the more reason to investigate the associated structural dynamics and driving modes using structural probes. The long-term goal will be to realize ultrafast diffraction experiments on both the non-protonated and the protonated forms and compare the planarization from the protonated *Z*-isomer to the non-protonated excited-state intermediate with atomic resolution.

Chapter 5 contains an extensive systematic comparison of three different diarylethene derivatives in crystal and solution by means of transient absorption. It was shown that the cyclization times were not primarily governed by the length of the substituents at the reactive carbons, ruling out steric hindrance as the predominant factor. Instead, the heteroatoms in the aryl moieties play a more dominant role, even exhibiting differences regarding the cyclization mechanisms, with dual pathways in case of the di(thienyl)ethenes and only a single pathway in case of the di(furyl)ethenes. In both crystal and solution, the DFE derivative showed the fastest ring-closing time (300-400 fs), motivating further research on this particular subset of diarylethenes. Furthermore, a clear signature of formation of the closed-ring species was observed in the preliminary electron diffraction experiments. This strongly encourages further UED studies on these derivatives, since resolving the structural dynamics should only be a matter of experimental time and optimized conditions.

In the introductory chapter, it was emphasized that a tremendous concerted effort is required in order to atomically resolve the dynamics of irreversible chemical reactions in organic materials, despite all the recent accomplishments. It is thus no surprise that the projects commenced in this work go beyond the scope of a single PhD thesis. The extensive transient absorption experiments in the dedicated and specifically designed setup are the first piece of the puzzle that is a comprehensive picture of the photoisomerization process of the investigated spiropyrans and diarylethenes and set the basis for future scientific endeavors.

---

# Bibliography

- [1] H. G. Khorana. Rhodopsin, Photoreceptor of the Rod Cell. *J. Biol. Chem.*, 267: 1–4, 1992.
- [2] F. Gai, K. C. Hasson, J. C. McDonald, and P. A. Anfinrud. Chemical Dynamics in Proteins: The Photoisomerization of Retinal in Bacteriorhodopsin. *Science*, 279: 1886–1891, 1998.
- [3] S. Hecht, S. Shlaer, and M. H. Pirenne. Energy, Quanta and Vision. *J. Gen. Physiol.*, 25:819–840, 1942.
- [4] K. C. Hasson, F. Gai, and P. A. Anfinrud. The photoisomerization of retinal in bacteriorhodopsin: Experimental evidence for a three-state model. *Proc. Natl. Acad. Sci.*, 93:15124–15129, 1996.
- [5] R. J. D. Miller. Femtosecond Crystallography with Ultrabright Electrons and X-rays: Capturing Chemistry in Action. *Science*, 343:1108–1116, 2014.
- [6] R. J. D. Miller. Mapping Atomic Motions with Ultrabright Electrons: The Chemists’ Gedanken Experiment Enters the Lab Frame. *Annu. Rev. Phys. Chem.*, 65:583–604, 2014.
- [7] M. Eigen. Methods for Investigation of Ionic Reactions in Aqueous Solutions with Half-Times as Short as  $10^{-9}$  Sec. Application to Neutralization and Hydrolysis Reactions. *Discuss. Faraday Soc.*, 17:194–205, 1954.
- [8] The Nobel Prize in Chemistry 1967. <https://www.nobelprize.org/prizes/chemistry/1967/summary/>.
- [9] G. Fleming. *Chemical applications of ultrafast spectroscopy*. Oxford University Press, 1986. ISBN 0195036441.
- [10] J. M. Hollas. *Modern Spectroscopy*. Wiley, 4th edition, 2003. ISBN 978-0470844168.
- [11] R. Berera, R. van Grondelle, and J. T. M. Kennis. Ultrafast transient absorption spectroscopy: principles and application to photosynthetic systems. *Photosynth. Res.*, 101:105–118, 2009.

- [12] C. Schnedermann, M. Liebel, and P. Kukura. Mode-specificity of vibrationally coherent internal conversion in rhodopsin during the primary visual event. *J. Am. Chem. Soc.*, 137:2886–2891, 2015.
- [13] A. J. Musser, M. Liebel, C. Schnedermann, T. Wende, T. B. Kehoe, A. Rao, and P. Kukura. Evidence for conical intersection dynamics mediating ultrafast singlet exciton fission. *Nat. Phys.*, 11:352–357, 2015.
- [14] R. J. Gordon and S. A. Rice. Active Control of the Dynamics of Atoms and Molecules. *Annu. Rev. Phys. Chem.*, 48:601–642, 1997.
- [15] V. I. Prokhorenko, A. M. Nagy, S. A. Waschuk, L. S. Brown, R. R. Birge, and R. J. D. Miller. Coherent Control of Retinal Isomerization in Bacteriorhodopsin. *Science*, 313:1257–1261, 2006.
- [16] A. H. Zewail. 4D ultrafast electron diffraction, crystallography, and microscopy. *Annu. Rev. Phys. Chem.*, 57:65–103, 2006.
- [17] G. Sciaini and R. J. D. Miller. Femtosecond electron diffraction: heralding the era of atomically resolved dynamics. *Rep. Prog. Phys.*, 74, 2011.
- [18] H. Schwoerer, H. N. Chapman, B. J. Siwick, and R. J. D. Miller. Special issue on imaging the dynamic structure of matter. *J. Phys. B: At. Mol. Opt. Phys.*, 49, 2016.
- [19] A. A. Ischenko, P. M. Weber, and R. J. D. Miller. Capturing Chemistry in Action with Electrons: Realization of Atomically Resolved Reaction Dynamics. *Chemical Reviews*, 117:11066–11124, 2017.
- [20] T. Ishikawa, S. A. Hayes, S. Keskin, G. Corthey, M. Hada, K. Pichugin, A. Marx, J. Hirscht, K. Shionuma, K. Onda, Y. Okimoto, S. ya Koshihara, T. Yamamoto, H. Cui, M. Nomura, Y. Oshima, M. Abdel-Jawad, R. Kato, and R. J. D. Miller. Direct observation of collective modes coupled to molecular orbital-driven charge transfer. *Science*, 350:1501–1505, 2015.
- [21] A. A. Ischenko, V. V. Golubkov, V. P. Spiridonov, A. V. Zgurskii, A. S. Akhmanov, M. G. Vabischevich, and V. N. Bagratashvili. A Stroboscopic Gas-Electron Diffraction Method for the Investigation of Short-Lived Molecular Species. *Appl. Phys. B*, 32:161–163, 1983.
- [22] S. Williamson, G. Mourou, and J. C. M. Li. Time-Resolved Laser-Induced Phase Transformation in Aluminum. *Phys. Rev. Lett.*, 52:2364–2367, 1984.
- [23] J. C. Polanyi and A. H. Zewail. Direct Observation of the Transition State. *Acc. Chem. Res.*, 28:119–132, 1995.

- 
- [24] H. Ihee, V. A. Lobastov, U. M. Gomez, B. M. Goodson, R. Srinivasan, C.-Y. Ruan, and A. H. Zewail. Direct Imaging of Transient Molecular Structures with Ultrafast Diffraction. *Science*, 291:458–462, 2001.
- [25] B. J. Siwick, J. R. Dwyer, R. E. Jordan, and R. J. D. Miller. An atomic-level view of melting using femtosecond electron diffraction. *Science*, 302:1382–1385, 2003.
- [26] J. Cao, Z. Hao, H. Park, C. Tao, D. Kau, and L. Blaszczyk. Femtosecond electron diffraction for direct measurement of ultrafast atomic motions. *Appl. Phys. Lett.*, 83:1044–1046, 2003.
- [27] P. Baum and A. H. Zewail. Breaking resolution limits in ultrafast electron diffraction and microscopy. *Proc. Natl. Acad. Sci.*, 103:16105–16110, 2006.
- [28] T. van Oudheusden, E. F. de Jong, S. B. van der Geer, W. P. E. M. Op ’t Root, O. J. Luiten, and B. J. Siwick. Electron source concept for single-shot sub-100 fs electron diffraction in the 100 keV range. *J. Appl. Phys.*, 102, 2007.
- [29] G. H. Kassier, K. Haupt, N. Erasmus, E. G. Rohwer, H. M. von Bergmann, H. Schwoerer, S. M. M. Coelho, and F. D. Auret. A compact streak camera for 150 fs time resolved measurement of bright pulses in ultrafast electron diffraction. *Rev. Sci. Instrum.*, 81:105103, 2010.
- [30] W. R. Huang, A. Fallahi, X. Wu, H. Cankaya, A.-L. Calendron, K. Ravi, D. Zhang, E. A. Nanni, K.-H. Hong, and F. X. Kärtner. Terahertz-driven, all-optical electron gun. *Optica*, 3:1209, 2016.
- [31] M. Gao, H. Jean-Ruel, R. R. Cooney, J. Stampe, M. de Jong, M. Harb, G. Sciaini, G. Moriena, and R. J. D. Miller. Full characterization of RF compressed femtosecond electron pulses using ponderomotive scattering. *Opt. Expr.*, 20:12048–12058, 2012.
- [32] M. R. Otto, L. P. René de Cotret, M. J. Stern, and B. J. Siwick. Solving the jitter problem in microwave compressed ultrafast electron diffraction instruments: Robust sub-50 fs cavity-laser phase stabilization. *Struct. Dyn.*, 4, 2017.
- [33] A. Gliserin, M. Walbran, F. Krausz, and P. Baum. Sub-phonon-period compression of electron pulses for atomic diffraction. *Nat. Commun.*, 6:1–8, 2015.
- [34] C. Kealhofer, W. Schneider, D. Ehberger, A. Ryabov, F. Krausz, and P. Baum. All-optical control and metrology of electron pulses. *Science*, 352:426–433, 2016.
- [35] F. Qi, Z. Ma, L. Zhao, Y. Cheng, W. Jiang, C. Lu, T. Jiang, D. Qian, Z. Wang, W. Zhang, P. Zhu, X. Zou, W. Wan, D. Xiang, and J. Zhang. Breaking 50 Femtosecond Resolution Barrier in MeV Ultrafast Electron Diffraction with a Double Bend Achromat Compressor. *Phys. Rev. Lett.*, 124:134803, 2020.
-

- [36] Y. Morimoto and P. Baum. Diffraction and microscopy with attosecond electron pulse trains. *Nat. Phys.*, 14:252–256, 2018.
- [37] Z. Li, S. Gyawali, A. A. Ischenko, S. Hayes, and R. J. Miller. Mapping Atomic Motions with Electrons: Toward the Quantum Limit to Imaging Chemistry. *ACS Photonics*, 7:296–320, 2020.
- [38] G. Sciaini, M. Harb, S. G. Kruglik, T. Payer, C. T. Hebeisen, F.-J. M. zu Heringdorf, M. Yamaguchi, M. H. von Hoegen, R. Ernstorfer, and R. J. D. Miller. Electronic acceleration of atomic motions and disordering in bismuth. *Nature*, 458:56–59, 2009.
- [39] R. Ernstorfer, M. Harb, C. T. Hebeisen, G. Sciaini, T. Dartigalongue, and R. J. D. Miller. The Formation of Warm Dense Matter: Experimental Evidence for Electronic Bond Hardening in Gold. *Science*, 323:1033–1037, 2009.
- [40] M. J. Stern, L. P. René de Cotret, M. R. Otto, R. P. Chatelain, J. P. Boisvert, M. Sutton, and B. J. Siwick. Mapping momentum-dependent electron-phonon coupling and nonequilibrium phonon dynamics with ultrafast electron diffuse scattering. *Phys. Rev. B*, 97:165416, 2018.
- [41] M. F. Lin, V. Kochat, A. Krishnamoorthy, L. Bassman, C. Weninger, Q. Zheng, X. Zhang, A. Apte, C. S. Tiwary, X. Shen, R. Li, R. Kalia, P. Ajayan, A. Nakano, P. Vashishta, F. Shimojo, X. Wang, D. M. Fritz, and U. Bergmann. Ultrafast non-radiative dynamics of atomically thin MoSe<sub>2</sub>. *Nat. Commun.*, 8:1–7, 2017.
- [42] M. Z. Mo, Z. Chen, R. K. Li, M. Dunning, B. B. L. Witte, J. K. Baldwin, L. B. Fletcher, J. B. Kim, A. Ng, R. Redmer, A. H. Reid, P. Shekhar, X. Z. Shen, M. Shen, K. Sokolowski-Tinten, Y. Y. Tsui, Y. Q. Wang, Q. Zheng, X. J. Wang, and S. H. Glenzer. Heterogeneous to homogeneous melting transition visualized with ultrafast electron diffraction. *Science*, 360:1451–1455, 2018.
- [43] M. Eichberger, H. Schäfer, M. Krumova, M. Beyer, J. Demsar, H. Berger, G. Moriena, G. Sciaini, and R. J. D. Miller. Snapshots of cooperative atomic motions in the optical suppression of charge density waves. *Nature*, 468:799–802, 2010.
- [44] S. Vogelgesang, G. Storeck, J. G. Horstmann, T. Diekmann, M. Siviš, S. Schramm, K. Rossnagel, S. Schäfer, and C. Ropers. Phase ordering of charge density waves traced by ultrafast low-energy electron diffraction. *Nat. Phys.*, 14:184–190, 2018.
- [45] R. C. Dudek and P. M. Weber. Ultrafast diffraction imaging of the electrocyclic ring-opening reaction of 1,3-cyclohexadiene. *J. Phys. Chem. A*, 105:4167–4171, 2001.

- [46] C.-Y. Ruan, V. A. Lobastov, R. Srinivasan, B. M. Goodson, H. Ihee, and A. H. Zewail. Ultrafast diffraction and structural dynamics: The nature of complex molecules far from equilibrium. *Proc. Natl. Acad. Sci.*, 98:7117–7122, 2001.
- [47] J. B. Hastings, F. M. Rudakov, D. H. Dowell, J. F. Schmerge, J. D. Cardoza, J. M. Castro, S. M. Gierman, H. Loos, and P. M. Weber. Ultrafast time-resolved electron diffraction with megavolt electron beams. *Appl. Phys. Lett.*, 89:184109, 2006.
- [48] J. Yang, M. Guehr, T. Vecchione, M. S. Robinson, R. Li, N. Hartmann, X. Shen, R. Coffee, J. Corbett, A. Fry, K. Gaffney, T. Gorkhover, C. Hast, K. Jobe, I. Makasyuk, A. Reid, J. Robinson, S. Vetter, F. Wang, S. Weathersby, C. Yoneda, M. Centurion, and X. Wang. Diffractive imaging of a rotational wavepacket in nitrogen molecules with femtosecond megaelectronvolt electron pulses. *Nat. Commun.*, 7:11232, 2016.
- [49] J. Yang, M. Guehr, T. Vecchione, M. S. Robinson, R. Li, N. Hartmann, X. Shen, R. Coffee, J. Corbett, A. Fry, K. Gaffney, T. Gorkhover, C. Hast, K. Jobe, I. Makasyuk, A. Reid, J. Robinson, S. Vetter, F. Wang, S. Weathersby, C. Yoneda, X. Wang, and M. Centurion. Femtosecond gas phase electron diffraction with MeV electrons. *Faraday Discuss.*, 194:563–581, 2016.
- [50] J. Yang, M. Guehr, X. Shen, R. Li, T. Vecchione, R. Coffee, J. Corbett, A. Fry, N. Hartmann, C. Hast, K. Hegazy, K. Jobe, I. Makasyuk, J. Robinson, M. S. Robinson, S. Vetter, S. Weathersby, C. Yoneda, X. Wang, and M. Centurion. Diffractive Imaging of Coherent Nuclear Motion in Isolated Molecules. *Phys. Rev. Lett.*, 117:153002, 2016.
- [51] J. Yang, X. Zhu, T. J. Wolf, Z. Li, J. F. P. Nunes, R. Coffee, J. P. Cryan, M. Gühr, K. Hegazy, T. F. Heinz, K. Jobe, R. Li, X. Shen, T. Vecchione, S. Weathersby, K. J. Wilkin, C. Yoneda, Q. Zheng, T. J. Martinez, M. Centurion, and X. Wang. Imaging CF<sub>3</sub>I conical intersection and photodissociation dynamics with ultrafast electron diffraction. *Science*, 361:64–67, 2018.
- [52] M. Gao, Y. Jiang, G. H. Kassier, and R. J. D. Miller. Single shot time stamping of ultrabright radio frequency compressed electron pulses. *Appl. Phys. Lett.*, 103:033503, 2013.
- [53] Y. Jiang, L. C. Liu, H. M. Müller-Werkmeister, C. Lu, D. Zhang, R. L. Field, A. Sarracini, G. Moriena, E. Collet, and R. J. D. Miller. Structural Dynamics upon Photoexcitation in a Spin Crossover Crystal Probed with Femtosecond Electron Diffraction. *Angew. Chem. Int. Ed.*, 129:7236–7240, 2017.
- [54] L. C. Liu, Y. Jiang, H. M. Mueller-Werkmeister, C. Lu, G. Moriena, M. Ishikawa, Y. Nakano, H. Yamochi, and R. J. Miller. Ultrafast electron diffraction study of

- single-crystal (EDO-TTF)<sub>2</sub>SbF<sub>6</sub>: Counterion effect and dimensionality reduction. *Chem. Phys. Lett.*, 683:160–165, 2017.
- [55] Y. Jiang, L. C. Liu, A. Sarracini, K. M. Krawczyk, J. S. Wentzell, C. Lu, R. L. Field, S. F. Matar, W. Gawelda, H. M. Müller-Werkmeister, and R. J. Miller. Direct observation of nuclear reorganization driven by ultrafast spin transitions. *Nat. Commun.*, 11:1530, 2020.
- [56] H. Jean-Ruel, M. Gao, M. A. Kochman, C. Lu, L. C. Liu, R. R. Cooney, C. A. Morrison, and R. J. D. Miller. Ring-closing reaction in diarylethene captured by femtosecond electron crystallography. *J. Phys. Chem. B*, 117:15894–15902, 2013.
- [57] H. Jean-Ruel. *Femtosecond Electron Diffraction and Spectroscopic Studies of a Solid State Organic Chemical Reaction*, 2014.
- [58] L. C. Liu. *Chemistry in Action: Making Molecular Movies with Ultrafast Electron Diffraction and Data Science*. PhD thesis, University of Toronto, 2019.
- [59] L.-M. Peng, G. Ren, S. L. Dudarev, and M. J. Whelan. Robust Parameterization of Elastic and Absorptive Electron Atomic Scattering Factors. *Acta Cryst.*, 52: 257–276, 1996.
- [60] E. C. Schulz, P. Mehrabi, H. M. Müller-Werkmeister, F. Tellkamp, A. Jha, W. Stuart, E. Persch, R. D. Gasparo, F. Diederich, E. F. Pai, and R. J. D. Miller. The hit-and-return system enables efficient time-resolved serial synchrotron crystallography. *Nat. Methods*, 15:901–904, 2018.
- [61] P. Mehrabi, H. M. Müller-Werkmeister, J. P. Leimkohl, H. Schikora, J. Ninkovic, S. Krivokuca, L. Andricek, S. W. Epp, D. Sherrell, R. L. Owen, A. R. Pearson, F. Tellkamp, E. C. Schulz, and R. J. D. Miller. The HARE chip for efficient time-resolved serial synchrotron crystallography. *J. Synchrotron Rad.*, 27:360–370, 2020.
- [62] R. Li, W. Huang, Y. Du, L. Yan, Q. Du, J. Shi, J. Hua, H. Chen, T. Du, H. Xu, and C. Tang. Note: Single-shot continuously time-resolved MeV ultrafast electron diffraction. *Rev. Sci. Instrum.*, 81:036110, 2010.
- [63] K. M. Siddiqui, G. Corthey, S. A. Hayes, A. Rossos, D. S. Badali, R. Xian, R. S. Murphy, B. J. Whitaker, and R. J. D. Miller. Synchronised photoreversion of spirooxazine ring opening in thin crystals to uncover ultrafast dynamics. *CrystrEngComm*, 18:7212–7216, 2016.
- [64] M. Irie, T. Fukaminato, K. Matsuda, and S. Kobatake. Photochromism of diarylethene molecules and crystals: Memories, switches, and actuators. *Chem. Rev.*, 114:12174–12277, 2014.

- [65] C. Mueller, M. Harb, J. R. Dwyer, and R. J. D. Miller. Nanofluidic cells with controlled pathlength and liquid flow for rapid, high-resolution in situ imaging with electrons. *J. Phys. Chem. Lett.*, 4:2339–2347, 2013.
- [66] S. Manz, A. Casandruc, D. Zhang, Y. Zhong, R. A. Loch, A. Marx, T. Hasegawa, L. C. Liu, S. Bayesteh, H. Delsim-Hashemi, M. Hoffmann, M. Felber, M. Hachmann, F. Mayet, J. Hirscht, S. Keskin, M. Hada, S. W. Epp, K. Flöttmann, and R. J. D. Miller. Mapping atomic motions with ultrabright electrons: towards fundamental limits in space-time resolution. *Faraday Discuss.*, 177:467–491, 2015.
- [67] M. Suzuki, T. Asahi, and H. Masuhara. Photochromic reactions of crystalline spiropyrans and spirooxazines induced by intense femtosecond laser excitation. *Phys. Chem. Chem. Phys.*, 4:185–192, 2002.
- [68] S. F. Bittmann, R. Dsouza, K. M. Siddiqui, S. A. Hayes, A. Rossos, G. Corthey, M. Kochman, V. I. Prokhorenko, R. S. Murphy, H. Schwoerer, and R. J. D. Miller. Ultrafast ring-opening and solvent-dependent product relaxation of photochromic spironaphthopyran. *Phys. Chem. Chem. Phys.*, 21:18119–18127, 2019.
- [69] R. Dsouza. *Revealing key modes in photoprocesses using Ab Initio molecular dynamics*. PhD thesis, University of Hamburg, 2019.
- [70] F. Traeger, editor. *Handbook of Lasers and Optics*. 2007. ISBN 9780387955797.
- [71] R. W. Boyd. *Nonlinear Optics*. Elsevier Inc., 3rd edition, 2008. ISBN 9780123694706.
- [72] W. T. Silfvast. *Laser Fundamentals*. 2004. ISBN 9780521833455.
- [73] R. Paschotta. Acousto-optic Modulators. [https://www.rp-photonics.com/acousto\\_optic\\_modulators.html](https://www.rp-photonics.com/acousto_optic_modulators.html).
- [74] T. Brabec, C. Spielmann, P. F. Curley, and F. Krausz. Kerr lens mode locking. *Opt. Lett.*, 17:1292–1294, 1992.
- [75] R. R. Alfano and S. L. Shapiro. Observation of Self-Phase Modulation and Small-Scale Filaments in Crystals and Glasses. *Phys. Rev. Lett.*, 24, 1970.
- [76] R. R. Alfano. *The Supercontinuum Laser Source*. Springer, 1989. ISBN 9780387245041.
- [77] A. Zheltikov. Multioctave supercontinua and subcycle lightwave electronics. *J. Opt. Soc. Am. B*, 36:A168–A182, 2019.

- [78] C. Nagura, A. Suda, H. Kawano, M. Obara, and K. Midorikawa. Generation and characterization of ultrafast white-light continuum in condensed media, 2002.
- [79] D. Strickland and G. Mourou. Compression of Amplified Chirped Optical Pulses. *Opt. Commun.*, 56:219–221, 1985.
- [80] Coherent Inc.: femtosecond laser systems, Web Page, 2017. <http://lasers.coherent.com>.
- [81] R. L. Field. *Photoinduced Spin Crossover in Single Crystal [Fe(II)-(bpy)3](PF6)2*. PhD thesis, University of Toronto, 2016.
- [82] Light Conversion U. A. B., Web Page. <https://lightcon.com/>.
- [83] H. Jean-Ruel, R. R. Cooney, M. Gao, C. Lu, M. A. Kochman, C. A. Morrison, and R. J. D. Miller. Femtosecond Dynamics of the Ring Closing Process of Diarylethene: A Case Study of Electrocyclic Reactions in Photochromic Single Crystals. *J. Phys. Chem. A*, 115:13158–13168, 2011.
- [84] P. Tzankov, I. Buchvarov, and T. Fiebig. Broadband optical parametric amplification in the near UV – VIS. 203:107–113, 2002.
- [85] Optics Toolbox by Light Conversion, Web Page, 2022. [toolbox.lightcon.com](http://toolbox.lightcon.com).
- [86] N. Turro. *Molecular Photochemistry*. W.A. Benjamin, 1965. ISBN 9780805393514.
- [87] P. Atkins and R. Friedman. *Molecular Quantum Mechanics*. OUP Oxford, 2011. ISBN 9780199541423.
- [88] P. Atkins and J. De Paula. *Atkins' Physical Chemistry*. Macmillan Higher Education, 2006. ISBN 9780716771111.
- [89] M. Born and J. R. Oppenheimer. Zur Quantentheorie der Molekeln. *Annalen der Physik*, 389:457–484, 1927.
- [90] R. Unanyan, M. Fleischhauer, B. W. Shore, and K. Bergmann. Robust creation and phase-sensitive probing of superposition states via stimulated Raman adiabatic passage (STIRAP) with degenerate dark states. *Opt. Commun.*, 155:144–154, 1998.
- [91] W. S. Warren, H. Rabitz, and M. Dahleh. Coherent Control of Quantum Dynamics: The Dream Is Alive. *Science*, 259:1581–1589, 1993.
- [92] M. Shapiro and P. Brumer. Coherent control of molecular dynamics. *Rep. Prog. Phys.*, 66:859–942, 2003.

- 
- [93] V. I. Prokhorenko, A. Halpin, P. J. Johnson, R. J. Miller, and L. S. Brown. Coherent control of the isomerization of retinal in bacteriorhodopsin in the high intensity regime. *J. Chem. Phys.*, 134:085105, 2011.
- [94] M. Kasha. Characterization of Electronic Transitions in Complex Molecules. *Discuss. Faraday Soc.*, 9:14–19, 1950.
- [95] E. Teller. The Crossing of Potential Surfaces. *J. Phys. Chem.*, 41:109–116, 1937.
- [96] R. Xian, G. Corthey, D. M. Rogers, C. A. Morrison, V. I. Prokhorenko, S. A. Hayes, and R. J. D. Miller. Coherent ultrafast lattice-directed reaction dynamics of triiodide anion photodissociation. *Nat. Chem.*, 9:516–522, 2017.
- [97] K. M. Siddiqui. *Investigating photoinduced phenomena in molecular crystals with prospects for atomically-resolved dynamics*. PhD thesis, University of Leeds, 2016.
- [98] J. R. Lakowicz, editor. *Principles of Fluorescence Spectroscopy*. Springer US, 2006.
- [99] Saint-Gobain Performance Plastics. <https://www.plastics.saint-gobain.com/products/tubing>.
- [100] TCS Micropumps. <https://micropumps.co.uk>.
- [101] Oxford Instruments - OptistatDN-X. <https://andor.oxinst.com/products/optical-cryostats-for-spectroscopy/optistatdn-x>.
- [102] Hamamatsu Photonics K. K. <https://www.hamamatsu.com/eu/en/>.
- [103] S. A. Kovalenko, A. L. Dobryakov, J. Ruthmann, and N. P. Ernsting. Femtosecond spectroscopy of condensed phases with chirped supercontinuum probing. *Phys. Rev. A*, 59:2369–2384, 1999.
- [104] M. N. Islam, L. F. Mollenauer, R. H. Stolen, J. R. Simpson, and H. T. Shang. Cross-phase modulation in optical fibers. *Opt. Lett.*, 12:625–627, 1987.
- [105] M. Lorenc, M. Ziolk, R. Naskrecki, J. Karolczak, J. Kubicki, and A. Maciejewski. Artifacts in femtosecond transient absorption spectroscopy. *Appl. Phys. B*, 74:19–27, 2002.
- [106] J.-K. Wang, T.-L. Chiu, C.-H. Chi, and C. K. Sun. Nonlinear refraction and absorption measurements with chirped femtosecond laser pulses: experiments and simulations. *J. Opt. Soc. Am. B*, 16:651–661, 1999.
- [107] M. Rasmusson, A. N. Tarnovsky, E. Akesson, and V. Sundström. On the use of two-photon absorption for determination of femtosecond pump-probe cross-correlation functions. *Chem. Phys. Lett.*, 335:201–208, 2001.
-

- [108] R. Field, L. C. Liu, W. Gawelda, C. Lu, and R. J. D. Miller. Spectral Signatures of Ultrafast Spin Crossover in Single Crystal [FeII(bpy)<sub>3</sub>](PF<sub>6</sub>)<sub>2</sub>. *Chem. Eur. J.*, 22: 5118–5122, 2016.
- [109] O. Paré-Labrosse. *Damage-Free Femtosecond Structural Dynamics of Proteins in the Biologically Relevant Regime*. PhD thesis, University of Toronto, 2021.
- [110] U. Megerle, I. Pugliesi, C. Schriefer, C. F. Sailer, and E. Riedle. Sub-50 fs broadband absorption spectroscopy with tunable excitation: putting the analysis of ultrafast molecular dynamics on solid ground. *Appl. Phys. B*, 96:215–231, 2009.
- [111] J. F. Nagle, L. A. Parodi, and R. H. Lozier. Procedure for Testing Kinetic Models of the Photocycle of Bacteriorhodopsin. *Biophys. J.*, 38:161–174, 1982.
- [112] I. H. M. van Stokkum, D. S. Larsen, and R. van Grondelle. Global and target analysis of time-resolved spectra. *Biochim. Biophys. Acta*, 1657:82–104, 2004.
- [113] I. H. M. van Stokkum. Global and target analysis of time-resolved spectra. *Lecture notes Troisième Cycle de la Physique en Suisse Romande*, 2005.
- [114] C. Slavov, H. Hartmann, and J. Wachtveitl. Implementation and evaluation of data analysis strategies for time-resolved optical spectroscopy. *Anal. Chem.*, 87:2328–2336, 2015.
- [115] C. Ruckebusch, M. Sliwa, P. Pernot, A. de Juan, and R. Tauler. Comprehensive data analysis of femtosecond transient absorption spectra: A review. *J. Photochem. Photobiol. C: Photochem. Rev.*, 13:1–27, 2012.
- [116] V. I. Prokhorenko. Global Analysis of Multi-Dimensional Experimental Data. *EPA Newsletter*, pages 21–23, 2012.
- [117] LMFIT: Non-Linear Least-Squares Minimization and Curve-Fitting for Python. <https://lmfit.github.io/lmfit-py>.
- [118] M. Koeberg, M. H. V. Werts, H. J. van Ramesdonk, and J. W. Verhoeven. Two-dimensional transient absorption spectroscopy using a streak camera for detection and singular value decomposition for data analysis. *EPA Newsletter*, 71, 2001.
- [119] L. J. G. W. van Wilderen, C. N. Lincoln, and J. J. van Thor. Modelling multi-pulse population dynamics from ultrafast spectroscopy. *PLoS ONE*, 6:e17373, 2011.
- [120] J. J. Olivero and R. L. Longbothum. Empirical Fits for the Voigt Line Width: A Brief Review. *J. Quant. Spectrosc. Radiat. Transfer*, 17:233–236, 1977.
- [121] Simon Bittmann’s profile on GitHub. <https://github.com/simonbittmann>.

- [122] N. W. Ashcroft and N. D. Mermin. *Solid State Physics*. Holt-Saunders, 1976. ISBN 978-0030839931.
- [123] C. Kittel. *Introduction to Solid State Physics*. Wiley, 2004. ISBN 978-0471415268.
- [124] L. Reimer and H. Kohl. *Transmission Electron Microscopy. Physics of Image Formation*. Springer, 5th edition, 2008. ISBN 978-0387400938.
- [125] P. Debye. Interferenz von Röntgenstrahlen und Wärmebewegung. *Annalen der Physik*, 348:49–92, 1913.
- [126] I. Waller. Zur Frage der Einwirkung der Wärmebewegung auf die Interferenz von Röntgenstrahlen. *Zeitschrift für Physik*, 17:398–408, 1923.
- [127] W. Friedrich, P. Knipping, and M. Laue. Interferenzerscheinungen bei Röntgenstrahlen. *Annalen der Physik*, 346:971–988, 1913.
- [128] A. Jablonski, F. Salvat, and C. J. Powell. Comparison of electron elastic-scattering cross sections calculated from two commonly used atomic potentials. *J. Phys. Chem. Ref. Data*, 33:409–451, 2004.
- [129] J. R. Dwyer, C. T. Hebeisen, R. Ernstorfer, M. Harb, V. B. Deyirmenjian, R. E. Jordan, and R. J. D. Miller. Femtosecond electron diffraction: 'making the molecular movie'. *Philos. Trans. R. Soc. A*, 364:741–778, 2006.
- [130] B. J. Siwick, J. R. Dwyer, R. E. Jordan, and R. J. D. Miller. Ultrafast electron optics: Propagation dynamics of femtosecond electron packets. *J. Appl. Phys.*, 92:1643–1648, 2002.
- [131] M. S. Robinson, P. D. Lane, and D. A. Wann. A compact electron gun for time-resolved electron diffraction. *Rev. Sci. Instrum.*, 86:013109, 2015.
- [132] T. van Oudheusden, P. L. E. M. Pasmans, S. B. van der Geer, M. J. de Loos, M. J. van der Wiel, and O. J. Luiten. Compression of subrelativistic space-charge-dominated electron bunches for single-shot femtosecond electron diffraction. *Phys. Rev. Lett.*, 105:264801, 2010.
- [133] H. Daoud, K. Floettmann, and R. J. D. Miller. Compression of high-density 0.16 pC electron bunches through high field gradients for ultrafast single shot electron diffraction: The compact RF gun. *Struct. Dyn.*, 4:044016, 2017.
- [134] S. Bittmann. Ultrafast Dynamics of Spirooxazine and Spiropyran Photochromics. Master thesis, University of Hamburg, 2017.

- [135] K. M. Krawczyk, A. Sarracini, P. B. Green, M. Hasham, K. Tang, O. Paré-Labrosse, O. Voznyy, M. W. B. Wilson, and R. J. D. Miller. Anisotropic, Nonthermal Lattice Disorder Observed in Photoexcited PbS Quantum Dots. *J. Phys. Chem. C*, 125:22120–22132, 2021.
- [136] R. J. Staples. Growing and Mounting Crystals Your Instrument Will Treasure, 2017. <http://scripts.iucr.org/cgi-bin/paper?S056773947000178X>.
- [137] H. Hwang, V. Tiwari, H.-G. Duan, S. F. Bittmann, F. Tellkamp, A. Jha, and R. J. D. Miller. Two-dimensional confinement for generating thin single crystals for applications in time-resolved electron diffraction and spectroscopy: an intramolecular proton transfer study. *Chem. Commun.*, 58:9774–9777, 2022.
- [138] G. H. Michler. *Electron Microscopy of Polymers*. Springer Laboratory, 2014. ISBN 978-0874216561.
- [139] J. Ayache, L. Beaunier, J. Boumendil, G. Ehret, and D. Laub. *Sample Preparation Handbook for Transmission Electron Microscopy*. 2013. ISBN 9788578110796.
- [140] H. Dürr and H. Bouas-Laurent. *Photochromism: Molecules and Systems*. Elsevier, 2003. ISBN 9780444513229.
- [141] R. Klajn. Spiropyran-based dynamic materials. *Chem. Soc. Rev.*, 43:148–184, 2014.
- [142] L. Kortekaas and W. R. Browne. The evolution of spiropyran: Fundamentals and progress of an extraordinarily versatile photochrome. *Chem. Soc. Rev.*, 48:3406–3424, 2019.
- [143] M. E. Gemayel, K. Börjesson, M. Herder, D. T. Duong, J. Hutchison, C. Ruzié, G. Schweicher, A. Salleo, Y. Geerts, S. Hecht, E. Orgiu, and P. Samorì. Optically switchable transistors by simple incorporation of photochromic systems into small-molecule semiconducting matrices. *Nat. Commun.*, 6:5054–5075, 2015.
- [144] E. Orgiu, N. Crivillers, M. Herder, L. Grubert, M. Pätzl, J. Frisch, E. Pavlica, D. T. Duong, G. Bratina, A. Salleo, N. Koch, S. Hecht, and P. Samorì. Optically switchable transistor via energy-level phototuning in a bicomponent organic semiconductor. *Nat. Chem.*, 4:675–679, 2012.
- [145] D. Bléger and S. Hecht. Visible-Light-Activated Molecular Switches. *Angew. Chem. Int. Ed.*, 54:11338–11349, 2015.
- [146] G. Berkovic, V. Krongauz, and V. Weiss. Spiroyrans and Spirooxazines for Memories and Switches. *Chem. Rev.*, 100:1741–1753, 2000.

- [147] M. Irie. Diarylethenes for Memories and Switches. *Chem. Rev.*, 100:1685–1716, 2000.
- [148] Y. Xiong, A. V. Jentsch, J. Osterrieth, E. Sezgin, I. V. Sazanovich, K. Reglinski, S. Galiani, A. W. Parker, C. Eggeling, and H. L. Anderson. Spiro-naphthoxazine switchable dyes for biological imaging. *Chem. Sci.*, 9:3029–3040, 2018.
- [149] A. Mustafa. The Chemistry of Spiropyran. *Chem. Rev.*, pages 509–523, 1948.
- [150] C. J. Roxburgh and P. G. Sammes. On the acid catalysed isomerisation of some substituted spirobenzopyrans. *Dyes Pigm.*, 27:63–69, 1995.
- [151] L. Kortekaas, J. Chen, D. Jacquemin, and W. R. Browne. Proton-Stabilized Photochemically Reversible E/Z Isomerization of Spiropyran. *J. Phys. Chem. B*, 122:6423–6430, 2018.
- [152] M. Campredon, G. Giusti, R. Guglielmetti, A. Samat, G. Gronchi, A. Alberti, and M. Benaglia. Radical Ions and Gernyloxyaminoxyls from Nitrospiro[indoline-naphthopyran]. A Combined Electrochemical and EPR Study. *J. Chem. Soc. Perkin Trans.*, 2:2089, 1993.
- [153] L. Kortekaas, O. Ivashenko, J. T. V. Herpt, and W. R. Browne. A Remarkable Multitasking Double Spiropyran: Bidirectional Visible-Light Switching of Polymer-Coated Surfaces with Dual Redox and Proton Gating. *J. Am. Chem. Soc.*, 138:1301–1312, 2016.
- [154] M. Li, Q. Zhang, Y. N. Zhou, and S. Zhu. Let spiropyran help polymers feel force! *Prog. Polym. Sci.*, 79:26–39, 2018.
- [155] N. P. Ernsting, B. Dick, and T. Arthen-Engeland. The primary photochemical reaction step of unsubstituted indolino-spiropyran. *Pure Appl. Chem.*, 62:1483–1488, 1990.
- [156] J. Buback, P. Nuernberger, M. Kullmann, F. Langhojer, R. Schmidt, F. Würthner, and T. Brixner. Ring-Closure and Isomerization Capabilities of Spiropyran-Derived Merocyanine Isomers. *J. Phys. Chem. A*, 115:3924–3935, 2011.
- [157] H. Takahashi, K. Yoda, H. Isaka, T. Ohzeki, and Y. Sakaino. Resonance Raman Studies of Transient Species in the Photochromism of 1',3',3'-trimethylspiro-[2H-1-benzopyran-2,2'-indoline]. *Chem. Phys. Lett.*, 140:90–94, 1987.
- [158] E. Fischer and Y. Hirshberg. Formation of Coloured Forms of Spirans by Low-temperature Irradiation. *J. Chem. Soc.*, pages 4522–4524, 1952.
- [159] Y. Hirshberg and E. Fischer. Low-temperature Photochromism and its Relation to Thermochromism. *J. Chem. Soc.*, pages 629–636, 1953.

- [160] Y. Hirshberg and E. Fischer. Photochromism and Reversible Multiple Internal Transitions in Some spiroPyrans at Lower Temperatures. Part I. *J. Chem. Soc.*, pages 297–303, 1954.
- [161] T. Kumpulainen, B. Lang, A. Rosspeintner, and E. Vauthey. Ultrafast Elementary Photochemical Processes of Organic Molecules in Liquid Solution. *Chem. Rev.*, 117:10826–10939, 2017.
- [162] R. Heiligman-Rim, Y. Hirshberg, and E. Fischer. Photochromism in Spiroprans. Part IV. Evidence for the Existence of Several Forms of the Colored Modification. *J. Phys. Chem.*, 66:2465–2470, 1962.
- [163] A. Kellmann, F. Tfibel, R. Dubest, P. Levoir, J. Aubard, E. Pottier, and R. Guglielmetti. Photophysics and Kinetics of two Photochromic Indolinospirooxazines and one Indolinospironaphthopyran. *J. Photochem. Photobiol. A*, 49:63–73, 1989.
- [164] N. P. Ernsting. Transient optical absorption spectroscopy of the photochemical spiropran-merocyanine conversion. *Chem. Phys. Lett.*, 159:526–531, 1989.
- [165] N. P. Ernsting and T. Arthen-Engeland. Photochemical Ring-Opening Reaction of Indolinospiroprans Studied by Subpicosecond Transient Absorption. *J. Phys. Chem.*, 95:5502–5509, 1991.
- [166] M. Rini, A. K. Holm, E. T. J. Nibbering, and H. Fidder. Ultrafast UV-mid-IR investigation of the ring opening reaction of a photochromic spiropran. *J. Am. Chem. Soc.*, 125:3028–3034, 2003.
- [167] J. Kohl-Landgraf, M. Braun, Özcoban Cem, D. P. N. Gonc, A. Heckel, and J. Wachtveitl. Ultrafast Dynamics of a Spiropran in Water. *J. Am. Chem. Soc.*, 134:14070–14077, 2012.
- [168] TCI America: Spironaphthopyran, 2017. <http://www.tcichemicals.com/eshop/en/us/commodity/T0423/>.
- [169] F. O. Kirchner, S. Lahme, E. Riedle, and P. Baum. All-reflective UV-VIS-NIR transmission and fluorescence spectrometer for  $\mu\text{m}$ -sized samples. *AIP Adv.*, 4: 077134, 2014.
- [170] M. L. Horng, J. A. Gardecki, A. Papazyan, and M. Maroncelli. Subpicosecond Measurements of Polar Solvation Dynamics: Coumarin 153 Revisited. *J. Phys. Chem.*, 99:17311–17337, 1995.
- [171] S. A. Kovalenko, J. L. P. Lustres, N. P. Ernsting, and W. Rettig. Photoinduced electron transfer in bianthryl and cyanobianthryl in solution: The case for a high-frequency intramolecular reaction coordinate. *J. Phys. Chem. A*, 107:10228–10232, 2003.

- [172] F. Liu, Y. Kurashige, T. Yanai, and K. Morokuma. Multireference ab initio density matrix renormalization group (DMRG)-CASSCF and DMRG-CASPT2 study on the photochromic ring opening of spiropyran. *J. Chem. Theory Comput.*, 9:4462–4469, 2013.
- [173] F. Liu and K. Morokuma. Multiple pathways for the primary step of the spiropyran photochromic reaction: A CASPT2//CASSCF study. *J. Am. Chem. Soc.*, 135:10693–10702, 2013.
- [174] J. Harada, Y. Kawazoe, and K. Ogawa. Photochromism of spiropyrans and spirooxazines in the solid state: low temperature enhances photocoloration. *Chem. Commun.*, 46:2593–2595, 2010.
- [175] R. J. D. Miller, M. Pierre, T. S. Rose, and M. D. Fayer. A Coherent Photoacoustic Approach to Excited-State-Excited-State Absorption Spectroscopy: Application to the Investigation of a Near-Resonant Contribution to Ultrasonic Diffraction. *J. Phys. Chem.*, 88:3021–3025, 1984.
- [176] K. A. Nelson and M. D. Fayer. Laser induced phonons: A probe of intermolecular interactions in molecular solids. *J. Chem. Phys.*, 72:5202–5218, 1980.
- [177] K. A. Nelson, R. Casalegno, R. J. D. Miller, and M. D. Fayer. Laser-induced excited state and ultrasonic wave gratings: Amplitude and phase grating contributions to diffraction. *J. Chem. Phys.*, 77:1144–1152, 1982.
- [178] CrystalMaker Ltd. Software Package. <http://www.crystalmaker.com/>.
- [179] J. Harada, Y. Kawazoe, and K. Ogawa. Photochromism of spiropyrans and spirooxazines in the solid state: Low temperature enhances photocoloration, Supporting Information. *Chem. Commun.*, 46:2567–2569, 2010.
- [180] Y.-S. Nam, I. Yoo, O. Yarimaga, I. S. Park, D.-H. Park, S. Song, J.-M. Kim, and C. W. Lee. Photochromic spiropyran-embedded PDMS for highly sensitive and tunable optochemical gas sensing. *Chem. Commun.*, 50:4251–4, 2014.
- [181] M. E. Genovese, A. Athanassiou, and D. Fragouli. Photoactivated acidochromic elastomeric films for on demand acidic vapor sensing. *J. Mat. Chem. A*, 3:22441–22447, 2015.
- [182] M. E. Genovese, E. Colusso, M. Colombo, A. Martucci, A. Athanassiou, and D. Fragouli. Acidochromic fibrous polymer composites for rapid gas detection. *J. Mat. Chem. A*, 5:339–348, 2017.
- [183] Z. Zhao and J. Tian. Ultraviolet–visible/fluorescence behaviors of a spiropyran/polydimethylsiloxane composite film under acid vapors. *J. Appl. Polym. Sci.*, 134:45199, 2017.

- [184] S. Ahmadi, M. Nasiri, and A. P. Miandoab. Synthesis and characterization of a pH and photoresponsive copolymer of acrylamide and spiropyran. *Polym. Adv. Technol.*, 31:2545–2551, 2020.
- [185] S. Kwangmettadam and T. Kudernac. Light-fuelled reversible expansion of spiropyran-based vesicles in water. *Chem. Commun.*, 54:5311–5314, 2018.
- [186] M. Reifarth, M. Bekir, A. M. Bapolisi, E. Titov, F. Nußhardt, J. Nowaczyk, D. Grigoriev, A. Sharma, P. Saalfrank, S. Santer, M. Hartlieb, and A. Böker. A Dual pH- and Light-Responsive Spiropyran-Based Surfactant: Investigations on Its Switching Behavior and Remote Control over Emulsion Stability. *Angew. Chem. Int. Ed.*, 61:e202114687, 2022.
- [187] F. M. Raymo and S. Giordani. Signal processing at the molecular level. *J. Am. Chem. Soc.*, 123:4651–4652, 2001.
- [188] F. M. Raymo, S. Giordani, A. J. White, and D. J. Williams. Digital processing with a three-state molecular switch. *J. Org. Chem.*, 68:4158–4169, 2003.
- [189] M. Colaço, A. Carletta, M. V. Gysel, K. Robeyns, N. Tumanov, and J. Wouters. Direct Access by Mechanochemistry or Sonochemistry to Protonated Merocyanines: Components of a Four-State Molecular Switch. *ChemistryOpen*, 7:520–526, 2018.
- [190] Y. Hirao, T. Taniguchi, M. Teraoka, and T. Kubo. Redox/pH Dual Stimuli-Responsive Acridine Spiropyran. *Asian J. Org. Chem.*, 8:863–866, 2019.
- [191] L. Kortekaas, J. D. Steen, D. R. Duijnste, D. Jacquemin, and W. R. Browne. Non-commutative Switching of Double Spiropyrans. *J. Phys. Chem. A*, 124:6458–6467, 2020.
- [192] A. B. Kanj, A. Chandresh, A. Gerwien, S. Grosjean, S. Bräse, Y. Wang, H. Dube, and L. Heinke. Proton-conduction photomodulation in spiropyran-functionalized MOFs with large on-off ratio. *Chem. Sci.*, 11:1404–1410, 2020.
- [193] J. J. van Thor, B. Borucki, W. Crielaard, H. Otto, T. Lamparter, J. Hughes, K. J. Hellingwerf, and M. P. Heyn. Light-induced proton release and proton uptake reactions in the cyanobacterial phytochrome Cph1. *Biochemistry*, 40:11460–11471, 2001.
- [194] H. Kashida, K. Sano, Y. Kara, and H. Asanuma. Modulation of pKa of Brooker’s merocyanine by DNA hybridization. *Bioconjugate Chem.*, 20:258–265, 2009.
- [195] S. Silvi, E. C. Constable, C. E. Housecroft, J. E. Beves, E. L. Dunphy, M. Tomasulo, F. M. Raymo, and A. Credi. Photochemical switching of luminescence and singlet oxygen generation by chemical signal communication. *Chem. Commun.*, pages 1484–1486, 2009.

- [196] Z. Shi, P. Peng, D. Strohecker, and Y. Liao. Long-lived photoacid based upon a photochromic reaction. *J. Am. Chem. Soc.*, 133:14699–14703, 2011.
- [197] L. A. Tatum, J. T. Foy, and I. Aprahamian. Waste management of chemically activated switches: Using a photoacid to eliminate accumulation of side products. *J. Am. Chem. Soc.*, 136:17438–17441, 2014.
- [198] C. Berton, D. M. Busiello, S. Zamuner, E. Solari, R. Scopelliti, F. Fadaei-Tirani, K. Severin, and C. Pezzato. Thermodynamics and kinetics of protonated merocyanine photoacids in water. *Chem. Sci.*, 11:8457–8468, 2020.
- [199] C. Kaiser, T. Halbritter, A. Heckel, and J. Wachtveitl. Proton-Transfer Dynamics of Photoacidic Merocyanines in Aqueous Solution. *Chem. Eur. J.*, 27:9160–9173, 2021.
- [200] L. Wimberger, S. K. Prasad, M. D. Peeks, J. Andreásson, T. W. Schmidt, and J. E. Beves. Large, Tunable, and Reversible pH Changes by Merocyanine Photoacids. *J. Am. Chem. Soc.*, 143:20758–20768, 2021.
- [201] S. R. Keum, K. B. Lee, P. M. Kazmaier, and E. Buncel. A novel method for measurement of the merocyanine-spiropyran interconversion in non-activated 1, 3, 3-trimethylspiro- (2H-1-benzopyran-2, 2'-indoline) derivatives. *Tetrahedron Lett.*, 35:1015–1018, 1994.
- [202] H. Shiozaki. Molecular orbital calculations for acid induced ring opening reaction of spiropyran. *Dyes Pigm.*, 33:229–237, 1997.
- [203] S. T. Abdel-Halim and M. K. Awad. Effect of protonation on the molecular structure and reactivity of a typical merocyanine dye: Experimental and theoretical investigation. *J. Phys. Chem.*, 97:3160–3165, 1993.
- [204] J. Zhou, Y. Li, Y. Tang, F. Zhao, X. Song, and E. Li. Detailed investigation on a negative photochromic spiropyran. *J. Photochem. Photobiol. A*, 90:117–123, 1995.
- [205] A. Fissi, O. Pieroni, N. Angelini, and F. Lenci. Photoresponsive polypeptides. Photochromic and conformational behavior of spiropyran-containing poly(L-glutamate)s under acid conditions. *Macromolecules*, 32:7116–7121, 1999.
- [206] J. T. Wojtyk, A. Wasey, N. N. Xiao, P. M. Kazmaier, S. Hoz, C. Yu, R. P. Lemieux, and E. Buncel. Elucidating the mechanisms of acidochromic spiropyran-merocyanine interconversion. *Journal of Physical Chemistry A*, 111:2511–2516, 2007.

- [207] P. B. Markworth, B. D. Adamson, N. J. Coughlan, L. Goerigk, and E. J. Bieske. Photoisomerization action spectroscopy: flicking the protonated merocyanine-spiropyran switch in the gas phase. *Phys. Chem. Chem. Phys.*, 17:25676–25688, 2015.
- [208] Shimadzu Web Page. <https://www.shimadzu.com>.
- [209] K. Iwata and H. Hamaguchi. Vibrational Cooling Process in Solution Probed by Picosecond Time-Resolved Raman Spectroscopy. Analysis of the Cooling Kinetics. *J. Mol. Liq.*, 65/66:417–420, 1995.
- [210] R. Ghosh, A. K. Mora, and S. Nath. Disentangling Time Scales of Vibrational Cooling, Solvation, and Hydrogen Bond Reorganization Dynamics Using Ultrafast Transient Infrared Spectroscopy of Formylperylene. *J. Phys. Chem. B*, 123:4408–4414, 2019.
- [211] C. Lenoble and R. S. Becker. Photophysics, Photochemistry, Kinetics, and Mechanism of the Photochromism of 6'-Nitroindolinospiryran. *J. Phys. Chem.*, 90: 62–65, 1986.
- [212] A. K. Chibisov and H. Görner. Singlet versus triplet photoprocesses in indodicarbocyanine dyes and spirocyanine-derived merocyanines. *J. Photochem. Photobiol. A*, 105:261–267, 1997.
- [213] C. Kaiser, T. Halbritter, A. Heckel, and J. Wachtveitl. Thermal, Photochromic and Dynamic Properties of Water-Soluble Spiropyran. *ChemistrySelect*, 2:4111–4123, 2017.
- [214] V. K. Seiler, K. Callebaut, K. Robeyns, N. Tumanov, J. Wouters, B. Champagne, and T. Leyssens. Acidochromic spirocyanine-merocyanine stabilisation in the solid state. *CrystEngComm*, 20:3318–3327, 2018.
- [215] M. Irie and M. Mohri. Thermally Irreversible Photochromic Systems. Reversible Photocyclization of Diarylethene Derivatives. *J. Org. Chem.*, 53:803–808, 1988.
- [216] S. Nakamura and M. Irie. Thermally Irreversible Photochromic Systems. A Theoretical Study. *J. Org. Chem.*, 53:6136–6138, 1988.
- [217] S. Kawata and Y. Kawata. Three-Dimensional Optical Data Storage Using Photochromic Materials. *Chem. Rev.*, 100:1777–1788, 2000.
- [218] A. Toriumi, S. Kawata, and M. Gu. Reflection confocal microscope readout system for three-dimensional photochromic optical data storage. *Opt. Lett.*, 23:1924–1926, 1998.

- [219] S. L. Gilat, S. H. Kawai, and J.-M. Lehn. Light-Triggered Molecular Devices: Photochemical Switching of Optical and Electrochemical Properties in Molecular Wire Type Diarylethene Species. *Chem. Eur. J.*, 1:275–284, 1995.
- [220] S. Kobatake, S. Takami, H. Muto, T. Ishikawa, and M. Irie. Rapid and reversible shape changes of molecular crystals on photoirradiation. *Nature*, 446:778–781, 2007.
- [221] E. Kim, Y. K. Choi, and M. H. Lee. Photoinduced refractive index change of a photochromic diarylethene polymer. *Macromolecules*, 32:4855–4860, 1999.
- [222] K. Shibata, K. Muto, S. Kobatake, and M. Irie. Photocyclization/cycloreversion quantum yields of diarylethenes in single crystals. *J. Phys. Chem. A*, 106:209–214, 2002.
- [223] M. P. Minitti, J. M. Budarz, A. Kirrander, J. S. Robinson, D. Ratner, T. J. Lane, D. Zhu, J. M. Glowonia, M. Kozina, H. T. Lemke, M. Sikorski, Y. Feng, S. Nelson, K. Saita, B. Stankus, T. Northey, J. B. Hastings, and P. M. Weber. Imaging Molecular Motion: Femtosecond X-Ray Scattering of an Electrocyclic Chemical Reaction. *Phys. Rev. Lett.*, 114:1–5, 2015.
- [224] P. R. Hania, A. Pugzlys, L. N. Lucas, J. J. D. Jong, B. L. Feringa, J. H. V. Esch, H. T. Jonkman, and K. Duppen. Ring closure dynamics of BTE-based photochromic switches: Perfluoro- versus perhydrocyclopentene derivatives. *J. Phys. Chem. A*, 109:9437–9442, 2005.
- [225] P. R. Hania, R. Telesca, L. N. Lucas, A. Pugzlys, J. H. V. Esch, B. L. Feringa, J. G. Snijders, and K. Duppen. An Optical and Theoretical Investigation of the Ultrafast Dynamics of a Bisthiénylene-Based Photochromic Switch. *J. Phys. Chem. A*, 106:8498–8507, 2002.
- [226] C. Elsner, T. Cordes, P. Dietrich, M. Zastrow, T. T. Herzog, K. Rück-Braun, and W. Zinth. Photochromic Bis(thiophen-3-yl)maleimides Studied with Time-Resolved Spectroscopy. *J. Phys. Chem. A*, 113:1033–1039, 2009.
- [227] M. Takeshita, C. Tanaka, T. Miyazaki, Y. Fukushima, and M. Nagai. Synthesis and photochromic properties of thiophenophan-1-enes containing a polyether bridge. *New J. Chem.*, 33:1433–1438, 2009.
- [228] Y. Ishibashi, T. Umesato, S. Kobatake, M. Irie, and H. Miyasaka. Femtosecond laser photolysis studies on temperature dependence of cyclization and cycloreversion reactions of a photochromic diarylethene derivative. *J. Phys. Chem. C*, 116:4862–4869, 2012.

- [229] Y. Ishibashi, T. Umesato, M. Fujiwara, K. Une, Y. Yoneda, H. Sotome, T. Katayama, S. Kobatake, T. Asahi, M. Irie, and H. Miyasaka. Solvent Polarity Dependence of Photochromic Reactions of a Diarylethene Derivative As Revealed by Steady-State and Transient Spectroscopies. *J. Phys. Chem. C*, 120:1170–1177, 2016.
- [230] M. Irie, O. Miyatake, and K. Uchida. Blocked Photochromism of Diarylethenes. *J. Am. Chem. Soc.*, 114:8715–8716, 1992.
- [231] T. Yamaguchi and M. Irie. Photochromism of bis(2-alkyl-1-benzothiophen-3-yl)perfluorocyclopentene derivatives. *J. Photochem. Photobiol. A*, 178:162–169, 2006.
- [232] T. Yamaguchi and M. Irie. Photochromism of 1,2-bis(2-alkyl-1-benzofuran-3-yl)perfluorocyclopentene derivatives. *Eur. J. Org. Chem.*, pages 3105–3111, 2006.
- [233] S. Aloïse, R. Yibin, I. Hamdi, G. Buntinx, A. Perrier, F. Maurel, D. Jacquemin, and M. Takeshita. The photochemistry of inverse dithienylethene switches understood. *Phys. Chem. Chem. Phys.*, 16:26762–26768, 2014.
- [234] K. Uchida, D. Guillaumont, E. Tsuchida, G. Mochizuki, M. Irie, A. Murakami, and S. Nakamura. Theoretical study of an intermediate, a factor determining the quantum yield in photochromism of diarylethene derivatives. *J. Mol. Struct.: (Theochem)*, 579:115–120, 2002.
- [235] S. Kobatake, K. Uchida, E. Tsuchida, and M. Irie. Single-crystalline photochromism of diarylethenes: reactivity–structure relationship. *Chem. Commun.*, pages 2804–2805, 2002.
- [236] H. Miyasaka, S. Araki, A. Tabata, T. Nobuto, N. Mataga, and M. Irie. Picosecond laser photolysis studies on photochromic reactions of 1,2-bis(2,4,5-trimethyl-3-thienyl)maleic anhydride in solutions. *Chem. Phys. Lett.*, 230:249–254, 1994.
- [237] N. Tamai, T. Saika, T. Shimidzu, and M. Irie. Femtosecond Dynamics of a Thiophene Oligomer with a Photoswitch by Transient Absorption Spectroscopy. *J. Phys. Chem.*, 100:4689–4692, 1996.
- [238] H. Miyasaka, T. Nobuto, A. Itaya, N. Tamai, and M. Irie. Picosecond laser photolysis studies on a photochromic dithienylethene in solution and in crystalline phases. *Chem. Phys. Lett.*, 269:281–285, 1997.
- [239] J. C. Owrutsky, H. H. Nelson, A. P. Baronavski, O.-K. Kim, G. M. Tsivgoulis, S. L. Gilat, and J.-M. Lehn. Optical properties and dynamics of a photochromic bisthienylethene in solution and in a polymer film. *Chem. Phys. Lett.*, 293:555–563, 1998.

- [240] J. Ern, A. Bens, A. Bock, H.-D. Martin, and C. Kryschi. Femtosecond transient absorption studies on photochromism of dithienylethene derivatives. *J. Lumin.*, 76/77: 90–94, 1998.
- [241] J. Ern, A. Bens, H.-D. Martin, S. Mukamel, D. Schmid, S. Tretiak, E. Tsiper, and C. Kryschi. Reaction dynamics of photochromic dithienylethene derivatives. *Chem. Phys.*, 246:115–125, 1999.
- [242] N. Ohtaka, Y. Hase, K. Uchida, M. Irie, and N. Tamai. Femtosecond Spectroscopic Study on Photochromic Diarylethenes with Terthiophene. *Mol. Cryst. Liq. Cryst.*, 344:83–88, 2000.
- [243] H. Miyasaka, M. Murakami, A. Itaya, D. Guillaumont, S. Nakamura, and M. Irie. Multiphoton gated photochromic reaction in a diarylethene derivative. *J. Am. Chem. Soc.*, 123:753–754, 2001.
- [244] H. Miyasaka, T. Nobuto, M. Murakami, A. Itaya, N. Tamai, and M. Irie. Solvent viscosity effects on photochromic reactions of a diarylethene derivative as revealed by picosecond laser spectroscopy. *J. Phys. Chem. A*, 106:8096–8102, 2002.
- [245] H. Miyasaka, M. Murakami, T. Okada, Y. Nagata, A. Itaya, S. Kobatake, and M. Irie. Picosecond and femtosecond laser photolysis studies of a photochromic diarylethene derivative: Multiphoton gated reaction. *Chem. Phys. Lett.*, 371:40–48, 2003.
- [246] C. Bertarelli, M. C. Gallazzi, F. Stellacci, G. Zerbi, S. Stagira, M. Nisoli, and S. D. Silvestri. Ultrafast photoinduced ring-closure dynamics of a diarylethene polymer. *Chem. Phys. Lett.*, 359:278–282, 2002.
- [247] J. Ern, A. T. Bens, H. D. Martin, K. Kuldova, H. P. Trommsdorff, and C. Kryschi. Ring-opening and -closure reaction dynamics of a photochromic dithienylethene derivative. *J. Phys. Chem. A*, 106:1654–1660, 2002.
- [248] M. Murakami, H. Miyasaka, T. Okada, S. Kobatake, and M. Irie. Dynamics and mechanisms of the multiphoton gated photochromic reaction of diarylethene derivatives. *J. Am. Chem. Soc.*, 126:14764–14772, 2004.
- [249] Y. Ishibashi, K. Tani, H. Miyasaka, S. Kobatake, and M. Irie. Picosecond laser photolysis study of cycloreversion reaction of a diarylethene derivative in polycrystals: Multiphoton-gated reaction. *Chem. Phys. Lett.*, 437:243–247, 2007.
- [250] K. Tani, Y. Ishibashi, H. Miyasaka, S. Kobatake, and M. Irie. Dynamics of cyclization, cycloreversion, and multiphoton-gated reaction of a photochromic diarylethene derivative in crystalline phase. *J. Phys. Chem. C*, 112:11150–11157, 2008.

- [251] Y. Ishibashi, M. Mukaida, M. Falkenström, H. Miyasaka, S. Kobatake, and M. Irie. One- and multi-photon cycloreversion reaction dynamics of diarylethene derivative with asymmetrical structure, as revealed by ultrafast laser spectroscopy. *Phys. Chem. Chem. Phys.*, 11:2640, 2009.
- [252] Y. Ishibashi, K. Okuno, C. Ota, T. Umesato, T. Katayama, M. Murakami, S. Kobatake, M. Irie, and H. Miyasaka. Multiphoton-gated cycloreversion reactions of photochromic diarylethene derivatives with low reaction yields upon one-photon visible excitation. *Photochem. Photobiol. Sci.*, 9:172–180, 2010.
- [253] S. Aloïse, M. Sliwa, Z. Pawlowska, J. Réhault, J. Dubois, O. Poizat, G. Buntinx, A. Perrier, F. Maurel, S. Yamaguchi, and M. Takeshita. Bridged photochromic diarylethenes investigated by ultrafast absorption spectroscopy: Evidence for two distinct photocyclization pathways. *J. Am. Chem. Soc.*, 132:7379–7390, 2010.
- [254] Y. Ishibashi, M. Fujiwara, T. Umesato, H. Saito, S. Kobatake, M. Irie, and H. Miyasaka. Cyclization reaction dynamics of a photochromic diarylethene derivative as revealed by femtosecond to microsecond time-resolved spectroscopy. *J. Phys. Chem. C*, 115:4265–4272, 2011.
- [255] J. Piard, Y. Ishibashi, H. Saito, R. Métivier, K. Nakatani, G. Gavrel, P. Yu, and H. Miyasaka. Multiphoton-gated cycloreversion reaction of a photochromic 1,2-bis(thiazolyl) perfluorocyclopentene diarylethene derivative. *J. Photochem. Photobiol. A*, 234:57–65, 2012.
- [256] M. S. Molloy, J. A. Snyder, and A. E. Bragg. Structural and solvent control of nonadiabatic photochemical bond formation: Photocyclization of o-terphenyl in solution. *J. Phys. Chem. A*, 118:3913–3925, 2014.
- [257] H. Sotome, T. Nagasaka, K. Une, S. Morikawa, T. Katayama, S. Kobatake, M. Irie, and H. Miyasaka. Cycloreversion Reaction of a Diarylethene Derivative at Higher Excited States Attained by Two-Color, Two-Photon Femtosecond Pulsed Excitation. *J. Am. Chem. Soc.*, 139:17159–17167, 2017.
- [258] A. Jarota, E. Pastorczak, W. Tawfik, B. Xue, R. Kania, H. Abramczyk, and T. Kobayashi. Exploring the ultrafast dynamics of a diarylethene derivative using sub-10 fs laser pulses. *Phys. Chem. Chem. Phys.*, 21:192–204, 2019.
- [259] H. Sotome, D. Kitagawa, T. Nakahama, S. Ito, S. Kobatake, M. Irie, and H. Miyasaka. Cyclization reaction dynamics of an inverse type diarylethene derivative as revealed by time-resolved absorption and fluorescence spectroscopies. *Phys. Chem. Chem. Phys.*, 21:8623–8632, 2019.

- [260] K. Seo, I. Eom, S. Shim, C. H. Kim, and T. Joo. Ring Closure Reaction Pathway of a Diarylethene in Solution Using Femtosecond Time-resolved Fluorescence Spectra. *Bull. Korean Chem. Soc.*, 40:352–358, 2019.
- [261] J. Ern, A. T. Bens, H.-D. Martin, S. Mukamel, S. Tretiak, K. Tsyganenko, K. Kuldova, H. P. Trommsdorff, and C. Kryschi. Reaction Dynamics of a Photochromic Fluorescing Dithienylethene. *J. Phys. Chem. A*, 105:1741–1749, 2001.
- [262] S. Shim, I. Eom, T. Joo, E. Kim, and K. S. Kim. Ring closure reaction dynamics of diarylethene derivatives in solution. *J. Phys. Chem. A*, 111:8910–8917, 2007.
- [263] C. Okabe, N. Tanaka, T. Fukaminato, T. Kawai, M. Irie, Y. Nibu, H. Shimada, A. Goldberg, S. Nakamura, and H. Sekiya. Raman spectroscopic study on photochromic reaction of a diarylethene derivative. *Chem. Phys. Lett.*, 357:113–118, 2002.
- [264] C. Okabe, T. Nakabayashi, N. Nishi, T. Fukaminato, T. Kawai, M. Irie, and H. Sekiya. Picosecond time-resolved Stokes and anti-Stokes Raman studies on the photochromic reactions of diarylethene derivatives. *J. Phys. Chem. A*, 107:5384–5390, 2003.
- [265] D. T. Valley, D. P. Hoffman, and R. A. Mathies. Reactive and unreactive pathways in a photochemical ring opening reaction from 2D femtosecond stimulated Raman. *Phys. Chem. Chem. Phys.*, 17:9231–9240, 2015.
- [266] D. Guillaumont, T. Kobayashi, K. Kanda, H. Miyasaka, K. Uchida, S. Kobatake, K. Shibata, S. Nakamura, and M. Irie. An ab initio MO study of the photochromic reaction of dithienylethenes. *J. Phys. Chem. A*, 106:7222–7227, 2002.
- [267] M. Boggio-Pasqua, M. Ravaglia, M. J. Bearpark, M. Garavelli, and M. A. Robb. Can Diarylethene Photochromism be Explained by a Reaction Path Alone? A CASSCF Study with Model MMVB Dynamics. *J. Phys. Chem. A*, 107:11139–11152, 2003.
- [268] Y. Asano, A. Murakami, T. Kobayashi, A. Goldberg, D. Guillaumont, S. Yabushita, M. Irie, and S. Nakamura. Theoretical study on the photochromic cycloreversion reactions of dithienylethenes; on the role of the conical intersections. *J. Am. Chem. Soc.*, 126:12112–12120, 2004.
- [269] C. L. Ward and C. G. Elles. Controlling the excited-state reaction dynamics of a photochromic molecular switch with sequential two-photon excitation. *J. Phys. Chem. Lett.*, 3:2995–3000, 2012.
- [270] K. Okuno, Y. Shigeta, R. Kishi, H. Miyasaka, and M. Nakano. Tuned CAM-B3LYP functional in the time-dependent density functional theory scheme for excitation

- energies and properties of diarylethene derivatives. *J. Photochem. Photobiol. A*, 235:29–34, 2012.
- [271] C. L. Ward and C. G. Elles. Cycloreversion dynamics of a photochromic molecular switch via one-photon and sequential two-photon excitation. *J. Phys. Chem. A*, 118: 10011–10019, 2014.
- [272] C. Wiebeler and S. Schumacher. Quantum yields and reaction times of photochromic diarylethenes: Nonadiabatic ab initio molecular dynamics for normal- and inverse-type. *J. Phys. Chem. A*, 118:7816–7823, 2014.
- [273] T. Sumi, Y. Takagi, A. Yagi, M. Morimoto, and M. Irie. Photoirradiation wavelength dependence of cycloreversion quantum yields of diarylethenes. *Chem. Commun.*, 50:3928, 2014.
- [274] S. Shim, T. Joo, S. C. Bae, K. S. Kim, and E. Kim. Ring opening dynamics of a photochromic diarylethene derivative in solution. *J. Phys. Chem. A*, 107:8106–8110, 2003.
- [275] C. R. Honick, G. M. Peters, J. D. Young, J. D. Tovar, and A. E. Bragg. Core structure dependence of cycloreversion dynamics in diarylethene analogs. *Phys. Chem. Chem. Phys.*, 22:3314–3328, 2020.
- [276] A. Khodko, V. Khomenko, Y. Shynkarenko, O. Mamuta, O. Kapitanchuk, D. Sysoiev, N. Kachalova, T. Huhn, and S. Snegir. Ultrafast ring-closing reaction dynamics of a photochromic furan-based difurylethene. *Chem. Phys. Lett.*, 669:156–160, 2017.
- [277] M. Herder, B. M. Schmidt, L. Grubert, M. Pätzelt, J. Schwarz, and S. Hecht. Improving the fatigue resistance of diarylethene switches. *J. Am. Chem. Soc.*, 137, 2015.
- [278] D. Mendive-Tapia, A. Perrier, M. J. Bearpark, M. A. Robb, B. Lasorne, and D. Jacquemin. New insights into the by-product fatigue mechanism of the photo-induced ring-opening in diarylethenes. *Phys. Chem. Chem. Phys.*, 16:18463–18471, 2014.
- [279] I. I. Vorontsov and P. Coppens. On the refinement of time-resolved diffraction data: Comparison of the random-distribution and cluster-formation models and analysis of the light-induced increase in the atomic displacement parameters. *J. Synchrotron Rad.*, 12:488–493, 2005.
- [280] R. B. Woodward and R. Hoffmann. *The Conservation of Orbital Symmetry*. Verlag Chemie, 1970. ISBN 978-0895731098.

- [281] D. H. Dowell and J. F. Schmerge. Quantum efficiency and thermal emittance of metal photocathodes. *Phys. Rev. Accel. Beams*, 12:1–10, 2009.
- [282] P. A. Anderson. Work Function of Gold. *Phys. Rev.*, 115:553–554, 1959.

---

# Appendix

## A.1 Analysis Software

All transient and static absorption spectroscopy data analysis discussed in this thesis was carried out in Python as part of the developed interactive software package with a graphical user interface using the `tkinter` module. For transient absorption, the GUI accesses a global instance of a main TA analysis class, which contains the transient data itself as well as methods for loading, averaging, processing and analyzing. The methods itself can create instances of other classes, most prominently a class for line traces such as spectral, kinetic or integral traces, and fit classes for line and global fits. A few screenshots of different subsections of the GUI as well as essential and/or useful code excerpts will be given in the following.

### A.1.1 Global and target analysis

In Fig. A.1, a screenshot of the software page for global and target analysis is shown, containing selection of the desired model, definition of the fit window, selection of the fit algorithm and additional parameter constraints, and a few more options for the fit.

The core method of the global and target analysis class calculates the fit matrix `fitMat` as well as the concentration vectors `Y`, which depend on the model and the fit parameters `p`, as well as the decay-associated spectra `X` via matrix inversion. The fit matrix is subsequently subtracted from the data matrix and returned to the optimization algorithm.

```
1 class GlobalFit():
2     #...
3     def calculate_results(self, p):
4         # both used during optimization and to obtain global fit
         parameters afterwards
5         #
6         # calculate Y components according to utilized model
7         Y = self.modelObj.fit_function(self.y, p, num_comp = self.
         number_of_decays,
8         sigma = self.sigma)
```

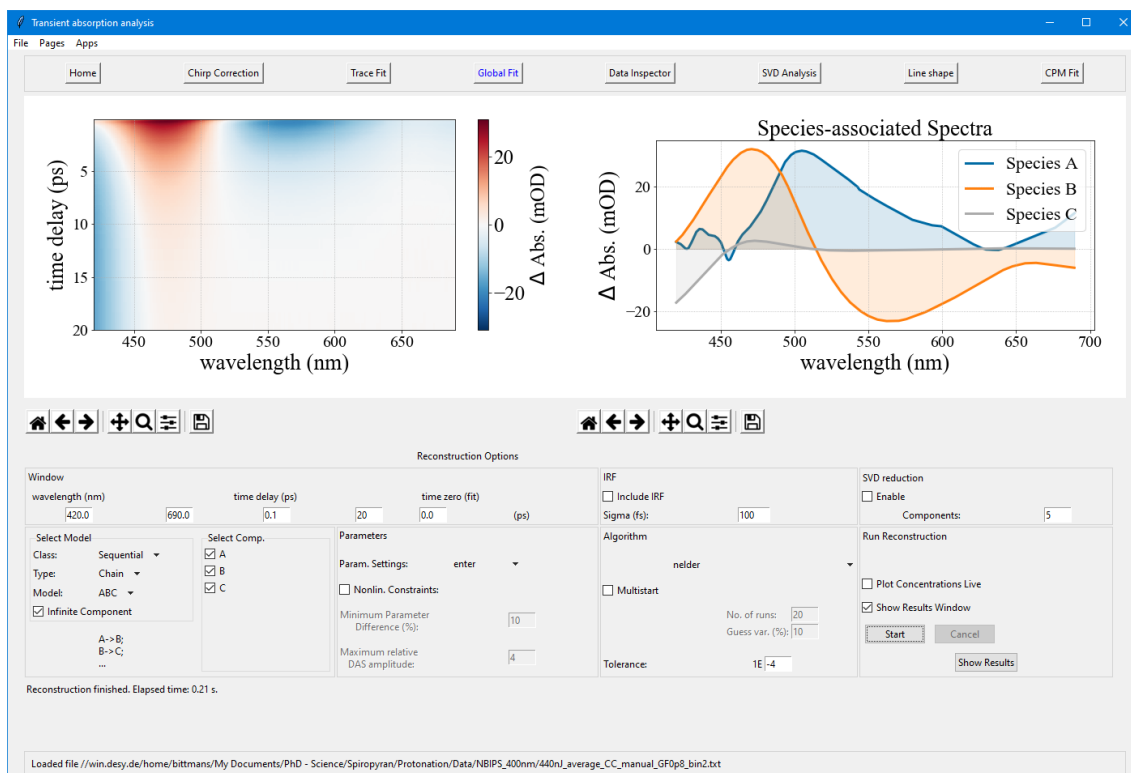


**Figure A.1:** Screenshot of the global fit page from the interactive TAS analysis software. All fit settings are made on this page of the main window, while the fit results are shown in a separate window (see Fig. A.2).

```

9      # calculate X components via matrix inversion
10     try:
11         X = np.dot(np.transpose(self.z), np.linalg.pinv(Y))
12     except Exception as e:
13         try:
14             X = np.dot(self.z, np.linalg.pinv(Y))
15         except Exception as ex:
16             print(e, ex)
17         X = np.zeros((np.shape(self.z)[1], self.number_of_
18 species))
19     # exclude invisible components
20     for inv in self._invisibleComps:
21         X[:,inv] = np.zeros((np.shape(self.z)[1]))
22     # calculate fit matrix (fitMat) from X and Y for
23     calculation of residual
24     fitMat = np.dot(np.asarray(X)[:,self._visibleComps],np.
25 asarray(Y)[self._visibleComps,:])
26     return Y, X, fitMat
27 #...
```

The optimization process itself is done using the `Minimizer` class of the `lmfit` package.<sup>[117]</sup> Once the optimization is finished, the results are displayed in a pop-up window (see Fig. A.2), which also contains further operations, e.g. a Fourier transform of the

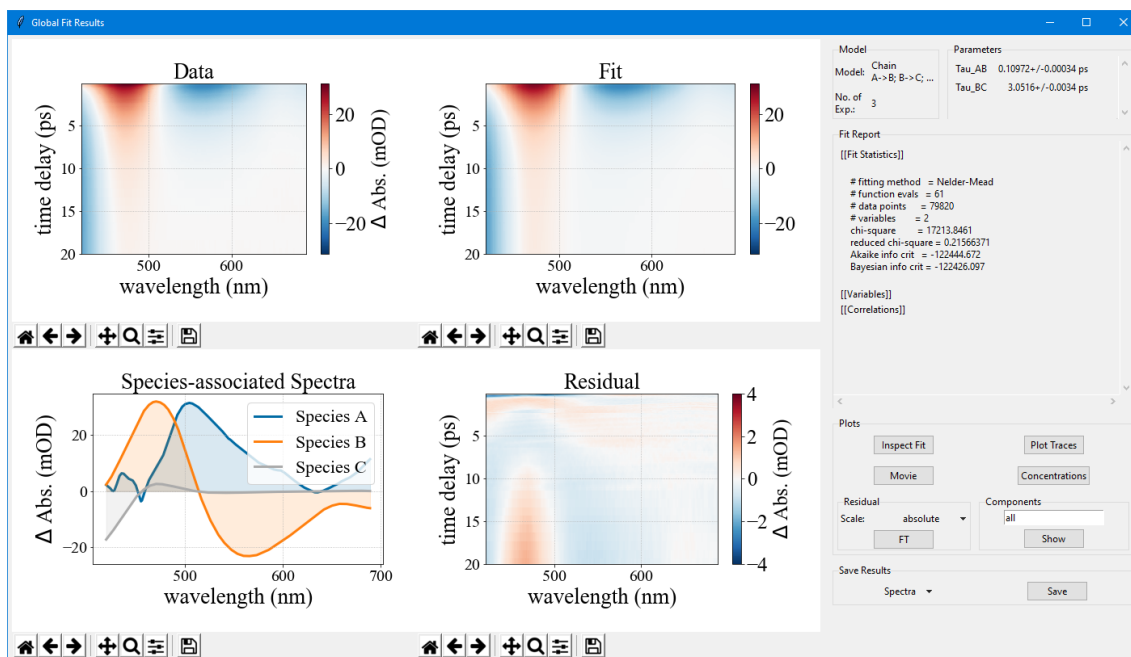


**Figure A.2:** Results window from global or target analysis (see Fig. A.1) in the TAS analysis software.

residual, plotting species concentrations or the superposition of individual components to assess their contribution to the entire fit.

The attribute `modelobj` of the global fit object is an instance of a separate fit model class, which manages the applied models, both parallel (global analysis) and kinetic (target analysis). The `fit_function` method being called by the global fit object is a wrapper for the applied temporal models to allow for an easy implementation of additional models. It contains universal operations and calls the specific model function, directly returning its result. The two simplest examples for such model functions, i.e. the parallel model and the unidirectional sequential model functions accept the arguments `f` (the temporal function, usually an exponential function), `t` (the time vector), `p` (the fit parameters) as well as the keyword argument `num_comp`, the number of decay components or species.

```

1 class FitModels():
2     #...
3     def _parallel(self, f, t, p, num_comp = 2, **kwargs):
4         y = np.zeros((num_comp, len(t)))
5         for i in range(num_comp):
6             y[i,:] = f(t, p['tau_' + str(i + 1)])
7         return y
8
9
10    def _kineticChain(self, f, t, p, num_comp = 2, inf_comp = None,
11                      **kwargs):
12        def amplitudes(j, l):

```

```

12         return np.prod([para for para in k[:l]])/np.prod([k[i]
- k[j]
13                 for i in range(l + 1) if i != j])
14     # rate constants
15     k, tau = self.convert_tau_k(p)
16     # species one
17     c = [np.array(f(t, p['tau_1']))]
18     #following species
19     for l in range(1,num_comp):
20         comps = [amplitudes(j,l)*f(t, tau[j]) for j in range(l
+ 1)]
21         c.append(np.abs(np.sum(np.array(comps),axis = 0)))
22     return np.array(c)
23 #...
```

N.B.: the fit parameters are generally contained in a dictionary, to enable being accessed using a key rather than for instance the position in a list. The fit functions return the concentration vectors as a list, the order of which is defined in another attribute of the fit model object.

### A.1.2 Trace fits and DLSA

Another in this thesis universally applied utility of the software package is the capability of line fits for any instance of the trace class, e.g. kinetic traces (see Fig. A.3). Various exponential fit functions and kinetic models are available, the latter utilizing the same fit model class as for global fits, but via the more versatile LineFit class. The latter is also the basis for the dynamic line shape analysis (see Fig. A.4), in which the transient spectra at the respective time delays are treated as a spectral trace whose ydata is changed for each time step.

## A.2 Steady-State Absorption Spectroscopy

In this section, steady-state absorption spectra not shown in the main text are provided along with calculated excitation fractions. Absorption spectra in general are obtained by measuring the transmitted light intensity  $I$  through a sample of thickness  $d$  as well as the light intensity  $I_0$  through a reference, which is either a cuvette containing the neat solvent or the blank UVFS substrate in case of solutions and crystalline samples, respectively. The extinction, here referred to as optical density ( $OD$ ) as well as the extinction coefficient  $\epsilon$  are obtained from the measurement via the Lambert-Beer law:

$$I = I_0 \cdot 10^{-\epsilon d} = I_0 \cdot 10^{-OD} \quad (\text{A.1})$$

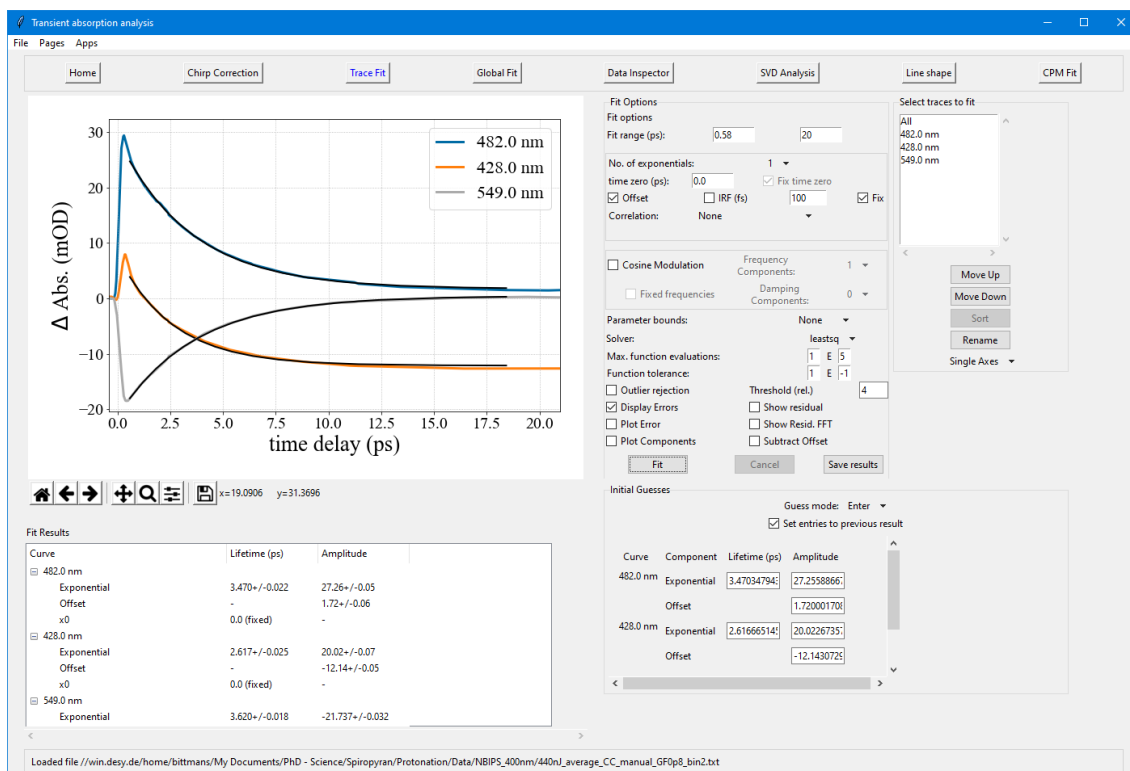


**Figure A.3:** Line fit page from the interactive TAS analysis software, showing exponential fits of kinetic TA traces.

Assuming the extinction to be due solely to absorption, the absorbance (Abs.) plotted in all spectra is treated as identical to  $OD$ .

### A.2.1 Excitation fraction calculation

An important estimate for the suitability of the experimental parameters is the excitation density or equivalently, the fraction of excited molecules  $\eta$ . For an irradiated sample volume  $V_s$ ,  $\eta$  can be calculated as the ratio between absorbed photons  $N_{abs}$  and total number of molecules in the volume  $N_V$  under the assumption that only one excitation process per molecule takes place ( $N_{abs} = N_{exc}$ ):

$$\eta = \frac{N_{exc}}{N_V} = \frac{N_{abs}}{N_V} \quad (\text{A.2})$$

Assuming that attenuation in the sample is entirely due to absorption,<sup>1</sup> the number of absorbed photons can be related to the number of incident photons  $N_{in}$  via the Lambert-

<sup>1</sup>This assumption is necessary, but not generally valid for single crystals where significant contributions from reflection and scattering are often present. This is why often only upper limits for the excitation fraction can be given.

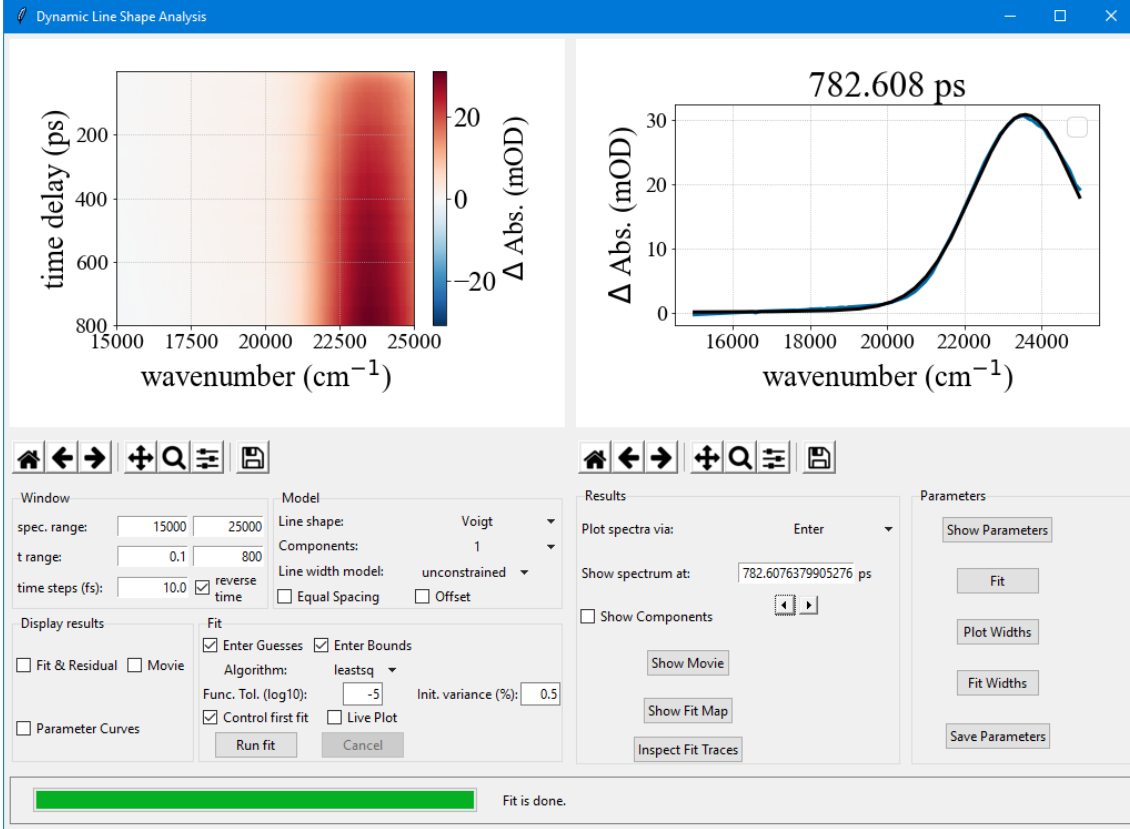


**Figure A.4:** Dynamic line-shape analysis window as part of the interactive TAS analysis software. From this window, the resulting parameter traces in time can be plotted or fit via the line fit window shown in Fig. A.3.

Beer law (see equation A.1):

$$\begin{aligned}
 N_{in} &= N_{trans} + N_{abs} \\
 \frac{N_{trans}}{N_{in}} &= \frac{I}{I_0} = 10^{-OD} \\
 \implies N_{abs} &= N_{in}(1 - 10^{-OD})
 \end{aligned} \tag{A.3}$$

with  $N_{trans}$  being the number of photons transmitted through the sample and  $OD$  the optical density. The number of incident photons is equal to the pulse energy  $E$  divided by the photon energy  $E_{phot}$ . The number of molecules  $N_V$  in the sample volume can be calculated in various ways, for instance using the number density of the material  $\rho_N$ , multiplied by the sample volume  $V_s$ . Thus equation A.2 becomes:

$$\eta = \frac{N_{in}(1 - 10^{-OD})}{N_V} \tag{A.4}$$

$$= \frac{E}{E_{phot}} \cdot \frac{(1 - 10^{-OD})}{\rho_N \cdot V_s} \tag{A.5}$$

$\rho_N$  is equal to the number of atoms  $Z$  per unit cell divided by the unit cell volume  $V_{UC}$  or, alternatively, the mass density  $\rho_m$  divided by the particular molecular (or atomic) mass  $M_{mol}$ .<sup>2</sup> Therefore, equation A.4 can be rewritten in two alternative ways, in order to express it in terms of more commonly used quantities. These include the fluence  $F$  and the sample thickness  $d$  ( $F/d = E/V_s$ ), and either the unit cell parameters or the mass density:

$$\eta = \frac{F \cdot V_{UC} \cdot (1 - 10^{-OD})}{E_{phot} \cdot d \cdot Z} = \frac{F \cdot M_{mol} \cdot (1 - 10^{-OD})}{E_{phot} \cdot d \cdot \rho_m} \quad (\text{A.6})$$

For solutions, the number density (in  $\text{cm}^{-3}$ ) is equal to the concentration  $c$  (in  $\text{mmol/l}$ ) multiplied by the Avogadro number ( $N_A = 6.022 \cdot 10^{23} \text{ mol}^{-1}$ ):

$$\eta = \frac{F}{E_{phot}} \cdot \frac{1 - 10^{-OD}}{d \cdot c \cdot N_A} \quad (\text{A.7})$$

Notably, in the linear excitation regime  $\eta$  is proportional to the fluence and thus, the excitation fraction can be calculated once, normalized to the fluence (i.e. calculated for  $1 \text{ mJcm}^{-2}$ ), and the values for any specific fluence obtained by simple multiplication.

## A.2.2 Protonated spiropyrans excitation fractions

Based on the measured static absorption spectra (Fig. 4.4), the excitation fractions for the TA of the Z/E-isomerization were calculated using equation A.7. The resulting excitation fractions for the Z-isomers, excited at 330 nm at a fluence of  $1 \text{ mJcm}^{-2}$  were 1.8 % for both  $\text{MCH}^+$  and  $\text{Nitro-MCH}^+$ . For the fluences used in the experiments, this corresponds to excitation fractions of 4 % and 3 %, respectively. For the E-isomers, only the photo-stationary state (PSS) spectra are known, which is why the concentration in equation A.7 has to be multiplied by the fraction of the E-isomer in the PSS. The latter have been determined for both derivatives by Kortekaas et al. and reported to be 58.9 % for  $\text{MCH}^+$  and 68.3 % for  $\text{Nitro-MCH}^+$ . Thus, the normalized excitation fractions become 2.1 % and 3.3 %, respectively, and the values for the datasets discussed in the main text 8 % in either case.

## A.2.3 Diarylethene absorption spectra

Since the steady-state absorption spectra for the investigated diarylethene derivatives have already been reported including those of the closed-ring isomers and the photostationary state, extensive measurements have not been carried out. Spectra of the open-ring forms were recorded nonetheless for verification as well as for an estimation of the excitation fractions in the experiments. The spectra of the open-ring diarylethene derivatives are

<sup>2</sup>N.B.:  $M_{mol}$  here refers to the actual weight of the molecule or atom in grams, i.e. the molar weight divided by the Avogadro number.

shown in Fig. A.5. The calculated excitation fractions, normalized to the fluence are collected in Tab. A.1. Due to the normalization, the values represent the linear coefficients (units of  $\%/(mJcm^{-2})$ ) for low fluences in the linear excitation regime.

Based on the absorption spectrum for crystalline Bu-DTE,<sup>3</sup> the excitation fraction in crystal was estimated as  $\approx 2 \%/ (mJcm^{-2})$  as an upper limit, neglecting influences from scattering in the absorption data.

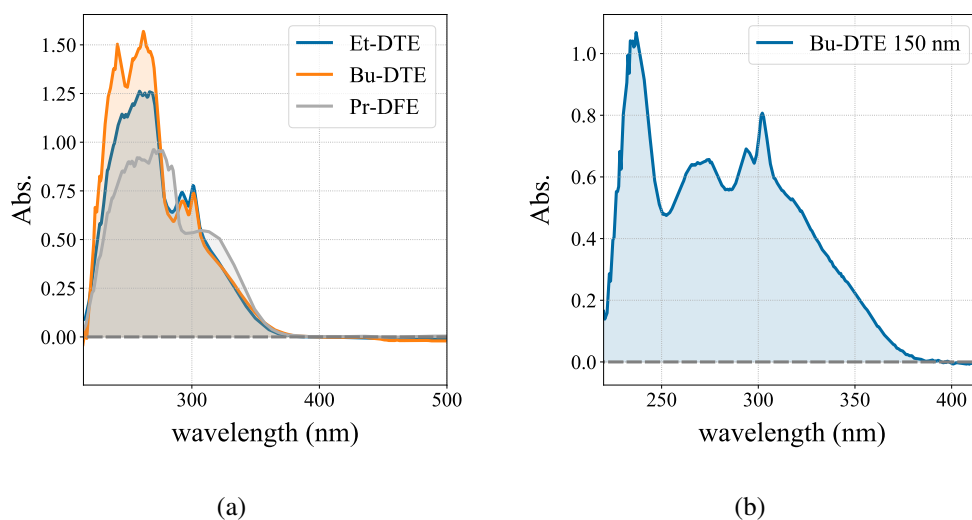


**Figure A.5:** Steady-state absorption spectra of the open-ring forms of the investigated diarylethene derivatives. (a) Spectra from all derivatives in solution, (b) spectrum of a 150 nm thin single crystal of Bu-DTE.

**Table A.1:** Excitation fractions for the three different diarylethenes in solution, calculated for a fluence of  $1 mJcm^{-2}$ .

	320 nm	330 nm	340 nm
Et-DTE	0.93 %	0.81 %	0.99 %
Bu-DTE	1.0 %	0.71 %	0.92 %
Pr-DFE	0.81 %	0.78 %	0.67 %

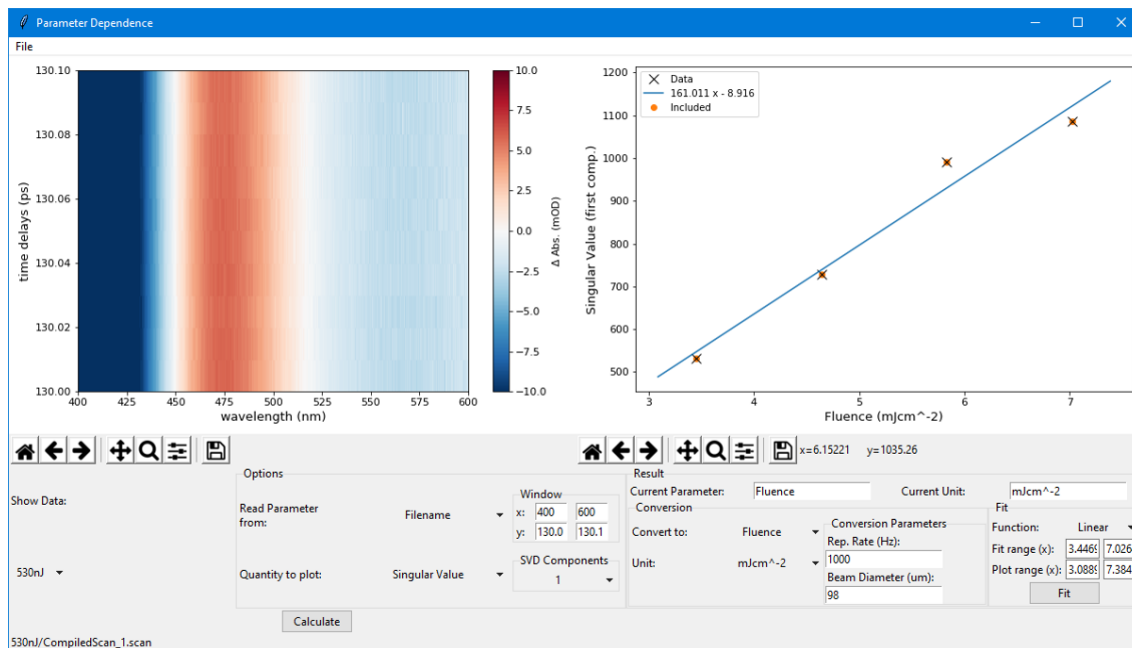
### A.3 Fluence Dependences

As mentioned in section 2.4.5, verification of the applied fluences to lie in the linear excitation regime is crucial and was carried out for all investigated samples. This can be done

<sup>3</sup>Absorption spectra of the other two derivatives were measured as well, but no usable data was obtained due to a strong scattering background in the ultraviolet. Since the crystals were grown from the same powder as the sample solutions were prepared (without any further steps), verification of their identity is provided via the solution absorption spectra.

via temporal and spectral integration of a constant signal in solution TA measurements, or via the first (or first few) singular values, which better accounts for multiple signals with opposite signs and was preferred in most cases.<sup>4</sup> Analysis of this data including linear fits of the power or fluence dependences was carried out routinely as part of the developed software package (see Fig. A.6).

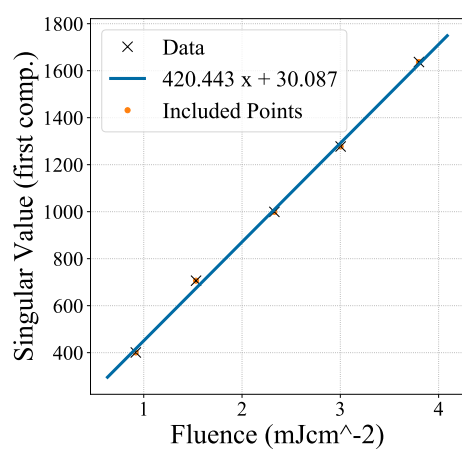
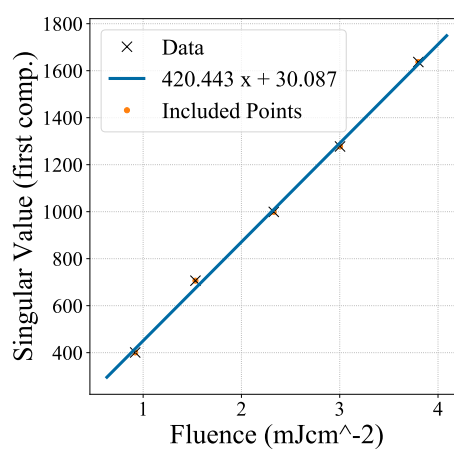
In the following, fluence dependence plots are shown for (non-protonated) spironaph-



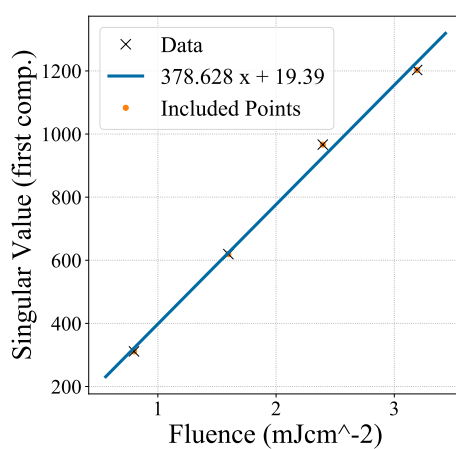
**Figure A.6:** Excitation parameter dependence analysis software. An example is shown for which use of the singular value was preferred due to opposite signs of the signal instead of integration. The plot on the left shows the window for a selected pump power (or fluence) and the plot on the left the singular values for the measured fluences including a linear fit.

thopyran for all utilized solvents (Fig. A.7), both directions of the Z-E-isomerization of protonated Nitro-BIPS (Fig. A.8), the TA data for photoexcited BIPS in both utilized acids, i.e. protonated and non-protonated (Fig. A.9) and the three investigated diarylethene derivatives (Fig. A.10).

<sup>4</sup>Ideally these experiments are to be carried out in crystals as well. However, a limited number of photocycles per sample area combined with slight variations in signal intensities between samples impeded the conduction of scientifically meaningful fluence series. Since the absorption cross-sections were not found to differ significantly between the crystalline and solution samples and circularly polarized pump pulses were utilized for crystalline samples, the linear excitation regimes determined via solution TA can be applied to the crystals as well.

(a) *n*-Hexane

(b) Ethanol



(c) Acetonitrile

**Figure A.7:** TA fluence dependence analysis of spironaphthopyran, excited at 266 nm and probed in the visible for the three different solvents, which were used for the experiments reported in section 3.2.2.

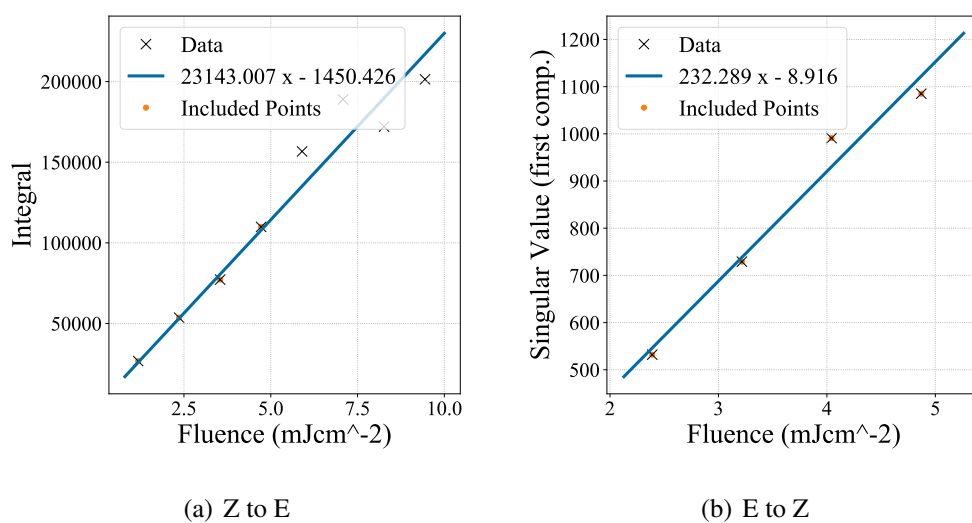


**Figure A.8:** TA fluence dependence analysis of protonated Nitro-BIPS in acetonitrile and in presence of H<sub>2</sub>SO<sub>4</sub> for both (a) the Z-to-E isomerization and (b) the reverse reaction.

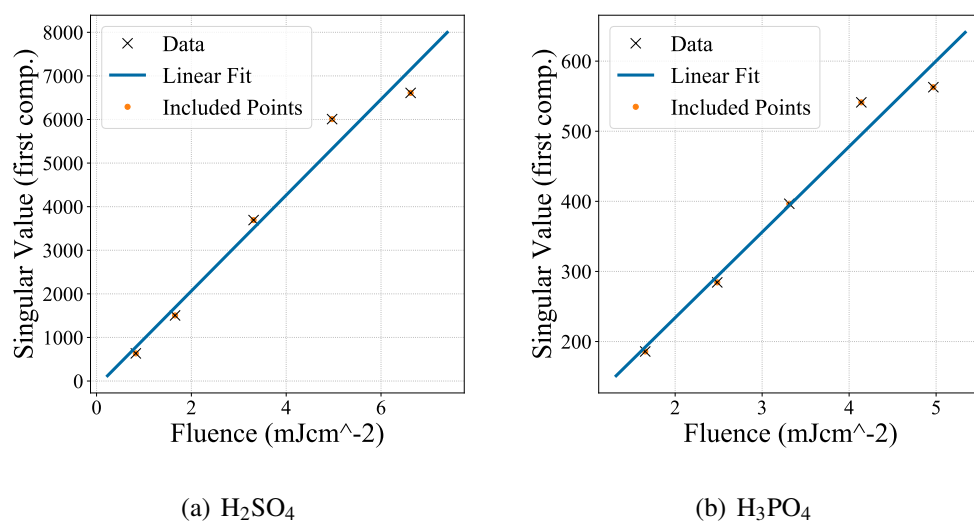
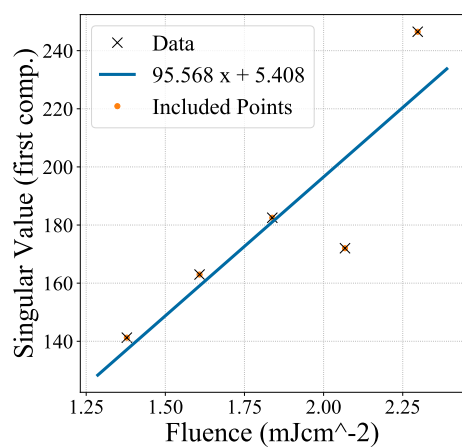
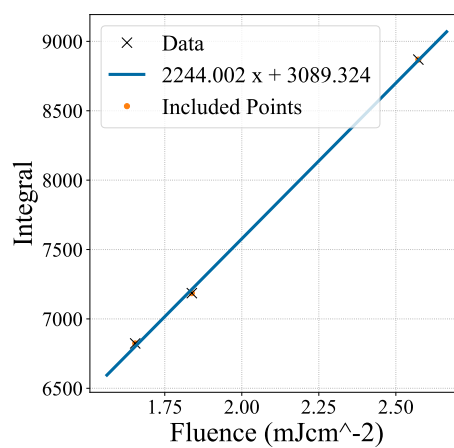


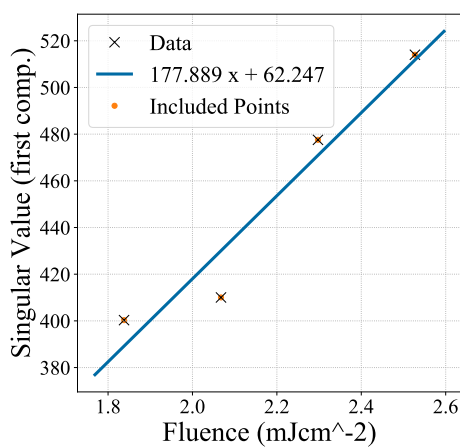
**Figure A.9:** TA fluence dependence analysis of BIPS in acetonitrile in presence of (a) H<sub>2</sub>SO<sub>4</sub> and (b) H<sub>3</sub>PO<sub>4</sub>, excited at 330 nm.



(a) Et-DTE



(b) Bu-DTE



(c) Pr-DFE

**Figure A.10:** TA fluence dependence analysis of the three diarylethene derivatives in an acetonitrile solution, probed in the visible. N.B.: two outliers due to pump power drifts were excluded in case of Bu-DTE.

## A.4 Transient Absorption Addendum

This section provides further data analysis for the investigated samples as well as in a few cases complementary data, both of which was not included in the main part of the thesis for conciseness.

### A.4.1 SNP solution

Global fits of the TA from SNP in solution for the entire measured range are depicted in Fig. A.11. Compared to the shorter fit window (Fig. 3.7), the intermediate component attributed to product equilibration is better represented, but the faster dynamics are not characterized as accurately. Since equilibration is described more appropriately by the line-shape analysis, these fits were not included in the main text, but are shown here.

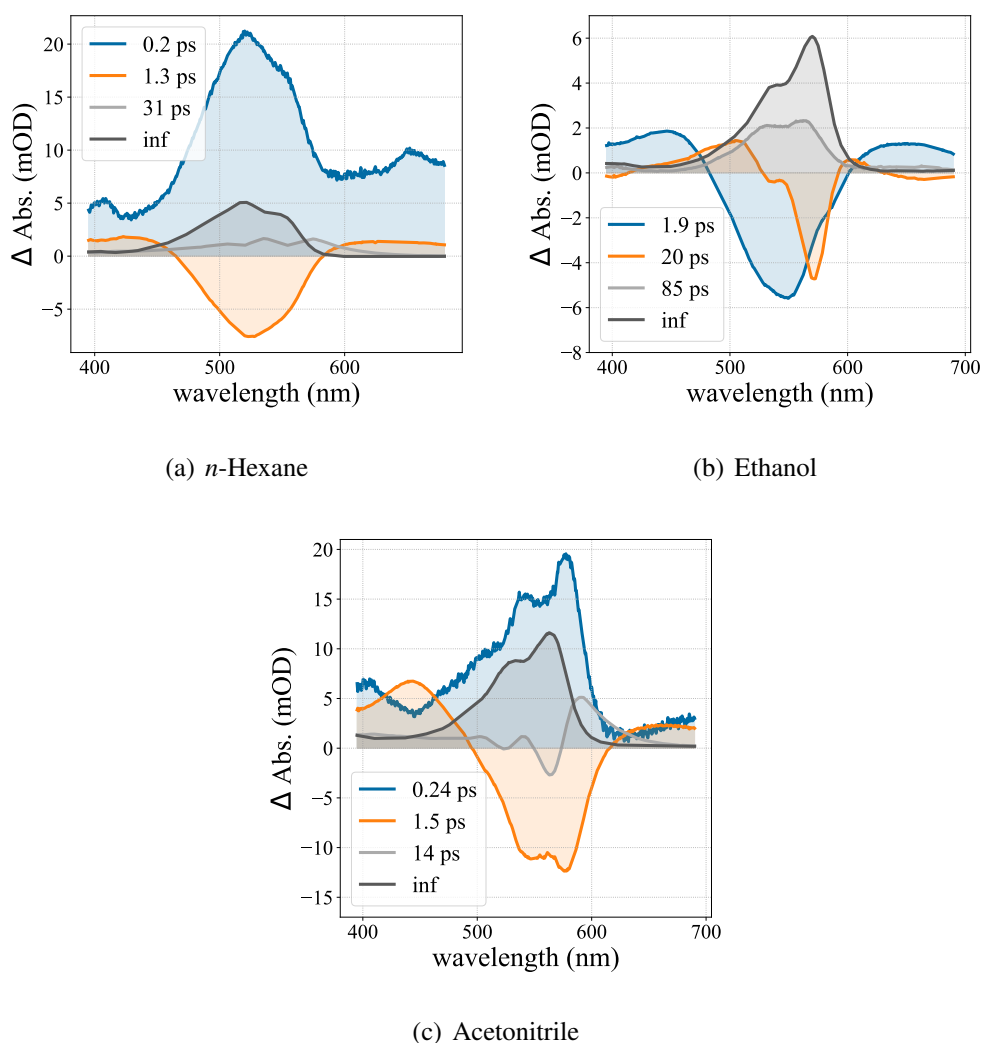


**Figure A.11:** Global fits of photoexcited SNP in the visible range for the entire measurement window of one nanosecond (100 ps in case of acetonitrile).

Calculated spectral centers of gravity for SNP in all three solvents are plotted along with the TA data in Fig. A.12, in order to demonstrate the spectral shifts on the sub-100 ps time scale, confirming the results from the dynamic-line shape analysis.

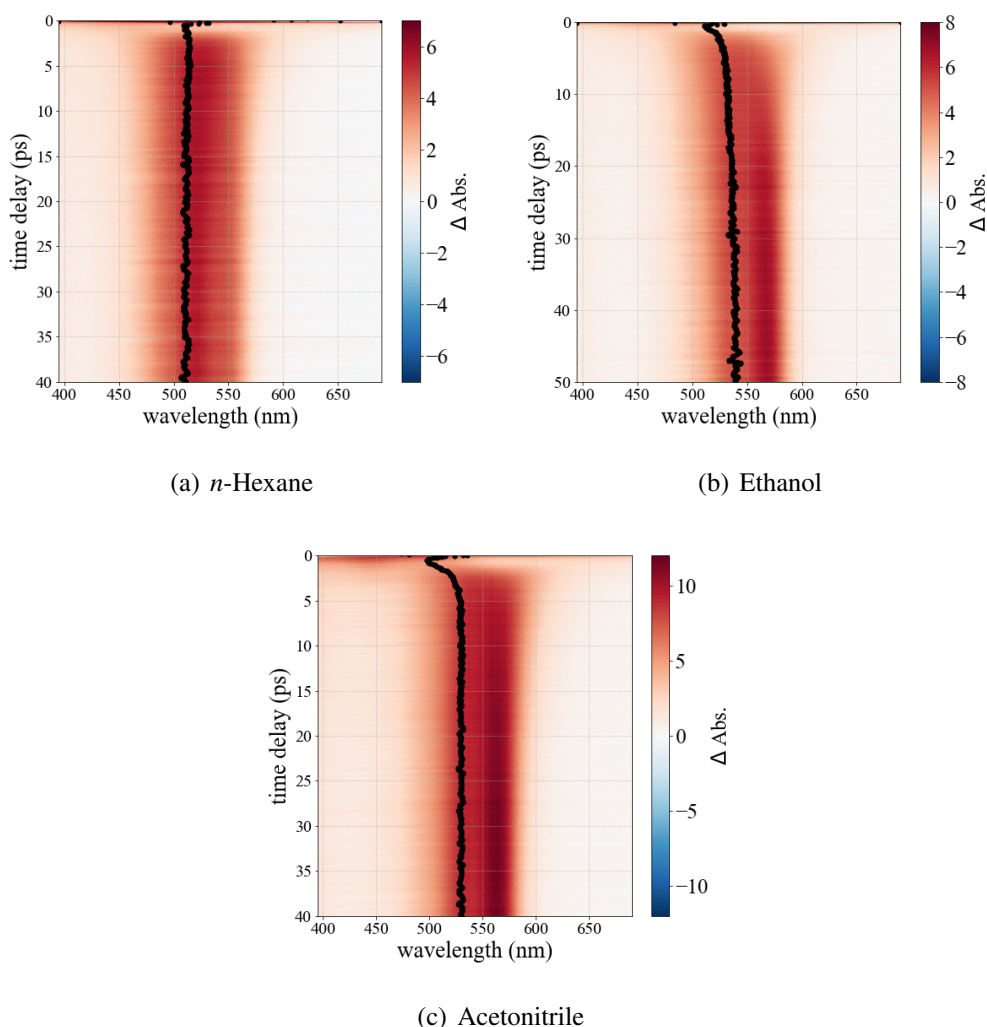


**Figure A.12:** Spectral centers of gravity (black circles) of photoexcited SNP in (a) hexane, (b) ethanol and (c) acetonitrile, overlaid with the corresponding TA data.

Further results from the DLSA including maps of the fits and the residuals as well as depiction of the individual components, if not part of the main text, are provided in Figs. A.13-A.15. In addition, results from the exponential fits of the Gaussian integrals are collated in Tab. A.2.

Populations of the electronic states from the TD-DFT molecular dynamics simulations of photoexcited SNP, carried out by Dr. Raison Dsouza, are plotted in Fig. A.16 including fits using a unidirectional sequential model. The time scales for internal conversion to  $S_1$  (88 fs) and relaxation to the ground state (1.3 ps) agree well with the excited-state absorption dynamics measured in the solution TA.

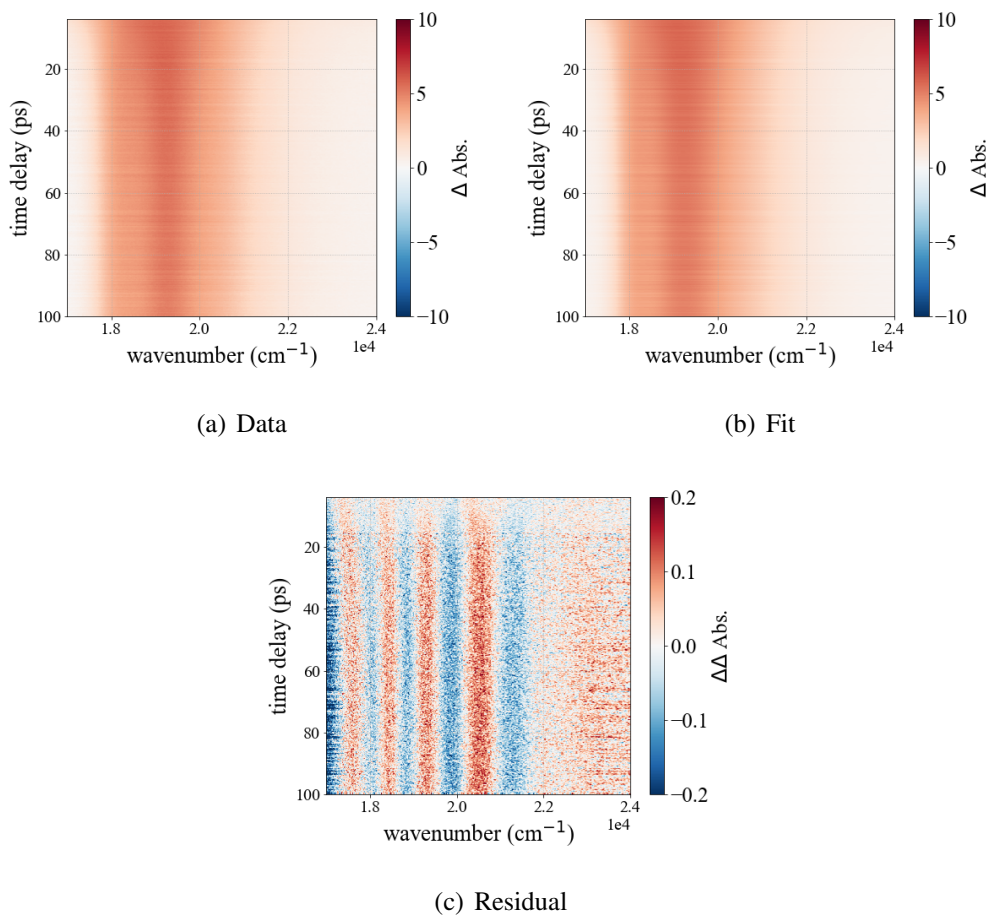


**Figure A.13:** Dynamic line shape analysis of SNP in *n*-hexane.

#### A.4.2 SNP crystal

In order to demonstrate that a meta-stable state was found in the data from photoexcited SNP in crystal between approximately 25 and 45 ps, spectral traces from this time window are depicted in Fig. A.17. They complement the spectral traces from the entire measurement window shown in Fig. 3.15 (d).

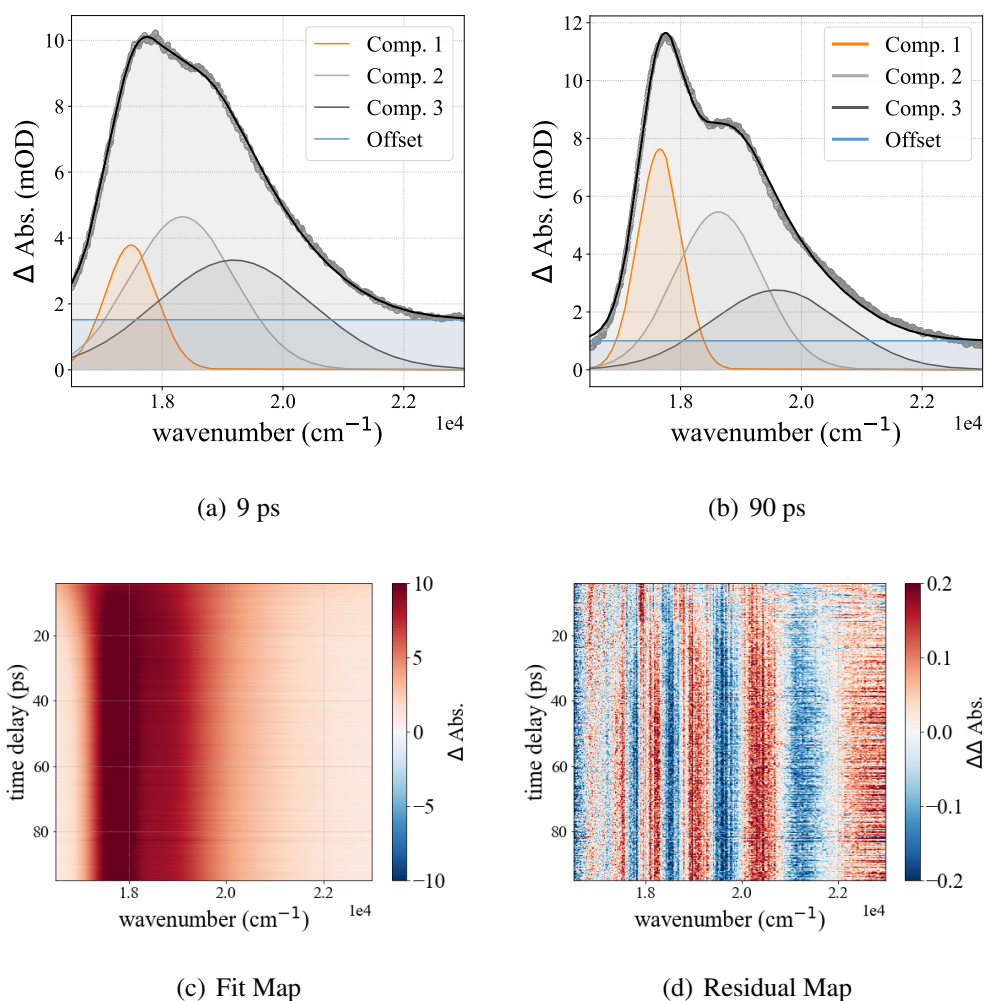


**Figure A.14:** Dynamic line shape analysis of SNP in acetonitrile.

**Table A.2:** Exponential fits of Gaussian areas using biexponential functions in case of the fits using four Gaussians and a single exponential with an offset in case of the ethanol fit with three Gaussians. In addition to the time constants the exponential amplitudes  $A$  are given for the former case and the offset for the latter.

	Hexane		Acetonitrile		Ethanol	
	$\tau$ [ps]	$A$ [ $\text{cm}^{-1}$ ]	$\tau$ [ps]	$A$ [ $\text{cm}^{-1}$ ]	$\tau$ [ps]	$A$ [ $\text{cm}^{-1}$ ]
Area 1	11.5 (r)	$-4.56 \cdot 10^3$	13.5 (r)	$-1.77 \cdot 10^4$	11.9 (r)	$-1.20 \cdot 10^4$
	$1.05 \cdot 10^3$	$7.08 \cdot 10^3$	$3.5 \cdot 10^3$	$2.8 \cdot 10^4$	inf	$1.64 \cdot 10^4$
Area 2	7.37 (r)	$-7.15 \cdot 10^3$	50.1 (r)	$-8.81 \cdot 10^3$	63 (d)	$7.47 \cdot 10^3$
	$1.28 \cdot 10^3$	$2.07 \cdot 10^4$	400 (d)	$5.13 \cdot 10^3$	inf	$2.06 \cdot 10^4$

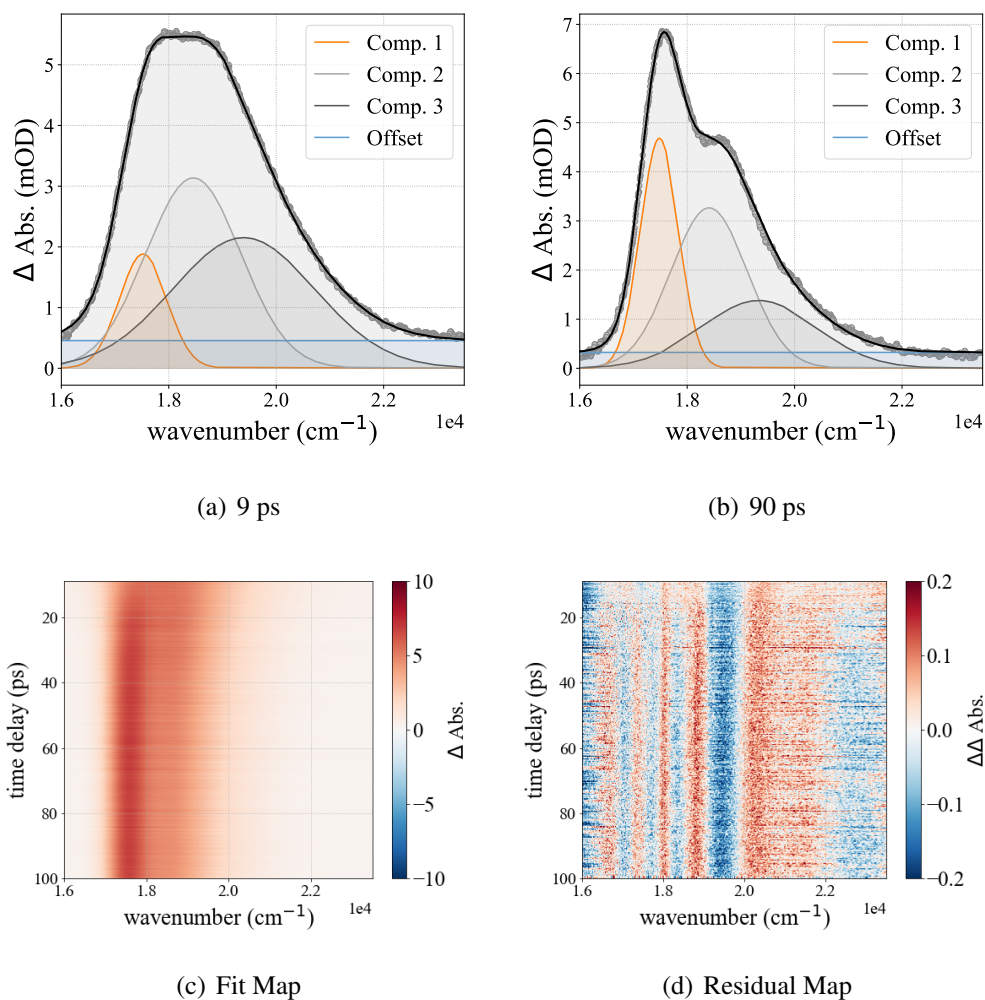


**Figure A.15:** Dynamic line shape analysis of SNP in ethanol.

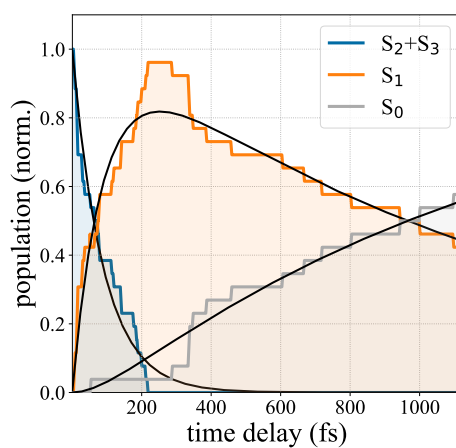


**Figure A.16:** SNP molecular dynamics simulation: Electronic state populations and kinetic fits using a two-step model.  $\tau_1 = 88$  fs,  $\tau_2 = 1.3$  ps.

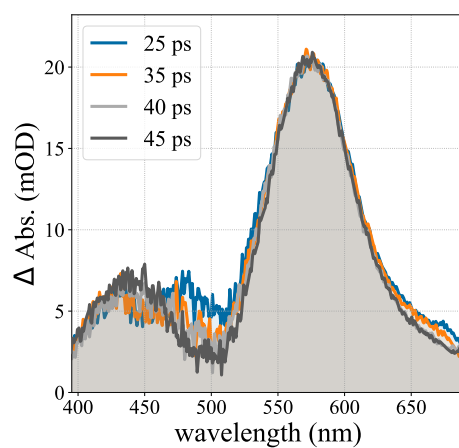


**Figure A.17:** Additional spectral traces from the TA data of photoexcited, crystalline spironaphthopyran for the time range between 25 and 45 ps.

### A.4.3 Protonated spiropyrans

Additional information on the DLSA results from photoexcited Z-MCH<sup>+</sup> (BIPS) and Z-NMCH<sup>+</sup> (Nitro-BIPS) is given in this section. Fig. A.18 and Fig. A.19 show fit and residual maps of the two different compounds. In addition, the two width parameters of the utilized Voigt profile (Gaussian parameter  $\sigma$  and Lorentzian parameter  $\gamma$ ) for Z-MCH<sup>+</sup> are plotted in Fig. A.20. The ratio between them is an indication whether the profile is more "Gaussian-like" or "Lorentzian-like".

Since in the main text, only the time constants from the applied kinetic models to the Voigt-profile amplitudes (= integrals) were shown and discussed, the exponential amplitudes (related to the transition dipole moments of the species) are shown in Tabs. A.3 and A.4 for Z-MCH<sup>+</sup> and its nitro-substituted analog, respectively.

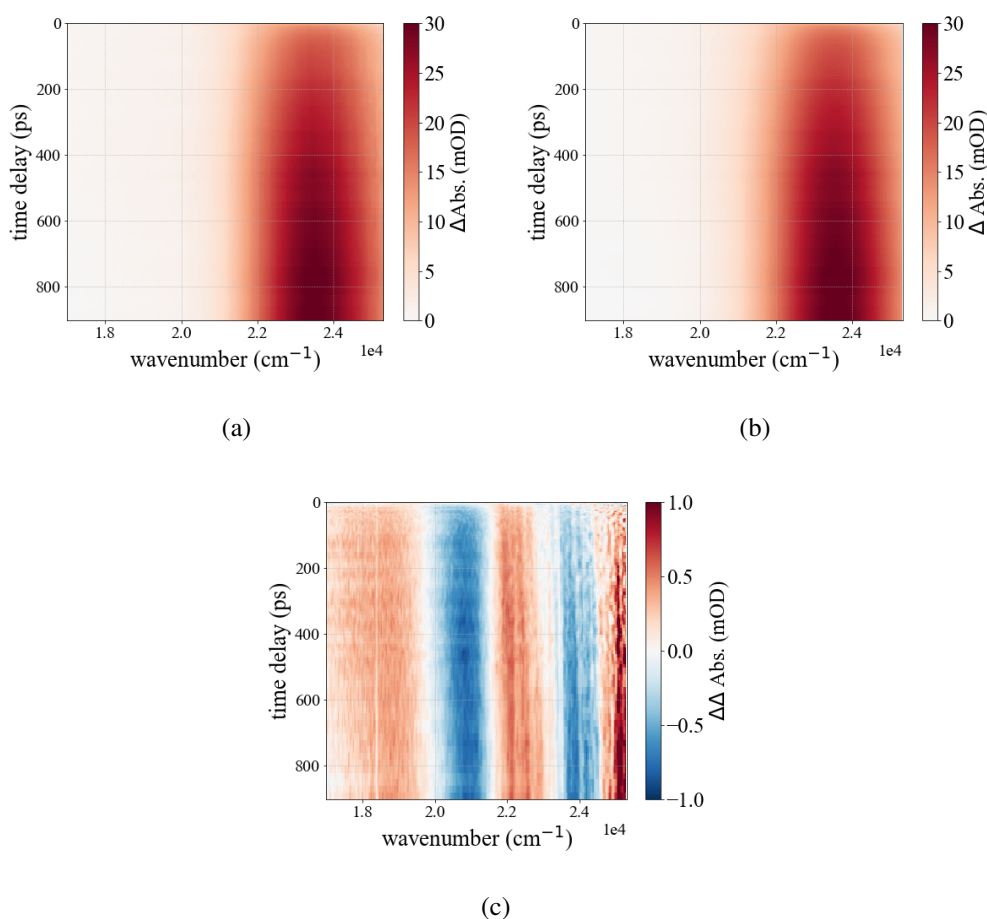


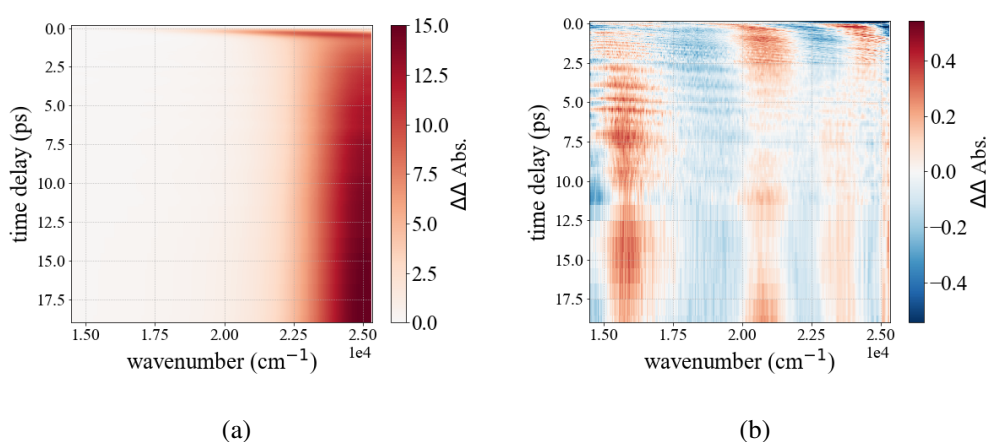
**Figure A.18:** Dynamic line shape analysis of photoexcited Z-MCH<sup>+</sup>: (a) Data range, (b) fit and (c) residual maps.

The left singular vectors from TA of E-Nitro-MCH<sup>+</sup> are shown for the entire measured range in Fig. A.21, in order to complement the view focusing on the short range depicted in Fig. 4.19 of the main text (section 4.4.2).

Results from the two kinetic models applied to the TA data from the same sample, but probed in the UV and discussed in section 4.4.2 are depicted in Fig. A.22 in terms of the

**Table A.3:** Amplitudes from the applied kinetic models for the line integrals from DLSA of photoexcited MCH<sup>+</sup>.

Species	Unidirectional	Branched	Branched*	Branched**
B	$1.5 \cdot 10^5 \pm 2.5 \cdot 10^4$	$1.6 \cdot 10^5 \pm 3 \cdot 10^6$	$2 \cdot 10^5 \pm 3 \cdot 10^5$	$2 \cdot 10^5 \pm 1 \cdot 10^5$
C	$3.3 \cdot 10^4 \pm 4 \cdot 10^2$	$5 \cdot 10^4 \pm 4 \cdot 10^8$	0.0 (fixed)	$5.7 \cdot 10^4 \pm 6 \cdot 10^2$
D	$6.5 \cdot 10^4 \pm 2 \cdot 10^2$	$1.5 \cdot 10^4 \pm 6 \cdot 10^8$	$4.5 \cdot 10^4 \pm 3.5 \cdot 10^2$	0.0 (fixed)
E	$1.11 \cdot 10^5 \pm 4 \cdot 10^2$	$1.12 \cdot 10^5 \pm 5 \cdot 10^2$	$1.12 \cdot 10^5 \pm 5 \cdot 10^2$	$1.12 \cdot 10^5 \pm 5 \cdot 10^2$

**Figure A.19:** Dynamic line shape analysis of photoexcited Z-Nitro-MCH<sup>+</sup>: Maps of (a) fit and (b) residual.

species-associated spectra and plots of the species concentrations in time. Chain refers to a unidirectional sequential model, while in the branched model, the initial species A reacts to the product C either directly or via the intermediate species B (see eq. 4.3). As evident from this comparison, both models describe the transient data reasonably well and the obtained time constants were identical and matched the lifetimes from global analysis (2.4 ps and 37 ps).

For completeness, global analysis results from BIPS in both an equimolar H<sub>3</sub>PO<sub>4</sub> solution and a non-acidic one are shown in Fig. A.23. They complement the results from target analysis (see Fig. 4.26 in section 4.5.2) and matching time constants were obtained.

**Table A.4:** Amplitudes ( $\text{mOD} \cdot \text{cm}^{-1}$ ) from the kinetic sequential fit of the DLSA line integrals of photoexcited Z-Nitro-MCH<sup>+</sup>, corresponding to the transfer time constants in Tab. 4.2.

Model	B	C	D	E
I	$1.2 \cdot 10^5 \pm 6 \cdot 10^4$	$4.4 \cdot 10^4 \pm 5 \cdot 10^2$	$6.3 \cdot 10^5 \pm 3 \cdot 10^3$	–
II	$1.4 \cdot 10^5 \pm 1.6 \cdot 10^5$	$3.1 \cdot 10^4 \pm 7 \cdot 10^3$	$5.3 \cdot 10^4 \pm 5 \cdot 10^2$	$4 \cdot 10^5 \pm 1 \cdot 10^6$

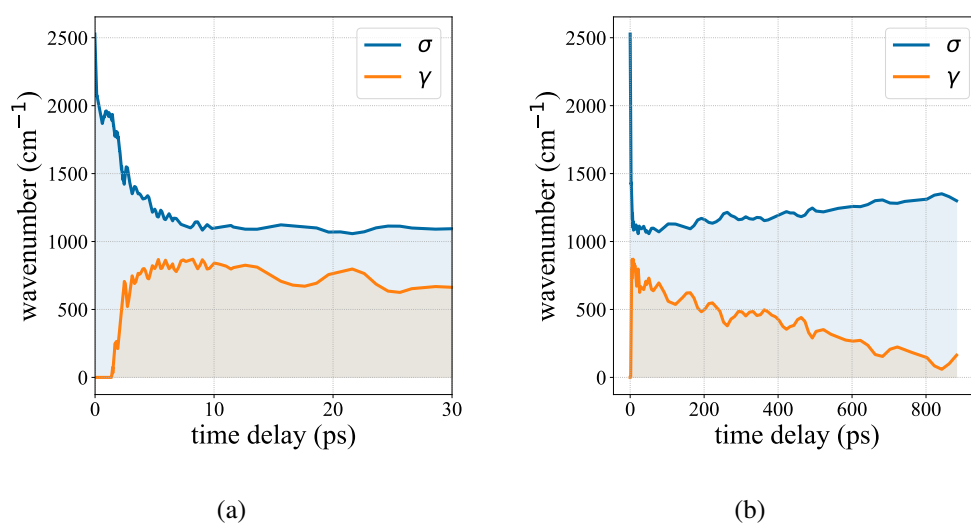


**Figure A.20:** Dynamic line shape analysis of photoexcited Z-MCH<sup>+</sup>: Parameter traces for the Gaussian and Lorentzian line width parameters  $\sigma$  and  $\gamma$ , shown for (a) the first 30 ps and (b) the entire fit range.

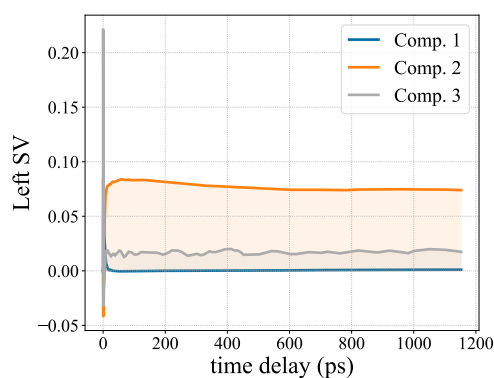


**Figure A.21:** Left singular vectors of the TA data from photoexcited E-Nitro-MCH<sup>+</sup>. Shown for the entire measurement range to complement Fig. 4.19.

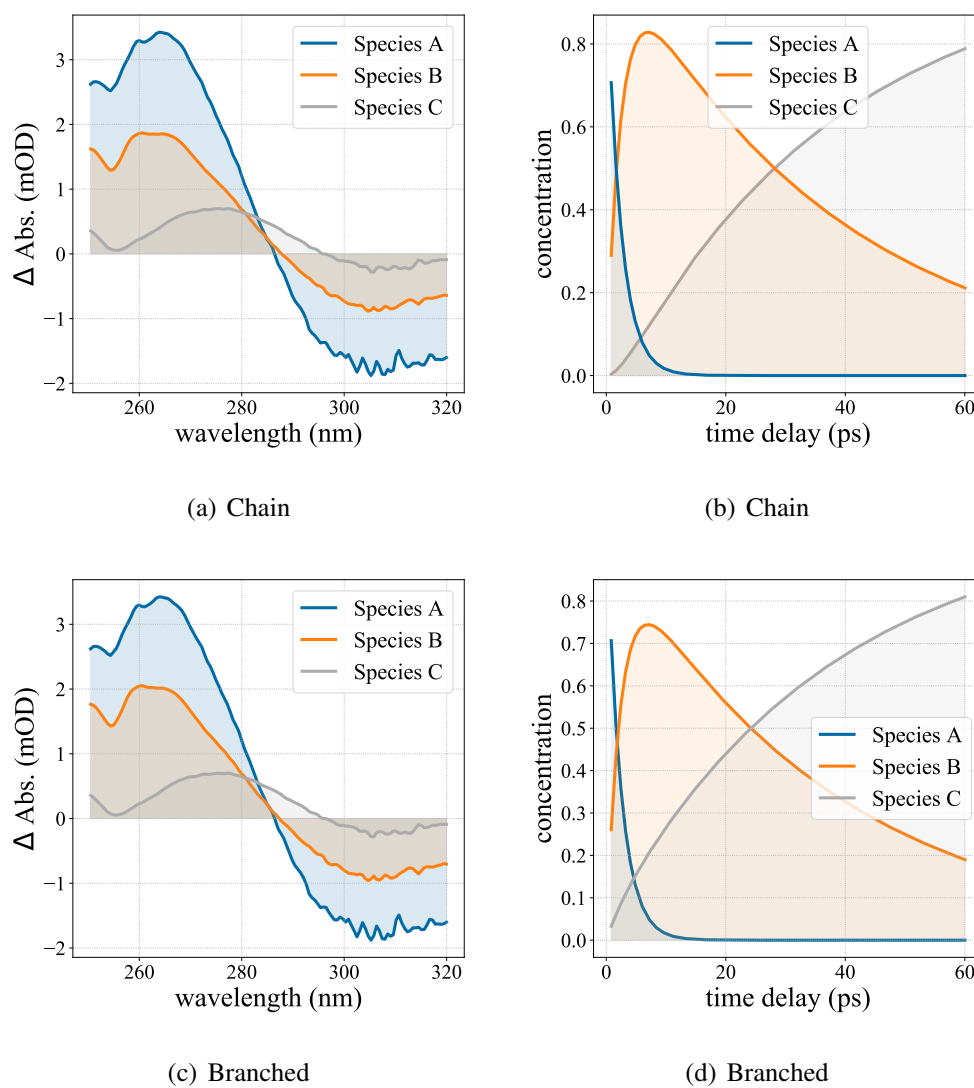


**Figure A.22:** Target analysis of photoexcited E-MCH<sup>+</sup>, probed in the UV.

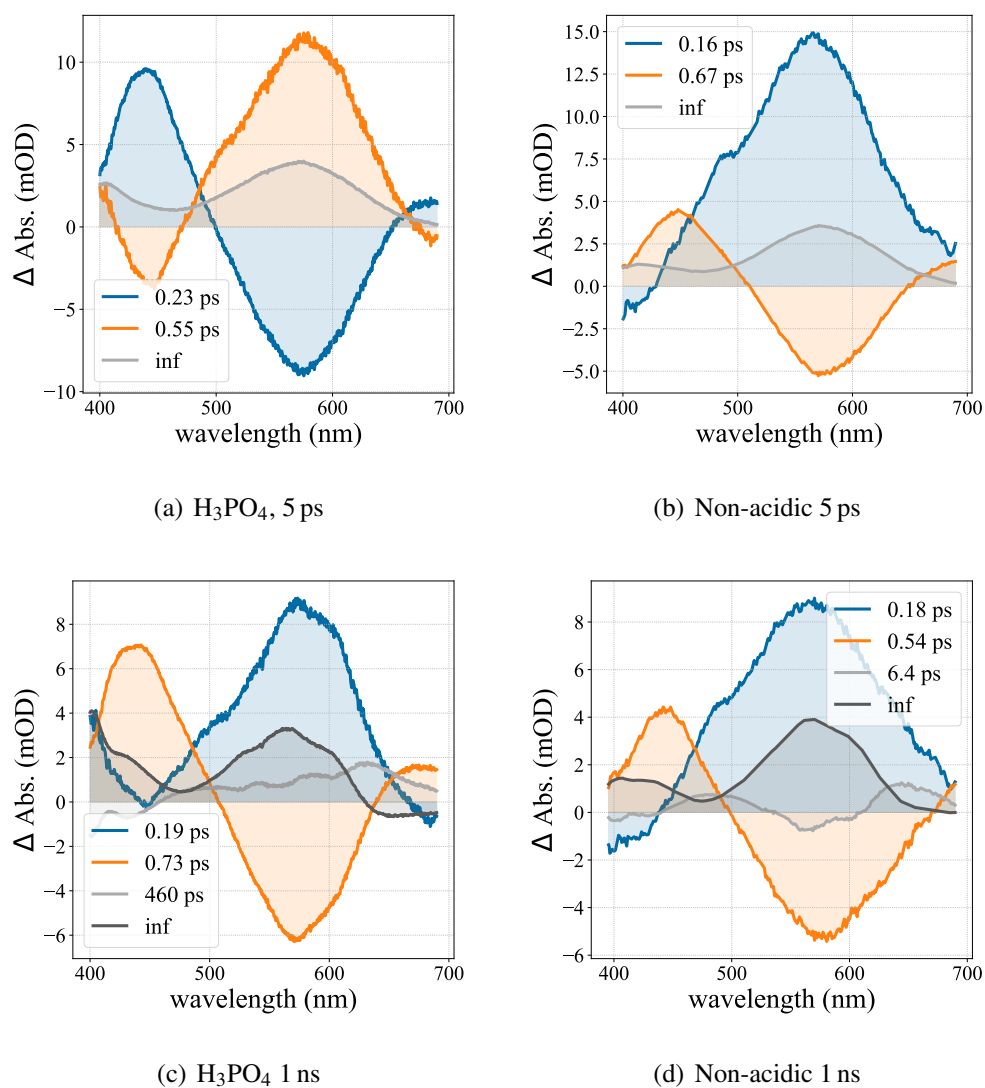


**Figure A.23:** Global analysis of BIPS in  $\text{H}_3\text{PO}_4$  (equimolar) and non-acidic acetonitrile solutions.

## A.4.4 Diarylethene

Kinetic trace fits of the tail regions of the closed-ring product absorption of Pr-DFE in crystal are shown in Fig. A.24. Associated decay constants of the exponential fits were 1 ps at 400 nm and 3.3 ps at 600 nm. For further discussion see section 5.3.2.

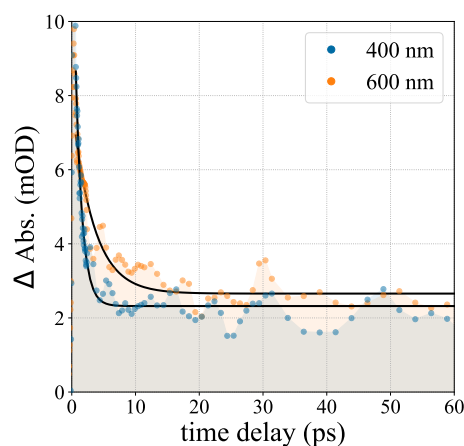


**Figure A.24:** Additional kinetic traces from the TA data of crystalline Pr-DFE including exponential fits. Decay times were determined as 1 ps at 400 nm and 3.3 ps at 600 nm.

## A.5 Electron diffraction

### A.5.1 Orientation finding and indexing

In order to facilitate the discussion of changes in individual peaks, coarse and manual orientation finding using CrystalMaker<sup>[178]</sup> was carried out using the reported crystallographic data of the samples and measured diffraction patterns. The results of this are shown in Fig. A.25 and Fig. A.26 for SNP and the diarylethenes, respectively. Evidently, only a rough agreement between measurements and simulation was possible to obtain, suffering in some cases from slight mismatches in lattice constants and/or peak intensities. Besides general shortcomings of the simulation itself, this is likely due to small distortions in the images and in case of Et-DTE and Bu-DTE mismatch in temperature of the measurements, as the reported data was measured at 123 K in these cases, while the electron diffraction patterns were recorded at 220-270 K. While for the qualitative purposes in this thesis, this indexing process is sufficient, more extensive data analysis should include appropriate simulation and algorithmic orientation finding.

### A.5.2 SNP ED addendum

Additional electron diffraction data from single-crystalline spironaphthopyran are provided in this section. Fig. A.27 shows a comparison between crystals grown via solvent

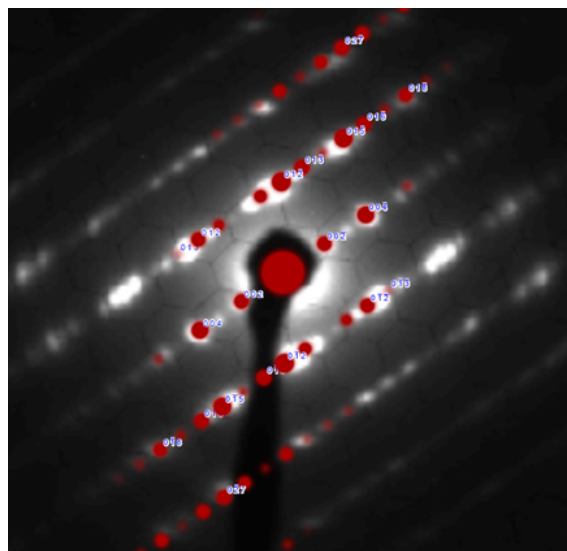


**Figure A.25:** Based on the reported crystallographic data ([174]), simulated patterns (red circles) using CrystalMaker were overlaid and compared with the measured electron diffraction images, to obtain a rough agreement.

evaporation and those grown via vapor diffusion. The drastic improvement by using the latter is imminent. Furthermore, the consistency between sample cuts from the same crystal was significantly better for the crystals grown via vapor diffusion. Overall, this method proved superior for SNP and is recommended for similar compounds if results from solvent evaporation are not satisfactory.

An example for the time-resolved differential diffraction signal from UED scans of SNP is shown in terms of the absolute signal difference in region-of-interests determined by a peak finding algorithm. A non-zero signal can be discerned when comparing later time-points to earlier ones. The time zero on this axis was determined via a different sample but appears to be earlier in this case (between -10 and 0 ps).

In order to estimate the reversibility of the sample and check for potential damage, the total diffraction intensity for individual frames in the time-resolved measurement was inspected and plotted in terms of the ROI intensities for the brightest peaks (see Fig. A.29). After an initial drop of about 3 %, potentially due to heating of the sample or induced crystal strain, the diffraction intensity remained relatively constant and the drop was only observed for fresh samples. Cumulative damage of the sample was thus not observed, which verifies the experimental conditions to be appropriate.

### A.5.3 DTE UED frame analysis

In order to estimate the required experimental parameters for a time-resolved electron diffraction experiment, the following procedure was carried out. Single-shot excitation of the sample with the 343 nm laser pulse at a fluence of  $1 \text{ mJcm}^{-2}$  using optical choppers and a mechanical shutter was realized in manually controlled cycles, between which static electron diffraction patterns were measured. These patterns were averages of indi-

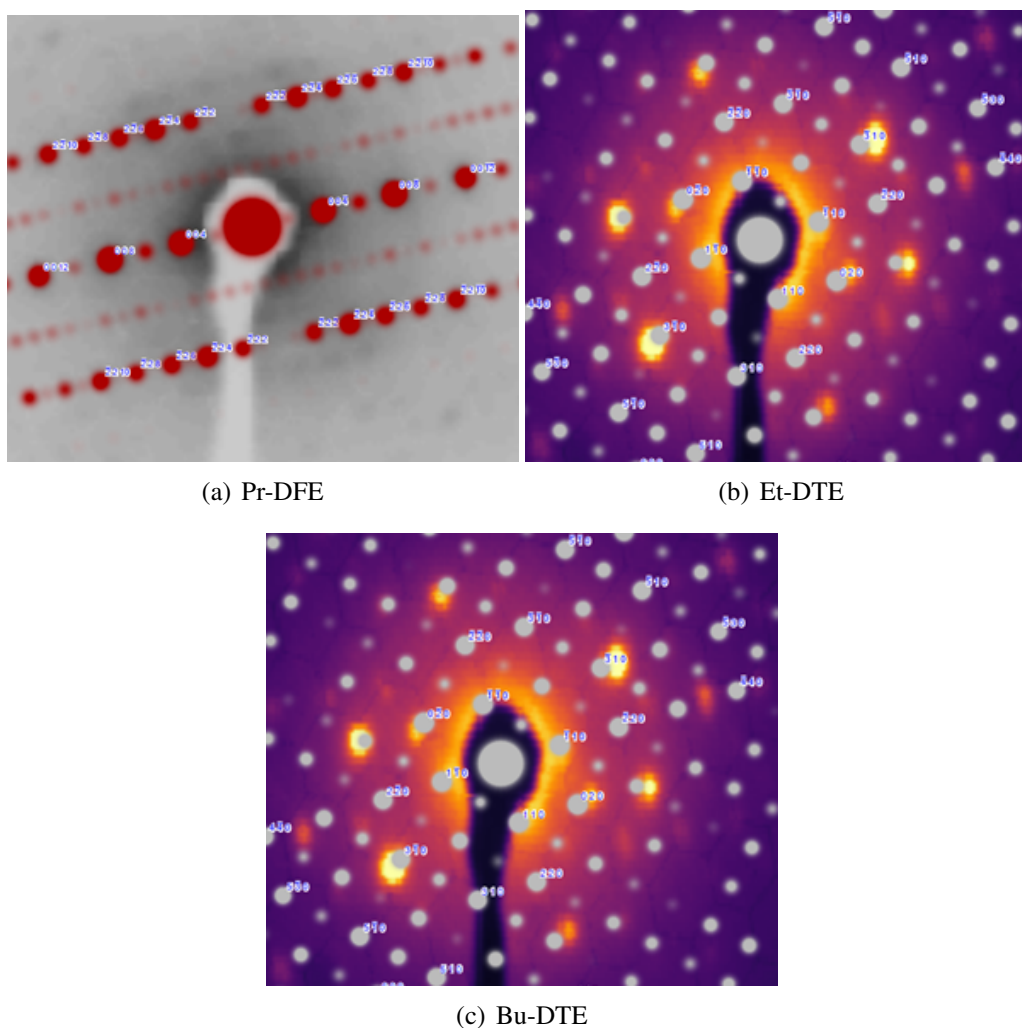


**Figure A.26:** Coarse indexing of the electron diffraction patterns from the three diarylethene derivatives. Based on the reported crystallographic data ([231, 232]), simulated patterns (grey circles) using CrystalMaker were overlaid and compared with the measured electron diffraction images, to obtain a rough agreement.

vidual frames, each containing the accumulated image of  $\approx 7.8 \cdot 10^6$  electrons.<sup>5</sup> Saving each frame separately allowed for a frame-by-frame accumulation of the patterns for each consecutive excitation cycle. A region-of-interest (ROI) analysis of the difference between these patterns and the initial pattern before any excitation was used to estimate the required number of electrons for averaging (related to the number of accumulated frames) and the required excitation density (related to the number of accumulated excitation pulses). The total absolute difference diffraction from the ROIs is plotted for Et-DTE and Bu-DTE in Fig. A.30. In terms of the number of frames, little change occurs after the first  $\approx 100$  frames, giving a rough estimate for how many electrons per time point are required in the time-resolved experiments ( $10^8$ - $10^9$ ). Of course, more averaging gen-

<sup>5</sup>The number of electrons was not measured directly, but determined through an electron beam current measurement for different photocathode beam pulse energies and a linear interpolation. This enabled adjusting the number of electrons per pulse via the power of the photocathode beam.

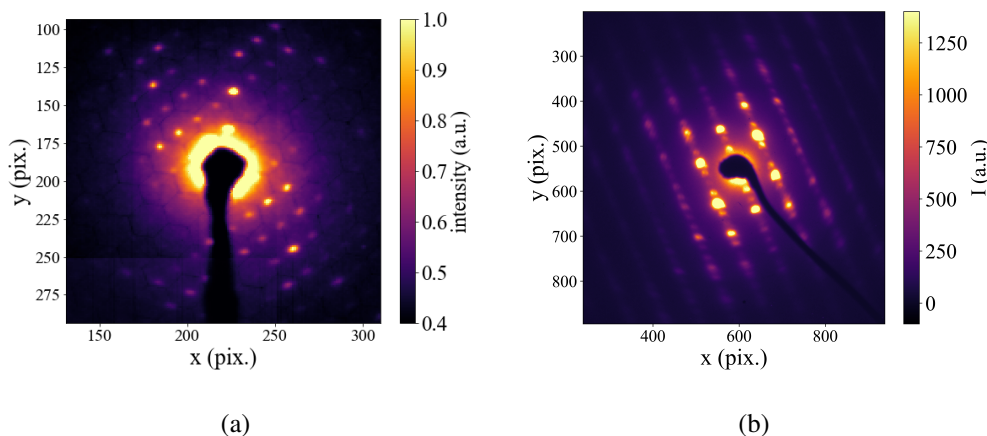
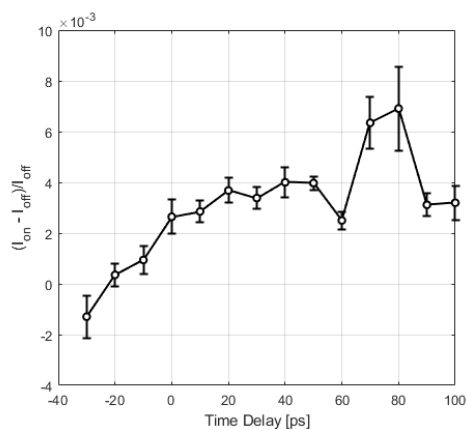


**Figure A.27:** Static diffraction pattern of SNP crystals, grown by (a) solvent evaporation and (b) vapor diffusion. The latter was adapted from Fig. 3.20 for comparison. The larger background from the unscattered beam in (a) compared to (b) is an indication for the drastically improved diffraction quality (Intensity scales were adjusted to the brightest diffraction peaks for either image).

erally leads to a higher signal-to-noise ratio, but the benefit has to be compared to the cost, i.e. the limited number of photocycles per sample. Increase of the difference signal via accumulated excitation pulses is only significant within approximately the first 10 cycles, although the variance between cycles prohibits definite statements. Beyond this, a decrease in signal can be distinguished, which is likely due to beginning sample deterioration, since the closed-ring product was not reverted but hit with the 343 nm laser beam. Furthermore, the UV pulses also revert a portion of the closed-ring product, which is why this is only a coarse estimate for the optimal fluence. It appears however, that fluences in the few- $\text{mJcm}^{-2}$  regime should be sufficient for the time-resolved experiment.

Like the time-resolved tests, these static measurements were limited by the time frame of the PhD project and ideally should be extended upon, before the realization of time-resolved scans, since this type of analysis is comparatively simple and can be carried out for many more samples within a reasonable time frame.



(a)

**Figure A.28:** Total absolute diffraction difference from a time-resolved electron diffraction scan of SNP.

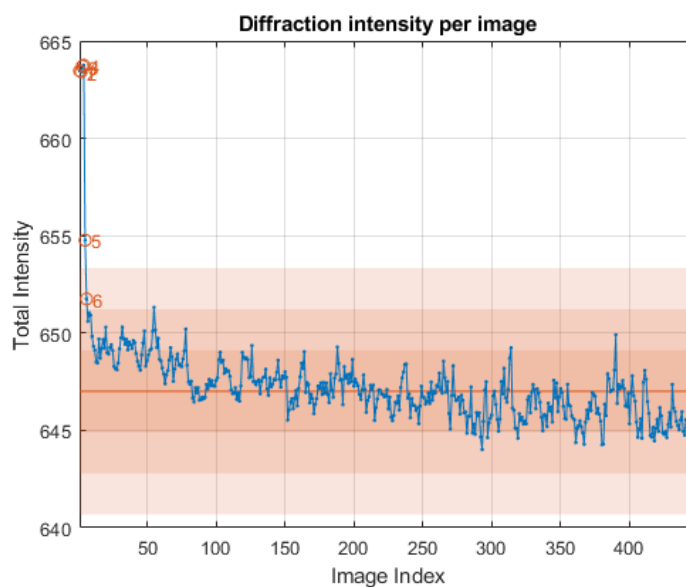
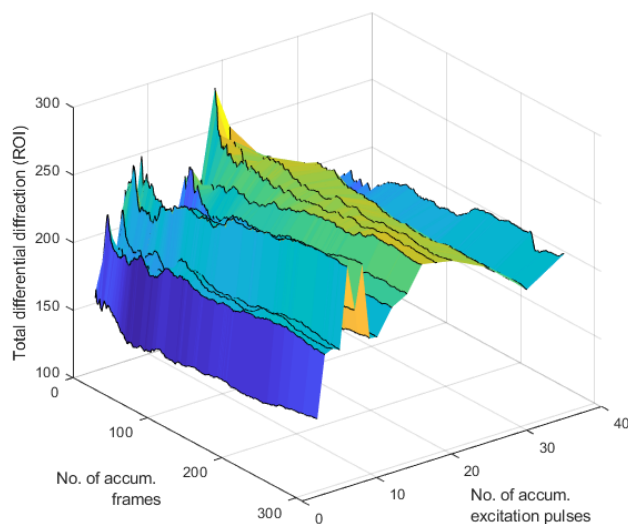
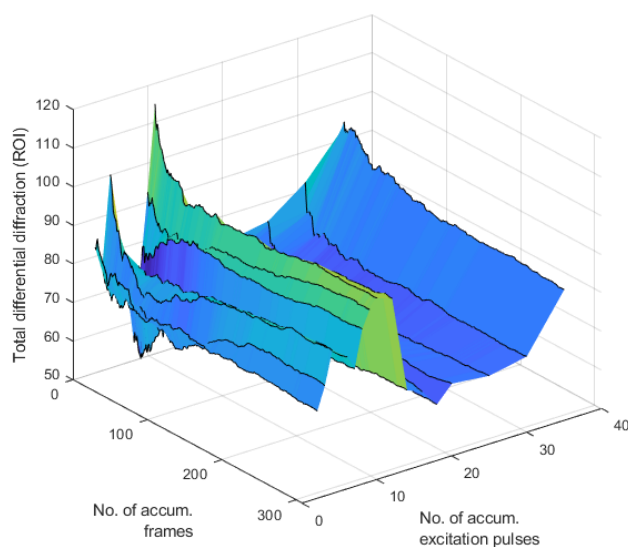


**Figure A.29:** Total electron diffraction intensity of a fresh, single-crystalline spironaphotopyran sample during time-resolved experiments. Within the first ten acquired frames, an intensity loss of 3 % was observed, before reaching an approximately constant level.



(a) Et-DTE



(b) Bu-DTE

**Figure A.30:** Per-frame analysis of static electron diffraction patterns of (a) Et-DTE and (b) Bu-DTE with accumulated UV excitation. Plotted is the differential diffraction in the most intense peaks, in which a steady-state difference is known to manifest from static diffraction patterns and how it improves or stabilizes with increased number of averaged diffraction patterns and UV excitation cycles.

## A.6 Optical Setups Addendum

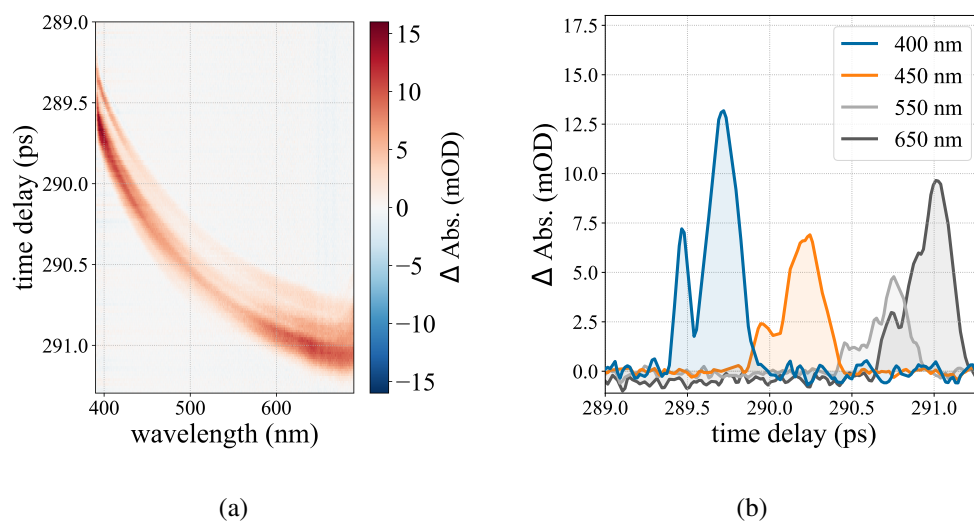


**Figure A.31:** CPM of the broadband UV laser pulse centered at 330 nm and the visible supercontinuum probe in the TA setup. (a) TA map, (b) select kinetic traces.

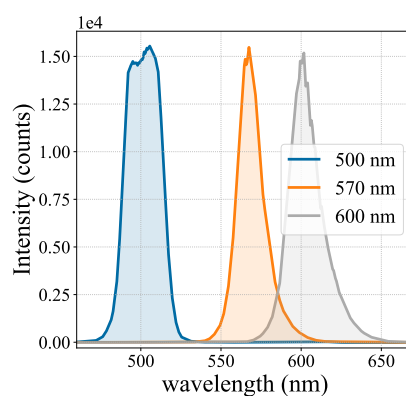


**Figure A.32:** Example spectra from the visible NOPA that was used exclusively for photoreversion, shown for three different central wavelengths.



the general form:

$$\frac{d}{dt}y(t) + f(t) \cdot y(t) = g(t) \quad (\text{A.8})$$

Differential equations of this form can be solved by the variation of the constant ansatz:

$$y(t) = \left[ \int g(t) \cdot e^{F(t)} dt + const \right] \cdot e^{-F(t)} \quad (\text{A.9})$$

with  $F(t) = \int f(t)dt$  and an arbitrary constant *const*.<sup>6</sup> This strategy was used for all utilized kinetic models in this thesis and will be demonstrated once for a relatively simple example in the following.

The exemplary model is a simple branched model, in which species A decays into two different species B and C with rate constants  $k_{AB}$  and  $k_{AC}$ , each of these species having finite lifetimes (rate constants  $k_B$  and  $k_C$ ):



The resulting differential equations for the associated concentrations A, B and C are:

$$\begin{aligned}
 \text{(i)} \quad & \frac{dA}{dt} = -k_{AB} \cdot A - k_{AC} \cdot A \\
 \text{(ii)} \quad & \frac{dB}{dt} = k_{AB} \cdot A - k_B \cdot B \\
 \text{(iii)} \quad & \frac{dC}{dt} = k_{AC} \cdot A - k_C \cdot C
 \end{aligned}$$

The solution for (i) is readily obtained as:

$$A = A_0 \cdot e^{-k_A \cdot t} \quad (\text{A.11})$$

wherein  $A_0$  is the initial concentration of species A upon excitation and  $k_A = k_{AB} + k_{AC}$ . Inserting the solution for A into DEq (ii) and (iii) yields the differential equations to be solved via variation of the constant (equation A.9). The obtained solution for  $B(t)$  is thus:

$$B(t) = A_0 \frac{k_{AB}}{k_B - k_A} \cdot e^{-k_A t} + const \cdot e^{-k_B t} \quad (\text{A.12})$$

<sup>6</sup>For the models applied here,  $f$  was time independent and its antiderivative  $F(t)$  simply equal to  $f \cdot t$ .

The constant can be determined via boundary conditions for  $t = 0$  using the initial concentrations  $A_0$  and  $B_0$ :

$$\text{const} = B_0 - A_0 \frac{k_{AB}}{k_B - k_A} \quad (\text{A.13})$$

While inserting this expression for *const* into equation A.12 yields the general solution for  $B(t)$ , for the applied models  $A_0$  and  $B_0$  were assumed to be 1 and 0, respectively, meaning that species A encompasses the entire distribution of the initially created excited-state population. Under these conditions, the solution for  $B$  becomes:

$$B(t) = \frac{k_{AB}}{k_B - k_A} \left[ e^{-k_A t} - e^{-k_B t} \right] \quad (\text{A.14})$$

Due to the equivalence of DEq (ii) and (iii), the solution for  $C(t)$  is readily obtained:

$$C(t) = \frac{k_{AC}}{k_C - k_A} \left[ e^{-k_A t} - e^{-k_C t} \right] \quad (\text{A.15})$$

Evidently, this is only due to the symmetry of the applied model. For more complex models, further differential equations have to be solved, but the underlying principle is always the same for the investigated unimolecular reactions.

## A.7.2 Beam size calculation

Assuming a Gaussian intensity profile, the beam diameter at full-width half maximum (FWHM) can be calculated from the transmission  $T$  ( $I/I_0$ ) through a pinhole with radius  $r$ :

$$\text{FWHM} = 2r \cdot \sqrt{\frac{\ln(2)}{\ln\left(\frac{1}{1-T}\right)}} \quad (\text{A.16})$$

## A.7.3 Peak fluence calculation

Important experimental parameters in the study of photochemical reaction dynamics are the peak fluence and the peak power, since too high values of these quantities can cause sample damage or induce multi-photon absorption processes, detrimental to both the experiment and data interpretation. Since approximate thresholds for these quantities are known, calculating and reporting the pump fluences gives an estimate of what are safe starting parameters. However, since the peak power is less readily obtained (requiring precise knowledge of the pulse duration), fluence dependences are carried out in addition. In the following, a way to calculate the peak fluence is laid out briefly and how it can be related to the peak intensity.<sup>7</sup> Although in practice, the beam sizes are to be set in such a way, that the probed volume is approximately homogeneously irradiated, the spatial intensity profile of the beam is not constant across the sample area and cannot be measured

<sup>7</sup>The calculation was adopted from ref. [85].

directly. Instead, the pulse energy is determined routinely via measuring the power at a known repetition rate. The pulse energy  $E$  is related to the fluence as its spatial integral over the sample plane. Assuming a Gaussian profile of the fluence  $F(r)$  with half width  $w_0$  at  $1/e^2$  intensity and peak fluence  $F_0$ :

$$F(r) = F_0 \left[ -2 \left( \frac{r}{w_0} \right)^2 \right] \quad (\text{A.17})$$

the integral can be solved and rearranged to yield the peak fluence:

$$F_0 = E \frac{2}{\pi w_0^2} \quad (\text{A.18})$$

$w_0$  is proportional to the full width at half maximum (FWHM) by a factor of  $\approx 0.849$ . The peak intensity  $I_0$  for a pulse with duration  $\Delta t$  (FWHM) is related to the peak fluence by:

$$I_0 = 2 \sqrt{\frac{\ln 2}{\pi}} \frac{F_0}{\Delta t} \quad (\text{A.19})$$

To give an example with values typical for the discussed experiments, a pump beam with a pulse energy of 100 nJ (100  $\mu$ W at 1 kHz), a beam diameter of 100  $\mu$ m (FWHM) and a duration of 100 fs (FWHM) has a peak fluence of 0.88 mJcm<sup>-2</sup> and a peak intensity of 8.3 GW.

#### A.7.4 NOPA phase matching angle calculation

The phase-matching angle  $\theta_{\text{pm}}$  for optical parametric amplification in a non-collinear geometry with (internal) angle  $\alpha$  between pump and seed is given by:

$$\theta_{\text{pm}}(\lambda_s, \lambda_p, \alpha) = \arcsin \left( \left[ \frac{n_{\text{op}}^2}{n_{\text{p}}^2} - 1 \right]^{\frac{1}{2}} \cdot \left[ \frac{n_{\text{op}}^2}{n_{\text{ep}}^2} - 1 \right]^{-\frac{1}{2}} \right) \quad (\text{A.20})$$

with

$$n_{\text{p}} = \frac{\lambda_{\text{p}}}{\lambda_{\text{s}}} n_{\text{os}} \left[ \cos(\alpha) + \sqrt{\frac{\lambda_{\text{s}}^2 n_{\text{oi}}^2}{\lambda_{\text{i}}^2 n_{\text{os}}^2} - \sin^2(\alpha)} \right] \quad (\text{A.21})$$

where the indices p, s and i designate pump, signal and idler parameters, o and e the respective polarisations (ordinary and extraordinary),  $n$  is the principal refractive index and  $\lambda$  the wavelength.<sup>[84]</sup>

### A.7.5 Electron pulse generation

According to the Schottky effect,<sup>[281]</sup> application of an external electric field lowers the effective work function  $\phi_e$  of a material with work function  $\phi_w$ :

$$\phi_e = \phi_w - \sqrt{\frac{e^3 E_z}{4\pi\epsilon_0}} \quad (\text{A.22})$$

with the elementary charge  $e$ , the applied electric field  $E_z$  and the vacuum permittivity  $\epsilon_0$ . For a gold photocathode ( $\phi_w = 4.83$  eV),<sup>[282]</sup> and an applied voltage of 100 kV at photocathode distance to the anode of 12 mm, the effective work function is reduced to  $\phi_e = 4.72$  eV. This puts it in the range where photo-emission using 266 nm or 257 nm pulses (4.66 eV and 4.82 eV) is feasible.